Microstructured Tellurite Glass Fibre Laser Development

by

Michael Raymond Oermann

A Thesis Submitted to the
University of Adelaide
for the degree of

DOCTOR OF PHILOSOPHY

in the

Faculty of Science
School of Chemistry & Physics

November 2011

Supervisors:

_____

Prof. Tanya Monro, Principal Supervisor

_____

A/Prof. Peter Veitch, Co-supervisor

_____

A/Prof. Heike Ebendorff-Heidepriem, Co-supervisor

_____

Dr. David Ottaway, Co-supervisor

The University of Adelaide
Adelaide, South Australia
November, 2011

CONTENTS

ABSTRACT

This thesis contains a study of the suitability of tellurite glass for use in microstructured fibre lasers. This thesis looks into the possibility for lasing at around 3μm, where tellurite glass is transparent. To test the lasing potential of fabricated tellurite glass microstructured fibres, lasing at 1.5μm was demonstrated.

The research contained within this thesis includes: The development and characterisation of the tellurite glass composition; including modifications made to this composition to match the refractive indices of the doped and undoped glasses, reducing the glass material loss, finding the glass crystallisation stability and density as well as measuring the temperature dependence of the glass melt viscosity, of which an understanding is required for its extrusion (Chapter 2). The fabrication of microstructured tellurite fibres which included large mode area fibres, motivated by the desire to fabricate a double clad fibre and the development of small core fibres which were used in the fibre laser experiments (Chapter 3). A spectroscopic study of the erbium III doped glass including lifetimes, absorption and emission measurements (Chapter 4) and a description of the laser modelling, experiments and results (Chapter 5).

DECLARATION

I confirm that this work contains no material which has been accepted for the award of any other degree or diploma in any university or other tertiary institution to Michael Oermann and, to the best of my knowledge and belief, contains no material previously published or written by another person, except where due reference has been made in the text.

I give consent to this copy of my thesis when deposited in the University Library, being made available for loan and photocopying, subject to the provisions of the Copyright Act 1968.

The author acknowledges that copyright of published works contained within this thesis (listed on page and presented in Appendix 3) resides with the copyright holder(s) of those works.

I also give permission for the digital version of my thesis to be made available on the web, via the University's digital research repository, the Library catalogue, the Australasian Digital Theses Program (ADTP) and also through web search engines, unless permission has been granted by the University to restrict access for a period of time.

Signed:

_____

Date:

_____

ACKNOWLEDGMENTS

I would like to acknowledge a number of people for the assistance they have given me throughout my PhD.

My supervisors, Tanya Monro, Peter Veitch, Heike Ebendorff-Heidepriem and David Ottaway, have provided me with an immense amount time and effort on assisting me through every component of this project.

The optics and photonics research group as a whole. The ideas and suggestions that have been provided to me by the group, whether in a group meeting or over lunch have seen the solving of many problems that have arisen throughout this research.

The technical support that I have been given. This includes Roger Moore for a significant amount of the fibre fabrication, Alastair Dowler for some of the fibre drawing and a large amount of assistance in the workshop, Adrian Selby for machining work early in this project and Blair Middlemiss for training me in the use of the workshop machinery and for the organisation of many group social barbeques.

I would like to acknowledge the assistance provided to me to generate the results presented in Chapter 2, particularly in the glass making which was a joint effort by Herbert Foo, Kevin Kuan and Katarina Markulic. Other measurements included the DSC measurements organised by Sean Manning, and FTIR measurements done by Kevin Kuan. A special thank you to Dr Jim Richards who assisted me with the alignment of the free space laser resonator. His experience and patience was much appreciated.

This research began as a collaborative project supported by DSTO. I would therefore like to thank DSTO for their initial funding and direction for this area of work. I would also like to thank Alex Hemming, Bradley Clare, Kerry Mudge and Ken Grant for the useful discussions that occurred during this time.

I would also like to thank DSTO for the use of their equipment including their CARY spectrophotometer, and ANU for the use for their prism coupler for refractive index measurements.

I would like to achnowledge the administrative support provided by Olivia Towers and Sara Boffa who constantly help with ensuring I have completed any required paper work as well as organise any university related travel.

On a personal side, I would like to extend my thanks to my friends and family. My parents, Ray and Heather, for supporting me and providing me with the educational background required to undergo this research. I would like to acknowledge my siblings, Alison, Andrew, Catherine and Elizabeth. I know they will all succeed in everything they pursue. Most importantly, I would like to thank my wife Belinda. She has been a great motivator and has supported me through my ups and downs during my research candidature, she is my world.

PUBLICATIONS DURING CANDIDATURE

Journal publications:

M.R. Oermann, H. Ebendorff-Heidepriem, Y. Li, T.-C. Foo, T.M. Monro, "Index matching between passive and active tellurite glasses for use in microstructured fiber lasers: Erbium doped lanthanum-tellurite glass", Optics Express 17 (18), 15578-15584, August 2009

M. Oermann, H. Ebendorff-Heidepriem, D. Ottaway, D. Lancaster, P. Veitch, T.M. Monro, "Extruded microstructured fiber lasers", Submitted to Photonics Technology Letters

First author refereed conference papers (accepted for invited talk):

M. Oermann, D. Ottaway, H. Ebendorff-Heidepriem, P. Veitch, T.M. Monro "Tellurite Glass for use in 2.3μm Thulium Fibre Lasers" IQEC/CLEO Pacific Rim 2011, Sydney, August 2011

First author refereed conference papers (accepted for oral presentation):

M. Oermann, D. Ottaway, H. Ebendorff-Heidepriem, P. Veitch, T.M. Monro "Microstructured Erbium Doped Tellurite Fibre Laser" 19th Australian Institute of Physics Congress/35th Australian Conference on Optical Fibre Technology (ACOFT/AIP), Melbourne, December 2010

M.R. Oermann, D. Ottaway, P. Veitch, H. Ebendorff-Heidepriem, T.M. Monro, "Erbium-doped bulk tellurite glass laser at 1.5 μm", Australian Conference on Optics, Lasers and Spectroscopy (ACOLS), Adelaide, December 2009.

M.R. Oermann, H. Ebendorff-Heidepriem, Y. Li, T.M. Monro, "Spectroscopy of erbium in La^{3+}-doped tellurite glass & fibres", Australian Conference on Optical Fibre Technology (ACOFT), Sydney, July 2008

Co-author refereed conference papers (accepted for oral presentation):

Y. Li, M. Oermann, H. Ebendorff-Heidepriem, T.M. Monro, "Simultaneous infrared and visible emission in Er^{3+}-doped ZBLAN fibre", International Commission for Optics (ICO), Sydney, July 2008

H. Ebendorff-Heidepriem, T.C. Foo, Y. Li, M. Oermann, T.M. Monro, "New tellurite glasses for erbium fibre lasers", Australian Conference on Optical Fibre Technology (ACOFT), Sydney July 2008

Conference abstracts (accepted for oral presentation):

M.R. Oermann, Y. Li, H. Ebendorff-Heidepriem, T.M. Monro, "Core doped tellurite microstructured optical fibre for erbium fibre laser at 2.7μm", AIP Congress 2008 AOS, Adelaide, December 2008

Michael R. Oermann, Heike Ebendorff-Heidepriem, David Ottaway, Peter Veitch, Tanya M. Monro, “Tellurite glass microstructured fibre laser development”, PACRIM 2011, Cairns, July 2011

LIST OF TABLES

LIST OF FIGURES

LIST OF ABBREVIATIONS

**CoEP ` **	**C**entre of **E**xpertise in **P**hotonics (component of IPAS)
CR	**C**ross **R**elaxation
CW	**C**ontinuous **W**ave
DSC	**D**ifferential **S**canning **C**alorimetry
EDFA	**E**rbium **D**oped **F**ibre **A**mplifier
ESA	**E**xcited **S**tate **A**bsorption
ET	**E**nergy **T**ransfer
ETU	**E**nergy **T**ransfer **U**pconversion
FEM	**F**inite **E**lement **M**odelling
FSM	**F**undamental **S**pace Filling **M**ode
FTIR	**F**ourier **T**ransform **I**nfrared
GSA	**Ground State Absorption**
IPAS	**I**nstitute for **P**hotonics and **A**dvanced **S**ensing
IR	**I**nfra**r**ed
JO	**J**udd **O**felt
LMA	**L**arge **M**ode **A**rea
MOF	**M**icrostructured **O**ptical **F**ibre
NA	**N**umerical **A**perture
OSA	**O**ptical **S**pectrum **A**nalyser
PBG	(**P**bO-**B**i$_2$O$_3$-**G**a$_2$O$_3$) glass composition
PTFE	**P**oly**t**etra**f**luoro**e**thylene (Teflon)
QCW	**Q**uasi-**C**ontinuous **W**ave
SEM	**S**canning **E**lectron **M**icroscope
SMF	**S**ingle **M**ode **F**ibre
TZN	**(T**eO2-**Z**nO-**N**a$_2$O) glass composition
TZNL	**(T**eO2-**Z**nO-**N**a$_2$O-**L**a$_2$O$_3$) glass composition
UV	**U**ltra**v**iolet
WNT	(25**W**O$_3$-15**N**a$_2$O-60**T**eO$_2$) glass composition
ZBLAN	(**Z**rF$_4$-**B**aF$_2$-**L**aF$_3$-**A**lF$_3$-**N**aF) glass composition

GLOSSARY

Glass viscosity – viscosity of the supercooled glass melt.

1. Introduction

1.1 Research Motivation

The research contained within this thesis was motivated by a need for additional fibre laser sources in the 2 to 5µm mid-infrared (IR) region. This is due to the high atmospheric transmission within this wavelength range. Sources emitting at around 3µm also have their use in laser surgery, due to the high absorption at this wavelength by the water contained within human cells [1].

Lasing near 3µm has been achieved in many erbium III doped solid state lasers [2-4] and fluorozirconate based fibre lasers [5-27]. This laser transition was therefore chosen for this work with the desire to overcome some of the undesirable properties associated with fluorozirconate based host glasses, which are discussed later in this section, through the use of a tellurite glass. A simple energy level diagram for erbium III, illustrating this 2.7µm transition from the $^4I_{11/2}$ energy level to the $^4I_{13/2}$ energy level, is provided in Figure 1. This diagram also includes the proposed pumping at 980 nm and the $^4I_{13/2}$ - $^4I_{15/2}$ transition corresponding to 1.5µm fluorescence.

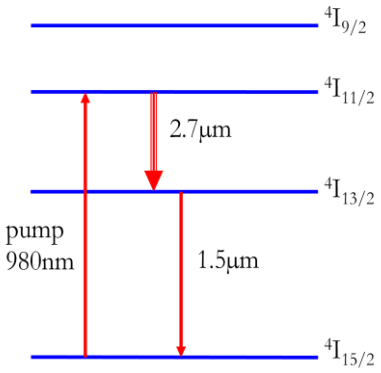

Figure 1: Electronic energy level diagram for the free erbium III ion.

The use of a fibre for the gain medium has advantages in that:

- It can have a long gain medium length, which allows for the use of lower dopant concentrations and due to the increased distance between adjacent dopant ions reduces clustering of the dopant and upconversion.
- Fibres can be cooled effectively since they have a large surface area to volume ratio and the cooling can be positioned close to where the heat is generated in the gain medium.
- Fibre lasers have the ability to control the beam quality through the fibre design rather than by the resonator. As such, they are not affected by thermal lensing.
- A low threshold can be achieved through the use of a small core fibre. On the other hand, the damage threshold of the fibres can also be increased through the use of a large mode area fibre or double clad fibre.
- Fibre lasers, especially when monolithic (i.e. when there are no free space optics), can be very robust and stable.
- Due to their long length, fibre lasers can be limited in their power by non-linear effects.

To date lasing around 3μm in a fibre laser system has only been achieved in fluorozirconate based glass fibres. This is due to the high transmission in the mid-infrared and the low maximum phonon energy of these glasses resulting in minimal non-radiative decay across this transition. The fluorozirconate glass ZBLAN (**Z**rF_4-**B**aF_2-**L**aF_3-**A**lF_3-**N**aF) has been refined for its potential use in telecommunications. This lead to a significant improvement in the glass quality [28, 29]. Due to the hygroscopic nature of fluoride based glasses it is, however, difficult to avoid the degradation of the glass that occurs when it's exposed to moisture in the atmosphere.

The aim of this research was therefore to investigate the potential of an oxide based glass that was suitable for use as an alternative host for a 3μm laser system. This motivated the development of a tellurite glass. The tellurite glasses also have good transmission between 0.35 and 5μm [30]. The mid-infrared transmission of the tellurite glass composition used in this research is presented in Section 2.2.2. The susceptibility

to crystallization and the degradation of fluoride glasses when exposed to atmospheric moisture are significantly improved in tellurite glasses [30].

Relative to other oxide glasses, tellurite glasses have a lower maximum phonon energy, between 650 and 800cm^{-1} (depending on the composition) [30]. The glasses also have a high rare earth solubility and refractive index. The higher refractive index causes higher absorption and emission cross-sections in the doped glass [30].

The glass composition chosen for this research is a zinc-sodium-tellurite (TZN) glass which was later changed to a lanthanum-zinc-sodium-tellurite (TZNL) glass for reasons described in Section 2.5. The suitability of glass compositions similar to these have been demonstrated through their use in previously developed tellurite glass fibre lasers [31-41].

In this project, a microstructured cladding was used to achieve better control over the confinement by the fibres fabricated. The microstructured fibres were fabricated using the extrusion technique, which gave versatility in the cladding structures that could be achieved. This was exploited through the fabrication of both the large mode area fibres (Section 3.2) and the small core fibre that were used in the laser experiments (Section 5.3).

1.2 State-of-the-Art

This research was motivated by literature reviews in the areas of;

- **Tellurite glass development (Section 1.2.1.1)**. An understanding of the properties of different tellurite glass compositions, presented in literature, motivated the choice of glass composition used in this research.

- **Spectroscopic properties of erbium III doped tellurite glass (Section 1.2.1.2)**. Previous spectroscopic studies on doped tellurite glasses were used to get a preliminary understanding of the behaviour of erbium III in this glass.

- **Microstructured fibre development (Section 1.2.2)**. The microstructured fibre geometries presented in the literature motivated the choice of fibre designs targeted in the tellurite glass fibre development.

- **Tellurite glass fibre development (Section 1.2.3)**. Previously fabricated tellurite glass microstructured fibres demonstrate the diverse range of structures that have been incorporated into fibres made from this glass.

- **Tellurite glass laser development (Section 1.2.4)**. The lasing that has been achieved in tellurite glass is the current state-of-the-art in the area of tellurite based fibre lasers.

- **Er^{3+} doped 3μm fibre laser development (Section 1.2.5)**. Fibre lasers at around 3μm, which to date have only been developed in fluorozirconate based fibres, were studied to realise the different techniques that have been used to overcome the self terminating nature of the 2.7μm transition in erbium III.

These areas of research are discussed in more detail below.

1.2.1 Tellurite Glass Development

A review of the literature on different tellurite glass compositions and the erbium III spectroscopy in these glasses was used to decide on the TZN glass as a suitable composition. Research in the development of tellurite glass as an erbium III laser host can be divided into two main areas: the properties of the glass itself (Section 1.2.1.1) and the spectroscopic properties of the erbium III-doped glass (Section 1.2.1.2).

1.2.1.1 Tellurite Glass Properties

The first tellurite glass fabricated was to the best of the Author's knowledge by Stanworth [42] in 1952. The first tellurite glass fabricated with a refractive index above

2 was presented by Yakhkind [43] in 1966, which included an indepth study into the glass forming region of a series of ternary tellurite glasses. The glass compositions presented were based on TeO_2, WO_3 and (Ta_2O_5, BaO, Bi_2O_3 or Tl_2O) components. Since then tellurite glasses have been developed for a number of different applications including: poling of the glass [44], using the glass for its high non-linearity [45-52], using the strong excited state absorption and up-conversion for its potential use in infrared pumped visible lasers [32, 53-66] and as a host for lasers and amplifiers in the 1 to 2.1μm range (described in Section 1.2.4).

The $75TeO_2$-20ZnO-$5Na_2O$ (TZN) glass composition used in this thesis was first proposed as a suitable laser host by Wang et al. [30] in 1994. This paper details their glass melting procedure which was used as the starting point in the refinement of our glass melting. Differential scanning calorimetry (DSC) measurements were used to find the glass transition temperature and crystallization onset temperature. This demonstrated that the glass had good crystallisation stability. It was also shown that the TZN glass composition had good transmission from 350nm to 5μm. The glass didn't degrade with time and it had a high rare earth solubility. The viscosity was measured and a fibre was drawn from this glass with a minimum loss of 1dB/m at 1.2μm.

The refractive index of many different tellurite glass compositions has been measured at 632nm [67-73]. The Sellmeier curves for the majority of the binary tellurite glasses were presented by Ghosh [74] in 1995. Tellurite glass' high refractive index has been an attractive glass property, motivating the development of the glass for its non-linearity [45-52]. A high refractive index is also desirable in laser applications as it corresponds to higher absorption and emission cross-sections and therefore increased laser gain.

Due to similarities in the glass composition, the most relevant study of the refractive index change caused by doping the glass was presented by Nunzi Conti et al. [67] where the refractive index of WNT glasses with composition $25WO_3$-$15Na_2O$-$60TeO_2$ and Er_2O_3 dopant concentrations of 0, 0.05, 0.5, 1, 1.5 and 2 mol% and TZN glasses with composition of 10ZnO-$10Na_2O$-$80TeO_2$ doped with 0, 1 and 2mol% Er_2O_3 were also presented. In both glass, types there was a linear reduction in the refractive index of the

glass with increasing erbium III content. At first glance this seems counter-intuitive since in silica glass the refractive index increases with Er_2O_3 concentration.

The important observation that increasing the level of rare earth ions in tellurite glass reduced the glass' refractive index, lead to the Author's addition of lanthanum to the glass. This provided a means to match closely the refractive indices of the doped and undoped glasses for use in the fibre fabrication component of this research as will be discussed further in Section 3.3.

1.2.1.2 Erbium III Doped Tellurite Glass Spectroscopy

Spectroscopic studies of the erbium III-doped glasses can be split into research focusing on the emission from the erbium III $^4I_{13/2}$ energy level for the development of erbium III fibre amplifiers [70, 75-81] and lasers [34, 78] or on upconversion for the development of visible laser sources [32, 53-66]. Although not frequently measured, there has also been report of measurements of the 2.7μm fluorescence from the erbium III-doped tellurite glass [82]. This variation in the desired spectroscopic properties of the erbium III doped glasses presented in literature has resulted in the development of a diverse range of tellurite glass compositions.

In 1974 and 1975, Reisfeld et al. [83, 84] presented the first spectroscopic analyses of rare earth doped tellurite glass. These papers reported on the non-radiative decay rates for a number of erbium III transitions in an erbium III-doped Na_2O-TeO_2 glass. The non-radiative decay across the $^4I_{11/2}$ to $^4I_{13/2}$ erbium III transition is detrimental to achieving 2.7μm emission. This paper was also the first of many to study the green and red fluorescence from erbium III in the glass. Both excited state absorption and the upconversion in erbium III can result in this visible fluorescence from the doped samples [32, 53-66]. Figure 2 illustrates the excited state absorption (ESA) and upconversion (ETU) processes that occur under 980nm excitation of erbium III. In the paper by Reisfeld et al. [83], the upconversion in the tellurite glass was compared to the amount observed in germanate, phosphate and borate glasses. The upconversion from the $^4I_{13/2}$ energy level has been used to depopulate the lower laser level ($^4I_{13/2}$) and maintain

population inversion in the 2.7μm fluorozirconate based fibre lasers, covered in more detail in Section 1.2.5.

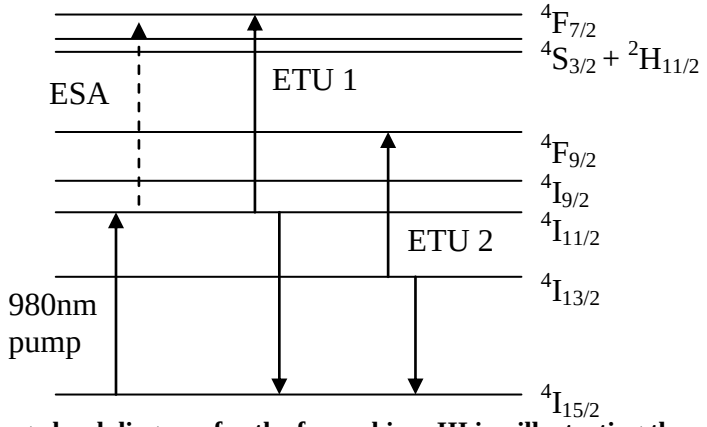

Figure 2: Electronic energy level diagram for the free erbium III ion illustrating the pumping at 980nm, excited state absorption (ESA) and the most significant upconversion (ETU) processes that occur in erbium III.

The papers that reported on the potential for tellurite glass in an erbium III doped fibre amplifier have focused on the $^4I_{13/2}$ to $^4I_{15/2}$ transition. The measurement of the erbium III absorption and emission cross-sections in tellurite glass is reported in many tellurite spectroscopy papers [78, 79, 85-87]. The paper by Kumar et al. [88] is representative of this analysis with the absorption cross-section calculated for the erbium III energy levels between 450nm and 1.7μm and the emission spectra from the $^4I_{13/2}$ energy level. From the absorption spectra, theoretical lifetimes are commonly derived using Judd-Ofelt theory [89, 90] which are then compared to measured results [10, 59, 67, 71, 85, 86, 88, 91-95]. Some of these papers have also included an analysis of the upconversion in the glass. In this case the upconversion is a loss mechanism that would hinder the amplifier's performance. This is also described in the paper by Kumar et al. [88].

The spectroscopic properties of erbium III across a wide range of available glass compositions influenced the choice of the TZN composition used for this research. In 2002, Le Neindre et al. [68] studied a number of glass properties including refractive

index, density and the erbium III absorption and emission spectroscopy when varying the alkali metal element in the alkali-zinc-tellurite glasses.

The results published by Wang et al. in 1994 [30] were based around the TZN glass composition and described the absorption and emission for the $^4I_{13/2}$ energy level along with theoretical and measured lifetimes for this energy level for a range of erbium III oxide concentrations. The precise glass composition has a significant effect on the absorption and emission by the erbium III in the glass. Figure 3, which is reproduced from that paper by Wang et al., illustrates the effect of using Li_2O, Na_2O or K_2O as the alkali metal oxide component in the glass. Although Na_2O did not correspond to the highest absorption cross-section and broadest emission spectra, it was used in this research due to the easier availability of high purity raw materials. The addition of lanthanum to that Author's glass composition (Section 2.5) motivated the spectroscopic measurements reported on in Chapter 4. These were used to determine if there were any significant changes in its spectroscopic properties when compared to the erbium III doped TZN glass.

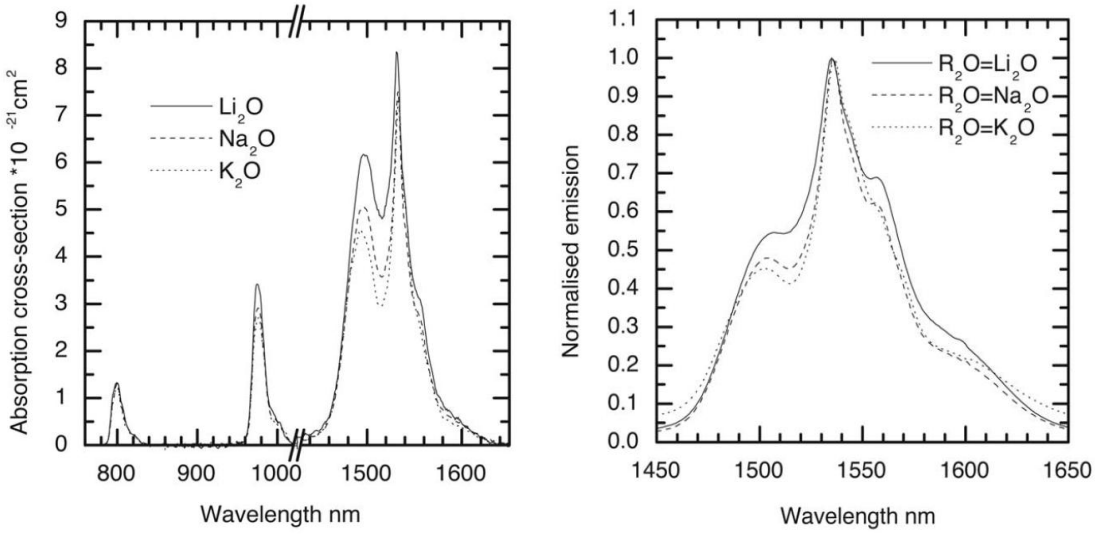

Figure 3: Absorption cross-sections and emission spectra for R_2O – ZnO – TeO_2 glasses, where R_2O is the alkali metal oxide: Li_2O, Na_2O or K_2O. [30].

1.2.2 Microstructured Fibre Development

When constructing a high power fibre laser, the ideal fibre would have a large core area, to increase the damage threshold and reduce Raman scattering. For other applications where pump power is limited, a fibre with a small core diameter and a low threshold pump power is desirable. The use of microstructured fibre technology offers an alternative route to the fabrication of these very different geometries. Large mode area fibres can be designed to propagate the high spatial mode quality desired of a laser system [96-106] or alternatively small core fibres can be designed to have very strong confinement to the core by an increased the amount of air in the cladding [107, 108].

The number of modes guided by a fibre is proportional to the numerical aperture (NA) of the core cladding interface and the core diameter. This is illustrated through the V-parameter which is defined by;

$$V = \frac{2\pi a}{\lambda}\mathrm{NA} \quad \textbf{(1)}$$

where a is the core radius, λ is the wavelength and $\mathrm{NA} = \sqrt{\mathrm{n^2}_{\mathrm{core}} - \mathrm{n^2}_{\mathrm{cladding}}}$. A fibre will guide only the fundamental mode if the V-parameter is < 2.405. To increase the damage limit of a fibre, the core diameter is increased, however, in order to maintain single mode guidance the NA of the fibre needs to be reduced proportionally. The limit to the mode diameter achievable through one of these fibres, whilst maintaining single mode guidance, is therefore determined by the smallest core-cladding index difference that can be controllably achieved in the fabrication process. The use of a microstructured cladding can provide this desired controllability over a fibre's NA [109].

The addition of an outer cladding to a large mode area microstructured fibre geometry, to create what are known as microstructured double clad fibres, allows for the coupling of high power, low brightness pump sources into the fibres. The use of these higher power pump sources has greatly increased the near single mode output power of microstructured fibre lasers to in excess of 100W CW [99, 101].

Alternatively, when developing a low threshold, core pumped laser system, a small core and high NA confinement is desired. To fabricate a step index fibre for this purpose, the glasses used for the core and cladding of the fibre would need to have very

different refractive indices. These glasses would also be required to be chemically and thermally compatible to allow them to be drawn together into a fibre. Such glass pairs are, however, very hard to find. By contrast, the use of air in the cladding can provide the large index difference required to achieve the desired tight confinement to the fibre core [107].

1.2.2.1 Microstructured Silica Fibre Development

This section summarises the state of microstructured fibre and fibre laser development in silica glass as it motivated the cladding geometries targeted in the fibre development component of this research. This summary covers some of the optical fibre designs that propagate only a single mode. These include the more conventional so called 'endlessly' single mode large mode area (LMA) geometry along with some leaky optical fibre designs that robustly propagate only the fundamental mode due to their high loss for the higher order modes. The development of lasers using these microstructured fibres is also described. This includes the incorporation of a microstructured outer cladding and the associated increase in output power achieved.

Single Mode Fibre Geometries

The first microstructured fibre was presented by Knight et al. [110] in 1996. It was fabricated through the stacking of silica glass tubes. Due to the tight stacking of these tubes, a hexagonally periodic cladding was generated. It had a core diameter of less than 5µm and an outer diameter of approximately 40µm. An image of the fibre cross-section, from this paper, is reproduced in Figure 4 (a). The first large mode area microstructured optical fibre was reported by Knight et al. in 1998 [97]. This fibre was fabricated using the same technique but was only pulled down to an outer diameter of 180µm and hence had a core diameter of approximately 22.5µm. A scanning electron microscope (SEM) image of the core region of this fibre is reproduced from this paper in Figure 4 (b).

Figure 4: (a) SEM images of the first microstructured-silica fibre reported by Knight et al. in 1996 [110] and (b) the large mode area fibre cross-section presented by Knight et al. in 1998 [97].

These two fibres are said to be endlessly single mode. This means that the fibres propagate only a single mode over a large wavelength range. The single mode guidance by this fibre was proven in the wavelength range from 458 to 1550nm [109]. An endlessly single mode fibre has its advantages as a laser gain medium as the fibre would only propagate the fundamental mode of both the pump and laser wavelengths. This would result in very good overlap between the pump and laser within the fibre [107]. Since these papers, there has been further modelling [102, 108, 111-119] and refinement of the cladding structure to reduce bend loss by increasing the diameters of the holes in the cladding while maintaining the endlessly single mode guidance by the fibre.

The first fibre laser incorporating this cladding geometry was reported by Wadsworth et al. [120] in 2000. The silica microstructured fibre had its core doped with ytterbium and had a laser threshold of 10mW. The low threshold was attributed to the small, 1.6μm, core diameter. The laser had an output power of 18mW which was achieved from 330mW of pump power at 970nm. A 50% coupling efficiency by the pump laser was reported for the system. Results presented in 2005 by Furusawa et al. [107] showed the generation of 25mW from an erbium III doped holey fibre pumped at 980nm. The fibre had a comparable structure to that presented by Wadsworth et al. [120] which had a cladding hole diameter of 1μm and a hole to hole spacing of 2μm. The laser

system had a slope efficiency, which represents the absorbed pump power to output power conversion efficiency, of 57.3%. It also had a lower laser threshold of 0.55mW. Due to the robust single mode guidance by this design of cladding geometry, and the capacity of such designs to have a large mode area, this type of geometry was the first to be considered in the fabrication component of this thesis.

Apart from the endlessly single mode fibre geometry, alternative fibre geometries featuring a large mode area that would theoretically propagate only the fundamental mode have been proposed. Of these fibre geometries, a structure consisting of only a single ring of large air holes as the cladding [105, 117, 121-126] was first analysed in detail by J. Fini in 2005 [124]. Later that year this fibre design was fabricated by Wong et al. [105] and its guidance was compared to the simulated guided mode. The structure of the fabricated fibre is reproduced in Figure 5 along with its guided mode. As with a large core diameter W-fibre, this particular geometry features a core diameter that would normally propagate multiple modes, however due to the significantly higher confinement loss for the higher order modes and a relatively low confinement loss for the fundamental mode, after a short length of fibre only the fundamental mode remains. For this reason this type of fibre is called an effectively single mode fibre or leakage channel fibre.

Following the fabrication of this fibre by Wong et al. [105], it was noted that as with other LMA fibres there was still significant distortion in the guided mode when the fibre was bent. In the following years there was some work done in modelling this bend induced distortion [116, 117, 121, 125, 127, 128] and through modelling, solutions were presented to reduce the effect [125, 129, 130]. There was, however, always a trade off between the mode area and the bend loss. This fibre geometry has, nevertheless, proven to be a suitable choice for the propagation of high power laser beams and core pumped amplifiers [121]. The geometry however is not suitable for conversion to a double clad fibre. This is because the addition of an outer cladding would act to confine the ‘leaky’ higher order modes.

NOTE:
This figure is included on page 13 of the print copy of the thesis held in the University of Adelaide Library.

Figure 5: Fibre cross-section of the effectively single mode six hole fibre (a) and the fibre's guided mode (b) [105].

Another proposed LMA fibre geometry that is effectively single mode, is the segmented cladding fibre, which consists of alternate regions of high and low refractive index in the azimuthal direction as illustrated in Figure 6 [131-134]. This geometry would, however, be non-trivial to fabricate. Since this fibre geometry also relies on highly lossy confinement of the higher order modes in the core, this geometry was also not considered a potential fibre design for the research in this thesis.

NOTE:
This figure is included on page 13 of the print copy of the thesis held in the University of Adelaide Library.

Figure 6: Cross-sectional profile of the segmented cladding fibre [134].

Double Clad Fibre Geometries

A double clad fibre consists of a core and inner cladding that guides only a fundamental mode and an outer cladding that confines pump light to the inner cladding. The basic geometry of a double clad fibre is illustrated in Figure 7.

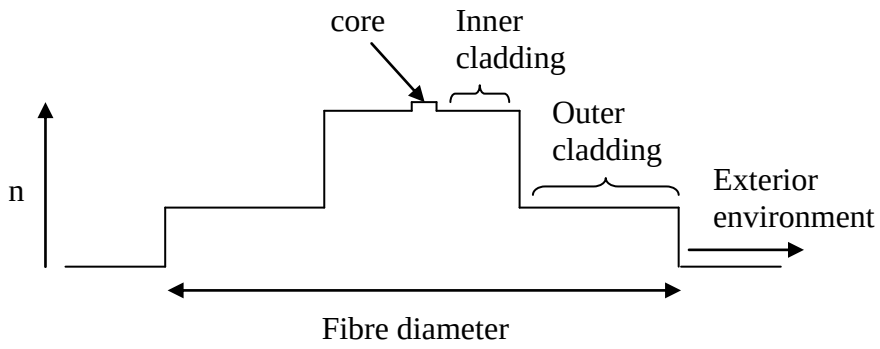

Figure 7: Double clad fibre structure

In a microstructured double clad fibre a small index contrast, and hence low NA, between the core and inner cladding is achieved by using a structure comprising of a small air fraction. The strong pump confinement is achieved by using a structure with a very high air fraction.

Of all reported microstructured fibre designs that have a large mode area and propagate only a single mode, only the endlessly single mode cladding geometry has its core guidance unaltered by the addition of an outer cladding. This agrees with what was found in literature [96, 98-101, 104, 106, 135, 136], where the majority of the microstructured double clad fibres have the hexagonally periodic, endlessly single mode inner cladding geometry as described in the previous section.

The first example of a cladding pumped fibre laser consisting of a holey inner and outer cladding was presented by Furusawa et al. [136] in 2001. A SEM of the fibre cross-section is reproduced in Figure 8. This laser generated an output power in excess of 1W demonstrating the potential of this type of geometry for use in high power laser systems.

Figure 8: Geometry of the first microstructured structured inner and outer clad fibre used in a laser [136].

Since then the output powers from these types of fibre lasers have greatly increased [137]. This is illustrated by the generation of 320W of output power using the ytterbium doped fibre pictured in Figure 9 [101] in 2006. For this laser system, the core area was about 2400μm^2, greatly reducing the fibre's non-linearity and the pumped area was 25000μm^2 reducing the thermal load on the glass.

Figure 9: The fibre geometry of a recently fabricated double clad fibre laser [101] generating 320W at 1064nm.

1.2.3 Tellurite Fibre Development

Tellurite glass fibre development is less mature than the silica, phosphate and fluoride fibres. This section covers the progress in tellurite glass fibre fabrication, including the development of step index fibres and the more recent microstructured optical fibres.

The tellurite glass fibre geometries that have been developed have had a range of different designs depending on their application:

- Step index fibres have been used in the tellurite fibre laser development [31-41].
- LMA microstructured fibres have been fabricated for mid-infrared transmission and non-linear super-continuum generation when damage threshold has been of concern [49, 50].
- Small core microstructured fibres have also been fabricated for non-linear applications [45-48, 51, 52].

The extrusion technique used within this research was also used in the fabrication of a number of these microstructured fibres [45-50, 52]. Other preform fabrication techniques include a modified rod in tube method, where a cast rod containing the desired cladding structure was inserted into a jacket tube. This technique was used for some of the small core fibres [51].

Step index fibres, used in the laser development, were fabricated using the suction and rotational casting techniques described by Mori et al. [81]. An illustration of this process is reproduced from Mori's paper in Figure 10. In this process, the core glass is cast on top of the cladding glass where it is drawn down the centre of a cladding glass tube as it cools. This rod, which contains the doped core, is then inserted into a rotationally cast jacket tube so that when pulled to fibre, the desired core diameter is achieved. This fabrication technique generates a good interface between the core and cladding, reducing the loss in the fibre.

The majority of the fibres used in the tellurite laser development have had a composition of $80TeO_2$-$10ZnO$-$10Na_2O$ doped with Tm^{3+}, Ho^{3+} and/or Yb^{3+} for the core and $75TeO_2$-$15ZnO$-$10Na_2O$ for the cladding [35-39]. The replacement of some of the tellurium with zinc in the cladding glass reduced its index to below that of the core. The

Figure 10: Step index tellurite fibre fabrication technique reproduced from Mori et al. [81].

fibres used in these fibre laser systems generally had core diameters of 7.5µm and a NA of around 0.28. The loss of these fibres was reported to be 1.2dB/m at 1.476µm. The lasing performance of these fibres is detailed in the next section (Section 1.2.4).

The large mode area tellurite glass fibre, published by Feng et al. [49, 50] in 2008, used the TZN ($75TeO_2$-$20ZnO$-$5Na_2O$) glass composition. As shown in Figure 11 (a) it featured three rings of air holes, an outer diameter of 410µm, a hole to hole spacing of 53µm and a hole diameter that reduced from 28µm for the inner ring of holes to 13.8µm for the outer ring of holes. The fibre propagated only the fundamental mode which had a mode area of approximately 3000µm^2. An image of the guided mode is reproduced in Figure 11 (b). The fibre had a loss of 2.9dB/m at 1550nm and needed to be mounted very straight to avoid having a high bend loss. This fibre loss is indicative of the transmission losses that have been achieved, to date, in microstructured tellurite fibres.

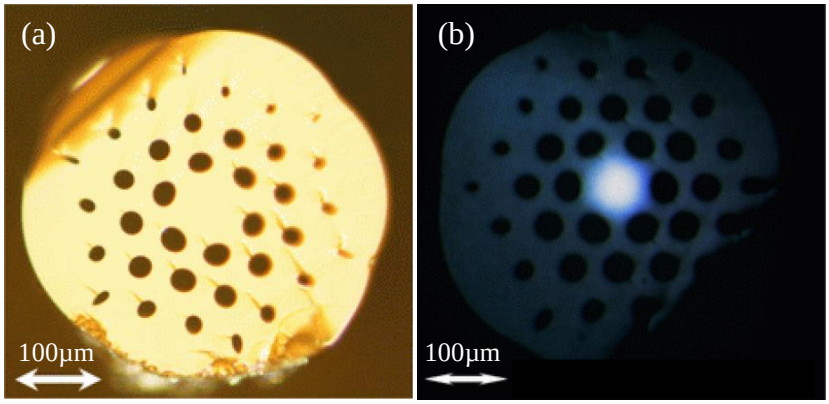

Figure 11: Large mode area tellurite fibre cross-section (a) and mode guided by the fibre (b) (ref).

Due to its high refractive index tellurite glass exhibits a very high non-linearity [138]. For this reason tellurite fibres are an attractive medium for super-continuum generation. The fibres fabricated for this purpose demonstrated the versatility in cladding design that could be achieved in tellurite glass fibres.

Figure 12: Photograph of the extrusion die (a), the extruded preform (b), the fibre fabricated (c) and an image of the fibre guiding light (d) for the fibre presented by Kumar et al. [52].

The first of these fibres was presented by Kumar et al. [52] in 2003. The fibre had six struts suspending a core with a diameter of 7μm. This fibre had a high loss in the order of 2.3dB/m at 1.2μm. The die used in the extrusion of the preform, the preform cross-section, the resultant fibre geometry and an image of the fibre guiding light for this so called "wagon wheel" fibre are reproduced from the paper by Kumar et al. [52] in Figure 12.

A number of high nonlinearity tellurite fibres, with nonlinear waveguide coefficients (γ) [139] ranging up to $5.7 m^{-1} W^{-1}$ [47], have since been presented [45, 46, 48, 50, 51]. Supercontinuum generation has been generated with bandwidths in excess of 4000nm [46]. These fibres were fabricated using the extrusion and casting methods mentioned previously. The small cores of these fibres cause a very high intensity per unit volume when they propagate a laser beam. This results in the fibre's very high non-linearity.

For a laser application, using this type of small core fibre geometry means that fewer ions need to be excited, and hence less pump power is required, to achieve population inversion across a laser transition. The development of these microstructured tellurite fibres has, however, been solely to exploit tellurite glass' high nonlinearity. Previously developed tellurite lasers, described in the next section, have only used step index fibres, making the fibre laser presented in this thesis quite novel.

The wagon wheel fibre used in the laser experiments described in Section 5.3 has a fibre geometry comparable to some of the smaller core nonlinear fibres presented in literature [46, 47, 52, 77].

1.2.4 Tellurite Glass Laser Development

Tellurite glass has been the host for both bulk glass and fibre lasers emitting at 1.06μm, 1.56μm and in the 1.9 to 2.1μm region. The first tellurite laser was a pulsed Nd^{3+} doped 1.06μm bulk glass laser, presented by Lei et al. in 1996 [33]. The first fibre laser was also presented that year by Wang et al. [40] and was CW with an output power of 4mW achieved from 45mW of absorbed pump power.

There is a number of papers detailing the feasibility of tellurite glass as a host for erbium III doped fibre amplifiers (EDFAs) [34, 75-78, 80]. Tellurite glass is an attractive host for an erbium III doped amplifier due to its high gain and broad emission spectra. In the report by Mori et al. [34] lasing was achieved during their amplification experiments. This laser had only the Fresnel reflection, which based on the glass' refractive index is approximately 11%, at both ends of the fibre to provide feedback into the laser cavity. As such the threshold for the laser operation was very high. The fibre was pumped with 600mW of coupled 980nm pump power and the lasing had a threshold of 120mW. A maximum output power of 2.5mW at 1.56μm was generated with a slope efficiency above threshold of 0.65%. The output power as a function of coupled pump power is reproduced in Figure 13. The fibre had a core diameter of 3μm, a length of 85cm and a minimum fibre loss of 3dB/m at 1.3μm. While the fibre was not optimised for its lasing performance, no explanation was given for the very low slope efficiency.

Figure 13: The laser output performance, which had a slope efficiency of 0.65%, for the erbium III doped tellurite fibre laser presented by Mori et al. extracted from Ref. [34].

This result presented by Mori et al. was improved on by Ohishi et al. [78] with 12mW of output achieved when pumping the erbium III doped fibre with 300mW of pump power at 1480nm. The 12mW output had a wavelength of 1625nm, however, the laser was tuneable from 1530 to 1625nm. By pumping directly into the upper laser level, the maximum theoretically achievable efficiency (the Stokes efficiency) was significantly higher than when pumping at 980nm (91% compared to 63%). The slope efficiency of this laser system, consisting of a ring cavity and 80% output coupling, was still only 3.6%. This could have been due to the high loss of the fibre, which is reported to have been 3dB/m at 1.3μm.

Tellurite glass has been tested as a host for longer wavelength systems through the doping of the glass with thulium, holmium and ytterbium [35-39]. Due to the increasing loss of silica glass beyond 2μm, the infrared transmission of the tellurite glasses would be advantageous in lasers in this wavelength region. The first report of a 2μm tellurite fibre laser was by Richards et al. [36] early in 2008. The fibre was co-doped with was a Tm^{3+} and Yb^{3+}. It was pumped at 1.088μm and lased between 1.91 and 1.99μm with output powers up to 67mW and a slope efficiency of 10% with respect to absorbed pump

power. The low output efficiency was due to strong pump excited state absorption (ESA).

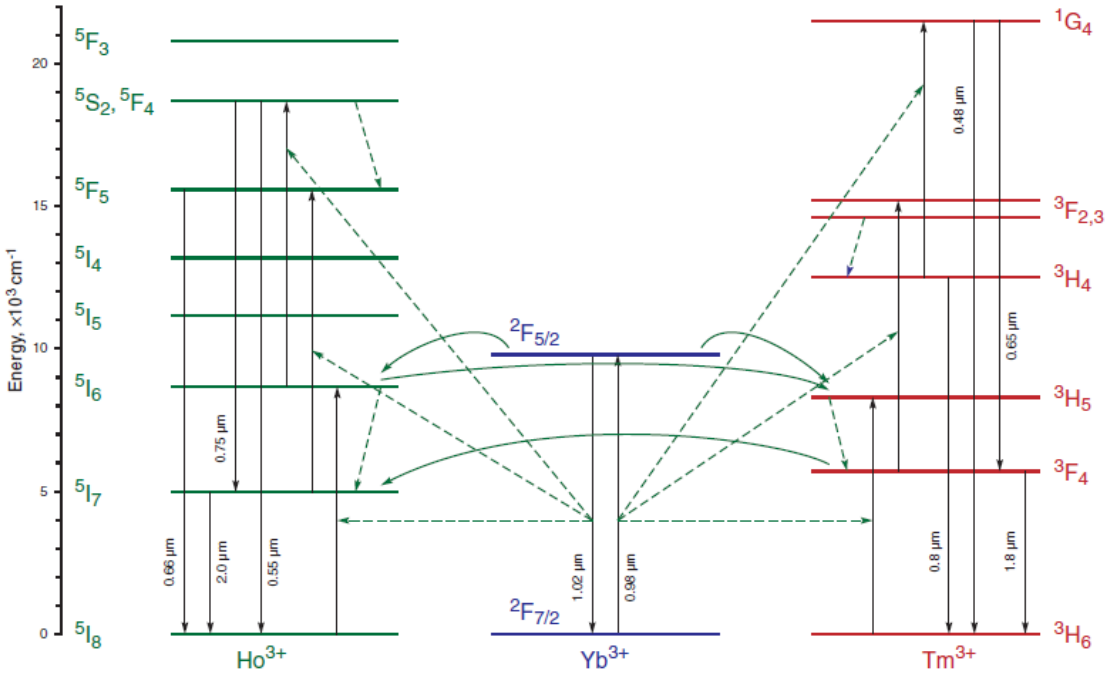

Figure 14: The electronic energy level diagram for free Ho^{3+}, Yb^{3+} and Tm^{3+} ions in tellurite glass and transitions associated with a Ho^{3+}-Yb^{3+}-Tm^{3+} system. Image reproduced from Ref. [35].

The output power of this laser system was improved through in-band pumping of the thulium with a 1.61µm Er^{3+}-Yb^{3+} silica fibre laser [35]. The fibre lased in the wavelength range between 1.88 and 1.99µm with a slope efficiency of up to 76% to the launched pump power. A maximum output power of 280mW was generated. The fibre used in this laser had a length of 32cm and the cavity consisted of a 99% reflective input mirror and the 12% Fresnel reflection as the output. The energy level diagram illustrating the transitions in a Ho^{3+}-Yb^{3+}-Tm^{3+} system, reproduced from this paper, is pictured in Figure 14. The output power as a function of launched pump power is reproduced in Figure 15.

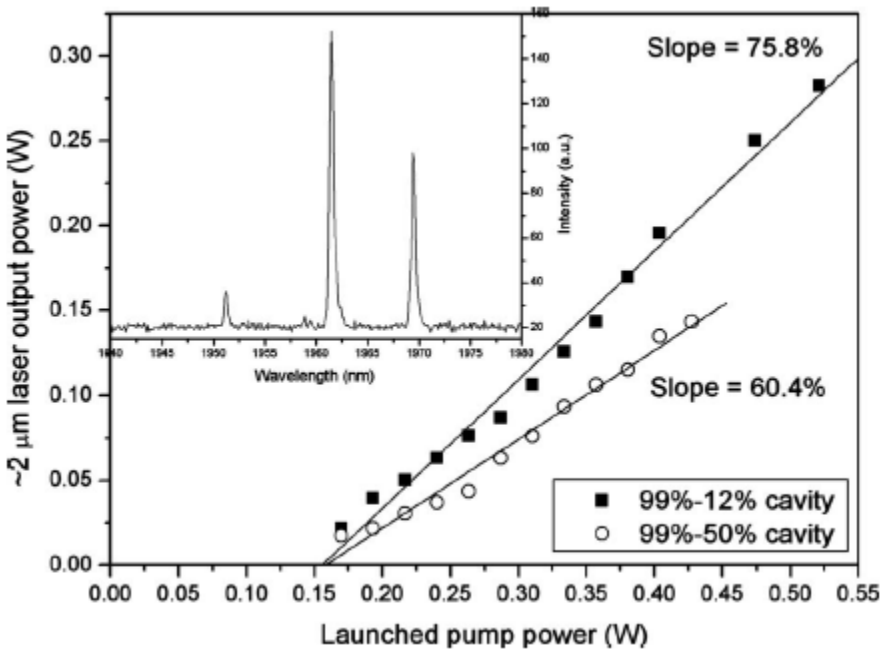

Figure 15: Laser performance of the Tm^{3+} doped tellurite fibre laser along with the laser's spectral output [35].

The output wavelengths of these systems were pushed further into the infrared through the co-doping with holmium [140]. These lasers were also pumped at 1.61μm and lased at around 2.1μm. An output power of 160mW has been achieved at this wavelength with a slope efficiency of 62%.

To exploit the mid-infrared transmission of the tellurite glasses, laser wavelengths of 2.3μm or beyond would need to be targeted. The potential for lasing at 2.7μm in erbium III doped tellurite glass is studied in this work.

1.2.5 Erbium 3μm Fibre Laser Development

Lasing across the 2.7μm erbium III transition in fibres has only been achieved in fluorozirconate based step index fibres [5-27, 141-146], most commonly ZBLAN (ZrF_4-BaF_2-LaF_3-AlF_3-NaF). ZBLAN has an infrared transmission cut-off of 6μm [17] compared to tellurite glass at 5μm. When compared to the tellurite glasses, the low OH concentration in the fluoride glasses also results in higher transmission at the 2.7μm laser wavelength [28, 29].

The self terminating nature of the 2.7μm laser transition is highly dependent on the lifetimes of the upper ($^4I_{11/2}$) and lower ($^4I_{13/2}$) energy levels. The fluoride glasses have a lower maximum phonon energy of around 550cm^{-1} compared to 800cm^{-1} for tellurite glass. This lower phonon energy means that the lifetime of the $^4I_{11/2}$ (980nm) energy level is not reduced significantly due to non-radiative multi-phonon decay. For a fluorozirconate based glass host, the lifetime of the $^4I_{11/2}$ energy level is reported in literature to be 6.9ms compared to the lifetime of the $^4I_{13/2}$ (1550nm) energy level of 9ms [17]. The lifetime of the $^4I_{13/2}$ energy level is, however, still longer than that of the $^4I_{11/2}$ upper laser level. When pumping the 3μm transition, the excited erbium III ions will build up in the lower laser level where they are unable to be re-excited. With the increasing population in this level, additional ions need to be excited into the upper laser level to maintain the population inversion required to lase. When insufficient ions are able to be excited, laser activity ceases. The 3μm erbium III transition between these two energy levels is therefore said to be self terminating.

Some of the techniques previously used to overcome the self terminating nature of the 3μm transition include;

- co-lasing at 1.5μm [15, 16, 18, 24],
- excited state absorption (ESA) [5, 11, 18, 23, 142, 147],
- energy transfer upconversion (ETU) between two excited erbium III ions [6, 7, 9, 18, 20-22, 26, 27, 148, 149] and
- co-doping where, along with the ETU between erbium III ions, the energy is transferred from the erbium III ions to praseodymium ions doped into the glass [8, 9, 14, 17-19, 26, 146, 150-153].

These techniques are reviewed in this section along with a summary of the 2.7μm fluoride based fibre lasers that have been developed. This section concludes with how these different approaches could be applied to a tellurite fibre laser at this wavelength.

When co-lasing at 1.5μm or relying on ESA to achieve CW lasing across the $^4I_{11/2}$ to $^4I_{13/2}$ transition low erbium III dopant concentrations are preferred. When using high dopant concentrations, the erbium-erbium and erbium-praseodymium energy transfer processes dominate the depopulation of the $^4I_{13/2}$ energy level. This is because a higher erbium III concentration means that the dopant ions more closely spaced increasing the

probability of an erbium-erbium or erbium-praseodymium energy transfer (ET) interaction.

The earlier 2.7µm lasers were doped with low erbium III concentrations and relied on excited state absorption, from the $^4I_{13/2}$ energy level, to achieve continuous population inversion across the erbium III $^4I_{11/2}$ to $^4I_{13/2}$ laser transition. The first report of lasing across this transition in a fibre was in 1988 by Brierley et al. [143]. The fibre was pumped at 476.5nm and lased at 2.7µm. The output from this laser system was minimal and no output power was given. In 1989 Allain et al. [10] improved on this performance by generating 250µW from 7mW of absorbed pump power. This was once again achieved through pumping at 476.5nm, however lasing was also achieved when pumping at 501.7nm and 647.1nm. It was also determined that it was excited state absorption that dominated the depopulation of the $^4I_{13/2}$ energy level, hence, facilitating the lasing. In 1990, the output power was increased further with 330µW achieved [141]. The laser had a slope efficiency of 3% and was pumped at 790nm. It lased at 2.71µm for low pump powers and at 2.78µm for higher pump powers. Later in 1990, an output power of 2.1mW with a slope efficiency of 8% was presented by Yanagita et al. [27]. It was pumped at 802nm also into the $^4I_{9/2}$ energy level and lased at 2.71µm just above threshold but also out to 2.78µm for higher pump powers. By 1994 an output power, for these laser systems that relied on ESA to maintain population inversion, of 6mW was reached by Frerichs [11]. It had a slope efficiency of 9.3% when pumped at 980nm directly into the $^4I_{11/2}$ energy level. In 1995 15mW was reported by Bedö et al. [142] whilst experimenting with the erbium III concentration. This system however had a slope efficiency of 5.7% and clearly illustrated the saturation of this laser transition.

Early in 1995, an evaluation of the cause for the low output powers was presented by Bedö et al. [5] and it was proposed that the low slope efficiencies were due to competitive lasing at 850nm from the $^4S_{3/2}$ energy level (see Figure 16). This saw the introduction of a range of cascade lasing schemes. By the end of the year, output powers had reached 150mW. This laser was presented by Pollnau et al. [15] and co-lased at 1.7µm and 2.7µm with a slope efficiency of 22.6%. The system relied on excited state absorption to deplete the lower laser level and the co-lasing at 1.7µm suppressed the competitive lasing of the 850nm transition and returned ions in the higher energy levels

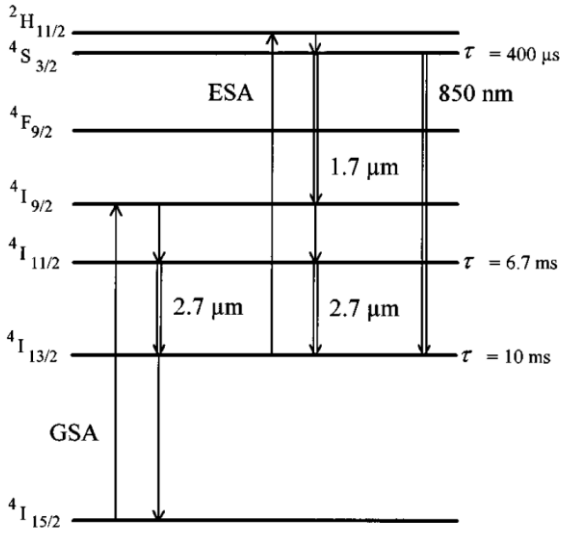

Figure 16: Energy level diagram from the paper by Pollnau et al. [15] describing the cascade lasing scheme that was presented.

NOTE:
This figure is included on page 26 of the print copy of the thesis held in the University of Adelaide Library.

Figure 17: Energy level diagram for erbium III including the energy transfer processes used to achieve lasing at 2.7µm. Image reproduced from [19]

back to the pumped energy level. A high finesse cavity for the 1.7μm transition generated the highest output powers. An energy level diagram illustrating these transitions is reproduced from this paper in Figure 16. In 1997, Pollnau et al. extended this concept by constructing a cascade laser that simultaneously lased at 1.6μm, 1.7μm and 2.7μm [16]. The additional lasing at 1.6μm from the $^4I_{13/2}$ energy level contributed to the depopulation of the lower laser level and when lasing at all three wavelengths, a slope efficiency for the 2.7μm laser emission was measured to be 25.4% which was very close to the maximum stokes efficiency of 29.1%.

In parallel to the literature detailing the low concentration singly erbium III doped fibre lasers at around 3μm, there have also been reports of laser systems using high erbium III concentrations and fibres co-doped with praseodymium [6-9, 14, 17-22, 26, 27, 146, 148-153]. Increasing the erbium III concentration enhances the energy transfer between adjacent erbium ions and allows for energy transfer upconversion (ETU) to assist with the depopulation of the lower laser level. In the ZBLAN glass, the upconversion from the pump level is less dominating than that from the lower laser level. The addition of praseodymium also removes ions from the lower laser level through energy transfer from the erbium ions to the praseodymium, which rapidly non-radiatively decays to the ground state. These processes are illustrated in Figure 17 [19] where the ETU process from the upper laser level is denoted by ETU_2 and from the lower laser level ETU_1. The energy transfer between the erbium and praseodymium are denoted with ET_1 and ET_2 from the lower and upper laser levels respectively. The cross-relaxation is another erbium-erbium interaction illustrated in the energy level diagram. An improvement in the 2.7μm output power through the co-doping of the glass with praseodymium was first demonstrated by Allain et al. in 1991 [154]. In this paper 13mW was achieved from 160mW of coupled pump power.

Since 1999, the use of an outer cladding has, to date, lead to an increase of over two orders of magnitude in output laser power. The use of an outer cladding allowed for the pumping of the fibres with higher power, low brightness lasers and also allowed for the doping of the glass to much higher concentrations without shortening the desired fibre length. The first 2.7μm fibre laser of this type was presented in a paper by Srinivasan et al. [6] where 400mW was achieved from an erbium III doped ZBLAN fibre laser when

pumped with just over 3W of pump power. The fibre was doped with 3.2 x 10^{20} ions/cm^3 erbium III oxide and relied on the ETU between the erbium ions to deplete the lower laser level. This was soon improved on with the addition of praseodymium to the glass and the generation of 660mW [26]. Later that year over 1W of output power was achieved by Jackson et al. [14]. The laser system generated 1.7W at 2.71µm with a slope efficiency of 17.3%. The fibre was doped with a higher than previous erbium oxide concentration of 6.3 x 10^{20} ions/cm^3 and praseodymium concentration of 5.4 x 10^{20} ions/cm^3 and was pumped at 790nm with up to 10W of pump power. The highest power achieved from a ZBLAN fibre laser emitting at 2.78µm was presented by Zhu et al. [8] in 2007 with an output power of >9W achieved from 42.8W of coupled 975nm pump power. This system featured the highest slope efficiency for a laser of this type at 21.3%.

Recent developments in these laser systems have focused on their tuneability. The most recent result was presented by Zhu et al. [7, 146] who demonstrated output powers in excess of 2W over a tuning range of 100nm between 2.7 and 2.83µm.

As is the aim of this work, some research has been done to determine the suitability of other glass hosts for use in 2.7µm laser systems. Some glass hosts that have been studied in the literature include GeGaS glasses [155] and PBG ($PbO\text{-}Bi_2O_3\text{-}Ga_2O_3$) glasses [156-158]. These studies looked into the ETU rates from the upper and lower laser levels. In GeGaS glasses, the upconversion from the lower laser level is stronger than that from the upper laser level allowing for this process to effectively depopulate the lower laser level. For the PBG glasses, the ETU from the upper laser level is stronger than that of the lower laser level. The high concentration doping of this glass and the associated upconversion, when it is pumped, would therefore be detrimental to maintaining population inversion across the 2.7µm laser transition. To achieve CW lasing in this glass, co-lasing at 1.5µm or relying on ESA would be required. To date there has been no measurement of the ETU rates in tellurite glass.

1.3 Projects Aims and Thesis Structure

The initial aim of this research was to develop a fibre laser that emitted at around 3µm. As such, the research contained within this thesis covers the development of the

mid-infrared transmitting tellurite glass, the fabrication of fibres out of this glass and a spectroscopic analysis of the doped glass. Due to the reasons detailed in Chapter 5, including a high material loss at this wavelength, the performance of the fibres fabricated, using the fabrication technique detailed in Chapter 3, were tested through the lasing of the fabricated microstructured fibres at 1.5μm.

To get an understanding of the performance of the TZN and later TZNL tellurite glasses, the following glass properties were evaluated;

- Refractive index of both the doped and undoped glasses, which is needed to get a full understanding of how the glass would guide as a fibre,
- Glass transition and crystallisation onset temperatures, which are needed to anneal properly the glass and gain an understanding of the crystallisation tendency of the glass,
- Viscosity/temperature relations for the supercooled tellurite liquid, which are needed to select suitable parameters for the extrusion and fibre drawing of the glass,
- Optical material loss, which is used to optimise the glass and fibre fabrication procedures. The material loss would need to be minimized to successfully achieve lasing when using this glass as a host,
- Density, which, although not used as an indicator of the glass quality, is required to calculate the required erbium III ion density that was added to the glass.

Since little research has been performed in the area of structured fibre fabrication using tellurite glass, described previously in Section 1.2.3, a significant amount of work needed to be done in fibre fabrication. Although previous structured tellurite fibres have been made using a range of different techniques, the extrusion technique [159] was used to generate the structured preforms used in this project. The low softening point of tellurite glass allowed for its extrusion (at relatively low temperatures) into the wide range of desired structures. The fibre development in this work began with the fabrication of large mode area fibres and was then directed towards the doping of only the core of these fibres. The final set of fibres that were fabricated featured a smaller

core with the aim that these fibres would be used as the gain medium of a core pumped structured tellurite laser system.

A full spectroscopic study of the erbium III doped tellurite glass was required due to differences in its composition and fabrication when compared to other tellurite glasses presented in literature. Spectroscopic measurements included the erbium III absorption and emission cross-sections as well as pump and laser level lifetime measurements giving an understanding of the optimum dopant concentration and alerting us to any concentration dependence associated with these lifetimes or the absorption or emission spectra.

This thesis concludes with the development of a fibre laser from one of the fabricated microstructured tellurite fibres. For reasons detailed in Chapter 5, the laser experiments were aimed at lasing at 1.5μm in the erbium III doped tellurite glass. The constructed fibre laser is the first reported microstructured tellurite glass fibre laser.

The structure of this research and the corresponding chapters are:

Chapter 2, Tellurite Glass Development:

- Develop the TZN and TZNL glasses and characterize their density, refractive index, glass transition temperature, crystallisation onset temperature, viscosity/temperature relation of the glass viscosity and the glass' optical loss.

Chapter 3, Fibre Modelling and Fabrication:

- Fabricate structured fibres from this glass beginning with undoped or uniformly doped large mode area structures.
- Extend the fibre fabrication to core doped fibres required for the future fabrication of double clad fibres.
- Develop fibres featuring a smaller core and high NA cladding structure to reduce the laser threshold of a core pumped laser system. The geometry of this cladding would also be suitable for use as an outer cladding.

Chapter 4, Erbium III doped tellurite spectroscopic properties:

- Spectroscopically analyse the erbium III doped tellurite glass.

Chapter 5, Laser Development and Results:

- Model the laser behaviour for erbium III in this glass host.
- Construct a laser system using a fabricated fibre as the gain medium. Compare its performance to the modelled results.

The thesis concludes with Chapter 6, a summary of what has been achieved throughout this research and indicates promising areas of the research for the future.

2. Tellurite Glass Development

The state-of-the-art in erbium doped tellurite glasses, discussed in Section 1.2, motivated the use of the TZN ($75TeO_2$-$20ZnO$-$5Na_2O$) glass composition and addition of lanthanum to this composition ($73.3TeO_2$ - $19.6ZnO$ - $4.9Na_2O$ - $2.2La_2O_3$) to cater for refractive index changes when doping the glass. The glass development component of this research was aimed at the fabrication of these glasses to test material loss, determine their suitability in the extrusion of structured preforms, fabrication of microstructured fibres and ultimately their use in new fibre lasers.

As discussed previously, the TZN glass was first presented by Wang et al. [30]. This paper reported on the mid-infrared transmission and fibre fabrication using this glass composition. Later, the extrusion of this glass composition was demonstrated by Feng et al. [45, 49, 50], where, taking advantage of the low softening temperature, the extrusion technique was used to fabricate structured fibres from the TZN glass.

Although largely motivated by the research contained within this thesis, the tellurite glass development was also motivated by other areas of research undertaken by the Centre of Expertise in Photonics (CoEP). This includes using the glass for its non-linearity which is an alternative use for this glass due to its high refractive index [45, 46, 50-52]. A breakdown of the contributions by other members of the research group during the glass development is detailed in Appendix 1, and summarised in this chapter.

The areas of research contributed to by technical staff and other researchers in the CoEP include the glass fabrication, density measurements and differential scanning calorimetry (DSC) measurements. Glass samples and billets fabricated ranged in size from 30g up to 400g. The small 30g glass blocks were used for spectroscopic measurements, the 100g billets were used for the optimization of the glass melting procedure through the fabrication of unstructured fibres and the up-scaling to the larger billets was required for the extrusion of the complex preforms.

Glass transmission loss, from 400nm to 1.65μm, was measured using cut back loss measurements on unstructured fibres. In the near-infrared region, for wavelengths up to 3μm, transmission measurements were made using a CARY spectrophotometer, and for wavelengths between 2.2μm and 10μm the glass transmission was measured using

Fourier Transform Infrared (FTIR) spectroscopy. The details of these measurement techniques and the results are provided in Section 2.2. These loss and transmission measurements provided insight into the glass quality including; the effect of adding lanthanum oxide to the glass composition and the effect of varying the glass and fibre fabrication procedures.

Section 2.3 describes the density measurements that were used to calculate accurately the doped glass' erbium ion density.

The glass transition temperatures of the glasses fabricated are presented in Section 2.4. These were measured via DSC measurements and gave an understanding of the glass' crystallisation onset temperature and glass stability against crystallisation.

The remainder of the chapter contains results obtained through measurements performed predominantly by the Author. These include measurement of the refractive index (Section 2.5) and the glass viscosity (Section 2.6). The index change caused by the erbium III ion concentration was studied and the measured indices were used in the calculation of the theoretical erbium III emission and absorption properties (Chapter 3) and in the fibre modelling (Chapter 4). The addition of lanthanum III ions to the glass composition is discussed in Section 2.5 as the solution to matching the refractive indices of the doped and undoped glasses. This index matching is required for the establishment of a double clad fibre geometry. An understanding of the glass viscosity was required to set appropriate furnace temperatures when extruding complex structures into the glass.

2.1 Glass Fabrication

The TZN and TZNL glasses for this research were fabricated by Russell Grew, Herbert Foo and Kevin Kuan. The original glass fabrication procedure as well as the changes to the procedure, made to improve the glass quality, is provided in Appendix 1.

The initial glass composition, which will be referred to as the base glass or TZN glass, was $75TeO_2$ - 20Zn0 - $5Na_2O$. This was later changed to what will be referred to as the lanthanum tellurite glass or TZNL glass with composition $73.3TeO_2$ - 19.6ZnO - $4.9Na_2O$ - $(2.2\text{-}x)La_2O_3$ - xEr_2O_3, where x is the mol % of erbium oxide in which replaces the lanthanum oxide in the glass composition. The addition of lanthanum oxide reduced the difference in refractive index between the doped and undoped glass (Section

2.5) and was later found to also improve the crystallisation stability of the glass (Section 2.4).

The main change made to the glass melting conditions was an increase in the temperature used to melt the raw materials. This increase in the melt temperature and the more rapid cooling of the glass melt resulted in what was believed to be a reduction in the gold particle size to an extent that the gold particles were no longer discernible to the naked eye. This in turn significantly reduced the optical loss of the glass. An image of a 300g billet melted at 850ºC containing the gold particles is compared to a billet melted at 900ºC in Figure 18.

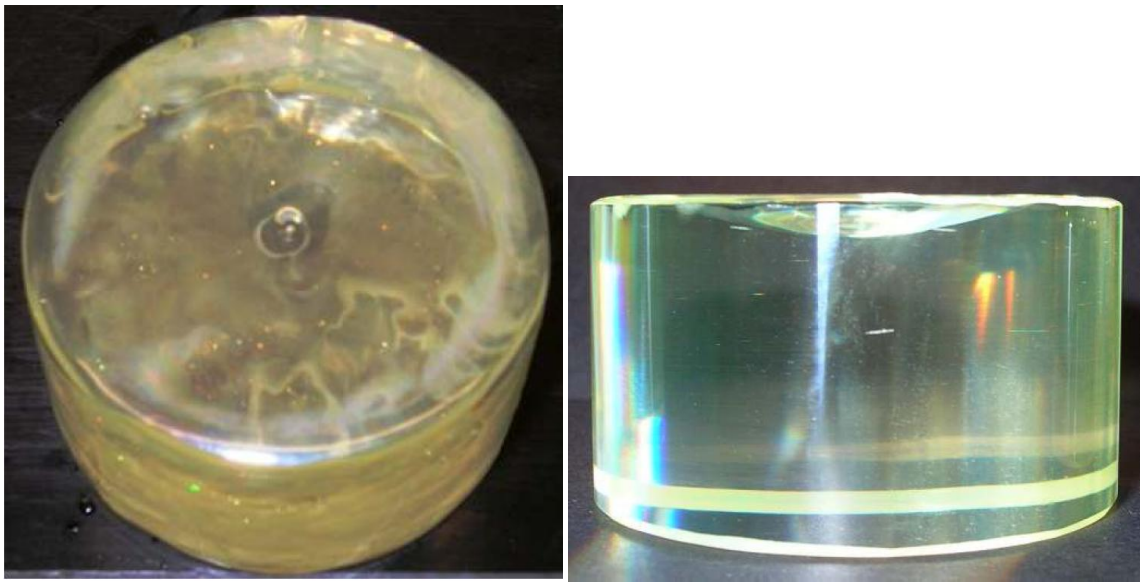

Figure 18: Photograph of a 300g tellurite glass billet containing shiny gold particles (left) compared to a 300g billet fabricated using the revised melting procedure aimed at reducing the scattering loss caused by these particles (right).

Experiments were performed to determine the best melting temperature, mould and crucible materials. A gold crucible used to melt the raw materials at 900ºC and the casting of the melt into well polished brass moulds produced the best results. The improvement gained through melting the raw materials at 900ºC is evident visually in Figure 18 and the increased glass loss associated with melting in a platinum crucible is described in Section 2.2. Different mould materials were used and the resultant glass qualities are compared in Appendix 1.

To improve the transmission of the glass at around 3μm, experiments aimed at reducing the OH concentration in the glass are described in Appendix 1 and the results are presented in Section 2.2.2 of this chapter.

2.2 Material Transmission Loss

The material loss in the visible and out to 1.65μm was determined through bare fibre loss measurements where the transmitted light was recorded with an optical spectrum analyser (OSA). The wavelength range was limited by the OSA's sensitivity band between 400 and 1650nm. Within this range, the use of bare fibres enabled the measurement of losses to an accuracy of ± 0.1 dB/m. These loss measurements were used to refine the glass and fibre fabrication process, as well as to study the effect of changing the supplier and the purity of the raw materials.

A CARY spectrophotometer was used to measure the absorption caused by the erbium III ions in the doped glass samples. The high absorption of the erbium III meant that thin samples were used with thicknesses of around 2mm (Chapter 3). The samples used in the FTIR measurements ranged in thickness from 1mm up to 8mm. The maximum sample size was limited by the mounting of the sample within the available space in the FTIR machine. The thicker samples generated less noisy transmission spectra, however, if the OH content in the glass was too high, thinner samples were needed to reduce the absorption in the 3μm region so that sufficient signal reached the detector.

2.2.1 Bare fibre loss measurements

Bare fibre loss measurements were used to get an understanding of the quality of the glasses, preforms and fibres fabricated. A cut-back bare fibre loss measurement was required for the accurate determination of the glass loss in regions where a transmission measurement of the bulk glass samples was not significantly accurate. To fabricate the bare fibres, billets that ranged in size from just less than 100g to 220g were extruded into 10mm diameter rods and pulled down to fibre with outer diameters between 160 and 200μm.

Once fabricated, light from either a tungsten filament globe or from a Koheras (Koheras SuperK Compact) supercontinuum source, which emits light out to 2.4μm, was collimated and focused into the end of the fibre. Due to the high NA and large diameter of a bare fibre, the tungsten filament source tended to produce a more stable measurement when compared to the results using the supercontinuum source.

When performing the cut-back measurement, the input end of the fibre was fixed so it did not move during the measurement. When light was observed to be emitted from the end of the fibre, the fibre was thread through a bare fibre adapter. The end of the fibre was cleaved, using a York cleaver, and the position of the fibre tip was adjusted such that it was just observable beyond the end of the bare fibre adapter. The bare fibre adapter was connected to the OSA and the spectrum of the transmitted light was recorded. The fibre was then disconnected from the OSA and re-cleaved removing a minimal amount of the fibre. The fibre tip was then once again positioned such that it just protruded from the bare fibre adapter and the adapter was reconnected to the OSA. By iterating this procedure and each time recording the transmitted light intensity, the initial transmitted power was found and errors caused by poor cleaves and variations in coupling into the OSA were reduced. Following the initial transmission measurement, a large length of the fibre was cleaved. The longer the length of fibre removed, at this stage, the smaller the error in the loss measurement as variation in the cleave quality was made less significant. The transmission through the remaining length of fibre was then recorded. As for the initial transmission measurement, the end of the fibre was re-cleaved a few times and the final transmission was calculated. The loss of the fibre was then calculated from the increase in the measured transmitted intensity when the fibre length was reduced. This is given in equation (2) where $P_{initial/final}$ is the initial/final measured intensity spectra in dBm and L is the length of fibre cleaved between the initial and final measurements.

$$loss(\lambda) = \frac{log_{10}\left(P_{final}(\lambda)\right) - log_{10}\left(P_{initial}(\lambda)\right)}{L} \quad \textbf{(2)}$$

This whole process was repeated a few times at varying positions along a fabricated unstructured fibre. The error in the loss measurement was determined by the variation in the loss calculated for a number of these cutback measurements. A representative example of a loss measurement of the undoped tellurite glass is given by the red curve in Figure 19. This figure also illustrates the loss of the TZNL glass, fabricated using the process detailed in Appendix 1, which, provided the same quality raw materials were used, became, by the end of this project, consistently less than 0.2dB/m at 1.3μm. This loss is comparable to the lower loss values presented in the literature [49, 50, 160]. From this plot it is evident that the glass loss between the absorption bands was unaltered by the addition of lanthanum oxide to the glass composition. Further doping the glass also caused a minimal increase in the material loss.

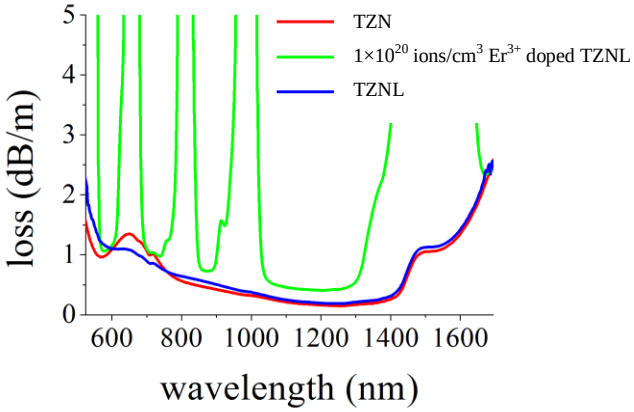

Figure 19: Loss plot for the TZN glass (red) as well as the TZNL glass both doped (green) and undoped (blue). The glasses were melted using the procedure described in Appendix 1.

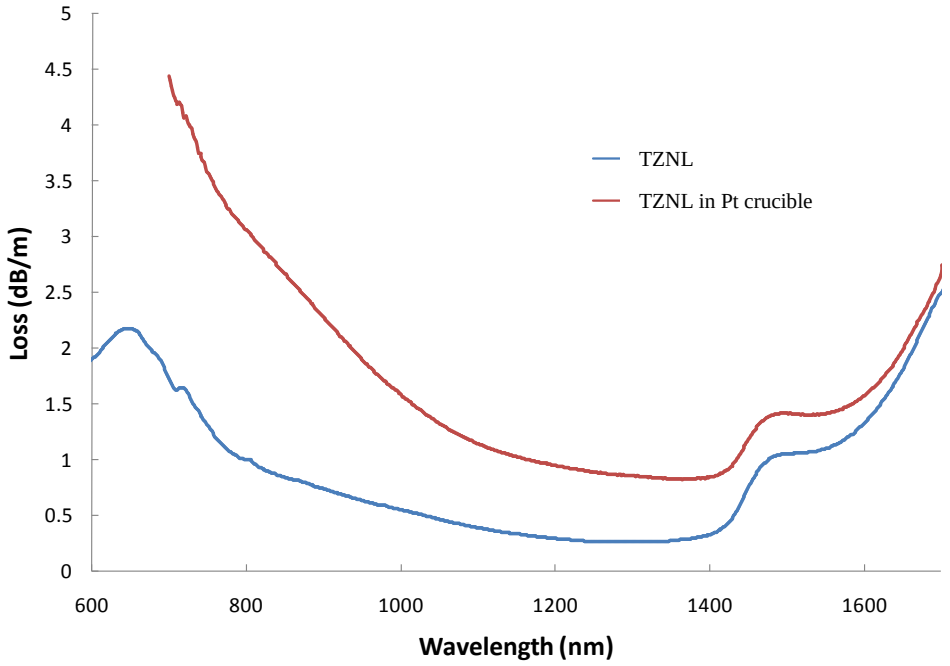

Figure 20: Loss spectra for the TZNL glass melted, using the melting procedure described in Appendix 1, in a platinum crucible compared to the loss of a glass melted the same way using a gold crucible

Bare fibre loss measurements have enabled the testing of the quality of the glass after varying elements of its fabrication. Generally the tellurite glass melts were heated in a gold crucible. At the 900°C melting temperature of the tellurite glass, the gold is quite soft and harder to handle due to deformation. From literature, platinum crucibles are used when melting tungsten-tellurite glasses due to their higher melting temperatures [67, 95, 161-163]. There is however no report on the material loss in the visible or of fibres fabricated from this glass. To determine if platinum was a more suitable crucible material for the fabrication the TZNL glass, unstructured fibres were fabricated using the same melting conditions as described in Appendix 1, however, replacing the gold crucible with a platinum crucible. The resultant optical material losses for glasses melted in gold and platinum crucibles are provided in Figure 20. This plot shows the glass melted in the platinum crucible had considerably higher loss in the visible and a higher minimum loss within the wavelength range measured. This measurement saw the continued use of the gold crucibles, however, they were made thicker to increase their rigidity during the melts.

The loss measurements have also allowed the testing of different raw materials of different purities purchased from a range of different companies. Figure 21 illustrates the effect that varying the raw materials used to fabricate the glass can have on the material loss. This plot illustrates how using higher purity materials does not necessarily result in a lower loss glass. This was an unexpected result, however, it indicated that the background loss of the glass was not only dependent on the metal impurities in the raw materials. An example of this increase is given in Figure 21, where an increase in the glass loss was observed when using a higher purity La_2O_3 raw material. The choice of raw materials was therefore optimised based on the measured glass loss.

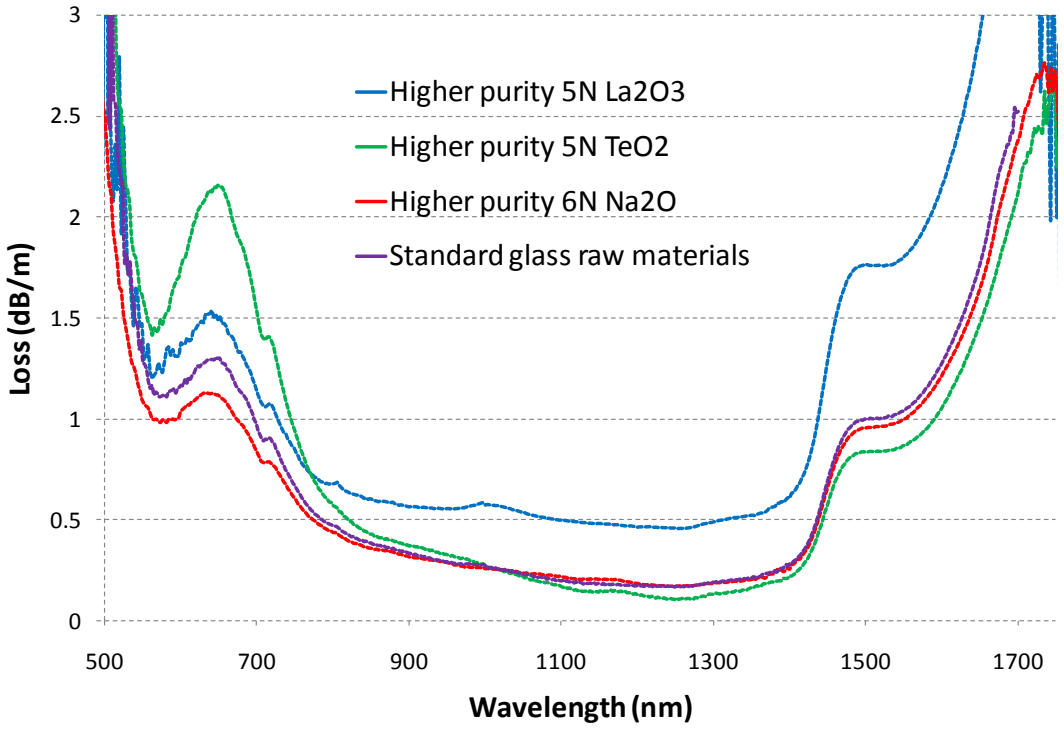

Figure 21: Plot of the glass loss for TZNL glass bare fibres melted from differing purities of raw materials. 4N, 5N and 6N correspond to a 99.99%, 99.999% and 99.9999% raw material purity, respectively. When a component's purity was increased, only that component was changed and the rest of the components remained at purities of 4N TeO_2, 4N La_2O_3, 4N ZnO and 5N Na_2CO_3.

Optical loss measurements have also allowed for further refining of the fibre fabrication procedure as follows, with further details below;

- The effect of different cleaning procedures on the glass billets prior to extrusion and on the preforms prior to being pulled to fibre,
- Whether the billets or preforms were annealed prior an extrusion and fibre drawing (see Section 3.1 for details on the extrusion and fibre drawing),
- Alterations to the gas flow rates used in the fibre drawing.

The billets and preforms were cleaned with isopropanol prior to their extrusion or fibre drawing. The use of a detergent (Decon 90) and distilled water mix for cleaning tended to stain the glass and the resultant fibres had a higher loss. Annealing the glass preforms, prior to the fibre drawing, caused a reduction in the glass loss by several dB/m and the fibres fabricated were significantly more robust. Preforms were therefore annealed at 315°C (see Section 2.4) prior to being pulled into fibre. Altering the gas flow rate, from the 7l/min incident on the top of the preform and 2l/min incident on the bottom as described further in Section 3.4.2, or gas mix, from the standard 80% N_2 and 20% O_2 to 100% N_2, during the fibre pulling, initially resulted in a loss of diameter control however this stabilised after a short duration and there was no change in material loss measured.

2.2.2 FTIR measurements looking at the OH absorption and IR transmission

30g-50g glass samples were prepared for FTIR measurements, the samples were cut to thicknesses of 1 and 2mm and later 8mm and polished, to a final polish using 1µm Al_2O_3 paste, on the two opposite faces. FTIR scans were used to observe the OH absorption peaks and the limit of the IR transmission of the glass. From the peak of the OH absorption at 3.3µm a relative comparison could be made between the OH concentrations in the glass samples. This is because within the same material the OH concentration is proportional to its absorption [164]. The sample thickness was measured as it was required to calculate the glass loss from its transmission. This is given through Equations (3)-(5)

$$E = log_{10}\frac{1}{T} \quad (3)$$

$$\alpha = \frac{ln10(E - E_0)}{d} \quad (4)$$

$$loss = \frac{10(E - E_0)}{d} \quad (5)$$

where T is the transmission through the sample, E is called the glass absorbance, E_0 is the background absorbance including the Fresnel reflection and other surface scattering loss by the sample, α is the absorption coefficient per unit length and d is the sample thickness.

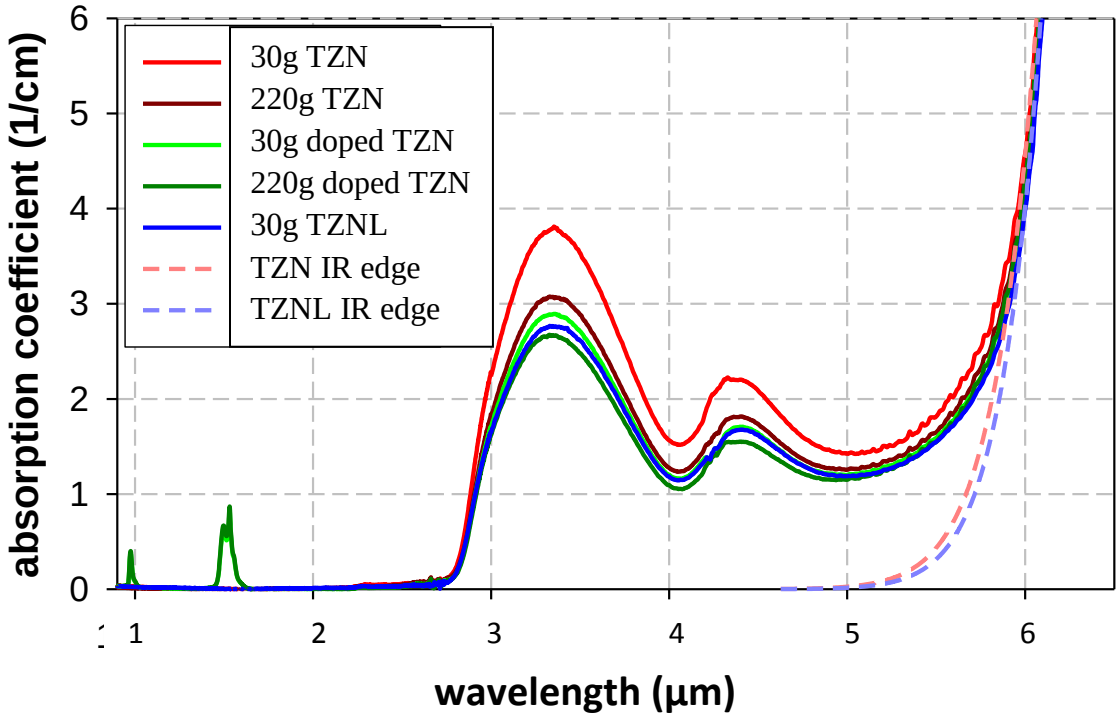

Figure 22: Plot of the IR absorption of undoped and doped (1×10^{20} ions/cm^3) TZN glasses of different batch size compared to the IR absorption of the TZNL glass. The theoretical location of the IR absorption for the two glass compositions is also plotted for comparison.

To measure the transmission of the glass samples the samples were mounted over an aperture on a metal slide in the FTIR instrument. From Figure 22, we can see the theoretical infrared transmission of the tellurite glass is out to 5μm, however from the absorption measurement this transmission is reduced considerably by the OH absorption which has its peak at 3.3μm. The peaks in the plot for the erbium III doped samples at 1μm and 1.5μm were caused by absorption of erbium III in those glasses. It can be seen that the infrared transmission of the glass was unaltered by the doping of the glass.

2.2.2.1 Open air melted samples

The bulk of the tellurite glass fabrication was performed in open air furnaces and cast and annealed under normal atmospheric conditions. A detailed description of the glass melting procedure is provided in Appendix 1. Under these conditions, OH groups are incorporated into the glass and as illustrated in Figure 22, these OH impurities lead to very high losses in excess of 1200dB/m ($\alpha = 2.7cm^{-1}$) at 3.3μm. Due to this high loss, the use of this glass for laser applications at 2.7μm is impractical, therefore, experiments were aimed at reducing this OH absorption. The development and fabrication of the low OH concentration samples was lead by Kevin Kuan and Heike Ebendorff-Heidepriem of the CoEP. These are covered in the next two sections.

2.2.2.2 Glove box re-melted sample

To reduce the OH content of the glass the first experiment involved re-melting one of the 300g billets that had previously been melted in open air, in a glovebox under a dry N_2/O_2 environment and casting the melt in a dry purely N_2 atmosphere. The glovebox furnace was a resistance furnace gas tight connected to the glovebox. An actuator arm was used to transfer the melts from the glovebox into the furnace. The dry N_2/O_2 mix was dried using a molecular sieve and was pumped through the furnace at a rate of 4l/min. The aim of repeating the melt was to evaporate off any OH in the glass that was absorbed into the melt, from moisture in the atmosphere, during its first open atmosphere melting. As can be seen in Figure 23, the loss in the mid-IR has been significantly reduced from that of the open air melted glasses.

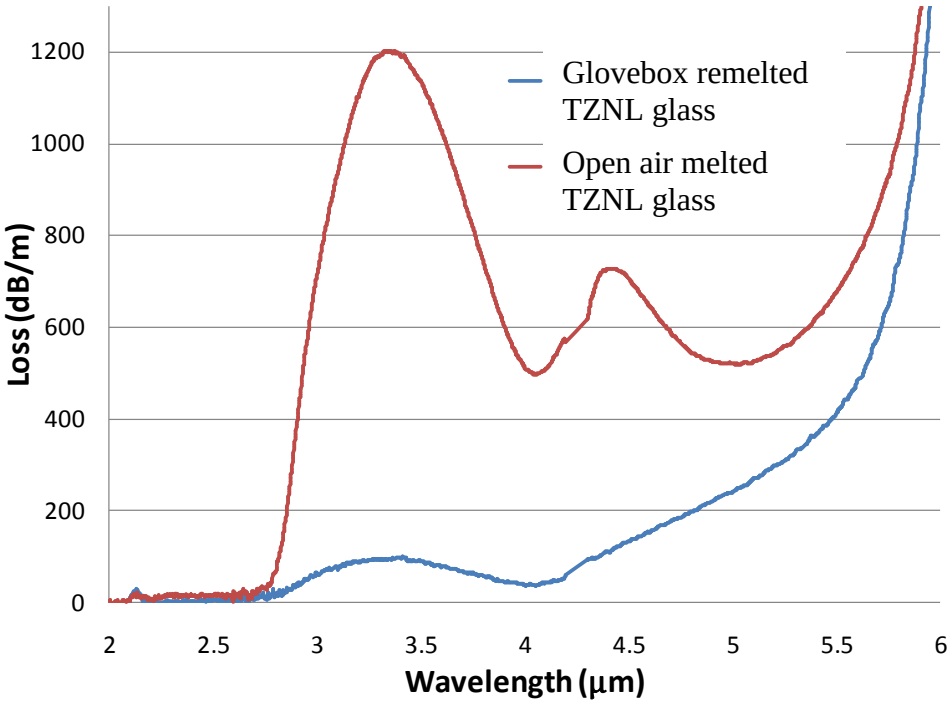

Figure 23: FTIR measurements of the bulk TZNL glass' optical material loss due to OH absorption when remelted in the glovebox (blue). The loss of an open air melted sample (red) is plotted for comparison

2.2.2.3 Glove box melted samples

Following the significant reduction in the OH concentration through remelting the glass in a dry environment, the next step was to fabricate the glass from its raw materials entirely within the glovebox under the same conditions. This was aimed at preventing the OH absorption into the glass that would have occurred during the initial open air melting of the previously described re-melted sample. A similar dry atmosphere melt has been performed by Shen et al. [160] which halved the OH absorption. The OH absorption measured for the first bulk glass samples fabricated this way are shown in Figure 24. This OH absorption covers the wavelength range from 2.6µm out to the glass' IR edge at 5µm as illustrated in Figure 24. The OH present in these glasses indicated that the OH impurities were not only caused by the absorption of moisture from the atmosphere but also by water or hydroxide impurities in the raw materials. Figure 24

also illustrates how melting a larger batch size resulted in the retention of more OH and agitation of the glass during melting reduced the OH concentration. Agitation of the melt consisted of removing the melt from the furnace and swirling the melt in the crucible and then returning it to the furnace. The swirling ensured homogeneity in the melt before it was returned to the furnace.

Experimentation was done to further reduce the IR loss of the glass without adding fluoride components to the glass which is commonly done in literature [165]. In order to keep the glass as a purely oxide based glass for reasons detailed in the introduction (Section 1.1), these experiments involved varying the melt times, removing the crucible lid and increasing the number of times the melt was agitated during melting. Melting the raw materials with the crucible lid removed enhanced the evaporation of water from the melt which in turn reduced the OH concentration. These samples were however, melted at a lower 850˚C to reduce additional evaporation of the other glass components.

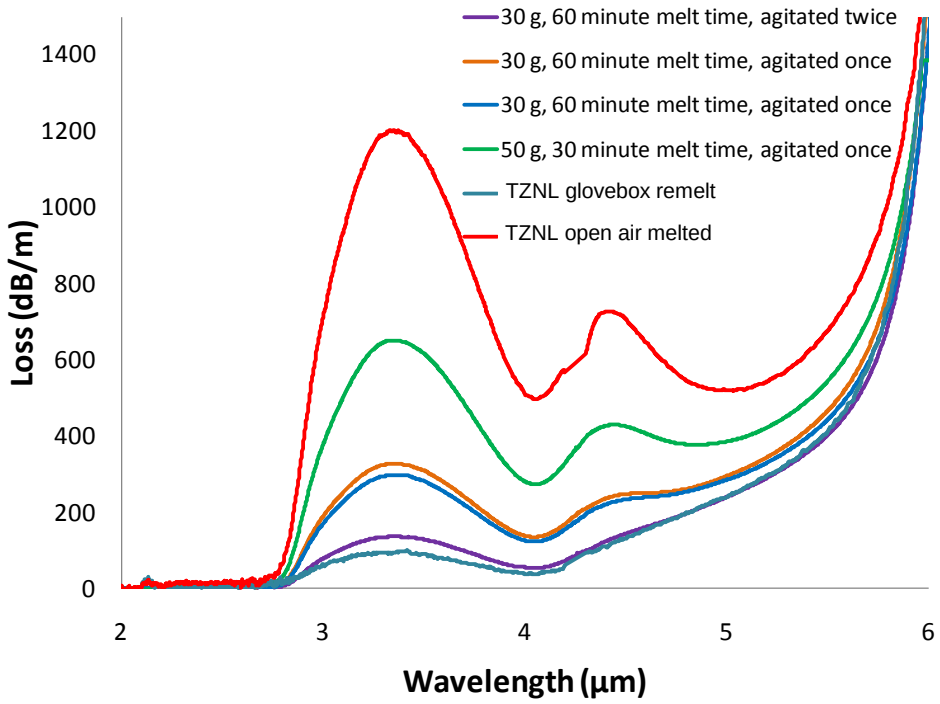

Figure 24: Plot of the IR loss for the initial glovebox fabricated TZNL bulk glass samples

The results of this study are summarised in Table 1, where the peak OH absorption, that occurs at 3.3µm, is given for different glass melting times and number of times the melt was agitated. The results presented in this table are plotted in Figure 25.

From this table it was determined that the OH concentration was reduced by increasing the melting time and either removing the crucible lid or frequently agitating the melt. It was found that increasing the melt time has the most significant improvement, however, there was less improvement obtained when increasing the melt time beyond 2 hours.

Table 1: Glass loss at 3.3µm for the bulk glasses varying the melt time and glass agitation

Melting experiment	Glass loss ± 2% (dB/m)	Glass melting procedure		Colour in Figure 24
		Melting time (min)	# times agitated	
Open air melted glass	1200	30	1	red
Glovebox remelt	100	30 (air) + 60 (dry)	3	teal
With lid Melting temperature = 900˚C	650	30	1	green
	186	30	3	purple
	136	60	2	
	58	120	3	
	50	120	9	
No lid Melting temperature = 850˚C	67	60	1	
	52	120	1	
	46	300	1	

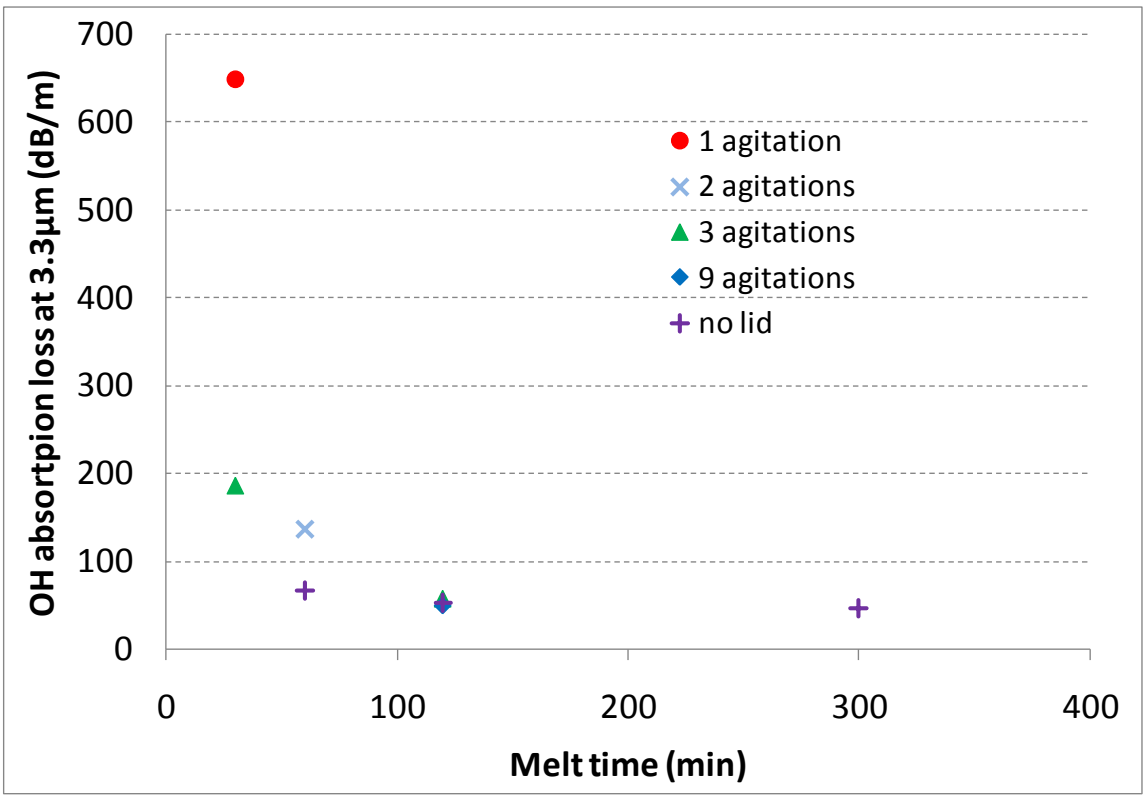

Figure 25: Plot of the bulk glass loss as a function of melting time while also varying the amount of agitation given to the melt during its melting.

The OH induced loss at 3.3µm was reduced from 1200dB/m to 50dB/m over the course of these experiments. This loss is comparable to a report of 20 – 30dB/m loss in fluorotellurite glasses melted for 2 hours [165]. Reducing the loss will facilitate the use of this glass in the mid-infrared. Despite this significant improvement the current value of the loss at 50dB/m was still considered to be too high for lasing at 2.7µm and hence the laser performance of the tellurite glass fibres was tested through lasing at 1.5µm (Chapter 5).

2.3 Density

The densities of the glass samples were measured in order to check the reproducibility of the glasses made and to accurately calculate the erbium III concentration from the

weight of erbium III oxide raw material added when batching. The technique used to calculate the density is provided in Appendix 1.

The addition of the erbium III dopant alters the glass density. When melting a glass with a new erbium III concentration, an estimate of the density is used to calculate the mass of erbium III oxide that is added to the batch of raw materials. Once the glass is made, the density was measured, using the technique described in Appendix 1, and the actual erbium III concentration was calculated. The equation used to calculate the weight of raw material (m_d) needed in order to achieve a desired ion density concentration of dopant is given in equation (6).

$$m_d\ (g) = \frac{N_{Er}\left(\frac{ions}{cm^3}\right) \times M(oxide) \times m(g)}{\rho\ (\frac{g}{cm^3}) \times N_A \times Multiplier} \quad \textbf{(6)}$$

where N_{Er} is the desired ion density of the dopant, the M is the weight of one mole of the dopant, m is the desired mass of the glass melt, ρ is the glass density, N_A is Avogadro's number (6.022×10^{23}) and the *Multiplier* is the number of dopant ions in the corresponding dopant compound (for example Er_2O_3 has a multiplier of 2).

The addition of lanthanum oxide to the glass, as with erbium, caused an increase in the glass density due to the higher molar mass of the lanthanum compared to the other components in the glass. The molar mass of the TZN glass is 139.1 g/mol compared to the molar mass of the TZNL glass of 143.1 g/mol. The densities of the doped and undoped TZNL glass as well as the base TZN glass are plotted against the erbium III concentration in Figure 26. The plot illustrates the linear increase in the glass density with erbium III concentration. This agrees with density measurements for other tellurite glass compositions presented in literature [69] and is consistent with the higher atomic mass of the erbium compared to the lanthanum which it replaces.

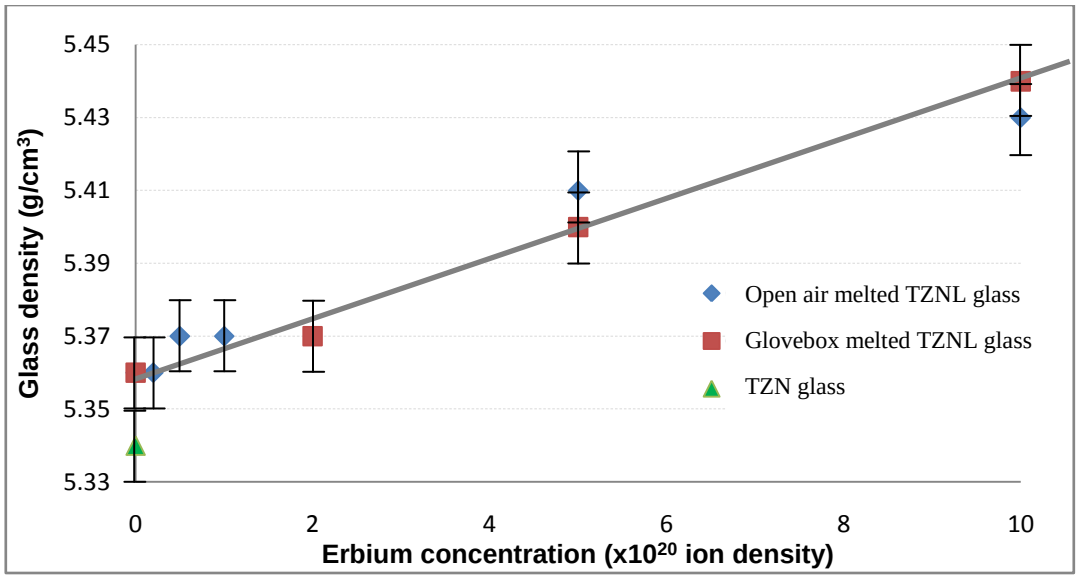

Figure 26: Plot of the TZNL glass density as a function of erbium III concentration. The densities of the samples melted in open atmosphere are given in blue and the base TZN glass given in green for comparison. The controlled atmosphere melted TZNL glass densities are given in red.

The accuracy of the density measurements were approximately ± 0.005 g/cm^3 and were dominated by the 0.1 % uncertainty in the weight measurements. It was found that any variation in density between the fabricated samples and billets, independent of their size, of the same composition, with same erbium III concentration was within the measurement error.

2.4 Glass Transition Temperature and Crystallisation Stability

The glass transition temperature and crystallisation stability were measured using Differential Scanning Calorimetry (DSC) where small samples of the tellurite glass were heated and the heat flow into the glass was measured as a function of temperature. Details are provided in Appendix 1. The DSC curves were measured at Flinders University by Sean Manning, however, the Author analysed the data thus obtained. An example of a DSC scan is given in Figure 27.

From the DSC scans the glass transition temperature (T_g) and the crystallisation onset temperature (T_x) were extracted. The glass transition temperature is the temperature above which less heat needs to be applied to the glass in order to increase its

temperature. This corresponds to a step in the DSC profile. At the crystallisation temperature there is a peak in the DSC curve. Both these values are illustrated in Figure 27.

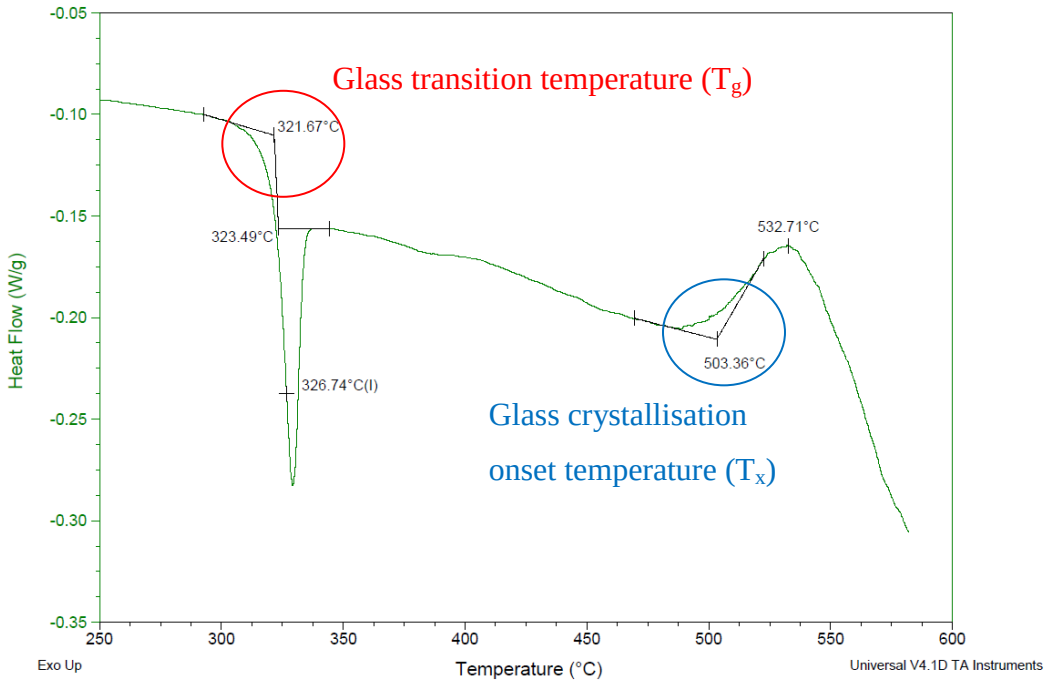

Figure 27: Example of a DSC scan for an undoped lanthanum tellurite sample.

The crystallisation stability is defined as the difference in temperature between the crystallisation temperature and the transition temperature ($T_x - T_g$) or Hruby parameter. The transition temperatures, crystallisation temperature and the crystallisation stability for the undoped and erbium III doped TZN and TZNL glass samples are given in Table 2 where the '-' signifies that the crystallization onset temperature was not observed before the DSC reached its maximum temperature (600°C). Compared to the base TZN glass, the transition temperature and crystallisation onset temperature both increase with addition of the lanthanum oxide. Due to the more significant increase in the crystallization onset temperature, the crystallisation stability is also improved. The higher transition temperature of the TZNL glass is consistent with its higher viscosity, illustrated in the next section.

Table 2: Measured glass transition temperatures and crystallization stability for doped and undoped base tellurite glass and lanthanum tellurite glass.

Er^{3+} concentration	Glass	DSC measurements		
		Tg (°C)	Tx (°C)	(Tg – Tx) (°C)
	TZN	302	435	133
	"	305	433	128
0.2×10^{20} ions/cm^3	TZN	305	≈430	≈125
2×10^{20} ions/cm^3	TZN	271	-	-
10×10^{20} ions/cm^3	TZN	282	421	139
	TZNL	318	-	-
	"	314	490	176
	"	322	503	181
1×10^{20} ions/cm^3	TZNL	319	-	-

The DSC measurement can be used to determine the optimum temperature for the annealing for the glass. During each of the fibre fabrication stages, local temperature variation across a glass melt or extruded preform can result in permanent strain being frozen into the glass. Annealing the glass, which involves heating the preform or billet to the glass' Tg and then cooling it slowly through the glass transformation region, is used to achieve the same configurational structure throughout the whole glass billet or preform alleviating any permanent strain in the glass [166]. By heating the glass to within or just above its transition temperature range and keeping it at this temperature for an extended period of time this stress is released from the glass. In the case of the TZNL glass, the glass is heated to 315°C and held there for 4 hours. The glass is then cooled at a rate of 0.1°C/min. This optimum annealing temperature was also tested experimentally by finding the deformation temperature. This was done by resting an extruded tellurite glass rod on a sharp edge in the furnace. By ramping up the temperature of the furnace and looking to see at what temperature the edge left an indent in the rod, the deformation point of the glass was found. With the deformation temperature as the upper temperature limit for annealing, the suitability of the annealing temperature was verified. The glass annealing range, deformation point, crystallisation

onset temperature and the viscosity values calculated in the next section are illustrated in Figure 28. This plot also includes the extrusion and fibre drawing temperature ranges and it can be seen both of these process occur at temperatures below the crystallization onset temperature for the glass.

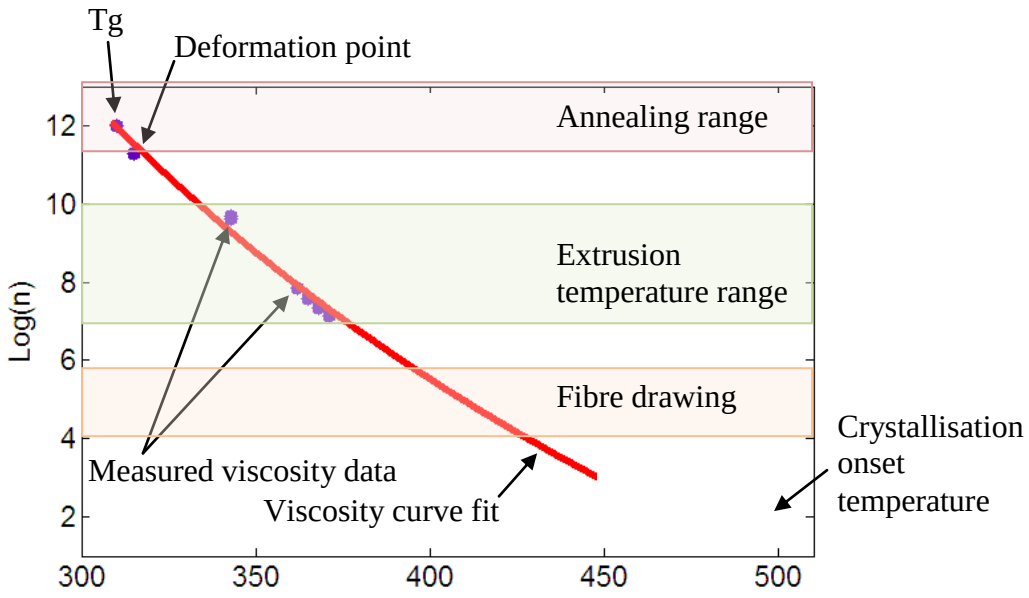

Figure 28: Viscosity-temperature plot of the TZNL glass including the Tg (DSC), deformation temperature and DSC crystallisation onset temperature. The curve is fitted from measured viscosity data discussed in section 2.6. The extrusion and fibre drawing temperature ranges are included to illustrate their location between the glass transition temperature and crystallization onset temperature.

2.5 Refractive Index

The refractive index of the TZN and TZNL tellurite glass compositions and in particular the differences in refractive index between the doped and undoped glasses were measured to enable accurate modelling of the guidance properties of a fibre made from this glass. The guidance of a microstructured optical fibre can be controlled by the structure of the fibre and not by the distribution of the dopant provided the index difference between the doped and undoped glass are insignificant. The effect on the guidance of the large mode area fibres when doping only the core is modelled in Section

3.2. The ability to dope only the core of the fibre allows for the addition of an outer cladding to the fibre geometry and the cladding pumping of the fibre. This is covered in more detail in Section 3.2.

Initial attempts at measuring the glass refractive index were performed using a thin film ellipsometer. This equipment was however designed for thin film thicknesses of around 8nm. The resultant measurements using this equipment were rather inaccurate as the samples analysed varied in thickness from 1 to 2mm and in some cases featured a significantly non-uniform thickness. More accurate measurements have since been made using a Metricon prism coupler. A diagram of the prism coupler setup is provided in Figure 29. These measurements were made by the Author at Australian National University initially using a HeNe laser at 633nm for all the available erbium III doped TZN glasses. The refractive indices were later measured for the undoped and 1×10^{20} ions/cm^3 erbium III doped TZNL samples at 532, 633, 1064, 1310 and 1550nm. Measurements were made to an accuracy of ±0.0005. This was determined statistically through repeated measurements at different locations on the same sample. For the refractive index measurements, a rutile (TiO_2) prism was used as the index of the tellurite glass was known to be around 2. When measuring the index, the samples were held firmly against one of the faces of the prism. A laser was collimated through the prism and reflected off the glass sample. The intensity of the reflected light was measured on a photodetector. The sample and prism were rotated and the reflected intensity was measured as a function of angle. In the resultant output, provided there was good contact between the prism and the glass sample, there was a sudden drop in the reflected intensity at an angle corresponding to the total internal reflection angle of the glass-prism interface. With the refractive index of the TiO_2 prism well known the glass index was calculated. Figure 30 illustrates the output from a scan where the scale on the x-axis has already been converted from the rotation angle to refractive index by the refractive index measurement software. The location of the drop in reflected intensity is circled in red.

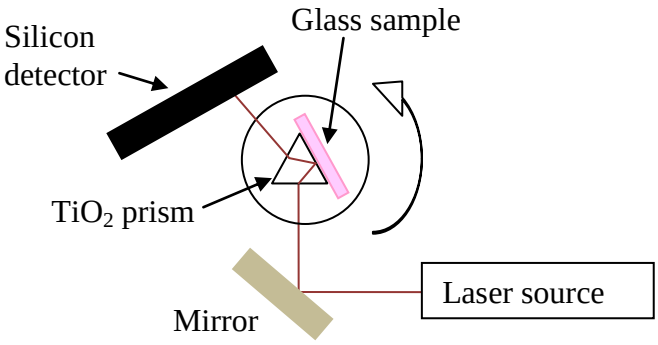

Figure 29: Experimental setup for the refractive measurements using the prism coupler. The glass sample and rutile (TiO_2) prism is rotated and the intensity of light reaching the silicon detector is measured as a function of angle.

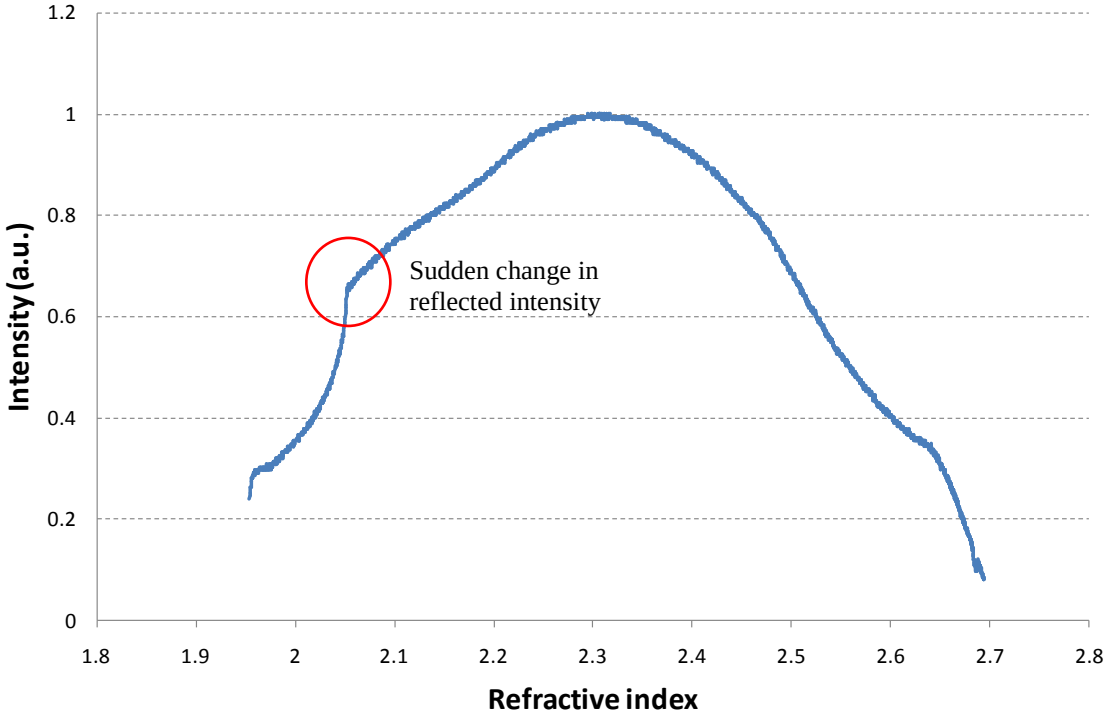

Figure 30: Scan of the reflected intensity from the prism/glass sample interface using a HeNe laser and a 1×10^{20} ions/cm^3 Er^{3+} doped TZNL glass sample. The sample angle has been converted to refractive index and the location of the sudden drop in intensity has been circled in red. The sampling of the data is every 1×10^{-4} refractive index units.

The measured refractive indices of the different erbium III-doped glass samples are provided in Table 3. These measurements show a reduction in the refractive index with increasing erbium III content. This reduction in the refractive index when doping is a result of the very high polarizability of the TeO_2 in the glass. When doping the glass some of the tellurium ions are replaced by the rare earth dopant ions, which have a comparatively low polarizability. As a result, when doping the glass, the refractive index, which is controlled by a combination of the glass density and its polarizability [167], decreases as the large reduction in the polarizability is more significant than the increased density observed in the previous section.

With the ultimate aim of fabricating a fibre where only the core is doped, a reduction in the core refractive index, corresponding to the index difference between the doped and undoped TZN glasses, would reduce the index of the core to below that of the cladding in the modelled fibres (Section 3.3). Without photonic bandgap effects, which are not considered here, such a fibre would not guide light. Some fibre geometry modelling (Section 3.3.1) was undertaken to determine whether by modifying the cladding geometry, the index of the cladding could be reduced sufficiently to below that of the doped TZN glass core. Modification of the cladding structure, however, proved not to be a valid solution to the problem given the large difference in refractive index between the doped and undoped TZN glasses and the large air fractions required in the cladding to achieve the desired cladding index.

The addition of lanthanum oxide to the glass composition, and replacing only the lanthanum oxide with erbium oxide when doping the glass, solved this problem as it significantly reduced the index difference between the doped and undoped glasses. To within the measurement error, the refractive indices of the doped and undoped TZNL glasses are equal.

Table 3: Table of the measured refractive indices for both doped and undoped glass samples for both the base glass and the lanthanum tellurite glass.

Glass	Ln^{3+} concentration (10^{20} cm^{-3})		density	Refractive index		
	Er^{3+}	La^{3+}		633nm	1310nm	1550nm
TZN	-	-	5.34	2.0515	-	-
	1	-	5.37	2.0505	-	
	5	-	5.40	2.0435	-	
TZNL	-	10	5.37	2.0360	1.987	1.983
	1	9	5.37	2.0355	1.987	1.983
error			*± 0.01*		*± 5×10^{-4}*	

Equal indices for doped and undoped glass

A Sellmeier curve was derived to describe the refractive index of a glass as a function of wavelength. A common technique to predict the refractive index of a silica based glass is to consider it as a linear combination of glasses made from its components [167]. Prior to the measurement of the refractive indices of my tellurite glass, predictions of the refractive index for the TZN glass composition used were made through the linear combination of the Sellmeier curves for the binary sodium and zinc tellurite glasses, that were found in literature [74]. Once the refractive indices of the glasses were measured, curve fitting was used to fit a Sellmeier curve to the data. In Figure 31 we can see the Sellmeier curves for the binary tellurite glasses, the predicted Sellmeier curve for the TZN glass calculated from a linear combination of these curves, these measured refractive index data for the TZN and TZNL glasses and a Sellmeier curve fitted to these data. This measured data also includes the refractive index for the TZNL glass measured at 532nm and 1064nm as well as the values given in Table 3. The Sellmeier curve plotted to fit the measured indices is given in equation (7) along with the Sellmeier coefficients used to fit to the measured data, where n is the refractive index and λ in the wavelength. When fitting to the measured refractive index data, the Sellmeier coefficients are calculated to be A = 2.42489, B = 1.5004, C = 0.0525775, D = 2.32884 and E = 225. From this plot it can be seen that using a linear combination of the refractive index of binary tellurite glasses, a technique commonly used for silicate

glasses [167], is not a good approximation to predicting the refractive index of this tertiary tellurite glass. This is evident in the significant change in the glass' refractive index that occurs when making small changes to its composition [74].

$$n^2 = A + \frac{B}{1 - C/\lambda^2} + \frac{D}{1 - E/\lambda^2} \tag{7}$$

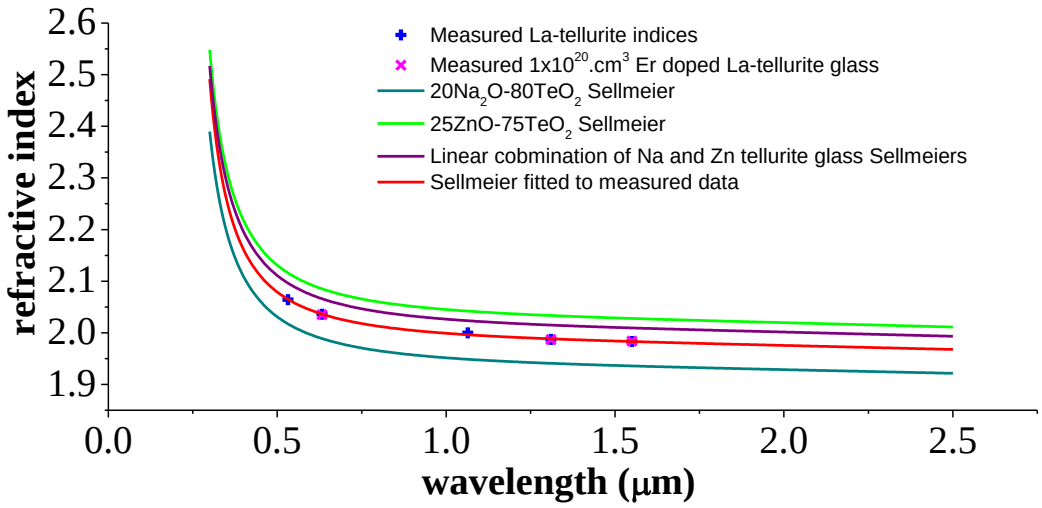

Figure 31: The measured refractive indices for the TZNL glass and a fitted Sellmeier curve are plotted. Sellmeier curves for the sodium and zinc binary tellurite glasses [74] along with a prediction of the TZNL glass as a linear combination of these two binary glass curves are also plotted for comparison.

2.6 Viscosity/Temperature Relations

An understanding of the temperature dependence of the glass viscosity is required to select the optimum glass extrusion and fibre drawing temperatures. The extrusion technique is described in Section 3.1. The use of appropriate extrusion temperatures and speeds can minimise preform tapering as well as minimise the extrusion time.

If the extrusion temperature is low, the extrusion force will be high, and the die could break during the extrusion. The force can be reduced by slowing the piston ram speed, however, the extrusion would then take longer and the glass will be held at a high

temperature for a longer duration, which can result in the formation of crystals in the glass.

If the glass is extruded at high temperature, the preform can be soft enough to taper under its own weight due to gravity. This tapering occurs at the die exit where the preform is at its softest. Tapering of the preform has its advantages and disadvantages. Extreme tapering can result in very thin performs (< 8mm outer diameter) which are difficult to draw into fibre. This is because it is hard to achieve good stability in the fibre drawing process when working with the small glass volume of the thin preform. Tapering is also responsible for preform structure deformation as it causes the air holes in the preform to reduce in size. Slight tapering of preforms that are extruded through dies with a large die exit can, however, be used to intentionally reduce the outer diameter of a preform down to between 10 and 15mm. This is especially important when using a complex die design where the diameter of the die is increased to add extra complexity to the preform structure. Tapering can also be used to increase the length of the preform generated, allowing for the use of smaller glass billets. The higher extrusion temperatures, however, can also result in the nucleation of crystals in the glass.

A viscosity gradient in the preform at the exit of the die, which can be caused by not having the extrusion furnace concentric around the die, causes a bending of the extruded preform. As expected from simulations found in literature [168], this preform bending occurs towards the direction of higher viscosity. The sensitivity of the viscosity to the temperature, which is indicated by the slope of the temperature viscosity curve, indicates the susceptibility of the preforms to this bending. An example of the temperature viscosity curve for the TZN and TZNL glasses is provided in Figure 33 following a description of how the viscosity of the glass was measured. A significant amount of work by the Author and the Centre of Expertise in Photonics research group, was done on reproducibly concentrically aligning the extrusion parts in the furnace. Figure 32 illustrates the slight bending still present in a TZNL glass rod despite careful alignment of the extrusion body, illustrating the sensitivity of the preform bending with this glass on the furnace alignment.

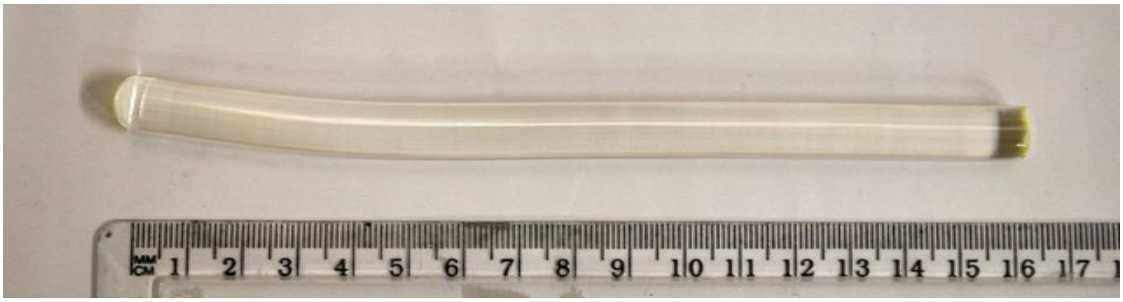

Figure 32: Undoped TZNL glass rod generated from the extrusion of a 100g glass billet.

From the research presented by Roeder et al. [169] and Ebendorff-Heidepriem et al. [170] the extrusion force through a die can be predicted. It is known that the pressure (P) applied by the extrusion machine, which correlates to the extrusion force (F), is proportional to the total volume flow rate (Q_0), calculated from the piston ram speed (v_0) and the glass viscosity (η), which is highly temperature (T) dependent. The proportionality constant, sometimes called the 'die constant' (K_{die}) [170], is a feature of the extrusion die and reflects the amount of friction applied by the die. This is given in Equation (8) [169, 170].

$$P = K_{die}\,\eta Q_0 \tag{8}$$

For a straight circular die channel, the die constant can be calculated from the die channel length (L_1) and the channel diameter (D_1). This relationship is given in Equation (9). In the case of a die consisting of multiple channels or feed holes the die constant is reduced proportionally to the number of feed holes (N). An example of this is in the multi-hole extrusion where the glass is forced through a sieve plate, used to hold the pins that form the holes in the preform structure, and recombine on the other side around these pins. The new equation is given in Equation (10).

$$K_{die} = \frac{128 L_1}{\pi D_1^4} \tag{9}$$

$$K_{die} = \frac{128L_1}{\pi N D_1^4} \quad \textbf{(10)}$$

The ram force and volume flow rate were calculated from the pressure and ram speed, respectively given the billet cross-section (A_0) through Equations (11) and (12).

$$P = \frac{F}{A_0} \quad \textbf{(11)}$$

$$Q_0 = A_0 v_0 \quad \textbf{(12)}$$

During the extrusion of simple and complex preforms, forces between 3 and 30kN were used. For the glass to be soft enough for its extrusion, the viscosity of the glass, which is set by the temperature of the extrusion, needed to be in the range of 10^7 – 10^{10} dPa.s [169]. This force range was chosen to minimise tapering of the preforms and reduce the stress the extrusion process puts on the glass. In order to calculate the viscosity of the glass for a given temperature, an Arrhenius equation was used [30]. The Arrhenius equation used to fit the measured temperature-viscosity data was a valid approximation as the curve fitting was only over a short temperature range. This equation is given as Equation (13). Experimentally determined viscosities were used to fit for the *A* and *B* parameters corresponding to our glass.

$$log_{10}\eta = A + \frac{B}{T} \quad \textbf{(13)}$$

In order to find the *A* and *B* parameters the viscosity of the glass was calculated from the extrusion force, and hence viscosity, for different die geometries and at different temperatures. The dies used for these extrusions featured a known channel length and diameter and the extrusion force was also recorded. The volume flow rate is calculated from the billet diameter and the ram speed set on the extrusion machine and the pressure was calculated from the steady state extrusion force. With all these

parameters, substitution into Equation (8) allowed for the calculation of the required extrusion force across the full extrusion temperature range. The temperature dependence of the viscosity is plotted in Figure 33.

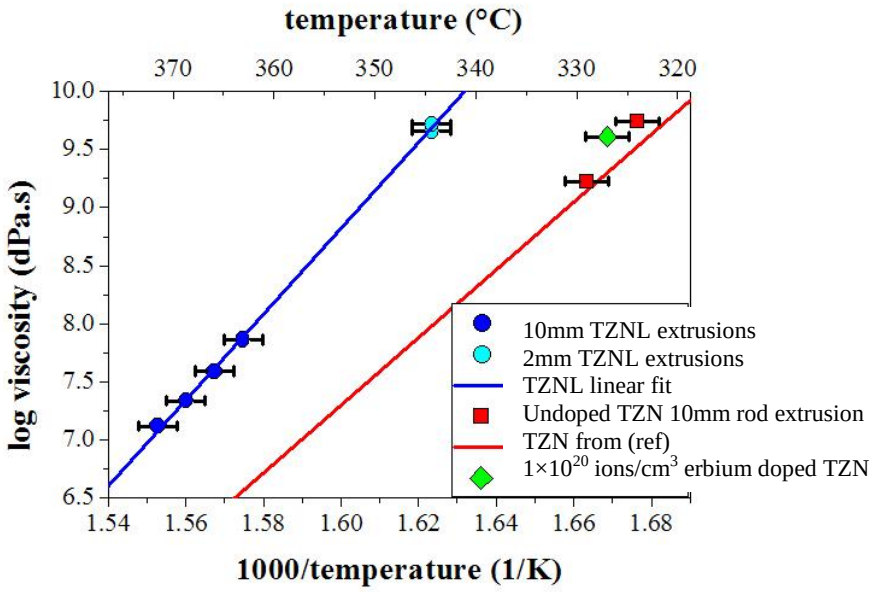

Figure 33: Plot of the temperature dependence of the tellurite glass viscosity. The fitted viscosity curve along with the measured viscosity data for the doped and undoped TZNL glass is given in blue and the viscosity data for the base TZN glasses are given in green (doped) and red (undoped). The red line is the Arrhenius equation found from [171] (i.e. it is not a fit to the measured data) for the TZN glass composition.

The bulk of the data presented in the plot was calculated from the extrusion force of a series of 10mm rod extrusions. In the case of the TZNL glass, an additional 4 data points were calculated using a 2mm rod extrusion where the temperature was varied over the course of the extrusion and the resultant steady state extrusion force was recorded. The use of a 2mm rod extrusion allowed for the determination of the glass melt viscosity at higher temperatures. These higher temperatures align well with the extrusion temperatures used for the more complex preform extrusions.

The viscosity-temperature curve $\eta(T)$ for the base TZN glass has been reported previously by Braglia et al. [171]. The Arrhenius based viscosity curve documented in

this paper is given as the red line in Figure 33. In the plot, the TZN glass viscosity data measured using the extrusion technique agrees well with this viscosity curve hence validating the use of rod extrusion as a technique for the calculation of the glass viscosity. For the TZNL glass, the fitted Arrhenius equation, given by Equation (13), along with the measured viscosities are also plotted. From Figure 33 it can also be seen that the addition of a dopant has a negligible effect on the glass melt's viscosity. It is also evident that the TZNL glass melt viscosity is higher and has a slightly steeper slope than the base TZN glass melt. This higher viscosity explains the higher temperatures used in the extrusion and pulling to fibre of the TZNL glass.

At extrusion temperatures, a temperature gradient of 1 ºC at the die exit would result in a viscosity difference of 25 % across the extruded preform. The significant viscosity gradient across the preform at the die exit explains why the bending of the tellurite glass preforms was highly sensitive to the alignment of the extrusion furnace.

From these viscosity curves the optimum extrusion speed and furnace temperature, for an appropriate extrusion force (>3kN and <30kN), were calculated to guide the choice of parameters to be used for the extrusion of more complex structured dies with multiple feed holes of different sizes (see Section 3.1).

2.7 Glass Tellurite Glass Development Summary

As part of this research, the tellurite glass was refined to have a minimum loss of 0.1dB/m at 1.3µm. When aiming to increase the transmission of the glass in the mid-infrared, the absorption due to OH impurities in the glass was reduced from 1200dB/m in the open air melted glasses to 50dB/m at the peak of the OH absorption at 3.3µm.

The densities of the glass samples were measured, demonstrating reproducibility in the glass melting. These densities were also used to accurately calculate the dopant concentrations in the glass samples and billets fabricated.

DSC measurements demonstrated the glasses good crystallisation stability and the increase in the crystallisation stability when lanthanum oxide was added to the TZN composition. DSC measurements were also used to determine the optimum annealing temperature of 315ºC for the TZNL glass.

The refractive indices of the glasses were measured primarily to get an understanding of the index difference between the doped and undoped glasses. With the requirement to doped only the core of a double clad fibre and have the dopant distribution not affect the guidance by the fibre, the refractive index difference needed to be minimised. The addition of lanthanum oxide to the glass composition and the replacement of the lanthanum oxide with the erbium oxide dopant reduced the index difference between the doped and undoped glasses to within the error if the refractive index measurement. A Sellmeier curve was also calculated for the glass to represent the wavelength dependence of the glass' refractive index.

The temperature dependence of the TZN and TZNL glass viscosities was measured to enable an accurate choice of the extrusion temperature and extrusion speed. A careful choice of these parameters minimised the risk of die breakage, crystallisation of the glass and the undesired tapering of the preforms extruded. Knowledge of the glass viscosity also provided an understanding of a preforms' susceptibility to bending if it was not heated uniformly during its extrusion.

3. Fibre Modelling and Fabrication

The structured optical fibre development component of this research was directed towards the fabrication of the gain medium for a laser. The fibre used in a high power fibre laser would ideally have a large mode area and propagate a single transverse mode guided down its core. Thus the fibre development began with the fabrication of large mode area fibres, which had core diameters around 50μm.

In a double clad fibre laser, the pump is confined by an outer cladding with a larger diameter. Ideally this outer cladding would have a high numerical aperture (NA) for strong confinement of the multimode pump laser and a single mode core for confinement of the laser mode. Since absorption of the pump should occur only in the core of the fibre, the erbium III dopant must be located only in the core. Following the fabrication of the large mode area fibres, fibres with only their core doped were fabricated.

To reduce the pump volume and hence the population inversion threshold for the fibre laser experiments described in Chapter 5, fibre fabrication was directed towards the development of fibres will smaller core diameters. The first smaller core fibre fabricated had seven rings of air holes in the cladding and a structure similar to that of the LMA fibres fabricated.

The core diameter was reduced further through adding a caning step to the fibre fabrication process. This process is described in more detail in section 3.4.2 and is a common technique used to achieve small core fibres [159]. The first fibre geometry targeted using this extra caning step was a four ring structure. To further simplify the fibre geometry, the fibre geometry was changed to consist of only three holes in the cladding. Since then attempts were made at modifying this geometry to increase its core size and ultimately improve the output laser power achieved.

This chapter begins with a general description of the fibre fabrication including the extrusion technique and fibre drawing. As described previously in Section 2.2.1, the glasses used in the development of the following fibres had been refined to a minimum loss of 1.3dB/m at 1.3μm.

3.1 Fibre Fabrication

Extrusion

The structured preforms for this work were fabricated by extruding the tellurite glass through a complex extrusion die. Tellurite glass is considered a soft glass due to its low softening temperature which, allows the extrusion with forces less than 50kN at temperatures around 360°C. The extrusion technique consists of heating the glass and using a piston to force it through a die containing the desired geometry.

The glass billets were polished prior to their extrusion. This reduced the trapping of small air bubbles and the seeding of crystals in the preform caused by the rough surface of a billet.

A picture of the typical extrusion parts for the 30mm and 50mm diameter billets are provided in Figure 34 (a) and (b), respectively. The low temperatures used in the extrusion of tellurite glass facilitates the use of stainless steel (grade 303 stainless steel) dies, extrusion tubes and piston plates. Due to oxidation of the steel parts during an extrusion, each of these steel parts that came in contact with the glass were used only once. All of the stainless steel die parts were machined using a CNC mill to a tolerance of 0.05mm.

A photograph of the extrusion machine and temperature controller was provided in Figure 35. The extrusion body was inserted into the centre of a resistance furnace and heated. Once at temperature, a thread driven press was used to controllably force the glass at a set piston speed through the stainless steel die. As discussed in Section 2.6, by setting an appropriate furnace temperature and piston speed the extrusion force could be maintained between 1 and 20kN.

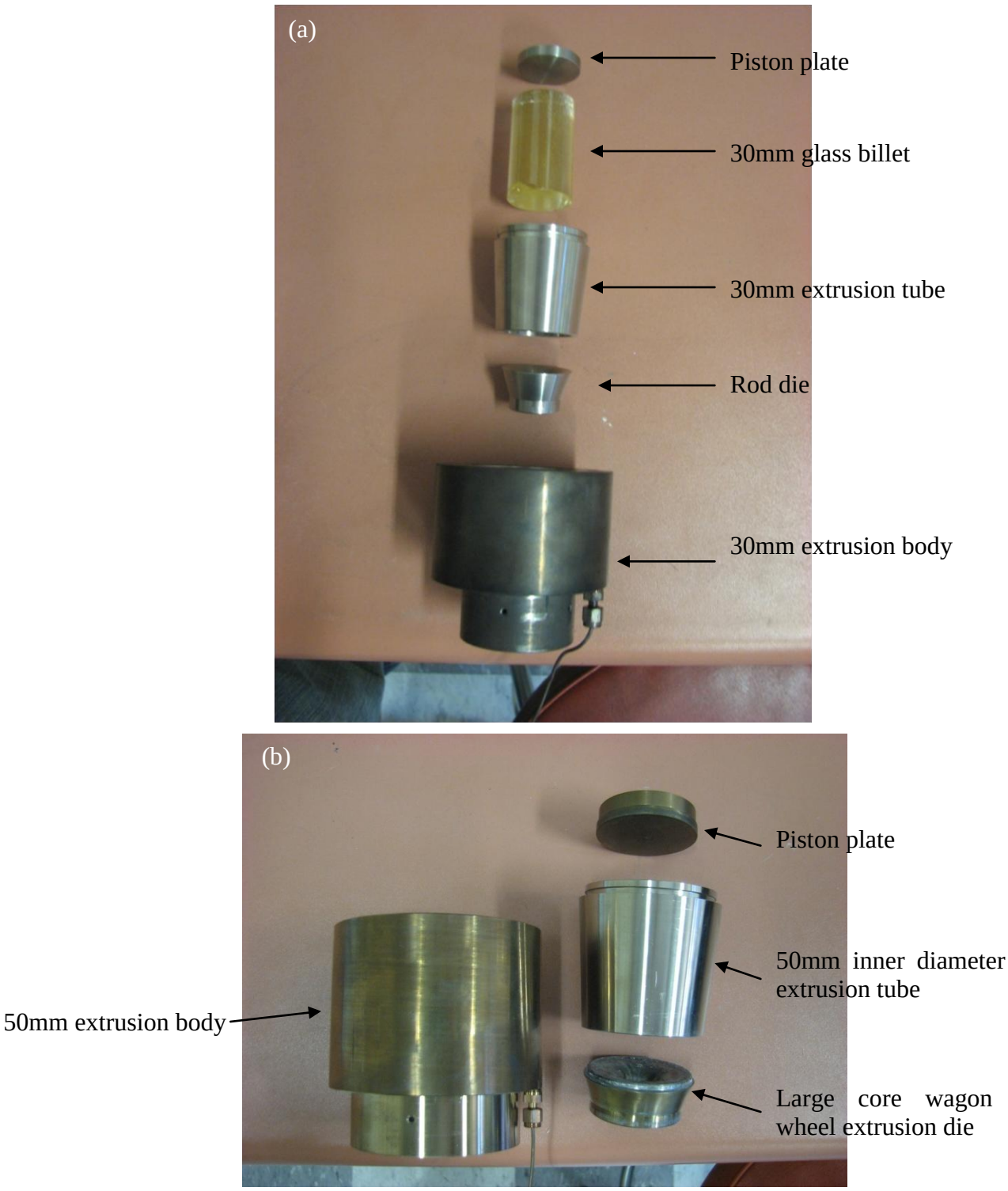

Figure 34: Extrusion body parts used to extrude 30mm (a) and 50mm (b) billets.

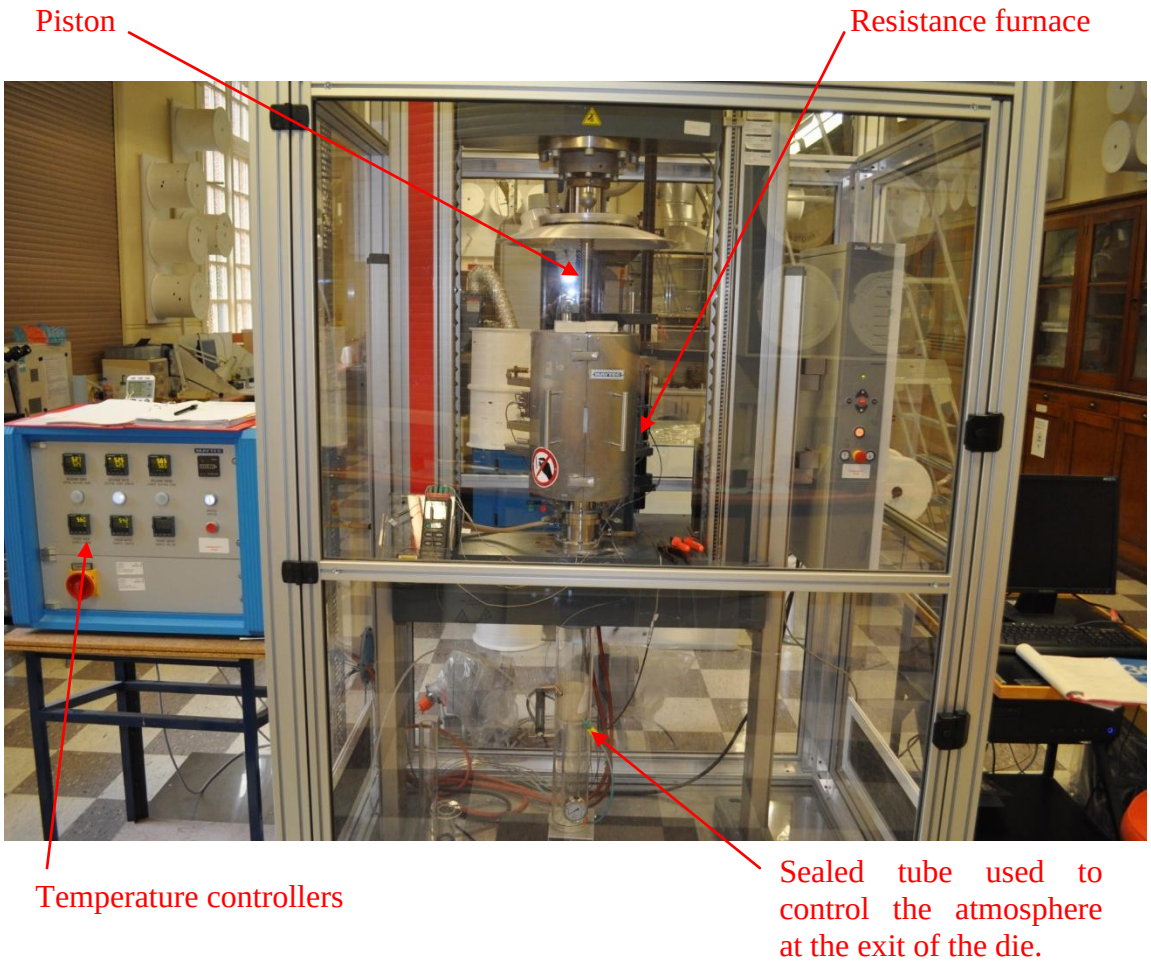

Figure 35: Photograph of the extrusion machine.

Fibre drawing

The extruded preforms were drawn down to fibres by either Roger Moore or Alastair Dowler, who were technical staff, at the time of this research, working in the Institute of Photonics & Advanced Sensing (IPAS) at the University of Adelaide. The fibre drawing tower pictured in Figure 36 was used to pull rods and the structured preforms down to fibre. The glass preform or rod was placed within the induction furnace at the top of the drawing tower. The preform was heated and the end of the preform began to "neck down" and dropped under gravity as illustrated in Figure 37. This end was attached to the drum at the base of the tower where it was pulled at a constant rate by the rotating drum. The outer diameter of the fibre was controlled by adjustment of the preform feed

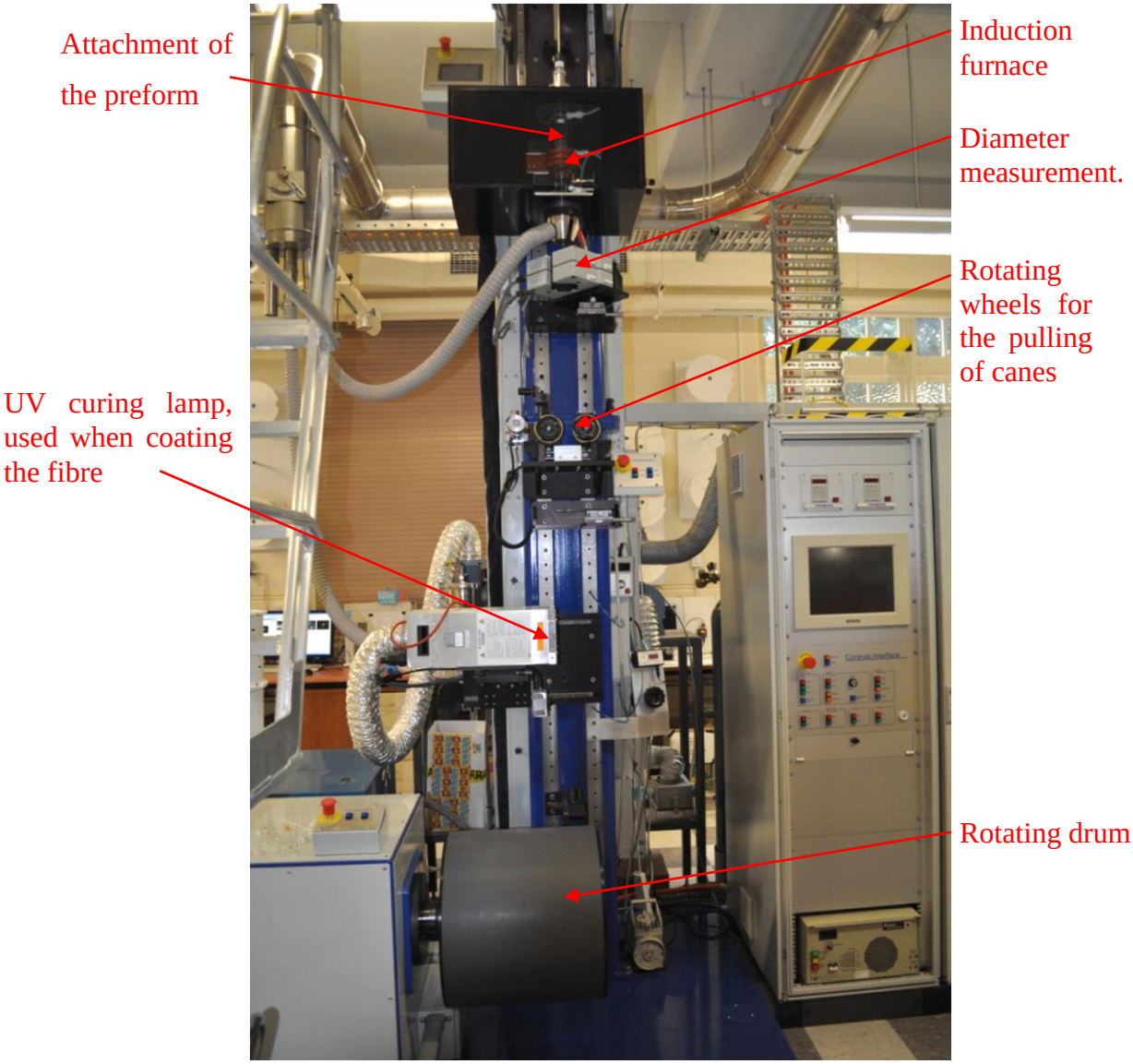

Figure 36: Photograph of the fibre drawing tower.

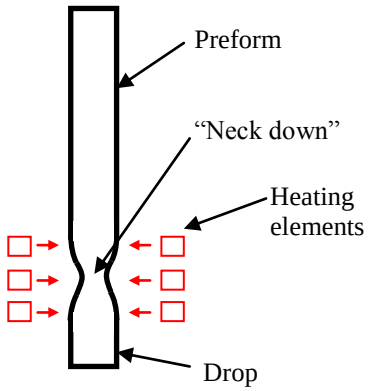

Figure 37: Illustration of the preform "neck down" and "drop" that forms at the start of a fibre pull

speed, which was the rate that the preform was lowered into the furnace, the preform temperature and the pull speed, determined by the rotating speed of the drum at the base of the tower. The diameter of the fibre was monitored continuously while the fibre was being pulled. The majority of the fibres fabricated had an outer diameter of approximately 200µm.

Unstructured fibres drawn from glass rods were used in the material transmission loss measurements described in Section 2.2.

When working with structured preforms, careful adjustment of the temperature of the furnace and the feed and drum speeds could be used to further control the fibre's structure. For example, if a preform was pulled at a lower temperature there were less surface tension effects that could affect the structure in the fabricated fibre. However, if the drum speed was not adjusted, the fibre would have been pulled under too much tension and would have broken.

The application of a vacuum or pressure to an element of the structure has also been explored. In section 3.3.2, a vacuum was applied to the preform to fuse the interface between the doped cane in the core of the fibre and the cladding.

3.2 Large Mode Area Microstructured Fibres

The first set of structured fibres fabricated within this research were LMA fibres consisting of four rings of holes in a hexagonal lattice. This structure was later modified to localize the erbium III absorption to the core. This was done through the insertion of a doped rod in the centre of an undoped structured cladding.

3.2.1 Modelling of four-ring LMA fibres

Prior to the fabrication of the LMA fibres, the number of modes that would be supported by a particular cladding geometry was modelled using finite element modelling (FEM) in Comsol. This allowed for the determination of the cladding geometries which would support only a single mode. Initially a finite element approach was used due to the complexity of the LMA cladding geometry. The Comsol package was run through a

Matlab program in which the required variables, including the wavelength and fibre geometry were defined.

Initial modelling used the entire fibre geometry, which consisted of four rings of air holes in a hexagonal lattice as shown in Figure 38. This geometry was defined in the Matlab code, by the cladding's hole to hole spacing, also called pitch (Λ), and the hole diameter (d) to pitch ratio (d/Λ). An example of the cladding geometry generated when the pitch was set to 25μm and the d/Λ to 0.4 is provided in Figure 38.

To get a rough understanding of the impact of varying a cladding geometry's pitch and hole size on its modal guidance, an equivalent step index fibre was used.

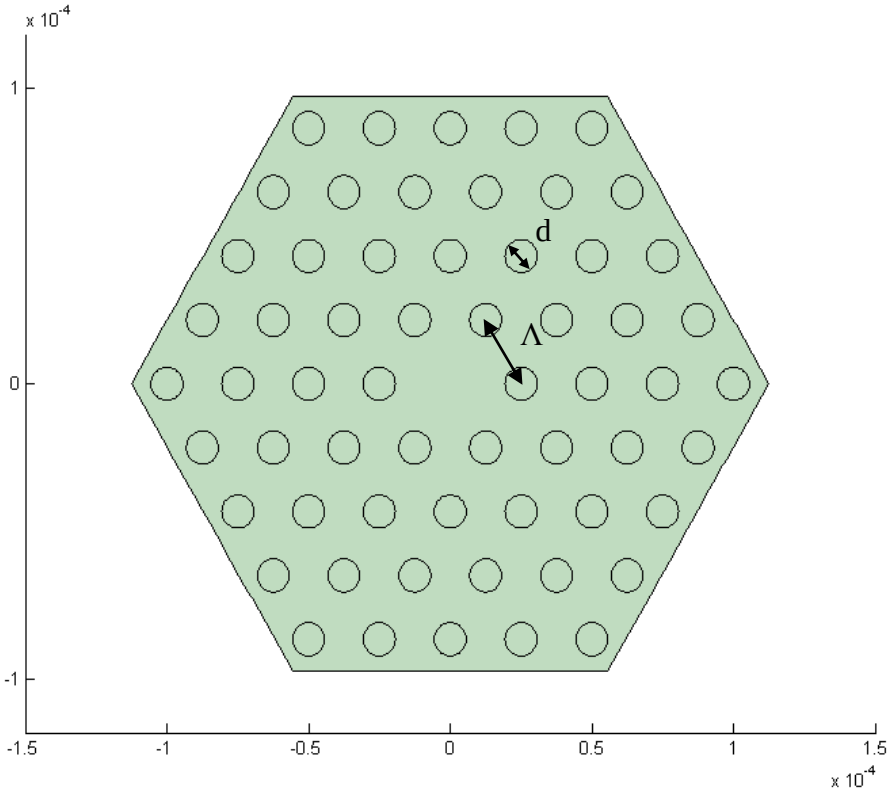

Figure 38: Microstructured optical fibre (MOF) geometry defining the structures air filling fraction (d/Λ) and pitch (Λ)

The refractive index for the cladding in the equivalent step index fibre was found through calculation of the fundamental space filling mode (FSM) [112-114]. The fundamental space filling mode is the mode that would propagate through the cladding

structure if it was infinitely periodic and there were no missing holes at the core. To simulate this endlessly periodic structure, the basis unit was modelled in Comsol with continuous boundary conditions.

The cladding index was taken to be the effective index of the FSM found through the FEM modelling. This effective index defined the speed that light would have propagated through the structure and was often slightly less than the glass index due to the mode's overlap with the air in the cladding structure. The greater this overlap, the lower the effective index of the FSM. The guided FSM is shown in Figure 39.

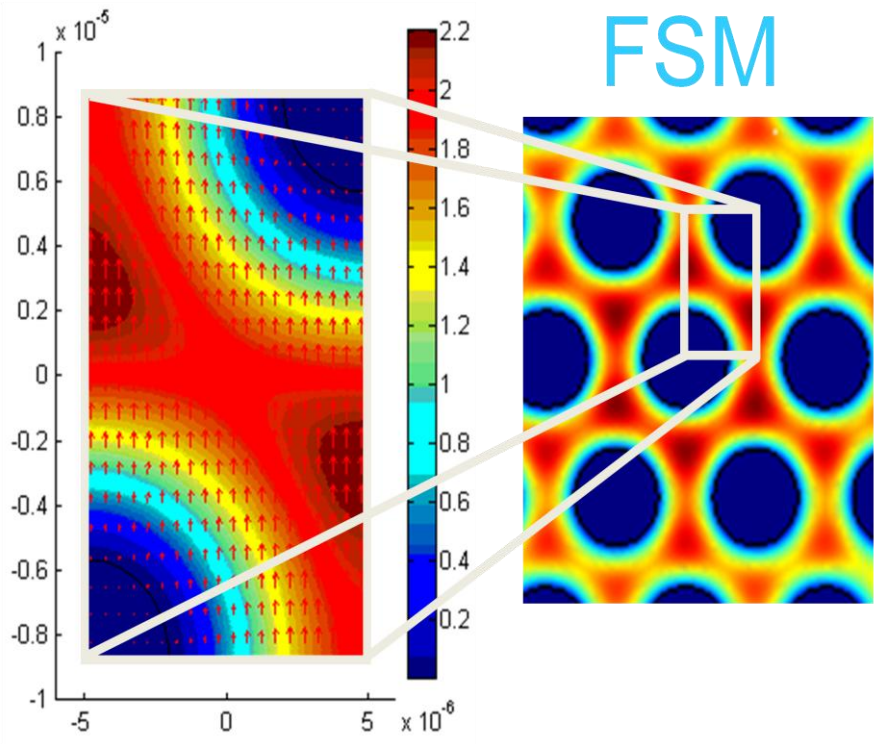

Figure 39: Fundamental space filling mode.

The cladding geometry was varied by changing the pitch and d/Λ and the difference between the effective index and the glass index was calculated. This index difference would correspond to the index difference between the core and the cladding of the equivalent step index fibre is used in the calculation of the number of modes that could

propagate down the fibre. Some of the results are provided in Table 4 for λ = 1.5μm. The NA of the fibre was calculated using

$$NA = \sqrt{n_{core}^2 - n_{FSM}^2} \quad \textbf{(14)}$$

where n_{core} is the refractive index of the glass and n_{FSM} is the effective index of the FSM. The pitch of 25μm corresponds to an outer diameter of 200μm for a fibre with this structure. This diameter was commonly targeted in the fibre fabrication as it is a good compromise between fibre fragility and flexibility.

The calculation of the NA of the geometries containing high air fractions was used to determine the feasibility of using a hexagonally periodic geometry as the high NA outer cladding of a double clad fibre. It was found however that even when increasing the d/Λ up to 0.9, for a pitch of 25μm, the difference in the core index from the glass index was only 5.4 x 10^{-3} which corresponds to a NA of 0.15 (Table 4). This was because for a 25μm pitch, the glass regions between the air holes are still considerably longer than the wavelength of light and due to the large index difference between the

Table 4: Difference in refractive index for differing cladding air fractions.

Pitch (Λ) μm	Air fraction (d/Λ)	Δn between core and cladding	NA	V-parameter
25	0.2	1.5 x 10^{-4}	0.024	1.583
	0.3	2.3 x 10^{-4}	0.030	1.979
	0.4	3.4 x 10^{-4}	0.037	2.440
	0.5	5.2 x 10^{-4}	0.046	3.035
	0.6	8.3 x 10^{-4}	0.058	3.826
	0.7	1.4 x 10^{-3}	0.075	4.948
	0.8	2.6 x 10^{-3}	0.102	6.729
	0.9	5.4 x 10^{-3}	0.147	9.700
12	0.5	2.2 x 10^{-3}	0.094	2.977
15		1.4 x 10^{-3}	0.075	2.968
20		8.1 x 10^{-4}	0.057	3.008
30		3.7 x 10^{-4}	0.038	3.008

tellurite glass and the air, this light had strong confinement to the glass. Hence there was little overlap with the air in the cladding holes to reduce the cladding's effective index. It was found, however, that the overlap between the guided mode and the air in the cladding structure and hence the NA increases rapidly for air fractions larger than this. For a more effective double clad geometry the air fraction of the outer cladding would therefore ideally be above 0.9.

To represent the modal guidance of a microstructured geometry through the use of an equivalent step index fibre, a core diameter is required. The process of calculating the core diameter of a given microstructured geometry used the following steps:

- Use FEM modelling to find the effective index of the fundamental mode that would propagate down the microstructured fibre geometry.
- Initially using a core radius equal to the pitch of the microstructure, calculate the effective index of the fundamental mode that would propagate down a step index fibre with the core-cladding index difference calculated previously using the FSM of the microstructured cladding geometry.
- Reduce the core radius, each time re-calculating the effective index of the fundamental guided mode.
- Find the core radius with equivalent fundamental mode guidance between the step index and microstructured fibres.

There was found to be a constant relationship between the pitch of the cladding structure and the effective core radius. The core radius of the equivalent step index fibre was found to be 0.63 of the pitch. This 0.63 factor will be referred to as the core correction factor and it was found to be unchanged when varying the wavelength of the propagating light in the range of 500nm to 4μm. It was also found to be independent of the pitch of the cladding for pitches between 5μm and 40μm and of the air filling fraction for d/Λs between 0.3 and 0.7. With the correction factor of a silica glass MOF of 0.64 [172], it was also found that the correction factor had a minimal dependence on the refractive index of the glass. A comparison between the mode guided by the microstructured fibre and the corresponding equivalent step index fibre is illustrated in Figure 40. In this case a pitch of 12μm and a d/Λ of 0.5 were used.

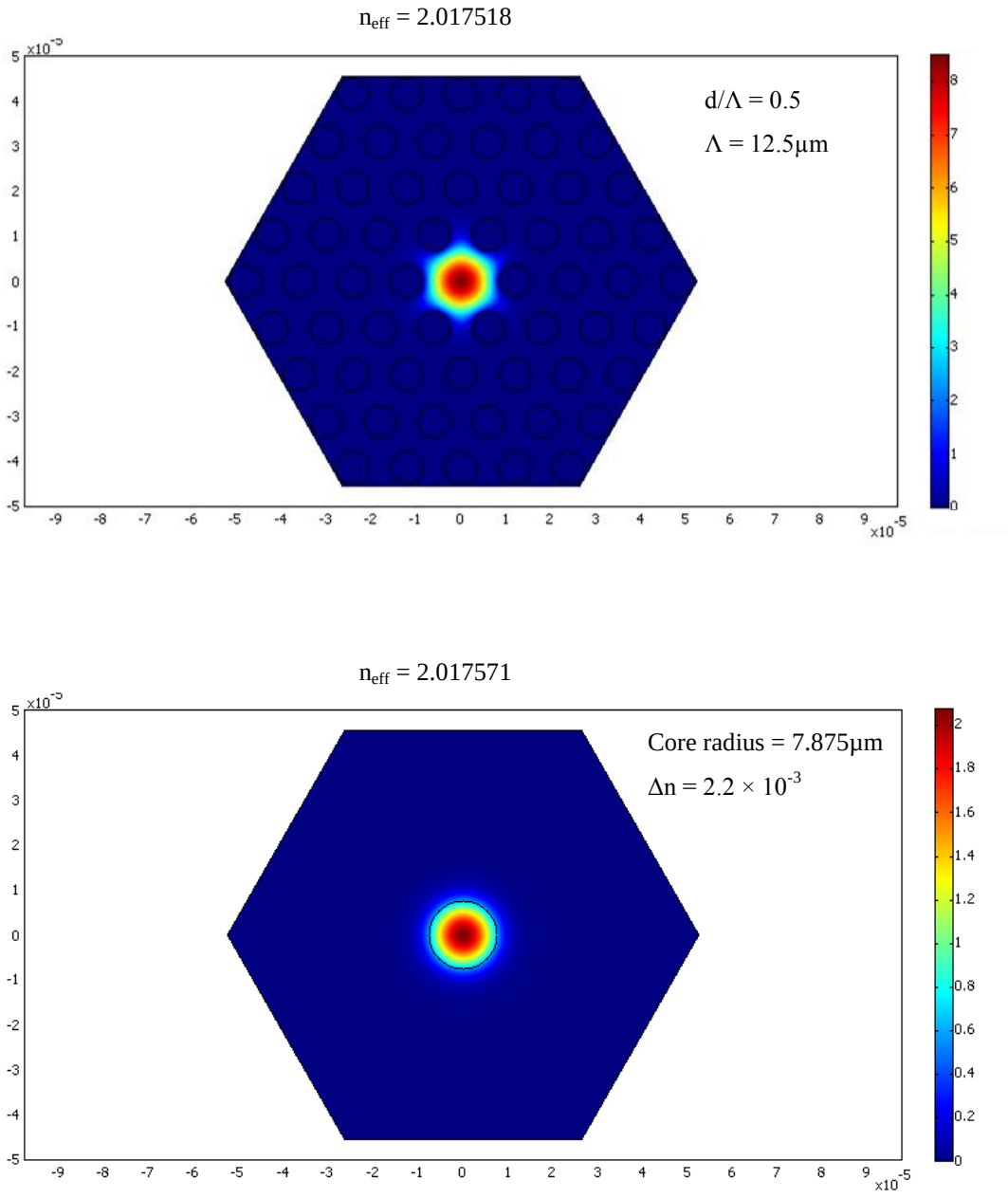

Figure 40: The propagating mode through a tellurite glass microstructured fibre with a pitch of 12.5µm and d/Λ of 0.5 (upper). The fundamental mode for the equivalent step index fibre, with no air holes (lower).

The V-parameter for the equivalent step index fibre was used to find how many modes the fibre supported. The V-parameter is calculated using Equation (15) where r is the fibre core radius, λ is the propagating wavelength and the fibre's NA is defined in Equation (14). The fibre will guide a single mode if the fibre's V-parameter is less than 2.405.

$$V = \frac{2\pi r}{\lambda} NA \quad \textbf{(15)}$$

As seen with the V-parameter values provided in Table 4 where the d/Λ was kept as 0.5, the V-parameter of the fibre was almost independent of the fibre's pitch. As the pitch was increased, the core diameter increased, but the NA of the fibre decreased proportionally resulting in a roughly unaltered V-parameter. The V-parameter was dependent on the air fraction where, from the calculated V-parameters provided in Table 4, it can be seen that for d/Λ < 0.4 the V-parameter was less than 2.405 and a fibre with this geometry would guide only the fundamental mode.

3.2.2 Fabrication of 4-ring LMA fibres

The first LMA fibre preforms were extruded from 200g glass billets that had a 30mm outer diameter. The stainless steel die used to generate the preforms consisted of a sieve plate, with a thickness of 5mm, which held pins, 10mm in length, in a hexagonal pattern and also allowed the glass to flow around these pins. The output face of the die is pictured in Figure 41 (top). The die had a height of approximately 15mm. The first preforms were extruded around 0.6mm diameter pins with a 2mm pin spacing resulting in a d/Λ in the preform of 0.3. The initial preforms generated were extruded from TZN glass billets and had lengths of approximately 12cm as shown in Figure 41 (bottom). The preform was sealed at one end using Polytetrafluoroethylene (PTFE) tape and was held above the fibre drawing furnace by this end. The other end of the preform was positioned such that the desired location of the "neck down and drop" was in the centre of the furnace. To maximise the amount of preform that could be drawn to fibre, in the short preforms, the "neck down and drop" (illustrated in Figure 37) were located close to the bottom of the preform. This however resulted in the preforms cracking. Initial success was achieved through the intentional tapering of the preform, which was

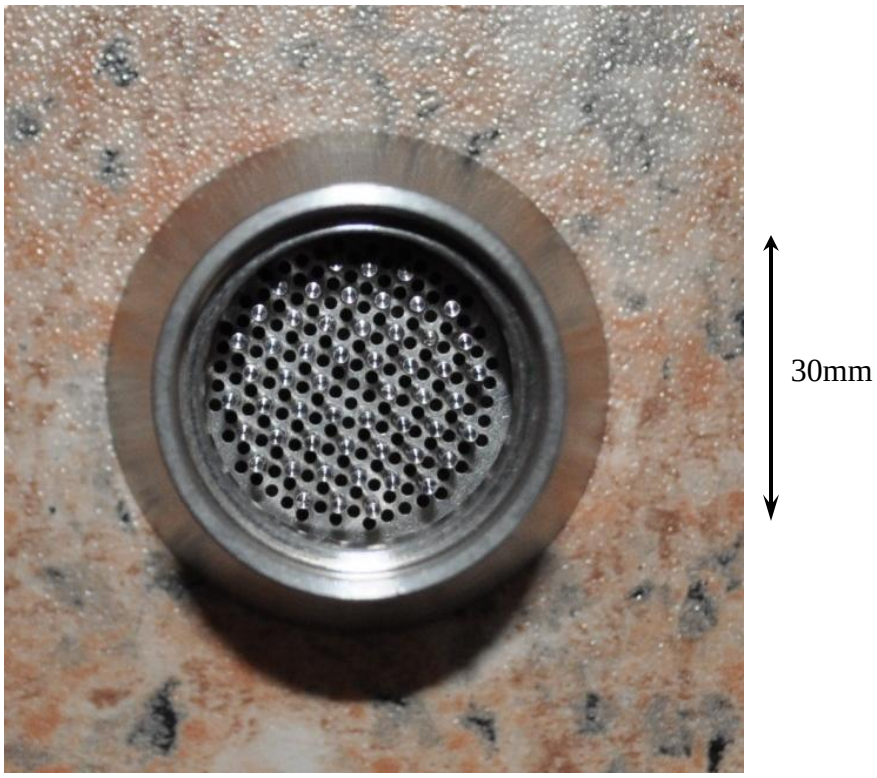

Figure 41: Four-ring stainless steel die output face (top) and a side view (bottom) of an extruded four-ring TZN glass preform.

achieved by extruding the glass at a higher temperature. This caused the glass to be less viscous at the die exit and stretch under its own weight, increasing the preform length to 18cm. The "neck down and drop" when this preform was pulled to fibre was further from the bottom of the preform and the preform did not crack during the fibre pull. This preform was drawn into the first LMA fibre of this research. A photograph of the tapered preform (a), its cross-section (b) and the structure of the first fibre fabricated (c) are shown in Figure 42. The pink preform colour is due to the erbium III that was doped into the TZN glass billet used. Unfortunately the diameter of the air holes was smaller than targeted due to the higher extrusion temperature, and further reduction of the d/Λ occurred during the fibre pull. The preform had a $d/\Lambda \approx 0.15$ and the resulting fibre that was pulled from this preform had a $d/\Lambda \approx 0.1$. This low d/Λ would have resulted in weak guidance by the fibre and hence the fibre would have been very susceptible to bend loss.

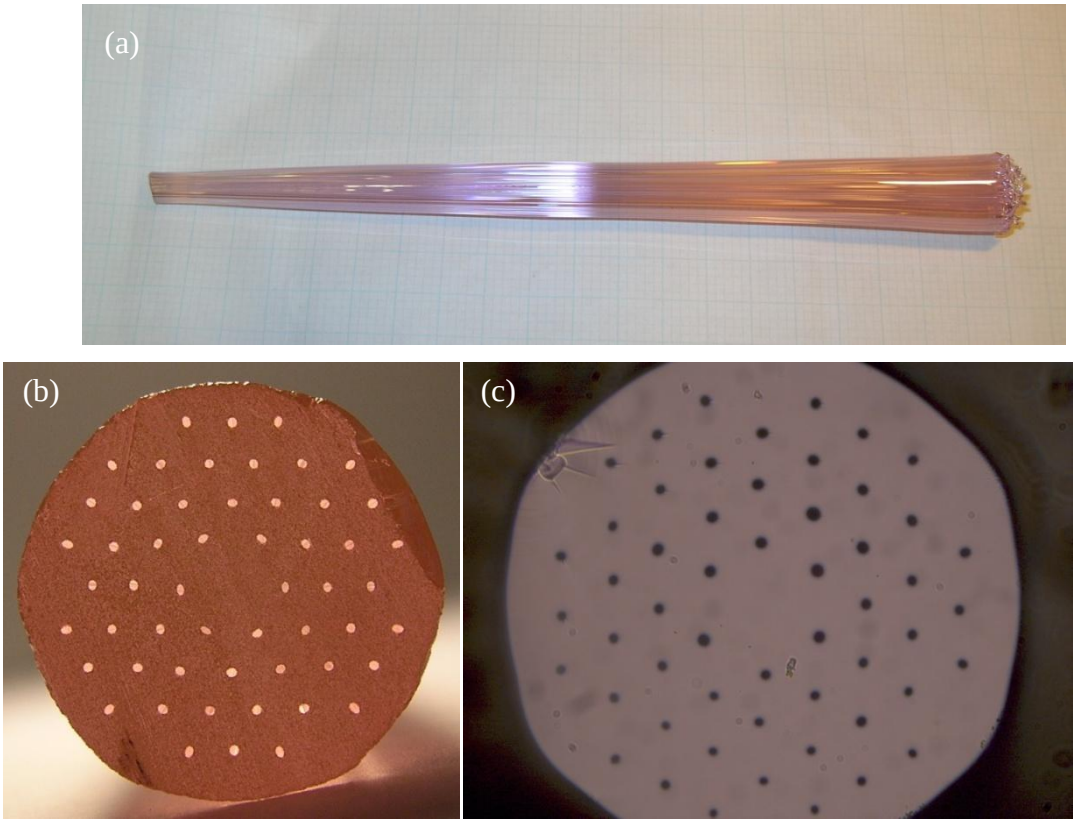

Figure 42: Side view (a) and end view (b) of the TZN glass preform used to fabricate the first LMA tellurite fibre and the cross-section of the fibre fabricated (c).

Guidance was not observed by the core of the LMA fibre pictured in Figure 42. The NA of this fibre was calculated from the numerical modelling using a d/Λ of 0.1 to be approximately 0.015. This very low NA would have resulted in an inability to couple into the fibre and a very high bend loss by the fibre.

The small hole size in the fibre and the need to have a tapered preform motivated an increase in the glass billet size and an increase in the pin diameter in the extrusion die. The pin diameter was increased from 0.6mm to 1mm to try to compensate for the hole closure during the extrusion and fibre pulling processes. This increased the d/Λ of the pins at the die exit from 0.3 to 0.5. Increasing in the billet size to 300g allowed the extrusion of significantly longer preforms, removing the need to intentionally taper the preforms as the untapered preforms had lengths in excess of 20cm, which is sufficiently long for the fibre drawing. At this stage the glass composition used was changed from the TZN glass composition to the TZNL glass composition.

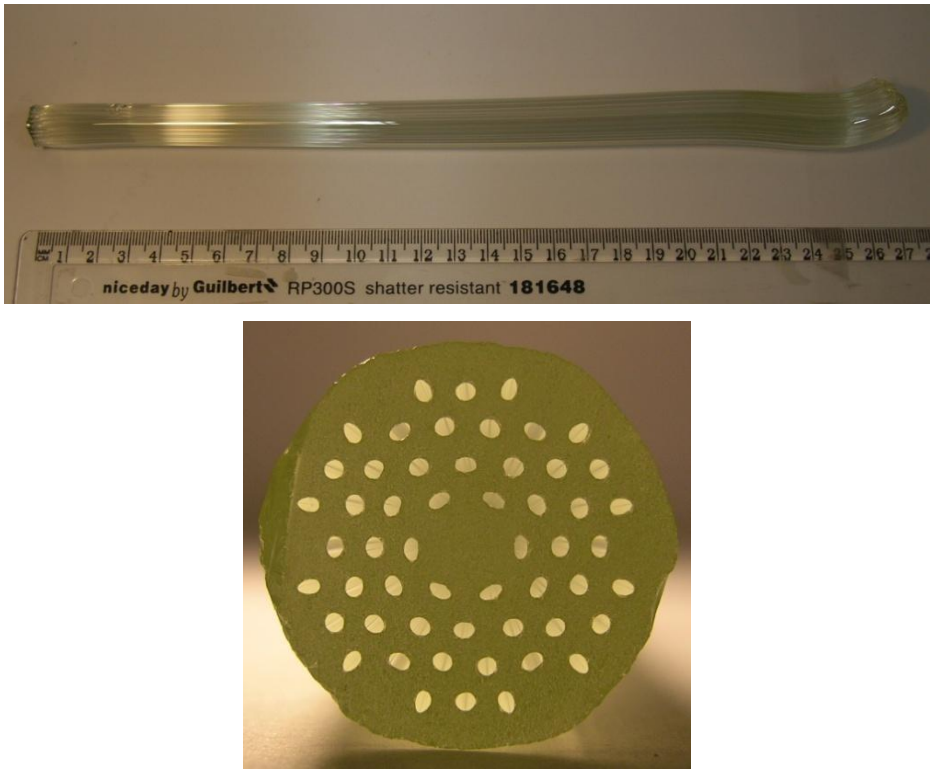

Figure 43: Side view (top) and end cross-section (bottom) of a LMA preform fabricated using the TZNL glass and a larger d/Λ in the preform die.

An example of a preform using the new die geometry and larger billet size is shown in Figure 43.

The fibres pictured in Figure 44 were fabricated from preforms like the one presented in Figure 43, using the larger glass billets (300g) and using the larger pin diameters (1mm) in the extrusion dies. For these fibres, using the d/Λ of the inner two rings of holes of 0.5, numerical modelling calculated the NA to be 0.05. Despite the high bend loss caused by this low NA, light was able to be coupled into a number of these fibres and confinement was observed over lengths of more than 30cm. Figure 44 includes SEM images of the fibre cross-sections and the mode propagated by these fibres. To minimise the bend loss when propagating light in these fibres they were mounted in straight V-grooves. The M^2 value at 1550nm for the guided mode pictured in Figure 44 (top) was approximately 1.7 ± 0.1. This was improved on slightly in the guided mode pictured in Figure 44 (bottom) which had an M^2 of 1.6 ± 0.1. Both fibres had a mode area in the order of 1000 ± 100μm^2, calculated by approximating the guided mode by a Gaussian. By observing the transmission by the fibre under different degrees

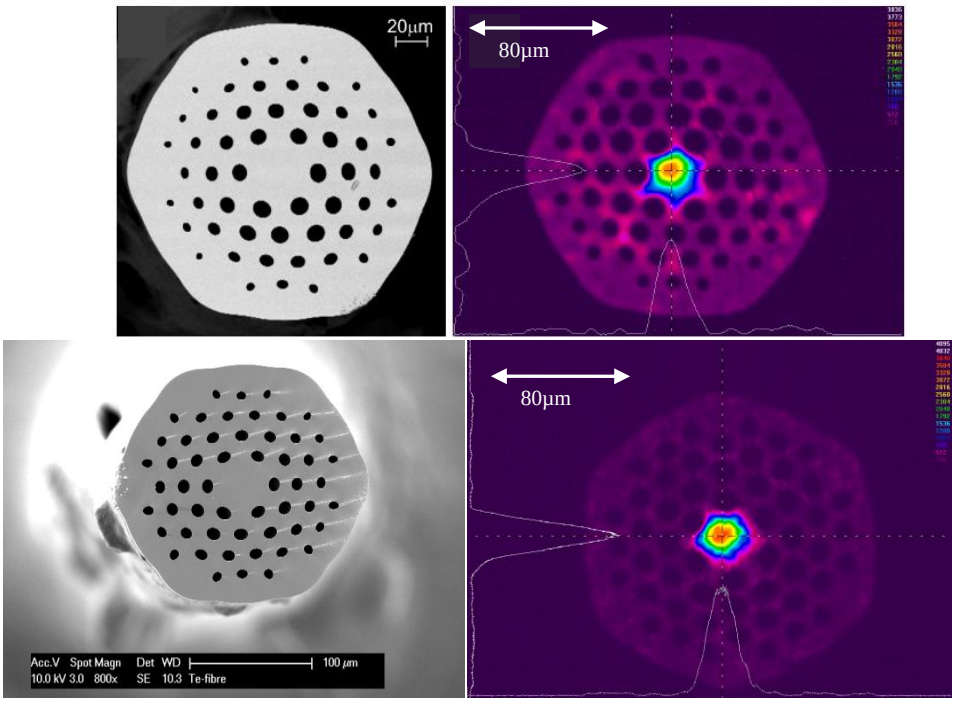

Figure 44: SEM images of some of the fabricated fibres using the TZNL glass and larger diameter preform pins (left) along with the modes guided by these fibres (right).

of bending, it was observed that the transmission by the fibre core was lost when it was bent tighter than a 0.5m radius of curvature. A reliable confinement loss measurement was not able to be made due to the fibre's susceptibility to this bend loss.

3.3 Core doped four-ring LMA fibres

The ultimate aim of the fibre development was to fabricate a double-clad fibre. As discussed previously in Section 2.5 when proposing the addition of lanthanum oxide to the glass composition in the TZNL glass, the dopant in a double clad fibre must be confined to the core. This restricts the absorption of the pump to the core where the laser mode is propagating.

Based on the refractive index measurements presented in Section 2.5, it was found that the refractive index of the tellurite glass decreased when it was doped. This was a problem when doping only the core of a MOF as the refractive index of the core could be reduced to below that of the cladding. Prior to the fabrication of the core-doped LMA fibres, the effect on the MOF guidance when reducing the refractive index in its core was investigated using FEM modelling (Section 3.3.1). Following the modelling, the development of the fabricated core doped fibres is described in section 3.3.2.

3.3.1 Modelling of core-doped LMA fibres

The refractive index of the doped and undoped TZN and TZNL glasses was discussed in Section 2.5. The minimising of the index difference motivated the addition of lanthanum oxide to the class composition. The difference in refractive index between the doped and undoped TZNL glasses when doped with 1×10^{20} ions/cm^3 of erbium III was less than the measurement error, which was of order $\pm 5\times10^{-4}$.

From the modelling of the uniformly doped LMA geometry in the previous section, for $d/\Lambda = 0.6$ and a pitch of 25μm, the refractive index difference between the core and cladding was found to be 8×10^{-4}. This index difference is larger than the index difference between the doped and undoped TZNL glasses, hence, it is larger than the amount the core index would decrease when doping only the core of a MOF fabricated from this glass. There would therefore still be a positive index difference between the core and

cladding regions of the fibre when using a structure with this d/Λ and the TZNL glass. Assuming an index drop in the core corresponding to the error in the refractive index measurement of 5×10^{-4}, the index difference that would remain between the core and the cladding would, however, be significantly less than the original structure. The fundamental mode guided by a depressed core fibre with a d/Λ = 0.6, an index drop of 5×10^{-4} in the core and a pitch of 25µm is shown in Figure 45. In this profile there was still a positive index difference between the core and the effective cladding index of 3×10^{-4} and the effective index of the guided mode lay between the core index and the effective index of the cladding.

Considering the refractive index difference between the doped and undoped TZN glass, a significantly smaller cladding pitch or larger air fraction would have been required to reduce the effective index of the cladding to below that of the doped glass. This would have required a significant change to the cladding geometry so it was not looked into in detail.

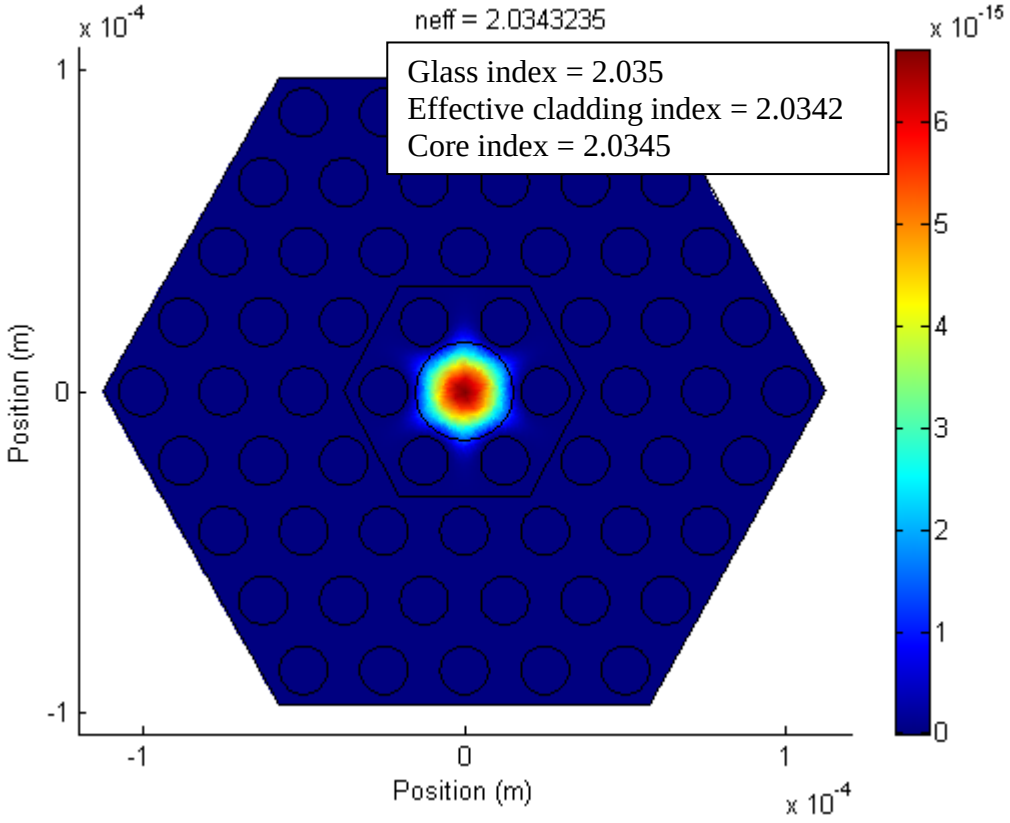

Figure 45: Mode profile for the mode that would propagate through a fibre with the depressed core refractive index.

3.3.2 Fibre fabrication and analysis

The core doped fibres were fabricated using the TZNL glasses to minimise the refractive index difference between the core and cladding materials. The preform used in the fabrication of the core-doped fibres consisted of an undoped structured cladding and a 1×10^{20} ions/cm^3 erbium III doped "cane" (1mm diameter rod) that was inserted into the centre hole of the cladding structure.

The die used in the extrusion of the structured cladding is pictured in Figure 46. When compared to the LMA die described in 3.2.2 the additional pin in the centre generated the hole for the "cane" to be inserted.

The doped "canes" were drawn from extruded doped 10mm rods using the same technique as described in Section 3.1, however, tractor wheels were used in place of the drum to pull the cane. These rods were extruded in the same manner as the bare fibres that were used in the loss measurements described in Section 2.2.1. The diameters of the canes were within 0.1mm of the 1mm target diameter. The canes were then inserted into the hole in the centre of the structured cladding and a cane that fit tightly was selected

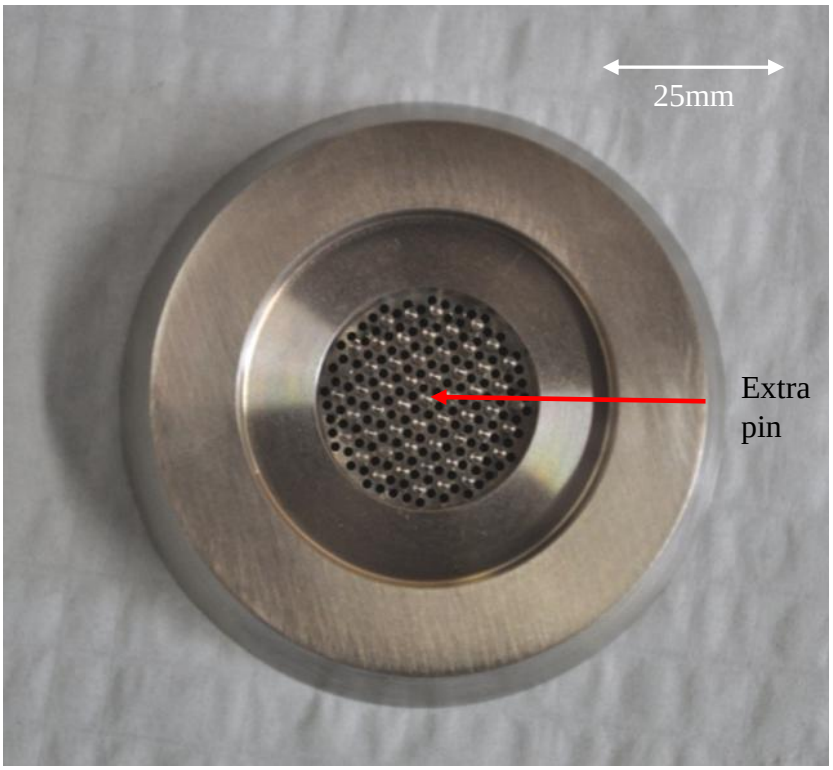

Figure 46: Die design for the core doped four-ring fibres.

and annealed (annealing is discussed in further detail in Section 2.4).

Together the annealed doped cane and undoped cladding were pulled to a fibre with an outer diameter of 240μm.

As with the LMA fibres fabricated, when the core doped preforms were pulled to fibre the cladding was sealed at its top using PTFE tape. The sealing of the top of the cladding structure was aimed at preventing the cladding holes from closing due to the build up in pressure in the air regions during the fibre pull. The sealing of the cladding holes also shielded the cladding structure from vacuum that was applied to the space between the cladding and the doped core.

The interface between the doped cane and the cladding preform was either left open or in subsequent fibres connected to a vacuum pump.

The first fibre fabricated, which is pictured in Figure 47, had no vacuum applied to the core-cladding interface. As a result, despite leaving the top of this interface open, there was still a build up in pressure which prevented its fusion and caused the inflation of this interface.

This fibre was pulled at a temperature of 585°C and a speed of approximately 5.4m/min. An induction furnace was used in the fibre drawing and the furnace temperature was measured at the susceptor with an accuracy of ±1ºC. The glass temperature was estimated to be approximately 200ºC below this temperature. The preform was feed into the drawing furnace at a rate of 1.5mm/min. This combination of fibre drawing parameters resulted in a stability of the fibre's outer diameter of less than ±5μm.

The next fibre was drawn 15ºC cooler at 570°C and used the same preform feed rate and fibre drawing speed. This increased the viscosity of the glass in its core and minimised the inflation of the gap at the core-cladding interface. The resulting fibre is pictured in Figure 48. In this fibre, the doped core fused to the cladding at multiple locations around the interface. Although there was still no vacuum applied, this fibre did not experience the same inflation of the doped core to cladding interface as occurred in the first attempt.

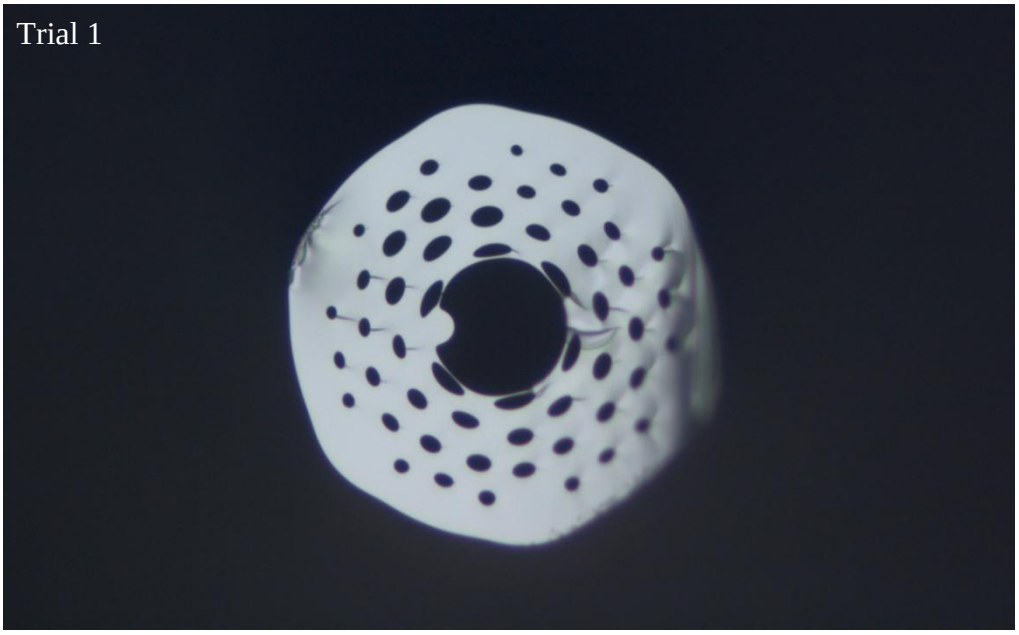

Figure 47: Optical microscope image of the first attempt at the core doped fibre. The cladding used the TZNL glass composition and the core used the same composition and was doped with 1×10^{20} ions/cm^3 erbium III. The fibre had an outer diameter of 240µm.

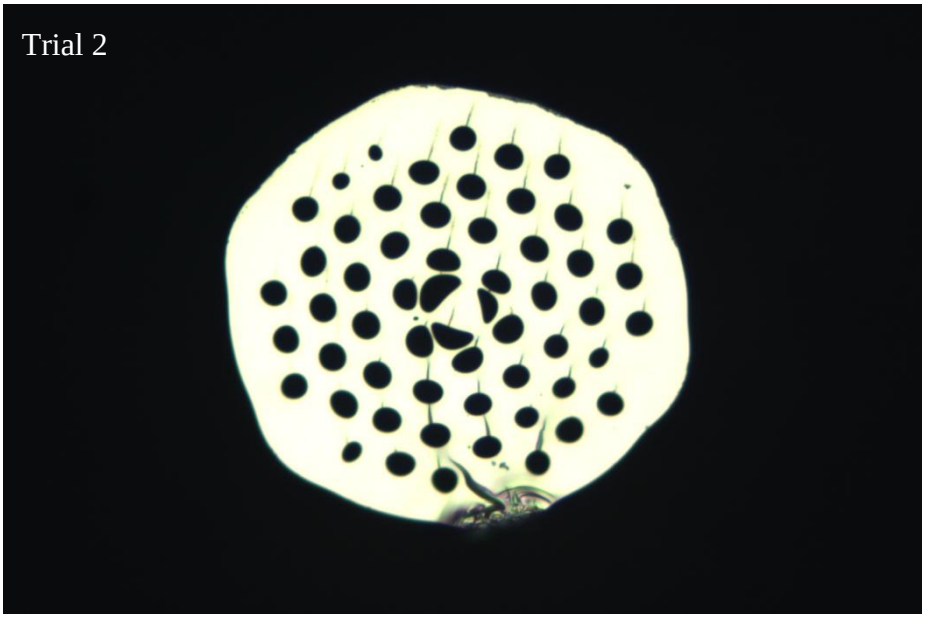

Figure 48: Optical microscope image of the core doped fibre using a tighter fitting cane and a lower fibre drawing temperature to reduce the inflation of the gap between the doped cane and the cladding. The cladding used the TZNL glass composition and the core used the same composition and was doped with 1×10^{20} ions/cm^3 erbium III. The fibre had an outer diameter of 240µm.

For the next series of fibre drawing trials, the interface between the core and cladding was evacuated during the fibre pull. In each attempt the strength of the vacuum was varied. Vacuum pressures applied to the mounted end of the preform were measured using a pressure gauge and ranged from 8 to 150 mmHg. Independent of the strength of the vacuum, only a short length of the fibre was able to be pulled, before the fibre broke. Even though the cladding structure was sealed, the use of the vacuum also tended to affect the cladding structure. The effect of the vacuum ranged from complete collapse of the cladding structure, which occurred in the third core doped fibre drawing trial (Figure 49 (a)), or collapse of the inner ring of holes, which is evident in the fibre cross-section images of the forth core doped fibre drawing trial (Figure 49 (b) and (c)). In the fifth attempt at achieving fusion between the core and cladding, fusion of the core-cladding interface appeared to have occurred prior to the collapse of the cladding holes and the breakage of the fibre. The cross-sections of these fibres are shown in Figure 50.

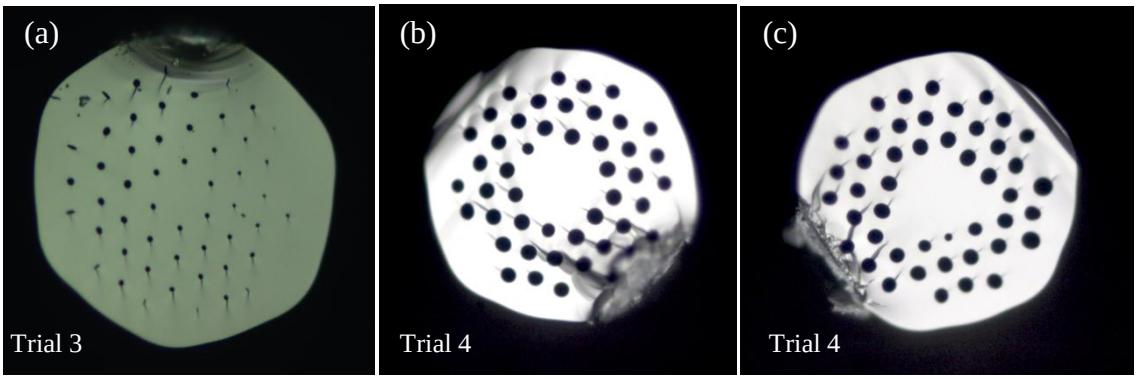

Figure 49: The resultant fibre geometries following the use of a vacuum to seal the core cladding interface. The cladding once again used the TZNL glass composition and the core used the same composition and was doped with 1×10^{20} ions/cm^3 erbium III. These fibres all had outer diameters of 240µm.

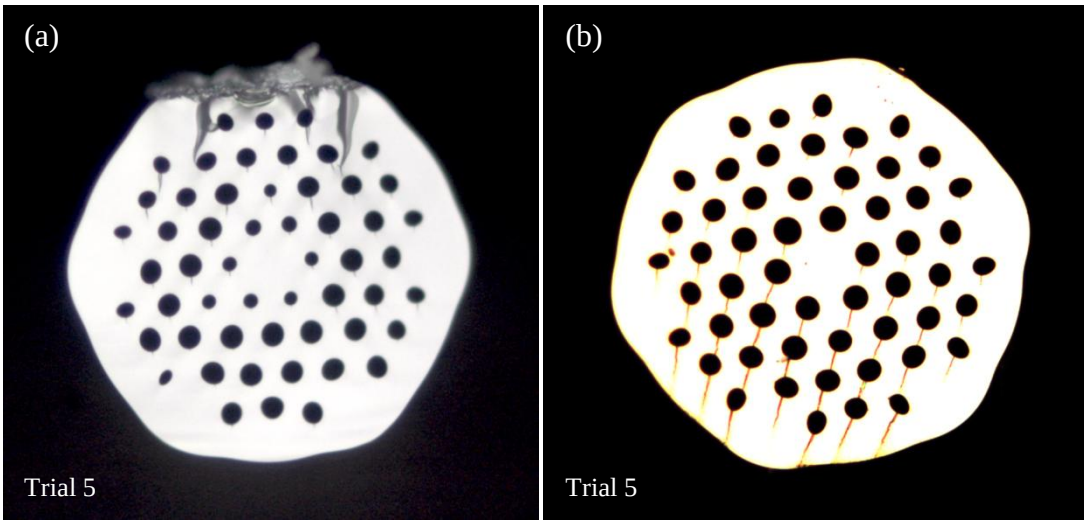

Figure 50: Fibre cross-sections with apparent fusion of the core-cladding interface. As with the previous core doped fibres, the cladding used the TZNL glass composition and the core used the same composition and was doped with 1×10^{20} ions/cm^3 erbium III. These fibres also had outer diameters of 240µm.

Attempts were made to couple light into these fibres, however, since confinement of the fundamental mode in these fibres was not observed, the index matching between the doped and undoped glass was questioned. Using a Philips XL30 field emission gun scanning electron microscope, a SEM image was taken of the fibre pictured in Figure 49 (a) to see if any index difference could be seen between the doped and undoped glass. Since the intensity of the back scattered electrons is strongly related to the atomic mass of the elements in the glass and hence the glass density, it was expected that an index difference caused by a change in glass density between the fibre core and cladding could be seen in the measured SEM image. A SEM of the core of the structured fibre is compared to the known difference in refractive index between the core and cladding of a standard commercial single mode fibre (SMF) in Figure 51. These images indicate that the difference in refractive index between the doped and undoped tellurite glass is significantly smaller than the index difference that could be observed in the SMF fibre. This agrees with the measured refractive index values for the doped and undoped TZNL glasses of $< 5\times10^{-4}$, as the refractive index difference between the core and cladding of a commercial SMF fibre is approximately 50×10^{-4}. The lack of guidance by the fibre,

therefore, could not be attributed to a lower refractive index of the doped glass in the fibre core.

The cracks observed running from each of the holes were due to the cleaving of the fibre.

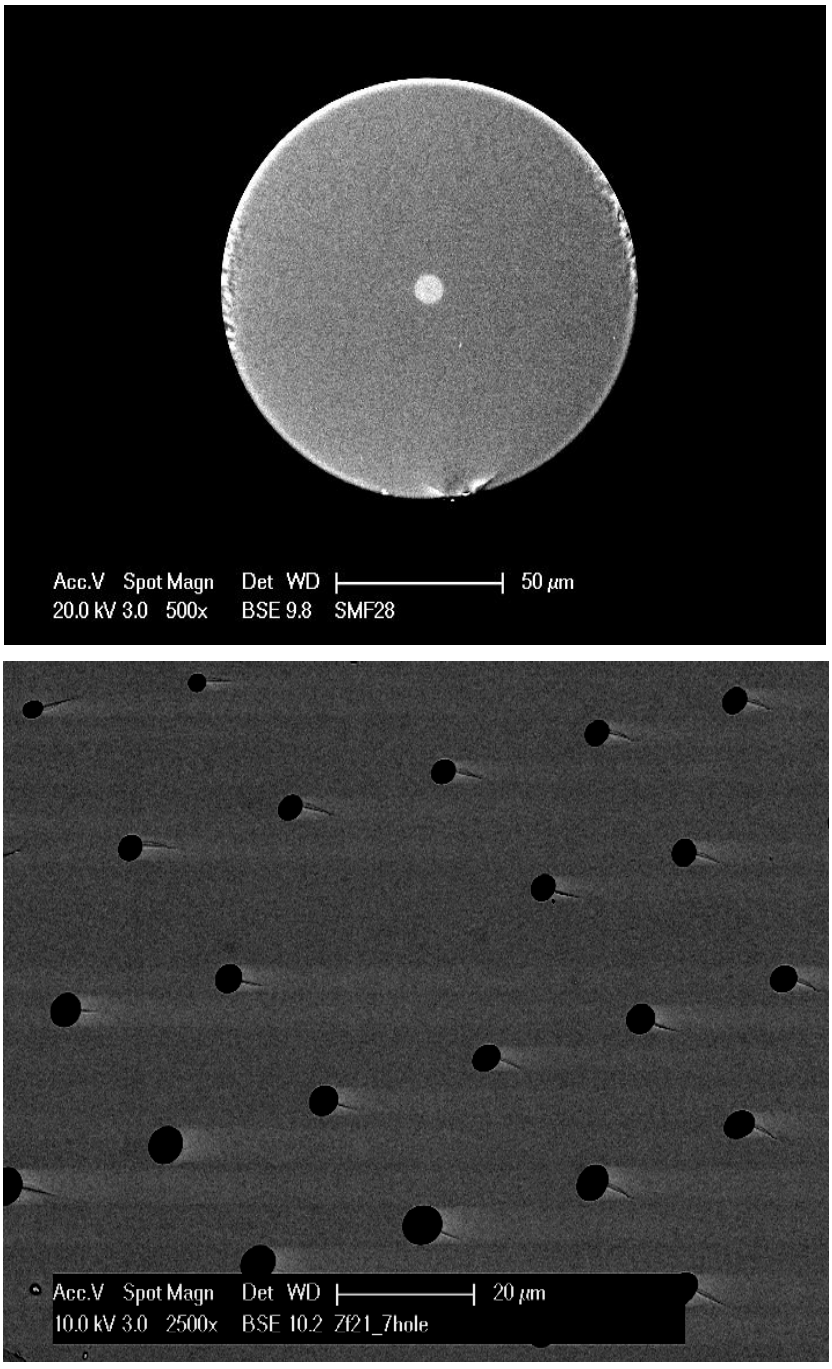

Figure 51: The index difference between the core and cladding of a commercial SMF silica fibre compared to a SEM of the core region of a core doped MOF.

In the SEM image, presented in Figure 52, of the fibre pictured in Figure 50 (b) a ring of nano scale holes was observed at the interface between the doped core and cladding, which was not evident under the optical microscope. It was believed that the scattering caused by these air holes could have been the cause of this fibre's high scattering loss and the reason why no fundamental mode guidance was observed through the fibre.

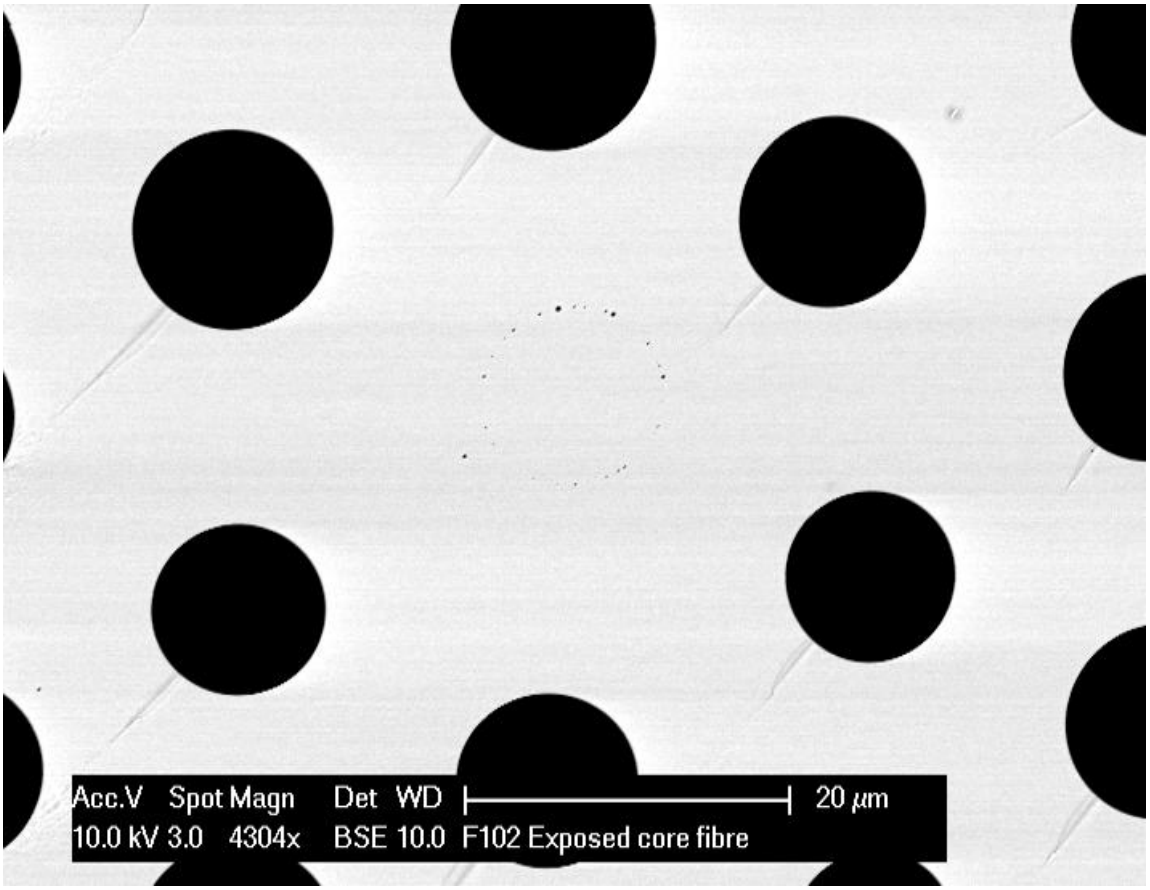

Figure 52: SEM image of the fibre pictured in Figure 50 (right) illustrating the nano scale holes present at the interface between the doped core and the cladding.

Future work in the development of these fibres would see the removal of these nano scale features through refinement of the fibre drawing procedure. Ultimately the aim would be to add an outer cladding, consisting of a very large air fraction, to this fibre geometry. With an outer cladding, this fibre geometry would be able to be cladding

pumped with significantly higher power, multimode pump diodes and constructed into a fibre laser.

The added loss caused by scattering at the region between the doped core and the surrounding undoped cladding meant that attempts were not made at adding an outer cladding to these fibres.

If attempts were made to construct a laser from one of the fabricated LMA fibres it would need to be core pumped. The large core diameter of these fibres would, however, require significantly more coupled pump power (in the order of 1W to achieve population inversion and reach threshold), than could be achieved with this fibre and the currently available in single mode pump diodes. The decision was made to reduce the core size of the fibres fabricated and, therefore, reduce the amount of pump power required to reach threshold in a laser constructed using one of these fibres.

Further fibre development within this thesis was therefore directed towards the fabrication of smaller core fibres.

3.4 Small Core Microstructured Fibres

As described previously, the fibre fabrication was directed towards the development of smaller core fibres with the aim of reducing the pump power required to reach threshold in these fibres. The intention was to core pump these fibres which meant that there would be little pump light in the cladding. This alleviated the requirement to dope only the core of the fibre so the following fibres fabricated were to be uniformly doped. This change to smaller core fibres allowed the development of the world's first tellurite glass microstructured fibre laser described in Chapter 5.

The development of this small-core fibre was an iterative process which started with changing the fibre geometry. The first small-core fibre using a cladding of 7 rings of air holes and was pulled straight to fibre from the preform, as was done with the 4-ring LMA fibres. Through increasing the number of cladding rings, the core diameter was reduced to 20μm from the 50μm for the 4-ring LMA fibres.

3.4.1 Small core seven-ring fibre

The first step towards reducing the core diameter of the fibres used a modified version of the four ring LMA extrusion dies featuring an additional 3 ring of pins, which formed the holes in the extruded preform, around the 4 rings previously used in the LMA fibres. An example of this die design is reproduced from Ref. [159] in Figure 53. The die has a pin spacing of 2mm, a d/Λ of 0.5 and an outer diameter of 30mm.

Figure 53: Pin configuration of the 7-ring die design reproduced from Ref [159].

A preform containing 7 rings of air holes was generated through the extrusion of a 300g undoped TZNL billet. The preform was intentionally tapered to reduce its outer diameter to less than 15mm so it could fit into one of the collets used to mount the preforms for the fibre pulling. A photograph of the cross-section of the extruded preform is given in Figure 54 (a). It had a diameter of 5mm and a length of approximately 1m. The SEM of the cross-section of the fibre that was pulled from this preform is provided in Figure 54 (b). From this image, the fibre core diameter is approximately 20μm. The cladding, however, featured a significant gradient in the hole size as you move further from the core. For the inner two rings of air holes, the d/Λ was 0.6. Since these two rings of holes would effectively dominate the optical properties of the fibre and using the modelling presented in Section 3.2.1 the NA of the fibre would be approximately 0.1. The V-parameter for this fibre would therefore be greater than 10 and the fibre would be

highly multimode. This was validated when looking at the spatial profile of the light coupled into the fibre core. A photograph of the fibre transmitting light from a HeNe is provided in Figure 54 (c). The speckled mode profile in the cladding was due to interference between the light guided by the core and the light propagating down the cladding. The large amount of light in the cladding was due to the mismatch in the mode diameter of the HeNe laser and the core diameter when coupling into the fibre. Any light coupled into the cladding was then confined by the high index contrast between the glass and the air around the fibre.

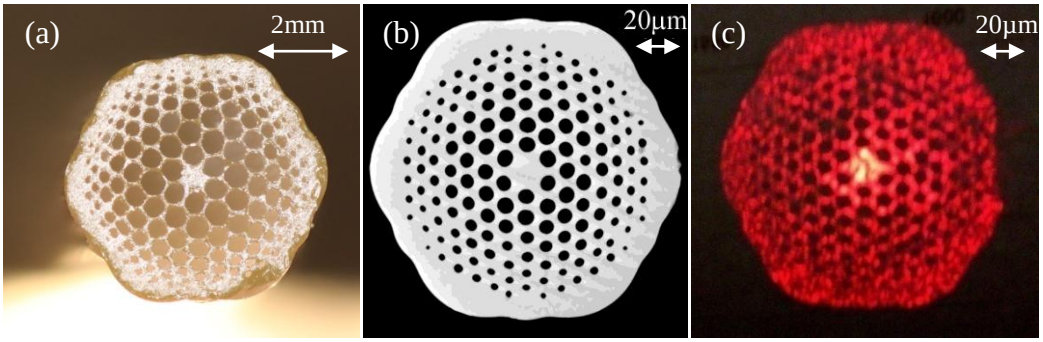

Figure 54: Extruded seven-ring preform and a SEM of the seven-ring fibre pulled from this preform.

Based on threshold calculations for lasing at 1.5µm (Chapter 5), the laser threshold for a doped version of this fibre was around 200mW. Assuming a maximum coupling efficiency of 50% and the availability of only 300mW of pump power it was decided that the core diameter needed to be reduced further.

3.4.2 Small core four-ring structure

Following the fabrication of the 7-ring fibre, the fibre fabrication procedure was changed to generate fibres with even smaller core diameters and hence lower laser thresholds. A three stage fibre fabrication procedure, illustrated in Figure 55, was used in the fabrication of the smaller core fibres. As with the core doped large mode area fibre development (Section 3.3) this process consisted of a “caning” step which reduced the

size of the cladding structure to an outer diameter of 1mm. The "caning" process is described in more detail in Section 3.3. The cane was inserted into a jacket so that when pulled to fibre the core was reduced to the desired diameter.

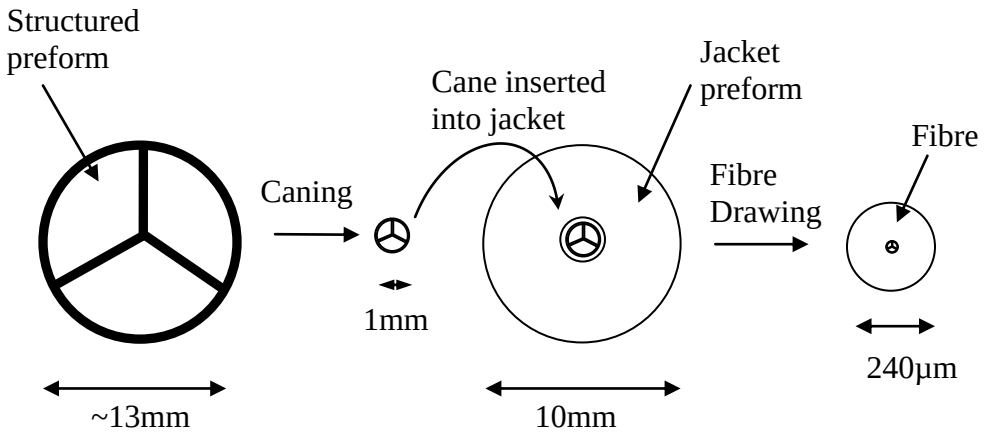

Figure 55: Three stage fibre drawing process consisting of the caning of the structured preform and the use of a jacket to get the desired core diameter.

In the following series of fibres fabricated, the aim was to generate a core diameter of 6µm. The structured preform of the first fibre geometry attempted consisted of the same four ring structure as was used for the LMA fibres. When compared to the LMA fibres, the significantly smaller features in this fibre, meant that keeping them from closing was difficult.

In the next attempt, the cladding geometry was changed to consist of only three larger holes, which were less likely to close during the fibre pull. This fibre had a core diameter of around 1µm and will be referred to as the "wagon wheel" or "suspended core" fibre. This geometry had previously been successfully fabricated into a fibre both within the IPAS research group at the University of Adelaide and by others in literature [46, 51, 52] for a number of different applications including sensing and for its non-linearity. This fibre was ultimately selected as the preferred geometry for the laser development (Chapter 5).

To improve the output power of the laser system recent work has been towards the fabrication of a 6µm core fibre with the same cladding structure.

The idea for the next series of fibres fabricated was also based around the 4-ring geometry. In this case, the 4-ring preforms were caned down and inserted into a tubular glass jacket. By pulling the jacket and cane down to fibre dimensions, the core diameter would have been reduced to less than 10µm. Unlike in the core doped LMA fibres described in the previous section, the interface between the cane and the jacket is located outside the cladding structure. It was therefore not as important to achieve good fusion at this interface.

This caning step and the use of a jacket increased the fibre fabrication from a two stage process to a three and required two glass billets [159]. The jacket was a tube extruded with an outer diameter of 10mm and had a 1mm inner diameter. The jacket and 4-ring structured preforms extruded for these fibres are pictured in Figure 56. The four ring structure is caned down to a 1mm outer diameter using the drawing tower and inserted into the jacket tube. The cane used was chosen to be a tight fit inside the jacket. The combination jacket and cane were then pulled to fibre. The target fibre diameter was around 240µm for these fibres, which would have resulted in a core diameter of approximately 6µm.

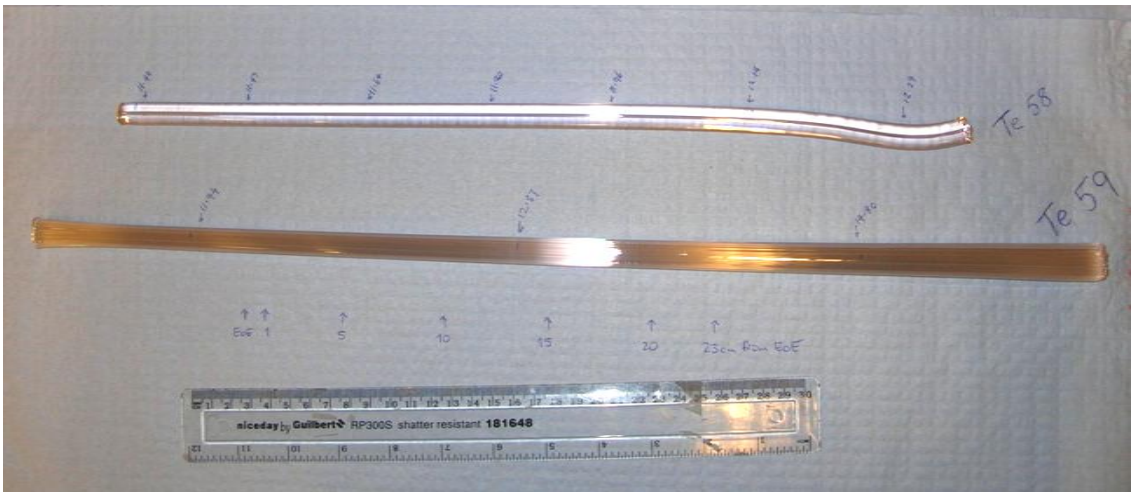

Figure 56: Photograph of the 0.1×10^{20} ions/cm^3 erbium III doped TZNL glass jacket and structured preform used for both small core four-ring fibre fabrication attempts.

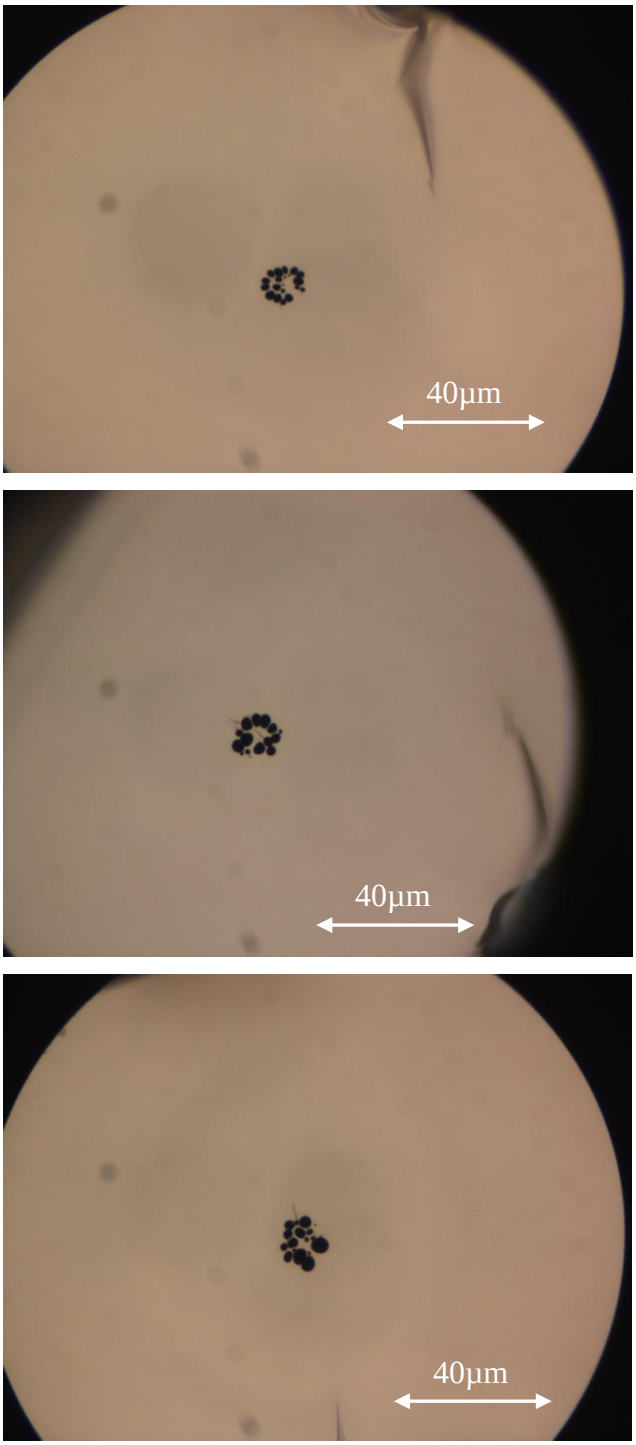

Figure 57: Optical reflection microscope images of the structure of the self pressurized small core four-ring fibre fabricated out of 0.1×10^{20} ions/cm^3 erbium III doped TZNL glass.

Before the fibre drawing, the top of the cladding structure was sealed by melting it with a small hand held torch. The bottom of the preform was left open. This was aimed at keeping the cladding structure open through self-pressurization. This self pressurisation is described, in detail, in the paper by Voyce et al. [173]. Microscope images of cross-sections of the resulting fibre using optical reflection are provided in Figure 57. As can be seen in these microscope images, the fibre structure was not stable and varied along the fibre's length. The instability in the structure in these fibres was believed to be caused by the low surface tension of the glass that was holding the structure. The temperature dependence of the tellurite glass melt viscosity, presented in Section 2.6, indicated that the glass viscosity was highly dependent on the fibre drawing temperature. The fibre drawing technique is discussed in detail in Section 3.1 of this chapter. During the fibre drawing, high purity commercial nitrogen was pumped through the furnace around the preform. This gas was pumped at a rate of 7l/min and 2l/min into the top and bottom of the furnace, respectively. This gas flow had a cooling effect on the outside of the preform and caused a temperature gradient in the preform cross-section while it was being pulled. The centre of the preform was significantly hotter than the surface and therefore less viscous. Due to the lower viscosity of the glass around the fibre structure, the microstructure was highly sensitive to the pressure variation in the air regions during the fibre pull. This made it difficult to maintain the desired structure.

The gas that flowed through the furnace was required to achieve good diameter stability in the fibres fabricated. In the future, to improve the structure achieved in these fibres, the gas that flows around the preform during the fibre pull could be heated prior to its injection into the furnace. The heated gas would increase the temperature of the preform surface and reduce the temperature gradient across the preform, making it easier to maintain the fibre structure.

3.4.3 Wagon Wheel Fibre

The most successful fibre fabricated consisted of a cladding of only three holes (see Figure 58). As with the small core four-ring fibre fabrication, this fibre required a three stage fabrication procedure. This fibre geometry was less sensitive to the fibre drawing conditions due to the significantly larger hole sizes in the cladding. The majority of the

fibre pulled had a core diameter of approximately 1.5µm, however in some sections of the pulled fibre the core diameter varied from less than 1µm to in excess of 2.5µm. The 0.1×10^{20} ions/cm^3 erbium III doped TZNL glass billet, the side and end views of the three strut preform, the end profile of the jacket tube and SEM images of the fabricated fibre are shown in Figure 58 (a) to (f), respectively.

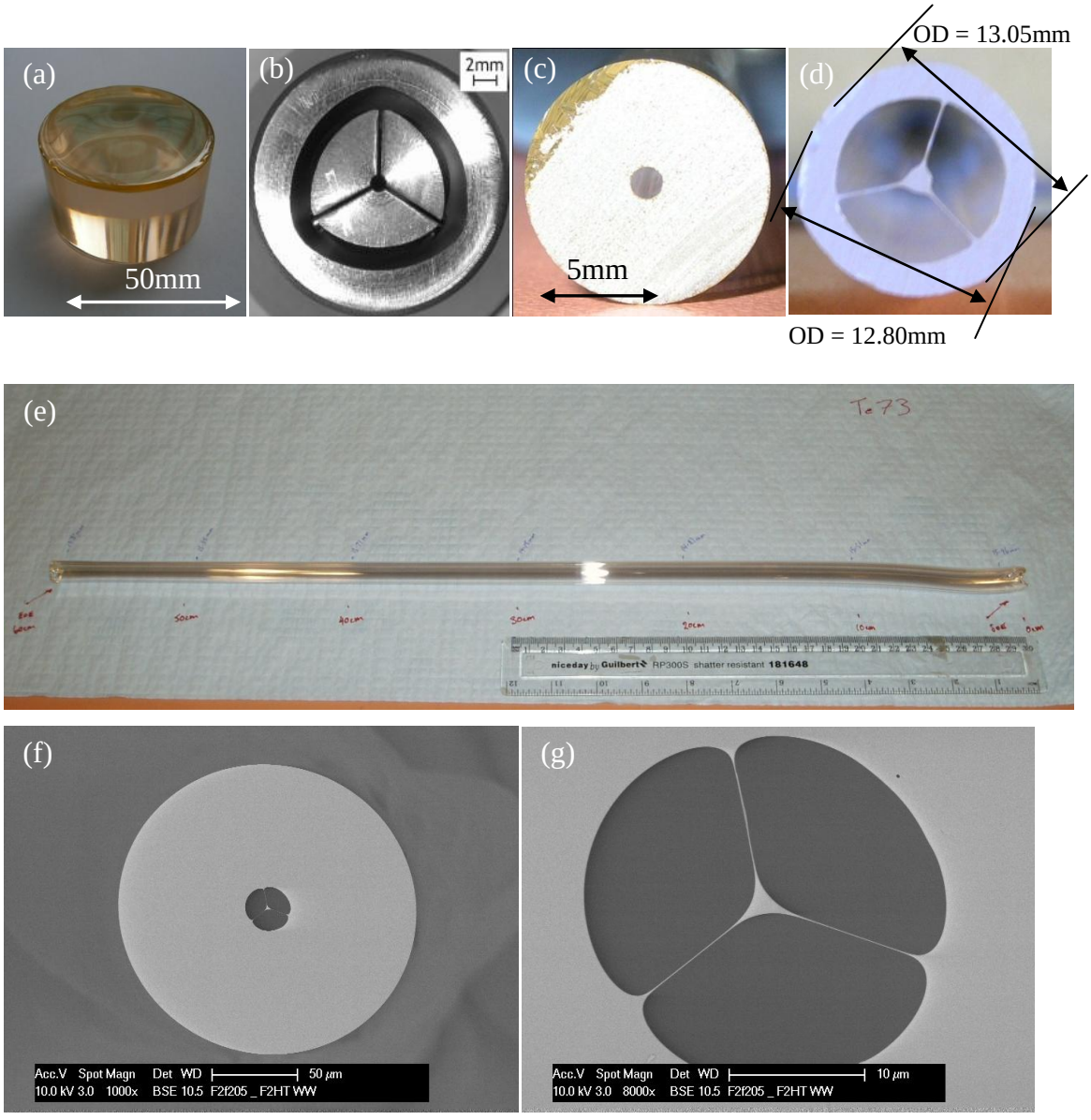

Figure 58: (a), the 0.1×10^{20} ions/cm^3 erbium III doped TZNL glass billet, (b), die exit geometry, (c) and (d), the preform cross-sections, (e), a side view of the three strut preform and (f) and (g), SEM images of the three-hole fibre.

This fibre was made from uniformly doped TZNL glass doped with 0.1×10^{20} ions/cm^3 erbium III and featured a very high NA and hence very strong confinement to its core. The average core diameter of this fibre was approximately 1.5μm which was smaller than the targeted diameter of 3μm. This reduction in the core diameter was due to the inflation of the air holes in the cladding structure and the movement of the glass in the core of the fibre to the cladding struts.

Confinement to the core of the fibre was easily achieved due to the high NA of the fibre, however, due to the small core diameter (1.5μm), the coupling efficiency into this fibre was poor. In the laser experiments described in Section 5.3, the 980nm pump laser was emitted from a 6μm core diameter fibre, collimated and focussed onto the fibre tip. A photograph of the erbium III doped TZNL glass fibre guiding light is shown in Figure 59, where we can see the difference between the output of the fibre when the light is not coupled, partially coupled and well coupled into the core. The difference between the couplings is due to miss-alignment of the pump beam. Due to the mismatch between the core diameter and the pump spot size at the fibre tip, despite optimising the coupling into the core some light is still coupled into the jacket of the fibre. This is illustrated in the photographs by the green fluorescence outside the fibre core.

The loss in the fiber was measured using the cutback technique to be 1.3 ± 0.2 dB/m at 1.31 μm. Based on this loss at 1.31 μm and the increased loss at 1.5 μm, observed in bare fibre loss measurements (Section 2.2.1) of approximately 1dB/m, the loss at 1.5 μm was predicted to be 2.3 dB/m.

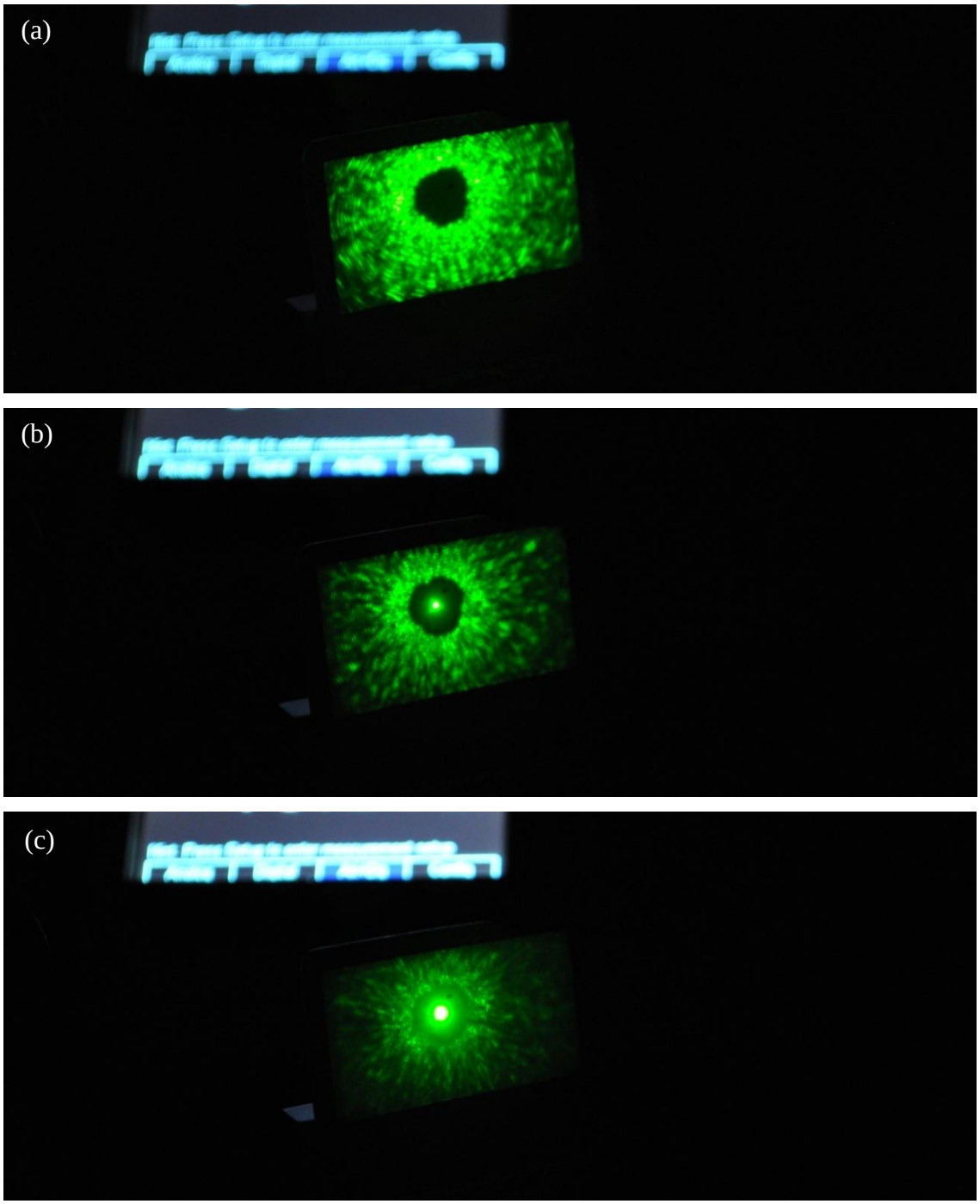

Figure 59: Image of the output of the 0.1×10^{20} ions/cm^3 erbium III doped TZNL glass three hole fibre showing no coupling in the core (a), moderate coupling in the core (b) and good coupling in the core (c).

3.4.4 6µm core, wagon wheel fibre

As an approach to improve on the laser efficiency reported in Section 5.3, there was a requirement to increase the core diameter from the 1.5µm core diameter wagon wheel fibre. The feasibility of the development of a fibre with a 6µm core diameter, with a structure similar to that of the wagon wheel fibre, was studied through a series of extrusions. The increasing of the core diameter in the targeted fibre was aimed at improving the coupling efficiency into the fibre and also increase the pumped volume so as to reduce the bleaching observed in the laser experiments.

A new die was designed to have the same strut (glass between the air holes) width and length, but have a larger core size. Increasing the core diameter, however, caused a change in the glass melt flow rates between the preform struts, the outer glass ring and the core. This caused an oscillation in the thickness of the struts of the preform and cracking of the struts. Figure 60 contains images of the die exit as well as the internal structure of the die. The extruded preform is pictured in Figure 61. The preform was fabricated from a 300g TZNL glass billet with the erbium III concentration increased to 0.5×10^{20} ions/cm^3. Using the same glass, an attempt was made to balance better the glass melt flow through increasing the size of the feed holes (illustrated in Figure 60 (b)) that moved the glass melt from the core to the outside of the preform. The side and end views of the resultant preform are given in Figure 62. A significant improvement was not observed as the preform still featured the same oscillation in its strut thickness and was very fragile.

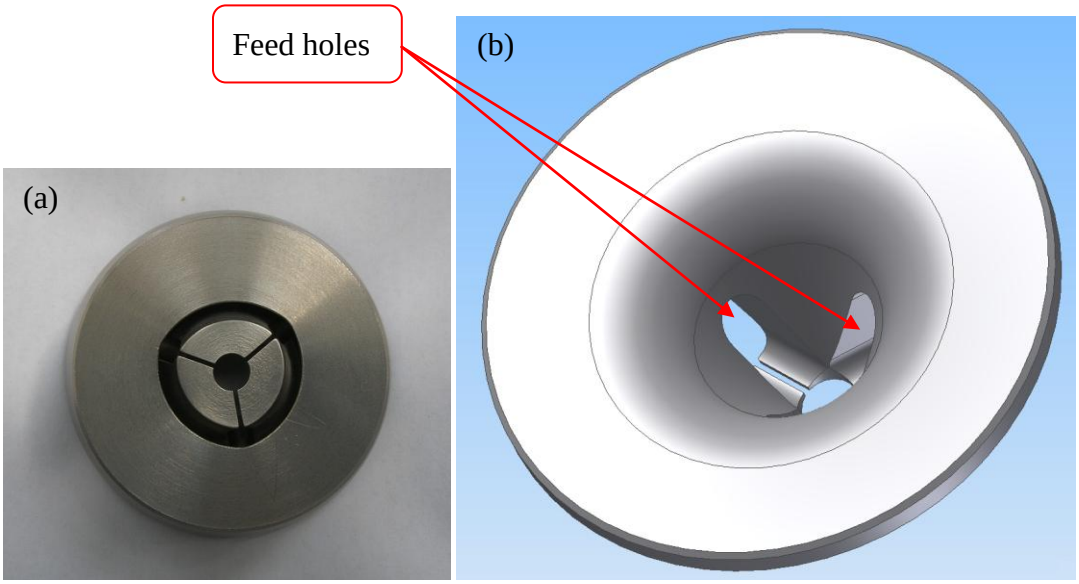

Figure 60: Photograph of the die exit (a) and an image of the internal structure of the die (b) including the feed holes the move glass from the inside of the die to the outer ring.

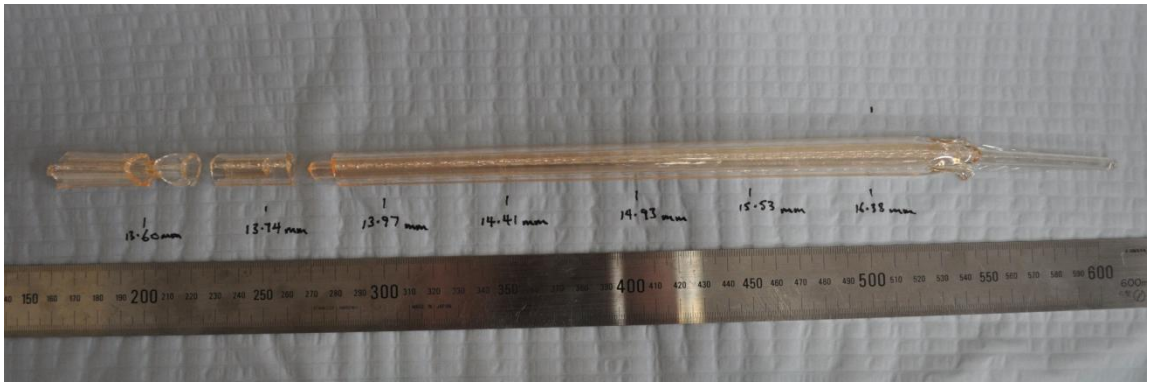

Figure 61: The large core three strut preform extruded from a 300g billet of 0.5×10^{20} ions/cm^3 erbium III doped TZNL glass.

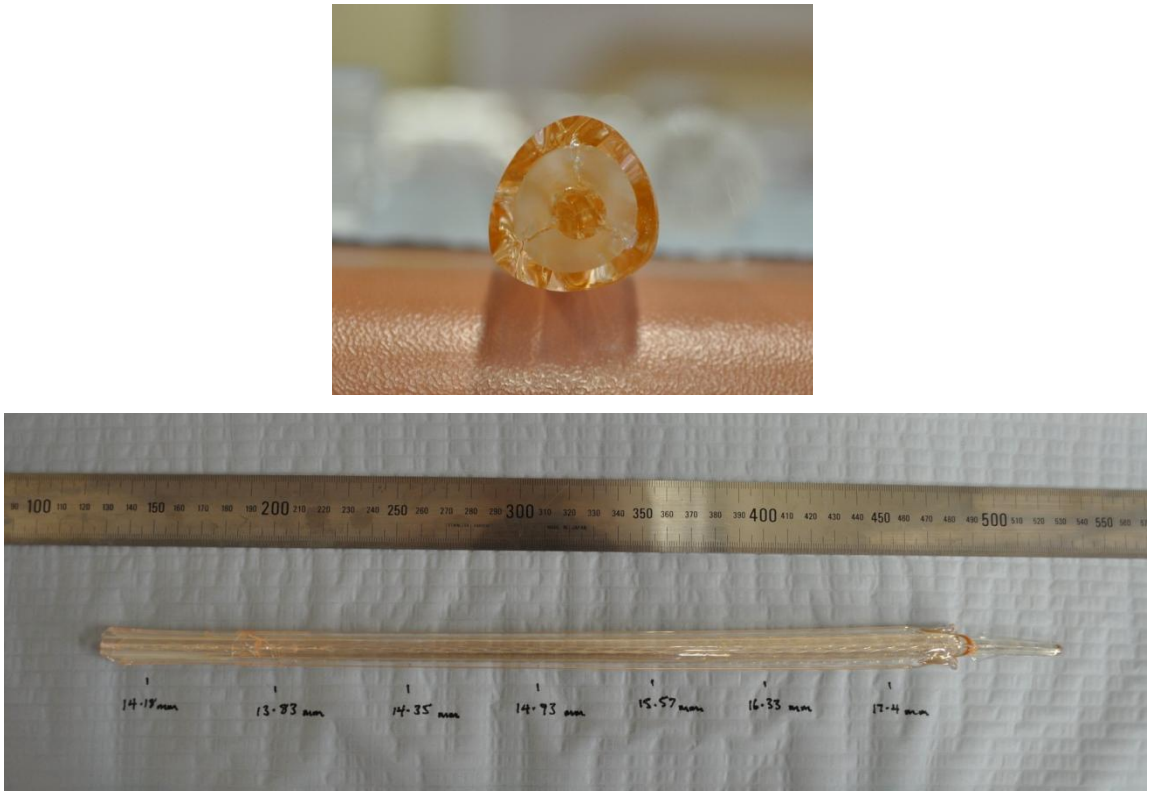

Figure 62: Side and end view of the extruded TZNL glass preform after increasing the amount of glass fed to the outside of the preform.

Further work is required in designing a new die which reduces the flow rate through the core of the preform. Once the flow is balanced across the die, a preform with a similar geometry could be extruded and drawn into fibre.

4. Erbium III doped tellurite glass spectroscopic properties

The spectroscopic properties of the erbium III doped tellurite glass, used to predict laser thresholds and efficiencies, are presented in this chapter. The energy level lifetimes and the absorption and emission cross-sections have been measured or are calculated from measured data. The absorption cross-section of the erbium III transitions were found to be independent of the erbium III concentration and the presence of lanthanum oxide in the glass. The radiative lifetimes of the erbium III energy levels have been calculated from the absorption spectra using the Judd-Ofelt theory [89, 90] and these theoretical lifetimes have been compared to measured lifetimes. When pumping a doped sample for a lifetime measurement, energy migration between adjacent erbium III ions can cause an increase in the measured lifetime of the excited energy level. This energy migration is also referred to as a "re-absorption effect" and needs to be minimized to get a direct measurement of the energy level lifetimes. Two different techniques were used to minimize this re-absorption. The first involved pumping along the edge of the samples and the second used a pinhole [174]. The results for both are provided. This chapter concludes with emission cross-sections which were calculated from the lifetimes of the 1.5μm laser level and measured spontaneous emission spectra. The emission cross-sections were used in Chapter 5 to calculate the available gain for a laser setup using this glass.

4.1 Absorption

The erbium III absorption was characterized in the visible and near infrared wavelength regions.

Absorption measurements were performed on samples with erbium III concentrations between 0.2×10^{20} ions/cm^3 and 25×10^{20} ions/cm^3. The 0.2×10^{20} ions/cm^3 concentration was chosen to get an understanding of the behaviour of a low doped sample. Similarly, the 25×10^{20} ions/cm^3 concentration sample was used to get an

understanding of the spectroscopy of a highly doped sample. This sample contained some crystals due to the high erbium III content so the erbium III concentration was not increased further. These samples were cut from fabricated 50g glass blocks and polished, using a 1μm Al_2O_3 slurry, to a thickness of 2 ± 0.1 mm. Some of the 50g glass blocks are illustrated in Figure 63. The concentrations increase from undoped (a), 0.2×10^{10} ions/cm^3, 0.5×10^{20} ions/cm^3, 1×10^{20} ions/cm^3 to 5×10^{20} ions/cm^3 (e).

NOTE:
This figure is included on page 104 of the print copy of the thesis held in the University of Adelaide Library.

Figure 63: Photograph made by Russell Grew of erbium III doped tellurite glass samples increasing in dopant concentration from left to right.

The absorption spectra were measured using a CARY spectrophotometer. The absorption cross section, σ_{abs}, was calculated from the measured absorption coefficient and dividing by the erbium III ion concentration (N) using Equation (16).

$$\sigma_{abs} = \frac{\alpha}{N} \quad \textbf{(16)}$$

If the output from the spectrophotometer was absorbance (E), the absorption coefficient (α) is calculated using Equation (4). The absorption cross-section of the erbium III ions is plotted for the base TZN and the TZNL glasses in Figure 64.

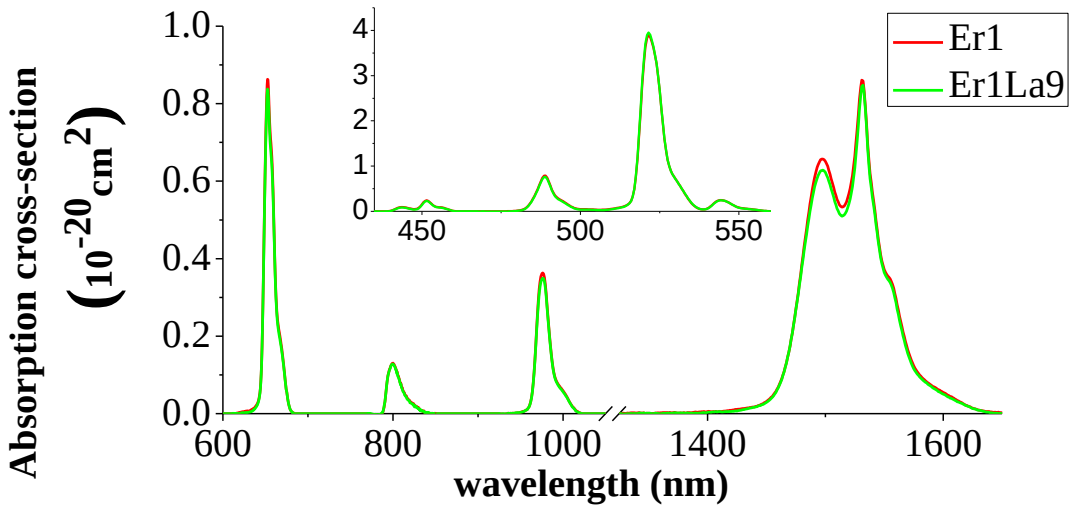

Figure 64: Plot of the absorption cross-sections for erbium III in TZN and TZNL glasses. The dopant concentration was 1 x 10^{20} ions/cm^3.

Figure 64 compares the absorption cross-section for the erbium III absorption bands that lie between 450 and 1700nm for the base TZN and TZNL glasses both doped with 1 x 10^{20} ions/cm^3 erbium III. This plot demonstrates that the addition of lanthanum oxide to the glass composition had a negligible effect on the erbium III absorption in the glass. The peak values of the absorption cross-section for each of the energy levels is provided in Table 5.

Table 5: Absorption cross-sections for the ground state absorption transitions in erbium III doped TZN and TZNL glasses.

Energy transition	Peak wavelength (nm)	Absorption cross-section ($\times 10^{-20}$ cm^2)
$^4I_{15/2} \rightarrow {}^4I_{13/2}$	1530	0.86
$^4I_{15/2} \rightarrow {}^4I_{13/2}$	980	0.39
$^4I_{15/2} \rightarrow {}^4I_{13/2}$	800	0.11
$^4I_{15/2} \rightarrow {}^4F_{9/2}$	660	0.87
$^4I_{15/2} \rightarrow {}^4S_{3/2}$	525	4.2

The absorption cross-section for a range of erbium III concentrations are plotted in Figure 65. From this plot it is evident that in the range of concentrations tested, the absorption cross-section is independent of the erbium III concentration. The small variation between the different measurements was due to measurement error, either in the sample thickness (1 %), uncertainty in the erbium III concentration (0.5 %), which effects the height of the absorption bands, or the subtraction of the background. When extracting the absorption cross-section from the absorbance, the background absorption is separated from the erbium III absorption. This background is caused by Fresnel reflection from the two faces of the glass sample, scattering losses from the glass and the glass surface and the intrinsic loss of the tellurite glass. The amount of Fresnel reflection follows the Sellmeier curve plotted in Figure 31 and is approximately 11% for tellurite glass. The scattering loss is taken to be independent of wavelength. It was assumed that the intrinsic glass loss was linear across each of the absorption bands. This background loss was subtracted from each absorption band for each sample and would have contributed to the slight variation in the shape of an absorption band between samples.

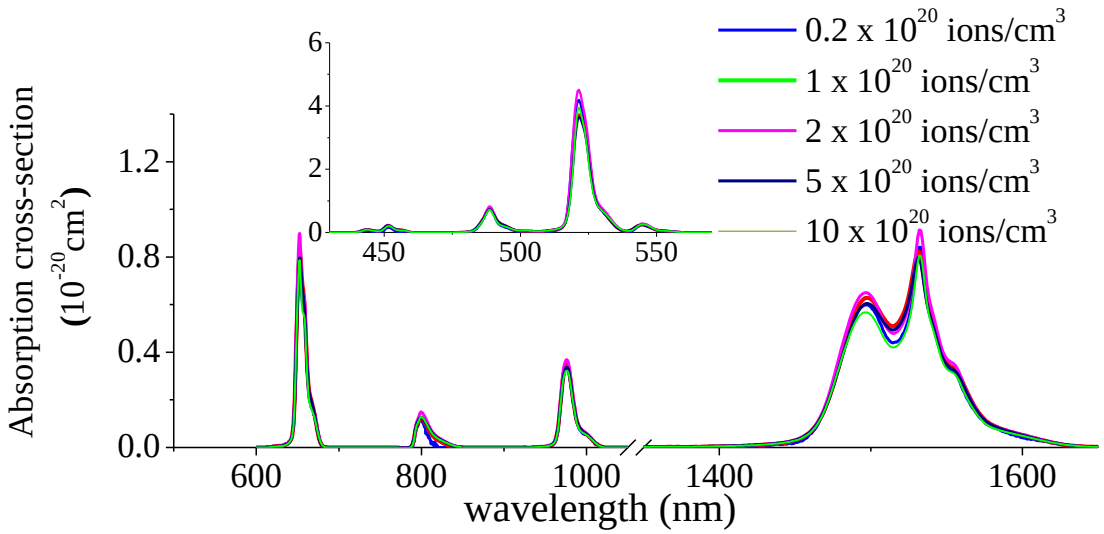

Figure 65: Absorption cross-section for a range of erbium III concentrations.

Based on Figure 64 and Figure 65, it can therefore be said that within measurement error the absorption cross-section can be considered to be independent of the erbium III concentration and unchanged by the addition of lanthanum oxide to the glass. The error in this measurement was taken to be 2%.

4.2 Energy Level Lifetimes

The lifetimes for the $^4I_{11/2}$ and $^4I_{13/2}$ energy levels are required to model the population dynamics of the erbium III energy level system when it is being pumped. The lifetimes for these two energy levels were calculated and determined experimentally. The radiative lifetimes were calculated using the Judd-Ofelt (JO) theory [89, 90]. The non-radiative decay rates were calculated using plots in literature [83, 84, 175, 176]. The energy level lifetimes were also measured. The non-radiative decay rate was calculated through a comparison between this measured lifetime and the theoretical radiative lifetime. When measuring the lifetimes, re-absorption was minimized through either pumping along the edge of the glass samples or pumping through a pinhole [174]. Re-absorption and hence re-emission of the emitted fluorescence causes an increase in the lifetime of the measured decay curve.

4.2.1 Judd-Ofelt analysis, predicting the radiative energy level lifetimes

A Judd-Ofelt analysis [89, 90] was used to calculate the theoretical radiative lifetimes for the erbium III energy levels in the TZN and TZNL glasses. The Judd-Ofelt parameters used to calculate these lifetimes are found by equating the experimentally found oscillator strength to the theoretically calculated electric and magnetic oscillator strengths [177]. The experimental oscillator strength (P_{exp}) of an absorption transition is calculated from the measured absorption through Equation (17) which relates the oscillator strength to the area under the absorption band. The absorption cross-section, $\sigma_{abs}(\tilde{\nu})$, in this equation was calculated from the measured absorbance through Equations (4) and (16).

$$P_{exp} = \frac{mc^2}{\pi e^2}\frac{1}{\lambda_b^2}\int \sigma_{abs}\, d\lambda \qquad \textbf{(17)}$$

where m is the electron mass in g, c is the speed of light in cm/s and e is the electron charge. As a convention, in this equation and throughout this analysis, e is in cgs units

and has the value of e^2 = 2.307 x 10^{-19} erg.cm. λ_b is the barycentre of the absorption band in units of cm. It is defined by;

$$\lambda_b = \frac{\int E\lambda \, d\lambda}{\int E \, d\lambda} \tag{18}$$

where *E* is the absorbance.

The theoretically calculated oscillator strength of an absorption transition $J \rightarrow J'$, where *J* is the quantum number for the ground state and *J'* for the excited state (i.e. $J = {}^{15}/_{2}$ for the $^4I_{15/2}$ to $^4I_{13/2}$ transition), can be calculated from values that can be found in the literature and three glass dependent parameters (Ω_2, Ω_4 and Ω_6). The electric and magnetic dipole contributions to the oscillator strength are defined in Equation (19).

$$P_{ed/md} = \frac{8\pi^2 mc}{3he^2} \frac{1}{2J+1} \frac{1}{\lambda_b} \hat{n} S_{ed/md} \tag{19}$$

where $P_{ed/md}$ is the electric and magnetic dipole components of the oscillator strength, respectively, $S_{ed/md}$ are the electric and magnetic line strengths defined in Equations (20) and (21) and $\hat{n} = \frac{(n^2+2)^2}{9n}$ which equals 1.972 for the TZNL glass at 1550nm.

$$S_{ed} = e^2 \sum \Omega_t \cdot \left\| U^{(t)} \right\|^2 \tag{20}$$

$$S_{md} = \left(\frac{eh}{4\pi mc}\right)^2 \cdot LS \tag{21}$$

where Ω_t are the glass dependent Judd-Ofelt parameters with *t* = 2,4 and 6 and $\left\| U^{(t)} \right\|^2$ and LS are host independent matrix values that can be found in the literature [178]. Substituting Equations (20) and (21) into Equation (19) simplifies the equation for the electric and magnetic dipole oscillator strengths to;

$$P_{ed} = \frac{8\pi^2 mc}{3h}\frac{1}{2J+1}\frac{1}{\lambda_b}\hat{n}\sum \Omega_t \cdot \left\|U^{(t)}\right\|^2 \quad \textbf{(22)}$$

$$P_{md} = \frac{h}{6mc}\frac{1}{2J+1}\frac{1}{\lambda_b}\, n\, LS \quad \textbf{(23)}$$

Separating the refractive index dependence from the magnetic dipole oscillator strength leaves the glass independent parameter P'_{md} which is related to the magnetic oscillator strength by $P_{md} = n \cdot P'_{md}$. The values for $\left\|U^{(t)}\right\|^2$ and P'_{md} are therefore both independent of the host material and can be found from literature [178-181]. In the case of erbium III as the dopant, these parameters are reproduced from Ref. [178] for the first five energy levels in Table 6. As can be seen in this table, of the five energy levels considered, only the oscillator strength for $^4I_{13/2} \rightarrow {}^4I_{15/2}$ transition has a significant magnetic dipole component.

By equating the experimentally calculated oscillator strength (Equation (17)) and the theoretical oscillator strength, which is the sum of its electric (Equation (22)) and magnetic (Equation (23)) components (as given in Equation (24)), the Ω_t parameters for the TZN and TZNL glass compositions can be calculated.

The resultant equation (Equation (25)) is solved for the Judd-Ofelt $\boldsymbol{\Omega_i}$. A minimum of three erbium III transitions must be used to calculate the three $\boldsymbol{\Omega_i}$ parameters of the TZN and TZNL glasses. As there are three Judd-Ofelt parameters that need to be calculated, this equation needs to be calculated for at least three of the erbium III transitions. Increasing the number of energy levels considered in the calculation of these parameters increases the accuracy of the $\boldsymbol{\Omega_i}$ values.

Table 6: The matrix elements $U^{(t)}$ and the magnetic dipole contribution to the oscillator strength for erbium III given a glass refractive index of 1.983 at 1550nm [179-181].

Energy transition	$\|U^{(2)}\|^2$	$\|U^{(4)}\|^2$	$\|U^{(6)}\|^2$	P_{md}
$^4I_{13/2} \rightarrow {}^4I_{15/2}$	0.0188	0.1176	1.4617	0.61 x 10^{-6}
$^4I_{11/2} \rightarrow {}^4I_{15/2}$	0.0259	0.0001	0.3994	-
$\rightarrow {}^4I_{13/2}$	0.021	0.11	1.04	-
$^4I_{9/2} \rightarrow {}^4I_{15/2}$	0	0.1452	0.0064	-
$\rightarrow {}^4I_{13/2}$	0.0003	0.0081	0.64	-
$^4F_{9/2} \rightarrow {}^4I_{15/2}$	0	0.5655	0.4651	-
$\rightarrow {}^4I_{13/2}$	0.0096	0.1576	0.087	-
$\rightarrow {}^4I_{11/2}$	0.0671	0.0088	1.2611	-
$\rightarrow {}^4I_{9/2}$	0.096	0.0061	0.012	-
$^4S_{3/2} \rightarrow {}^4I_{15/2}$	0	0	0.2285	-
$\rightarrow {}^4I_{13/2}$	0	0	0.3481	-
$\rightarrow {}^4I_{11/2}$	0	0.0037	0.0789	-
$\rightarrow {}^4I_{9/2}$	0	0.0729	0.256	-

$$P_{exp} = P_{ed} + P_{md} \quad \textbf{(24)}$$

$$\sum_t \Omega_t \cdot \left\| U_i^{(t)} \right\|^2 = \frac{3\hbar c}{8\pi^3 e^2} \frac{ln10}{N\,d} \frac{2J+1}{\lambda_{b,i}} \frac{1}{\widehat{n_i}} \int E d\lambda - \frac{3\hbar}{8\pi^2 mc} (2J+1)\, \lambda_{b,i} \frac{n}{\widehat{n_i}} P'_{md} \quad \textbf{(25)}$$

The Judd-Ofelt parameters calculated for the erbium III doped TZN glass were 5.23×10^{-20}, 1.48×10^{-20} and 1.20×10^{-20} for $\boldsymbol{\Omega_2}$, $\boldsymbol{\Omega_4}$, and $\boldsymbol{\Omega_6}$, respectively. For the TZNL glass samples the $\boldsymbol{\Omega_i}$ parameters were calculated to be 5.54×10^{-20}, 1.70×10^{-20} and 1.22×10^{-20} for $\boldsymbol{\Omega_2}$, $\boldsymbol{\Omega_4}$, and $\boldsymbol{\Omega_6}$, respectively.

To test the accuracy of the $\boldsymbol{\Omega_i}$ parameters they were substituted back into Equation (22) and the resultant oscillator strength was compared to the measured oscillator strength (Equation (17)). The accuracy of these $\boldsymbol{\Omega_i}$ parameters was within 10%.

Once the $\boldsymbol{\Omega}_i$ parameters were calculated they were used to calculate the decay rates for the relevant erbium III transitions. Equation (26) was used to calculate the electric component of the spontaneous radiative decay rates for each of the erbium III energy levels (A_{ed}) from the $\boldsymbol{\Omega}_i$ parameters. The magnetic component was calculated from the refractive index of the glass and the host independent magnetic dipole oscillator strengths. A_{md} is calculated from the P_{md} values provided in Table 6 using Equation (27).

$$A_{ed} = \frac{64\pi^4}{3h}\frac{\tilde{\nu}_b^3}{2J+1}n^2\hat{n}e^2\sum_{t=2,4,6}\Omega_t \cdot \left\|U_i^{(t)}\right\|^2 \quad \textbf{(26)}$$

$$A_{md} = \frac{8\pi^2 e^2 \tilde{\nu}_b^2 n^3}{mc\hat{n}}P_{md} \quad \textbf{(27)}$$

where $\tilde{\nu}$ (=1/λ) is the wavenumber, with units cm^{-1}.

The spontaneous radiative decay rate was found from the sum of the electric and magnetic components.

$$A = A_{ed} + A_{md} \quad \textbf{(28)}$$

For the $^4I_{13/2} \rightarrow {}^4I_{15/2}$ erbium III transition which has a considerable magnetic dipole contribution, the electric and magnetic components of the radiative decay rate are calculated to be 70 and 221 s^{-1}, respectively.

The lifetime (τ_i) of a particular energy level is then the inverse of all the spontaneous decay rates from that level through Equation (29). The branching ratios were calculated for the different transitions from an energy level through Equation (30).

$$\tau_i = \frac{1}{\sum_j A_{i,j}} \quad \textbf{(29)}$$

$A_{i,j}$ is the radiative decay rate from energy levels *i* to *j*, including both the electric and magnetic components.

$$\beta_{i,j} = \tau_i A_{i,j} \quad \textbf{(30)}$$

The spontaneous decay rates calculated for the transitions between the first five energy levels, the branching ratios for each of the transitions and the lifetimes of the energy levels calculated from the glass samples are provided in Table 7.

Table 7: Results for the Judd-Ofelt analysis on the TZN glass including the transition, the emission wavelength between the barycentres of the transitions, radiative decay rate, $A_{i,j}$, for the transition from the *i*th to the *j*th energy levels, branching ratios, $\beta_{i,j}$, for the *i* to *j* transition, and lifetime, τ_i, for the *i*th energy level.

Transition	Wavelength (nm)	$A_{i,j}$ (s^{-1})	τ_i (ms)	β_{ij} (%)
$^4I_{13/2} \rightarrow {}^4I_{15/2}$	1518.63	291	3.4	100
$^4I_{11/2} \rightarrow {}^4I_{15/2}$	979.72	332	2.7	88.2
$\rightarrow {}^4I_{13/2}$	2770.85	44	-	11.8
$^4I_{9/2} \rightarrow {}^4I_{15/2}$	805.41	266	2.8	75.2
$\rightarrow {}^4I_{13/2}$	1733.70	88	-	24.9
$^4S_{3/2} \rightarrow {}^4I_{15/2}$	546.48	2870	0.4	100
$^4F_{9/2} \rightarrow {}^4I_{15/2}$	656.30	3198	0.3	91.3
$\rightarrow {}^4I_{13/2}$	1158.07	159	-	4.3
$\rightarrow {}^4I_{11/2}$	1989.65	146	-	4.2
$\rightarrow {}^4I_{9/2}$	3487.96	10	-	0.3
$^4F_{7/2} \rightarrow {}^4I_{15/2}$	489.57	7399	0.1	100
$^4F_{5/2} \rightarrow {}^4I_{15/2}$	452.96	3600	0.3	100
$^4F_{3/2} \rightarrow {}^4I_{15/2}$	444.46	3119	0.3	100
$^2H_{11/2} \rightarrow {}^4I_{15/2}$	523.23	17765	0.1	100

From Table 7 the radiative lifetime of the $^4I_{13/2}$ and $^4I_{11/2}$ energy levels are 3.43ms and 2.66ms, respectively. Although these lifetimes were calculated for the TZN glass, due to the very similar absorption of the TZNL glasses when compared to the TZN

glasses (Section 4.1), the lifetimes of the erbium III energy levels in the TZNL glasses are also equal to the values presented in Table 7.

The lifetimes measured for these energy levels are however shortened from these radiative lifetimes by non-radiative decay. This is discussed further in the next section. Measured lifetimes for the $^4I_{13/2}$ and $^4I_{11/2}$ energy levels are presented in Section 4.2.3.

4.2.2 Non-radiative decay

Tellurite glasses have a relatively low maximum phonon energy of between 690 and 800 cm^{-1} [30], depending on the glass composition, which is well below that of the silica glasses and slightly lower than the germanate glasses, but above that of the fluoride and chalcogenide glasses. The maximum phonon energy is determined by the maximum vibrational energy of the inter-ionic bonds in the glass. If an energy gap can be bridged by three or fewer phonons, the decay from the upper energy level will be dominated by non-radiative multi-phonon decay and the lifetime is significantly reduced from the radiative lifetime [182].

The non-radiative decay rate as a function of the energy gap between adjacent energy levels in tellurite glass was calculated from the experimentally measured lifetimes and also from values presented in literature by Reisfeld et al. [83, 84, 175, 183]. These non-radiative decay rates are summarized in Table 8. These papers were based on a sodium tellurite glass and served as a good comparison for the non-ratiative decay rates measured for the TZN and TZNL glasses used in this work.

Table 8: Table of the non-radiative decay rates for various energy gaps in a binary sodium tellurite glass [83, 84, 175, 183]

Transition	Energy gap (cm^{-1})	$A_{non\text{-}radiative}(s^{-1})$
Er ($^4F_{9/2} \rightarrow {}^4I_{9/2}$)	2600	$\approx 2 \times 10^5$
Er ($^4S_{3/2} \rightarrow {}^4F_{9/2}$)	3000	$\approx 1 \times 10^4$
Tm ($^1D_2 \rightarrow {}^1G_4$)	6300	$\approx 2 \times 10^2$

Interpolation of these values from the literature enabled a prediction of the non-radiative decay rate from the pumped $^4I_{11/2}$ down to the $^4I_{13/2}$ energy level for the TZN

and TZNL glass compositions. The energy gap for this transition is approximately 3600 cm^{-1} which corresponds to a non-radiative decay rate of ≈5 x 10^3 s^{-1}. The 1.5μm transition from the $^4I_{13/2}$ energy level down to the ground state corresponds to an energy gap of >7000 cm^{-1} and a non-radiative decay rate of ≈10 s^{-1}. The non-radiative decay from the $^4I_{13/2}$ energy level is not significant compared to the radiative decay from this energy level ($291s^{-1}$).

Using the Judd-Ofelt analysis (Section 4.2.1) the total of the radiative decay rates from the $^4I_{11/2}$ and$^4I_{13/2}$ energy levels were calculated to be 376 s^{-1} and 291 s^{-1}, respectively. The experimental decay rate is given as the sum of the radiative and non-radiative decay rates. By including the non-radiative decay, the theoretical lifetime for the $^4I_{11/2}$ energy is reduced from 2.7ms down to 0.19ms. This significant difference in the lifetime indicates that decay from this energy level is dominated by non-radiative decay. In the next section the non-radiative decay rate is calculated from the measured decay rates by comparing the measured lifetimes to the theoretical radiative lifetimes using $1/\tau_{experimental} = 1/\tau_{radiative}+1/\tau_{non\text{-}radiative}$

This additional shortening of the upper energy level of the 2.7μm transition along with minimal shortening of the lower energy level adds to the difficulty in overcoming the self terminating nature of this laser transition in tellurite glass using the processes described in Section 1.2.5.

4.2.3 Experimental lifetime measurements

The lifetimes for the $^4I_{11/2}$ and $^4I_{13/2}$ energy levels, corresponding to the pump and 1.5μm laser levels, were measured for use in the laser rate equation modelling (Chapter 5) and to find the doping concentration for the glass when clustering begins to significantly reduce the lifetimes.

The experimental setup used for the initial lifetime measurements is illustrated in Figure 66. These measurements were performed using a chopped LIMO 12W multimode pump source, which had a peak emission wavelength of 974nm. The samples studied were pumped along their edge to minimize re-absorption of the fluorescent light. The fluorescence was captured perpendicular to the pump direction with a 30mm lens and

focused through a filter onto an InGaAs photodiode. For the lifetime measurement of the $^4I_{11/2}$ erbium III energy level, a bandpass filter (850nm to 1100nm) to block the fluorescence from the other energy levels. For the lifetime measurement of the $^4I_{13/2}$ erbium III energy level a silicon wafer was used to block all wavelengths below 1.1µm. The signal strength was recorded using an oscilloscope. For the 1.5µm fluorescence measurements a long pass 1.5µm filter was used to block any 980nm fluorescence and scattered pump light. When measuring the lifetime of the pump energy level a 900nm to 1.15µm bandpass filter was used to block any emission from other erbium III energy levels. Measuring the fluorescence perpendicular to the pump direction minimized the amount of pump that was scattered into the detector, however, in the measurement pump light appeared as a DC shift in the fluorescence signal while the pump was not blocked by the chopper. The measurement of the $^4I_{13/2}$ lifetime at 1.5µm while pumping at 974nm required the lifetime of the $^4I_{11/2}$ energy level to be significantly shorter than that of the $^4I_{13/2}$ level. The decay within a millisecond of the chopping of the pump was not used in the calculation of the lifetime for this energy level as, while there were still ions in the higher energy levels, the $^4I_{13/2}$ energy level is still being re-populated.

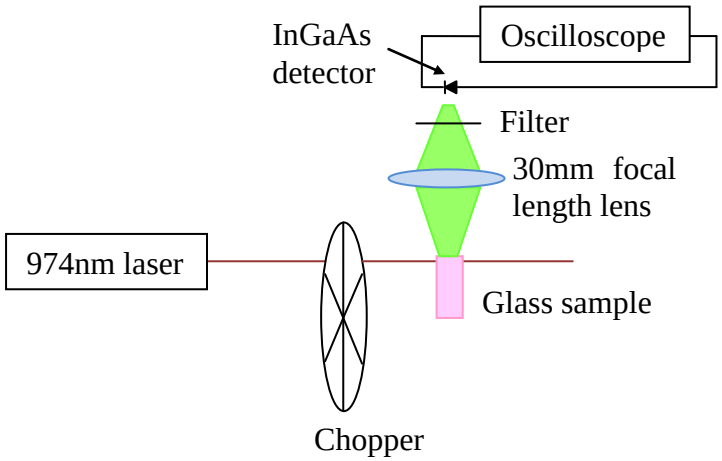

Figure 66: Experimental setup used in the lifetime measurements of the $^4I_{13/2}$ and $^4I_{11/2}$ erbium III energy levels.

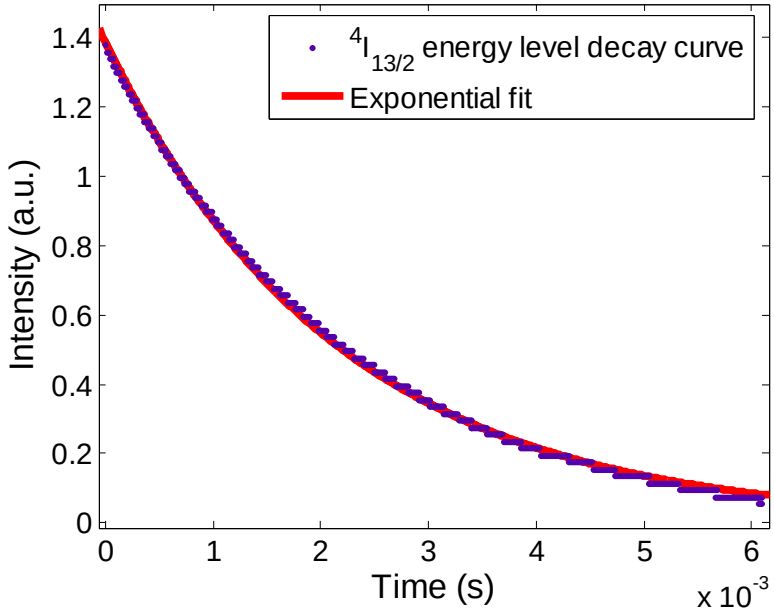

Figure 67: Exponential decay of the 1.5µm fluorescence in the 10 x 10^{20} ions/cm^3 erbium III doped TZN glass after excitation for 6ms and waiting for 1ms before sampling. The measured data were fit to a single exponential, $I = Ae^{Bt}$ where I is the intensity and the fitting parameters A and B were calculated to be 1.386 ± 0.002 and -462.7 ± 0.9, respectively.

An example of a fluorescence decay curve is provided in Figure 67. This decay corresponds to the $^4I_{13/2}$ energy level in the 10 × 10^{20} ions/cm^3 erbium III doped TZN glass. From this figure the B parameter in the curve fitting gives the decay rate of 462.7 ± 0.9 s^{-1}, which corresponds to a lifetime of 2.157 ± 0.005ms. From the curve fitting, it was fount that the decay was a good fit to an exponential curve.

Figure 68 illustrates the lifetimes of the $^4I_{13/2}$ energy level for different erbium III concentrations in a TZN host glass. From this plot we can see that for some concentrations, the measured lifetimes appeared to be longer than the theoretical radiative lifetimes calculated using the Judd-Ofelt analysis (Section 4.2.1), this is due to excitation migration. The measured lifetime is lengthened due to the re-absorption and re-emission of the fluorescence. When pumping into the centre of the samples the measured lifetimes are significantly longer (as much as double). Without careful pumping along the edge of the samples, this effect could cause significant variation in the measured lifetimes. Detailed later in this section, the re-absorption effects were

minimised using a pin-hole technique and the measurements were repeated for comparison.

For concentrations > 5 x 10^{20} ions/cm^3 the lifetime drops suddenly possibly due to energy migration between adjacent erbium III ions and the phonon decay through OH impurities in the glass.

The lifetimes for the $^4I_{11/2}$ energy are presented in Figure 69. The lifetime of this energy level was roughly independent of the erbium III concentration and there was no evidence of the lifetime being lengthened due to re-absorption. The measured values agree with the theoretical lifetime that includes the non-radiative decay.

The error in the these lifetime measurements was due to shot to shot variation in the decay curves acquired and was within 10%.

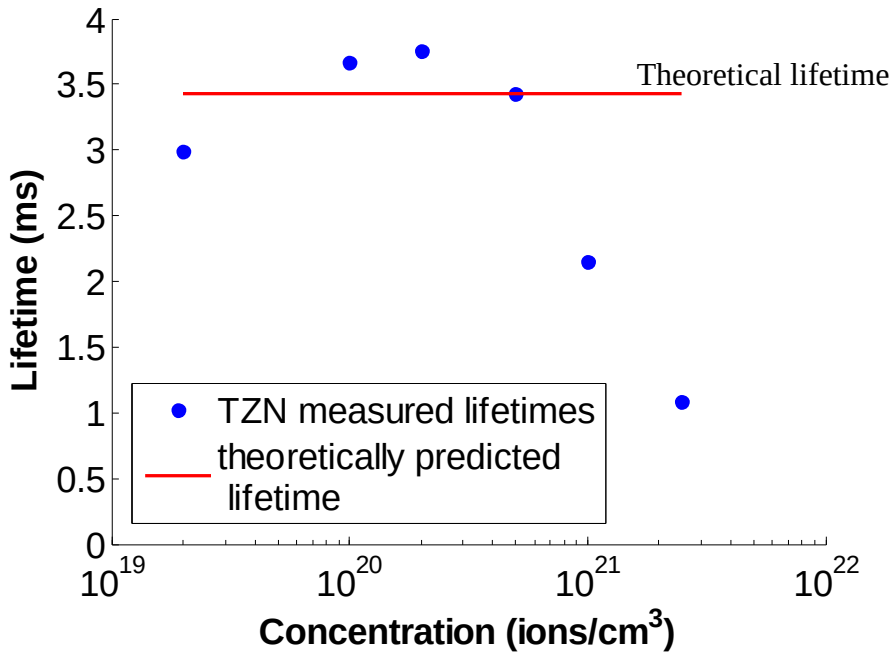

Figure 68: Measured lifetimes of the $^4I_{13/2}$ energy level to ground level transition, for a range of erbium III concentrations in the TZN glass, compared to the theoretical lifetime. The samples were pumped along their edge to minimize re-absorption effects. As the most significant source of systematic error in these measurements was due to re-absorption, the error of these plotted data points was minimized through pumping the glass samples as close as practical to their edge. Shot to shot variation was then in the order of 3%.

(a)

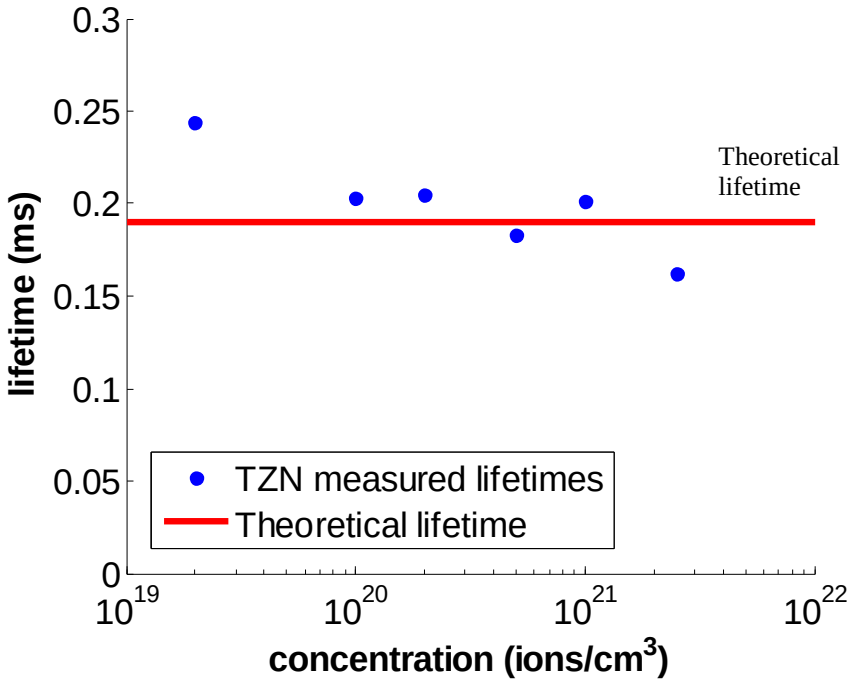

(b)

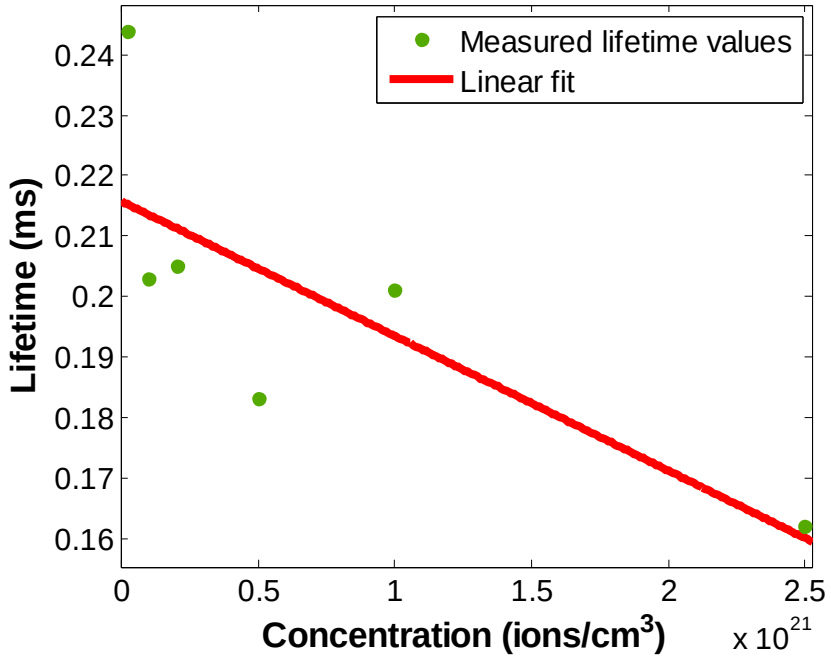

Figure 69: Measured lifetimes for the $^4I_{11/2}$ energy level for a range of erbium III concentrations in the TZN glass compared to the theoretical lifetime (a). As with the 1.5µm lifetime measurements, the error in these measurements was primarily due to shot to shot variations in the decay curves and was ≈ 5%. The lifetimes on a linear concentration scale are also plotted in (b) along with the linear fit $\tau = c + a[Er^{3+}]$. The values for c and a are 0.2157 ± 0.03 and -2.2 x 10^{-23} ±2 x 10^{-23}, respectively.

The non-radiative decay rate was calculated using the lifetime measurements of the $^4I_{11/2}$ energy level in the TZN glass. Re-absorption effects were not significant for this energy level so minimising this effect was not warranted. The equation $A_{experimental} = c + a[Er^{3+}]$ where $[Er^{3+}]$ is the erbium III concentration was fitted to the measured lifetimes. The value for c from this fit is the concentration independent lifetime which includes the radiative and non-radiative decay. The non-radiative decay rate is found from the difference between this value and the radiative lifetime that was calculated using the Judd Ofelt analysis. For the $^4I_{11/2}$ energy level the non-radiative decay rate was calculated to be $4600 \pm 300\ s^{-1}$ which, agrees with an interpolation of the non-radiative decay rates provided in Table 8. The large error in this measurement could be due to variations in the position of the pump spot in the samples and hence the amount of re-absorption. The erbium III to OH energy transfer increases the decay rate for the higher erbium III concentration samples. This can be seen by the negative slope in the line of best fit plotted in Figure 69 (b), however, due to the uncertainty in the slope, accurate determination of the erbium III to OH energy transfer rate could not be made.

The lifetimes of the $^4I_{13/2}$ energy level were re-measured using the same 12W LIMO diode as described previously and the pinhole technique, described in Ref. [174], to further reduce the re-absorption and lengthening of the measured lifetimes. The pinhole technique works by pumping the glass sample through a pinhole and measuring the fluorescence emitted back through the hole. This ensured that the fluorescence captured by the detector was emitted from the surface of the sample. The experimental setup when using the pinhole is provided in Figure 70. The pinhole diameter used for these results was 300μm which would have resulted in less than a 5% increase in the lifetime due to excitation migration [174]. The measured lifetimes for the TZNL glass using this technique for the $^4I_{13/2}$ and $^4I_{11/2}$ energy levels are presented in Figure 71 and Figure 72, respectively. It was seen that these measured lifetimes were within the error of the theoretically calculated values. Compared to the 13% uncertainty in the $^4I_{11/2}$ energy level lifetime measurements made without the use of the pinhole (Figure 69), the 5% uncertainty in the lifetime measurements for this energy level when using a pinhole was a significant improvement. This agrees with the belief that re-absorption effects caused the higher uncertainty in the lifetimes plotted in Figure 69.

In Figure 71 and Figure 72 it can also be seen that the glass samples melted in a dry atmosphere have longer lifetimes when compared to the open air melted samples. This is thought to be due to reduced OH quenching. OH quenching reduces the lifetimes in the open air melted glasses particularly for the high erbium III concentrations through Er^{3+} to OH energy transfer [184]. In the glovebox melted samples, the increased re-absorption effects associated with the higher concentrations along with the reduced OH concentration, could have resulted in the measured lifetimes of the $^4I_{11/2}$ energy level that increased with concentration.

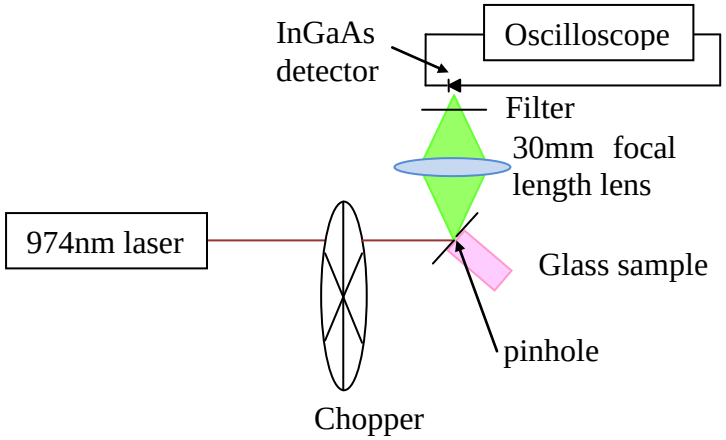

Figure 70: Experimental setup for the lifetime measurements using the pinhole to reduce re-absorption.

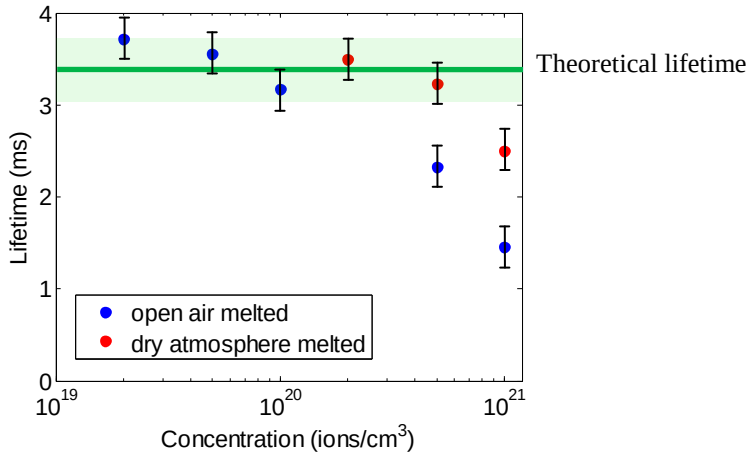

Figure 71: Measured lifetimes of the $^4I_{13/2}$ energy level for different erbium III concentrations in a TZNL glass host. The samples melted in open atmosphere (blue) are compared to those melted in the dry environment (red). The theoretical lifetime including radiative and non-radiative decay is also included along with its uncertainty for comparison.

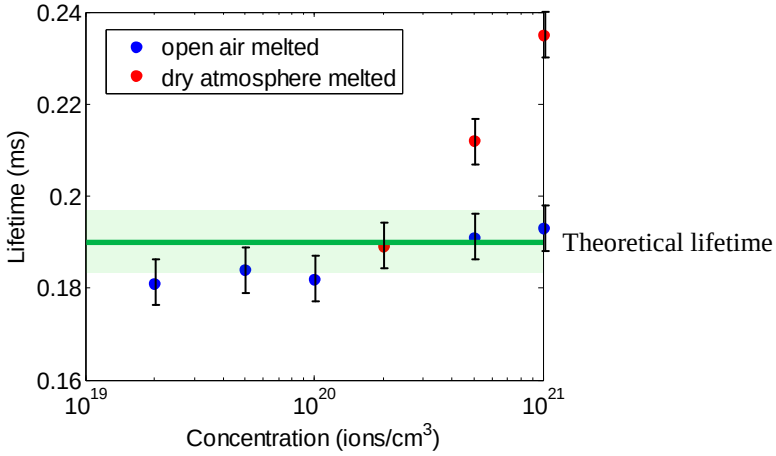

Figure 72: Measured lifetimes of the $^4I_{11/2}$ energy level for different erbium III concentrations in a TZNL glass host. The samples melted in open atmosphere (blue) are compared to those melted in the dry environment (red). The theoretical lifetime including radiative and non-radiative decay is also included along with its uncertainty for comparison.

4.3 Emission Cross-section

An understanding of the stimulated emission cross-section, which is a measure of the emission probability, is required to calculate a doped fibre's gain and hence assist with the design of the laser setup. Different techniques can be used to calculate the emission cross-section. The simplest method uses the Einstein relations which relate the emission cross-section to the absorption cross-section. By contrast, the McCumber technique [185] calculates the emission spectra from the absorption spectra and also calibrates the emission cross-section from the absorption cross-section through the calculation of the radiative lifetime. This calculation is best presented in Ref. [186], which takes a measured emission spectra and calculates the magnitude of the cross-section based on the radiative lifetime of this energy level. The absorption measurements and determination of the radiative lifetimes are presented above (Section 4.1 and 4.2).

Although the stimulated emission cross-section can be directly measured spectroscopically, this measurement is difficult as it needs to be performed at low temperatures or knowledge of the ground population distribution is required. The emission cross-section is more easily calculated from the absorption cross-section. The McCumber relation is used to relate the emission cross-section to the absorption cross-section [185]. The only approximation made when using this relation was that the time required to establish a thermal distribution of ions within an energy level is short compared to the lifetime of that energy level which is the case in the erbium III doped tellurite. The absorption and emission spectra are related by [187];

$$\sigma_{emis}(v) = \frac{Z_1}{Z_u}\sigma_{abs}(v)e^{\frac{Z_{zpl}-hv}{kT}} \quad \textbf{(31)}$$

where hv is the energy per photon and Z_{zpl} is the energy required to excite one free electron from the $^4I_{15/2}$ energy level up to the $^4I_{13/2}$ energy level at the temperature T and usually corresponds to the peak of the absorption [188]. In the high temperature limit, Z_1/Z_u becomes the degeneracy weighting of the two energy levels in the emission [189]. From this equation the emission or absorption spectra can be calculated from the other. With accurate calculation of the lifetime of the $^4I_{13/2}$ energy level from the absorption

cross-section using the Judd Ofelt analysis, the emission cross-section can also be calculated through Equation (32) from the emission spectra [186, 187]. In this case the lifetime of an energy level is used to re-normalize the scale of the emission spectra.

$$\frac{1}{\tau} = \frac{8\pi n^2}{c^2} \int v^2 \sigma_{emis}(v) dv \quad \textbf{(32)}$$

The emission spectra measurements were performed using 2mm thick spectroscopic samples. A 12W 100μm fibre coupled pump source was used to excite the samples and the optical spectrum analyser was used to record the emitted spectra from a range of erbium III concentrations. The measured emission spectra are illustrated in Figure 73 where the peaks of the spectra have been normalized to 1 for comparison. Initial measurements were made without a pinhole, using the setup illustrated in Figure 66, and significant broadening was observed with increasing erbium III concentration in the measured spectra (Figure 73 (a)). The emission spectra were re-measured using a pinhole and the same setup illustrated in Figure 70. The use of the pinhole reduced re-absorption of the shorter emission wavelengths. From Figure 73 (b), there was still a slight difference between the spectra. Despite reducing re-absorption of the emitted fluorescence through the use of the pinhole, it was believed that this re-absorption caused the slight difference between the spectra. Excluding this re-absorption, the emission spectra are independent of the erbium III concentration.

(a)

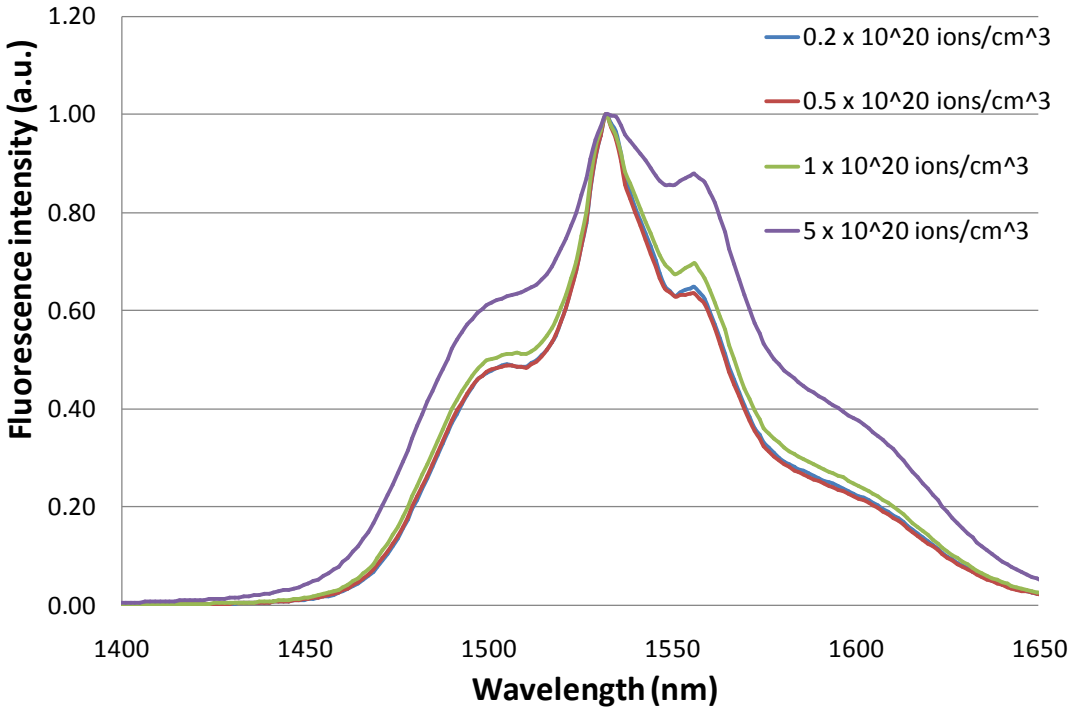

(b)

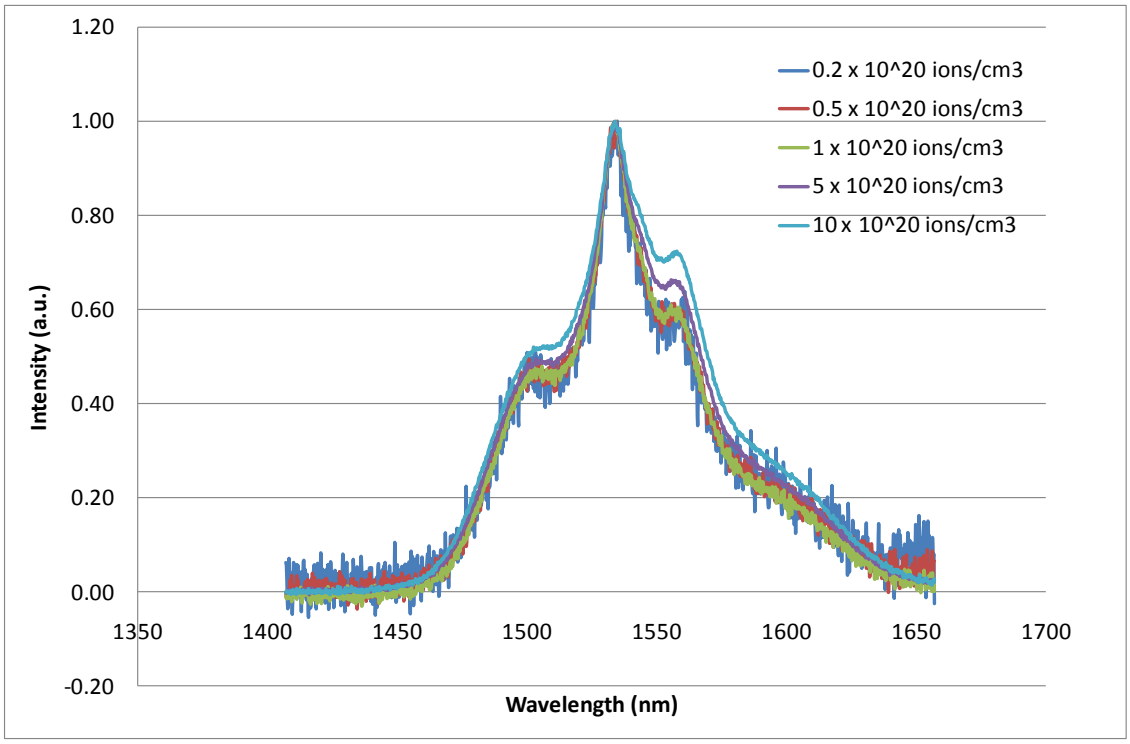

Figure 73: Fluorescence emission spectra for different erbium III concentrations in a TZNL glass host with (a) and without (b) the use of a pinhole to reduce re-absorption.

The emission spectra were also measured for a range of pump powers (Figure 74) for a 0.5 x 10^{20} ions/cm^3 erbium III doped sample. From this plot it is seen that the shape of the emission spectra is unchanged with the increase of excitation power. There was, however, a roll-off in the emitted fluorescence intensity for higher pump powers (Figure 75). This roll-off was due to a wavelength shift in the pump diode as it heated up. As the pump wavelength shifted off the peak of the absorption, less of the pump is absorbed and the amount of fluorescence decreases. This was evident when pumping the samples quasi-continuous wave (QCW), the roll-off is significantly reduced, however it is still observed. Using a pulse duration of 6ms and a frequency of 10Hz, the fluorescence intensity for the QCW and continuous wave (CW) measurements are provided and compared in Figure 75. This plot corresponded to the 0.5 x 10^{20} ions/cm^3 erbium III doped sample and as for the higher concentration samples the glass began to melt when excited with higher pump powers.

The increase in the emitted fluorescence with increasing pump power even when exciting the glass sample with the higher pump powers indicated that this energy level was not being bleached by upconversion processes. Upconversion processes would start to depopulate this energy level if the excitation density (density of the excited ions) was sufficiently high. This upconversion process has its advantages in depopulating the lower laser level of the 2.7μm transition, however, without bleaching of the fluorescence emitted from the $^4I_{13/2}$ energy level observed, for the pump powers and erbium III concentrations used, this process was not evident in this measurement.

(a)

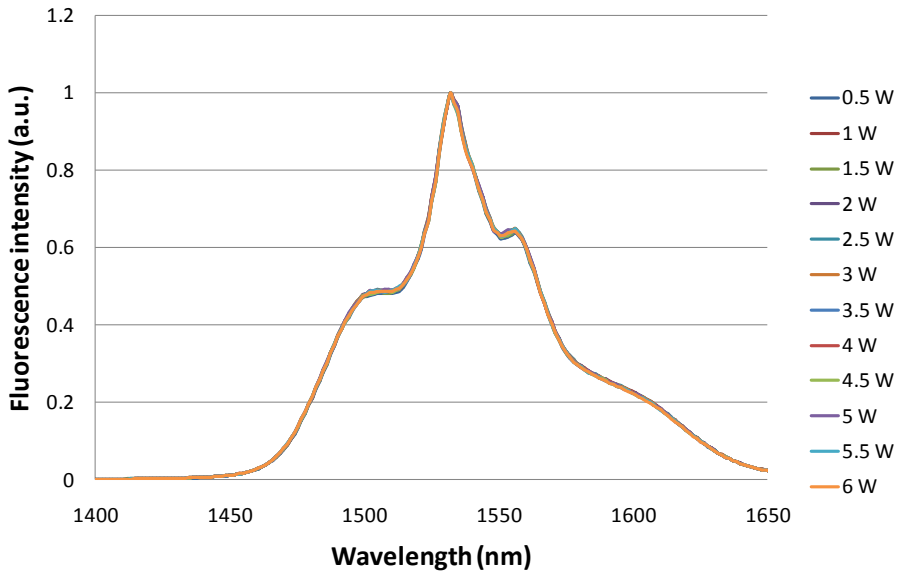

(b)

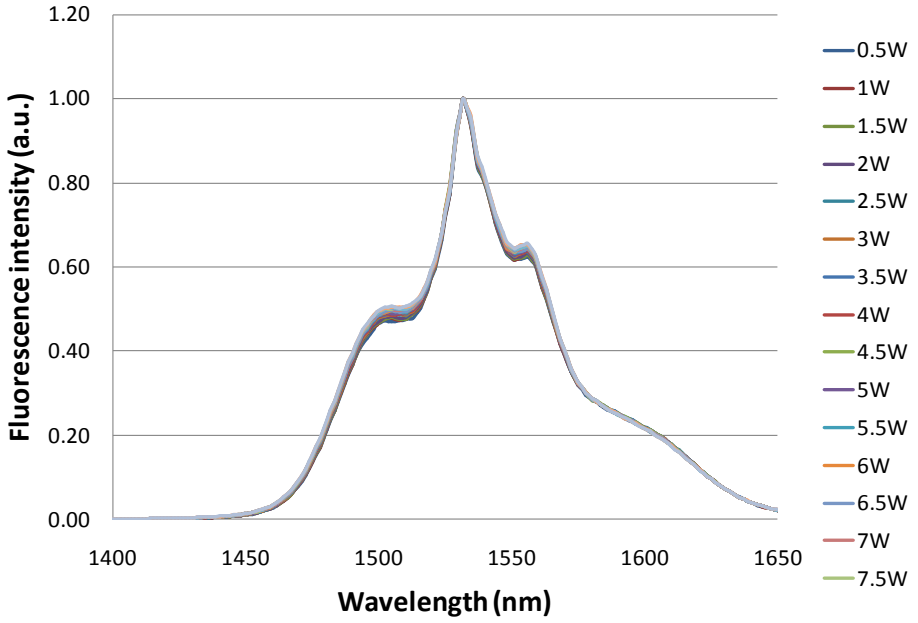

Figure 74: Fluorescence emission spectra for varying pump powers of (a) 0.2 × 10^{20} ions/cm^3 and (b) 0.5 × 10^{20} ions/cm^3 doped samples in the TZNL glass host.

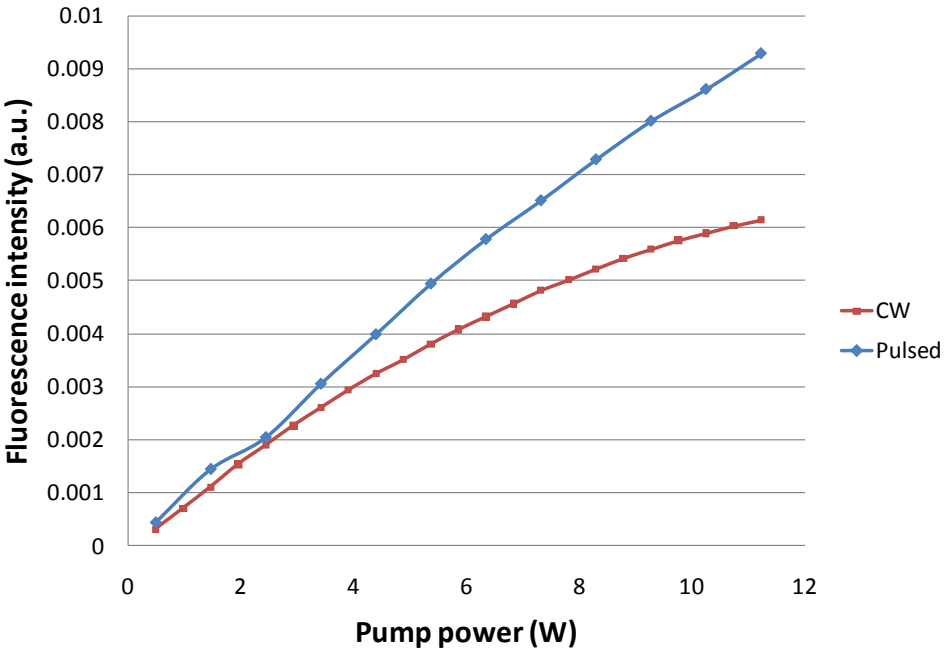

Figure 75: Pump power dependence of the fluorescence intensity from the 0.5 x 10^{20} ions/cm^3 doped TZNL glass

The measured emission spectra were calibrated into the emission cross-section using Equation (32) and plotted along with the absorption cross-section in Figure 76.

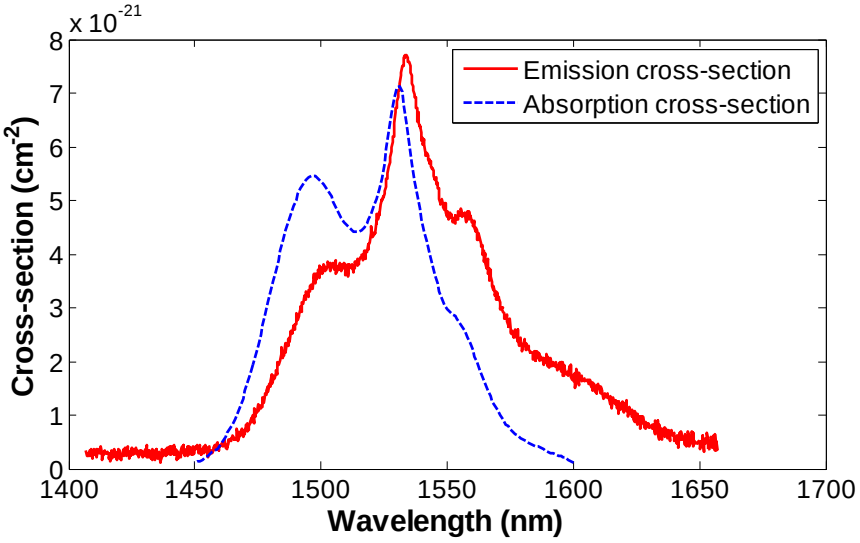

Figure 76: Plot of the emission cross-section and absorption cross-section for the $^4I_{13/2}$ energy level of the doped TZNL glass.

Figure 76 illustrates the similar peak locations at 1.532μm for both the absorption and emission cross-sections. The peak of the emission cross-section was calculated to be 7.7×10^{-20} cm^2 compared to the absorption cross-section peak of 7.2×10^{-20} cm^2. The shifting of the emission spectra to longer wavelengths is evident in this plot. This red shifting of the emission spectra when compared to the absorption spectra is caused by the preferential distribution of the excited ions at the bottom of the $^4I_{13/2}$ energy level and hence emission of lower energy photons when the ions return to the top of the ground state. The re-absorption losses at the shorter wavelengths of the emission spectra would reduce the round trip gain at these wavelengths. Lasing would therefore preferentially occur at wavelengths longer than the peak of the emission spectra.

The results presented in this chapter are used in the prediction of laser thresholds and efficiencies reported in the next chapter (Chapter 5). Absorption measurements are used to determine the amount of pump absorption, the lifetimes measured are used in the threshold calculations and the emission cross-section calculations allow the determination of the available gain in the laser setup.

5. Laser Development and Results

This research project was directed towards the development of a tellurite glass fibre laser at around 3μm. This research also looks into the potential of the extrusion technique to generate the structured preforms in the fibre fabrication.

The initial target for the laser development was a 2.7μm erbium III-doped microstructured tellurite fibre laser. The longer lifetime of the lower energy level of this transition would have resulted in the self-termination of CW lasing at this wavelength. The self-terminating nature of the $^4I_{11/2}$ to $^4I_{13/2}$ transition would be exaggerated in tellurite glass due to the additional multiphonon non-radiative decay across this transition. This was described in Chapter 4 where it was indicated that the upper energy level lifetime is reduced by a factor of 10 due to this non-radiative decay.

The transmission of the tellurite glass was presented in Chapter 2. Despite significant improvements in reducing the OH induced loss at 3μm, the loss at 2.7μm was still of the order of 10dB/m. A combination of the high loss at 2.7μm and the shortened lifetime of the $^4I_{11/2}$ energy level resulted in the decision to test the lasing performance of the fabricated erbium III-doped tellurite fibres across the $^4I_{13/2}$ to $^4I_{15/2}$ transition. When pumping this laser transition in erbium III, which emits at around 1.5μm, the same 980nm laser diodes, that were to be used in the 2.7μm laser experiments, were able to be used.

The laser development began with a rate equation analysis, initially considering only a steady state two level laser system. This allowed the calculation of approximate thresholds for both the bulk glass and fibre laser experiments described within this chapter.

This chapter discusses the bulk glass laser experiments (Section 5.2). QCW pumping was used to reduce the thermal load on the glass during these experiments. This motivated a modification to the steady-state threshold calculations to incorporate the filling of the energy levels. As a consequence of these bulk glass laser experiments, the upconversion in the tellurite glass and temperature dependence of the glass' optical properties were looked into in more detail.

This chapter concludes with the fibre laser setup and results, which describes the microstructured tellurite glass fibre laser constructed using the "wagon wheel" (suspended core) fibre described in Chapter 3. This fibre laser was the first of its kind, the first microstructured tellurite glass fibre laser and more generally the first fibre laser fabricated using the extrusion technique.

To understand better the measured output powers from the fibre laser system, two different models were used. The first model included the pumped energy level in the modelling which allowed for the incorporation of ground state depletion due to the bottle-necking of ions in the energy levels above the laser transition. This bottle-necking restricted the output powers achievable from the laser system. The second model was used to study the impact of the fibre loss on the laser efficiency.

5.1 Steady state laser threshold calculations

To get an understanding of the pump powers required to enable the erbium III doped tellurite glass to lase, the steady state laser threshold was calculated. This preliminary modelling approximated the system as a loss-less two level system where the erbium III ions are excited directly into the upper laser level. This type of modelling would also apply to pumping to an energy level where all of the excited ions immediately decayed into the upper laser level. This was believed to be a valid assumption for erbium III in tellurite glass where the lifetime of the $^4I_{11/2}$ energy level, measured to be 0.2ms, was significantly shorter than the 3.4ms lifetime for the $^4I_{13/2}$ energy level. The modelling also uses the assumption that each pump photon absorbed results in the excitation of one erbium III ion into the upper laser level. This is a reasonable approximation since, due to the non-radiative decay across the $^4I_{11/2}$ to $^4I_{13/2}$ transition, 93% of the excited ions decay from the pump level into the upper laser level.

Equation (33) was used to calculate the pump power required to reach transparency. In this equation, the absorption is determined by the absorption coefficient of the erbium III in the glass and the decay rate is the inverse of the lifetime of the laser level.

$$P_{trans} = \frac{h\nu}{\eta}\frac{N}{2}\frac{V}{\tau}\frac{1}{1-e^{\alpha l}} \quad \textbf{(33)}$$

Where P_{trans} is the pump power required to reach transparency, h is Planck's constant, ν is the frequency of the pump, η is the overlap efficiency, N is the erbium III concentration, V is the excited volume, τ is the lifetime of the laser level, α is the absorption coefficient and l is the fibre length or thickness of the bulk sample. The requirement to excite $N/2$ ions to reach transparency was a valid approximation given the peaks of the emission to absorption cross-sections are approximately equal.

The absorption and emission properties of the erbium III doped TZN and TZNL glasses, used in these calculations, were discussed previously in Chapter 3.

When using Equation (33) to study the dependence of the transparency threshold on the erbium III concentration, maintaining a gain medium length equal to the absorption length means the threshold is independent of the erbium III concentration. The absorption length is defined as the length over which the intensity of propagating light has decreased to $1/e$ of its input intensity. Since the output intensity as a function of propagation length can be calculated using the relation $I_o = I_i e^{-\alpha l}$, where I_o and I_i are the input and output powers, respectively, α is the absorption coefficient and l is the propagation length, the absorption length corresponds to $1/\alpha$.

The threshold dependence on the gain medium length was also studied and is presented in Figure 77 (a). In this plot the gain medium length is presented as a fraction of the absorption length making it independent of concentration and a pumped diameter of 250μm was used.

Figure 77 (b) is a plot of the threshold dependence on the pumped volume. In this case, the gain medium length was kept constant as the absorption length.

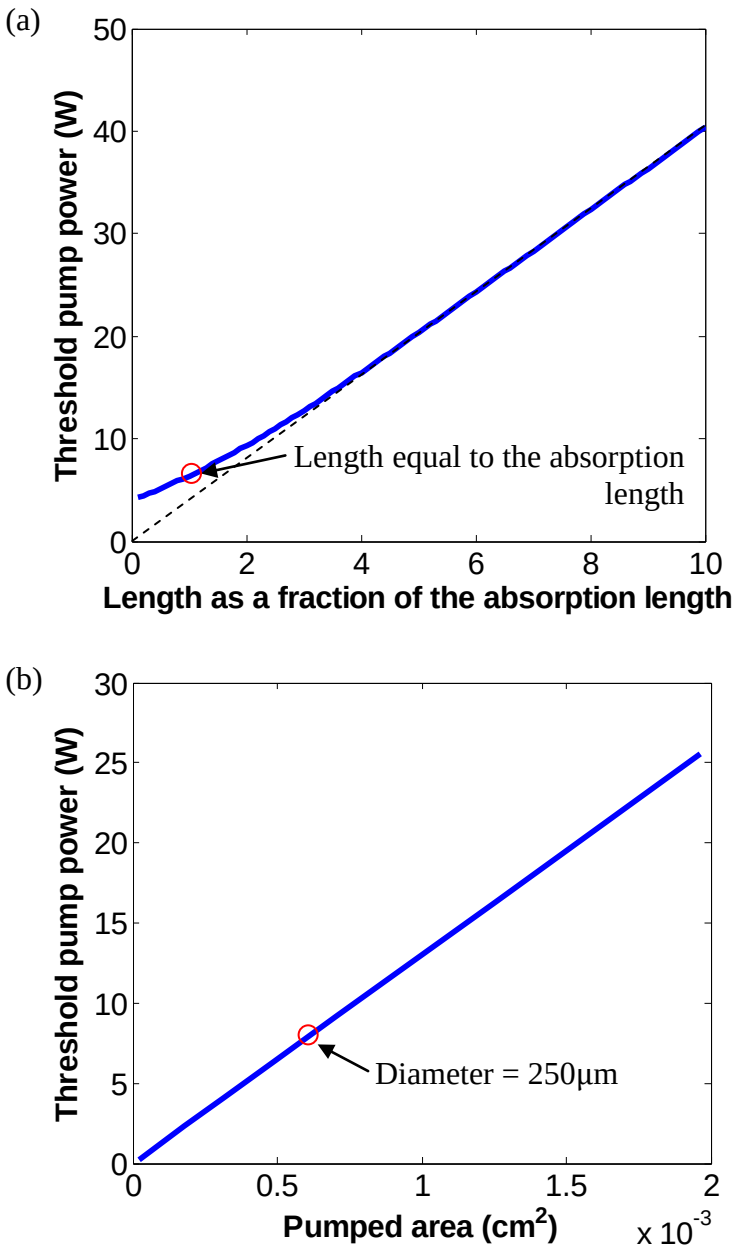

Figure 77: Plots of the threshold dependence on the gain medium length (a), where a pumped diameter of 250µm was used and the fibre length was given in terms of the absorption length making this plot independent of the erbium III concentration, and the pumped cross-sectional area (b) using a concentration of 1 x 10^{20} and a length of 2.5cm, which corresponds to 1/α for this concentration. The result where the diameter equalled 250µm is indicated for comparison.

The results presented in Figure 77 (a) illustrate a roughly linear dependency on the gain medium length. A straight line is plotted for comparison. This almost linear

increase in the threshold, particularly for the longer fibre lengths, was caused by the linearly increasing volume and hence, the number of ions that need to be excited before threshold is reached.

Figure 77 (b) demonstrates, as expected, that the threshold increases linearly with the pump area. The pumped area that corresponds to a pumped diameter of 250μm is circled for comparison to Figure 77 (a).

For the dimensions of the "wagon wheel" fibre used in the laser development (Section 5.3), the threshold was calculated to be 1.5mW for a 1m fibre length and 3.5mW for the 2.2m fibre length. These values were comparable to the measured thresholds presented later in this chapter (Section 5.3.4).

This modelling was limited to CW pumping and in the next section, to allow for the modelling of a QCW pumped system, it was modified to look at the temporal filling of the energy level and at the same time included the depletion of the ground state when it is exposed to the pump light.

5.2 Bulk glass laser modelling and experiments

The primary aim of the bulk glass experiments was to explore the behaviour of the tellurite glass as a laser host without the need to fabricate a fibre, thus allowing for rapid feedback on the glass' performance. This included looking into different loss mechanisms, for example upconversion, that would increase the threshold of the laser system. The primary differences between using bulk glass in place of a fibre are the pumping and the fibre confinement. For the bulk glass experiments, the pump was focused through the glass sample rather than confined to a fibre core. Consequently significantly longer gain medium lengths are available when using a fibre.

The modelling contained within this chapter was relevant to the bulk glass laser experiments as the pump configuration was modelled assuming a multimode pump source. Gaussian beam propagation would need to be considered when pumping with the single mode pump source used in the fibre laser experiments (Section 5.3).

Ray tracing of the multimode pump propagation was used to predict the location of the pump beam's focus and its diameter through the glass slabs (Section 5.2.1.2).

Free space resonator cavity modelling was used to study the effect of the cavity length on the cavity mode diameter (Section 5.2.1.3). This modelling was used to ensure that the cavity mode was completely contained within the pumped volume.

The free space cavity was then realised using a commercial erbium-ytterbium doped phosphate glass slab (Section 5.2.2). This test slab was later replaced with an erbium III doped tellurite glass slab, and an erbium-ytterbium doped tellurite glass slab. The erbium-ytterbium slab had a dopant concentration, glass thickness, absorption cross-section, emission-cross-section and gain that matched that of the phosphate glass test slab (Section 5.2.3).

Following the bulk glass laser experiment, the different loss mechanisms that relate to the tellurite glass were considered. The upconversion in the glass, which filled the $^4S_{3/2}$ energy level, stood out as a possible loss mechanism due to the bright green fluorescence emitted from the fibre when it was pumped. The thermal lensing in the tellurite glass was a property that also differed significantly from the phosphate glass test slab. As such, the upconversion and thermal properties in the tellurite glass are considered in more detail in Sections 5.2.4.1 and 5.2.4.2, respectively.

5.2.1 Laser setup modelling and results

Following the steady state threshold calculations presented previously in this chapter, an understanding was gained on the threshold dependence of the pumped diameter and gain medium length. In the bulk glass experiments, the thermal stress in the glass samples was minimised through pumping at a low duty cycle. The two level modelling described in the previous section (Section 5.1) was modified to include the temporal filling of the laser level. This allowed for the determination of a pulse duration after which near steady state energy level populations were reached.

Prior to the bulk glass laser experiments, modelling was also performed on the pump configuration and on the cavity mode diameter of a free space laser cavity. These allowed the designing of a pump configuration that minimised the laser threshold. The cavity mode diameter was modelled as a function of cavity length to ensure there was a full overlap between the resonator mode and the pumped volume.

This section concludes with the laser setup used in the bulk glass laser experiments reported in Sections 5.2.2 and 5.2.3.

5.2.1.1 Modelling of QCW pumping for bulk glass experiments

As stated previously (Section 4.3) when focusing greater than 4W of 980nm pump light through the higher concentration samples the glass samples began to melt. To reduce the thermal load on the glass, the decision was made to pulse the pump diodes in the bulk glass laser experiments. The CW model was therefore modified to include the temporal filling of the laser level which gave an understanding of the time taken to reach a steady state population. Modelling of the filling of the two energy level system was used to determine the duration that the pump needed to be on in order to excite sufficient ions in the glass. This modelling was also used to calculate the energy level populations, this time including ground state depletion (which is not included in the CW model that used Equation (33)).

The equations used to calculate the population inversion and from that the gain are given in Equations (34) to (36),

$$\frac{dN_1}{dt} = P_{in}\left(1 - e^{-\sigma_{12}\,(N-N_1)\,l}\right)\frac{1}{h\nu}\frac{1}{V} - \frac{N_1}{\tau} \quad \textbf{(34)}$$

$$\Delta N = 2N_1 - N \quad \textbf{(35)}$$

$$G = e^{2\,\sigma_{21}\,\Delta N\,l} \quad \textbf{(36)}$$

where the excited state population is N_1. P_{in} is the input pump power, σ_{12} and σ_{21} are the absorption and emission cross-sections, respectively, N is the erbium III concentration, $h\nu$ is the photon energy of the pump photons, V is the pumped volume, τ is the lifetime of the $^4I_{13/2}$ energy level, ΔN is the inverted population, l is the gain medium length and G is the maximum achievable gain. Matlab was used to re-calculate N_1 after a short time interval of excitation based on the previous energy level populations. The excited state and ground state populations can therefore be calculated as a function of time. In Equation (36), the emission cross-section was taken as its peak value of 7.7×10^{-20} cm^2.

The equations used in this modelling include ground state depletion as the available ground state population is recalculated for each of the iterative steps when calculating the population in the excited energy level.

Figure 78 (a) illustrates the excited state population for a range of pump powers given a concentration of 5×10^{20} ions/cm^3 and a pumped diameter and length of 0.25 and 2mm, respectively. These values are comparable to the characteristics of the bulk glass samples and the setup used in the laser experiments covered within this chapter. This plot indicates that population inversion would be reached with 10W of pump power provided the glass was pumped for a duration longer than 4ms. Figure 78 (b) is a plot of the available gain calculated from the population inversion. This plot also demonstrates that threshold can be reached with 10W of pump power. It can also be seen that the available gain is not significantly above 1. When using the bulk glass samples in the laser experiments, the cavity losses would need to be minimised if the laser gain is to remain above 1.

From Figure 78 it can be seen that the excited state population has almost reached its steady state population after 10ms of excitation. In the bulk glass experiments, the pumping cycle, therefore, had a pump duration of 10ms and a frequency of 10Hz.

The calculated threshold using this model (10W) was larger than that calculated using the two level threshold equation (Equation (33)) which for the same input parameters calculated a threshold of 6.4W. This difference was due to the inclusion of the ground state population into the model. A reduction in the ground state population would have resulted in reduced absorption of the pump and a higher pump power was therefore needed to achieve population inversion.

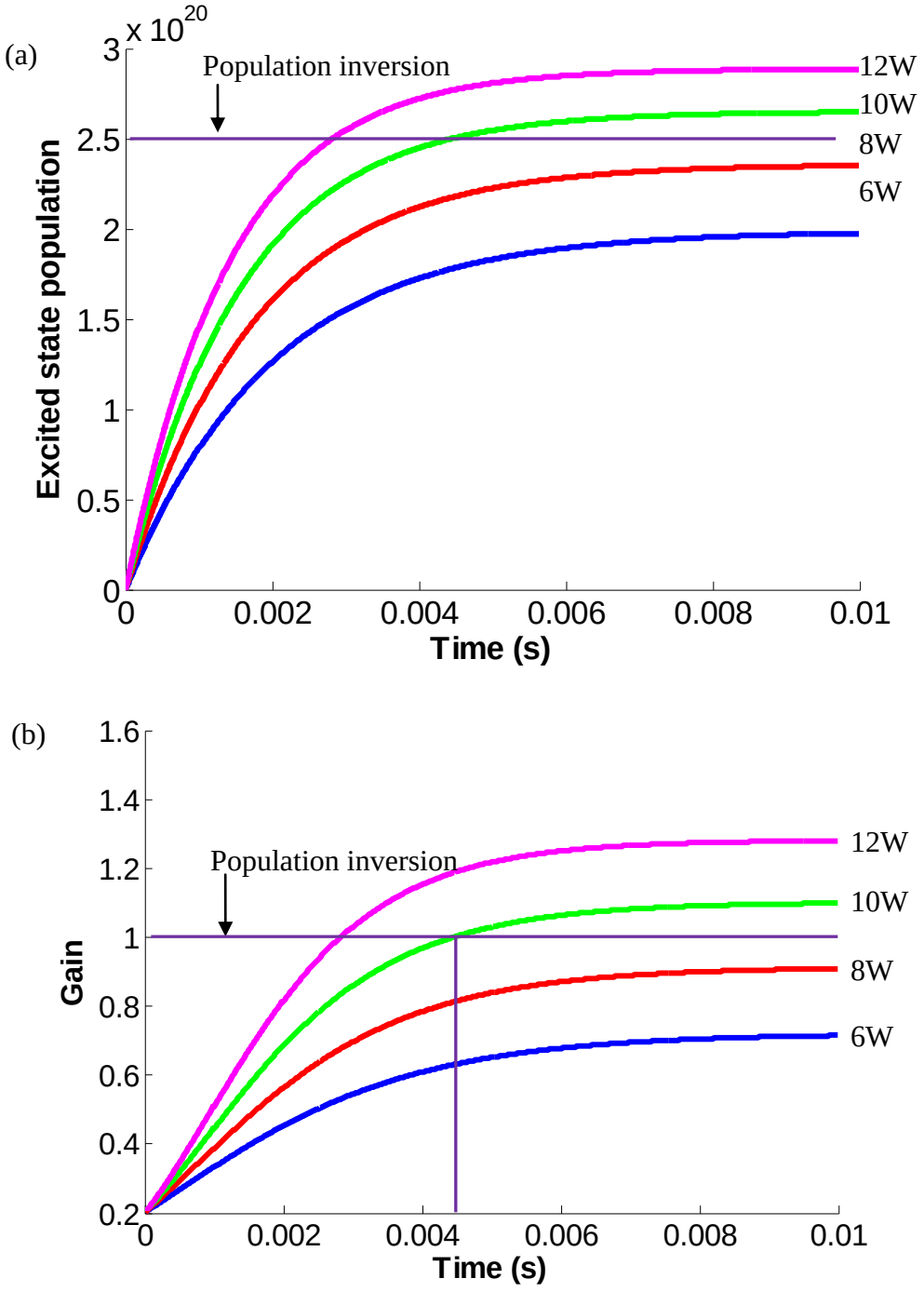

Figure 78: Plots of the predictions for the filling (a) and gain (b) of the 1.5μm energy level as a function of time for a range on incident pump powers. The modelling used a concentration of 5 × 10^{20} ions/cm^3 and a pumped diameter and length of 0.25 and 2mm, respectively.

5.2.1.2 Pump configuration

Modelling of the pump configuration was used to calculate the location of the pump focus and pump volume within the bulk glass samples.

A ray tracing model was written in Matlab and used ABCD matrices to track the pump beam from the output of the pump patch fibre and through the glass sample. The aspheric lenses used to collimate and re-focus the pump beam were approximated by thin lenses. The multimode pump was emitted from a fibre with a 200µm core diameter and a NA of 0.22. The model therefore calculated the propagation of rays emitted across the output of the patch fibre emitted at a range of angles up to 12.7º. This divergence angle corresponds to the NA of 0.22.

The increase in the focal distance due to passing through the dichroic was also incorporated into the model.

Figure 79 illustrates the output of the ray tracing model when 1:1 imaging the output of the pump fibre through the glass sample using two 20mm focal length lenses. These 20mm focal length lenses had large diameters to capture the entire diverging pump light from the patch fibre. In this figure, different scales are used for the x and y axes which exaggerates the divergence from the pump fibre and the re-focussing by the second lens.

Since the pump beam is focussed to achieve the desired small diameter, it therefore varied in diameter through the bulk glass slabs. The threshold of a bulk glass laser was re-calculated using the average pump beam diameter across the glass slab thickness and the model was used to optimise the pumping configuration to minimise the average pump diameter across this length. If the focus location is shifted from the centre of the glass sample, the pump volume is increased.

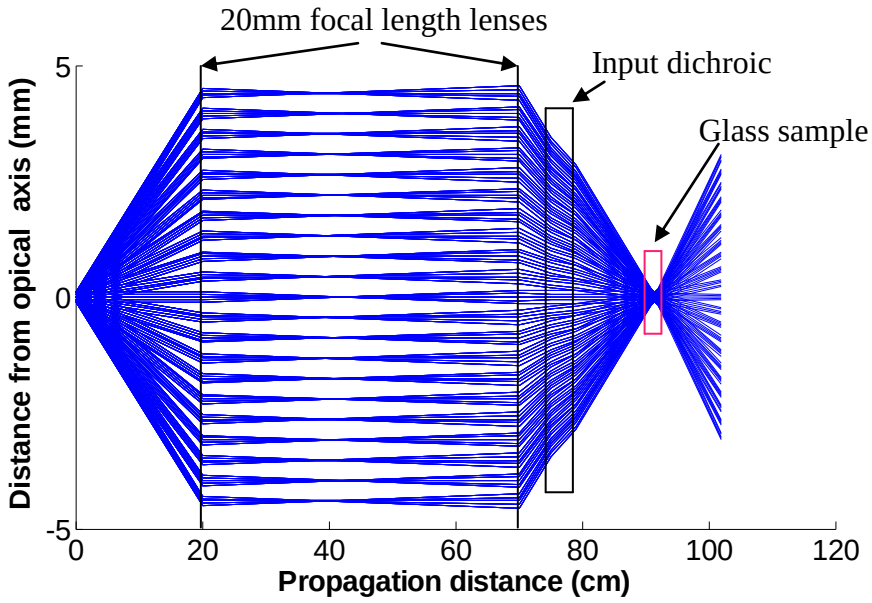

Figure 79: Ray tracing of the output from the multimode pump source used to determine the optimum pump configuration and the location of the focus of the pump.

When 1:1 imaging into the centre of a 2mm thick slab, the beam diameter would be 640µm at the edges of the slab. This corresponds to an average diameter of 420µm. When using a 1mm thick glass slab, the pump diameter at the edges of the slab is reduced to 350µm and the average diameter is reduced to 275µm.

Using a 1mm slab thickness and 275µm diameter, the threshold pump power required to achieve population inversion was calculated to be 11W. To maintain a high pump absorption, when using a 1mm slab thickness, the concentration of the glass was increased to 10×10^{20} ions/cm^3.

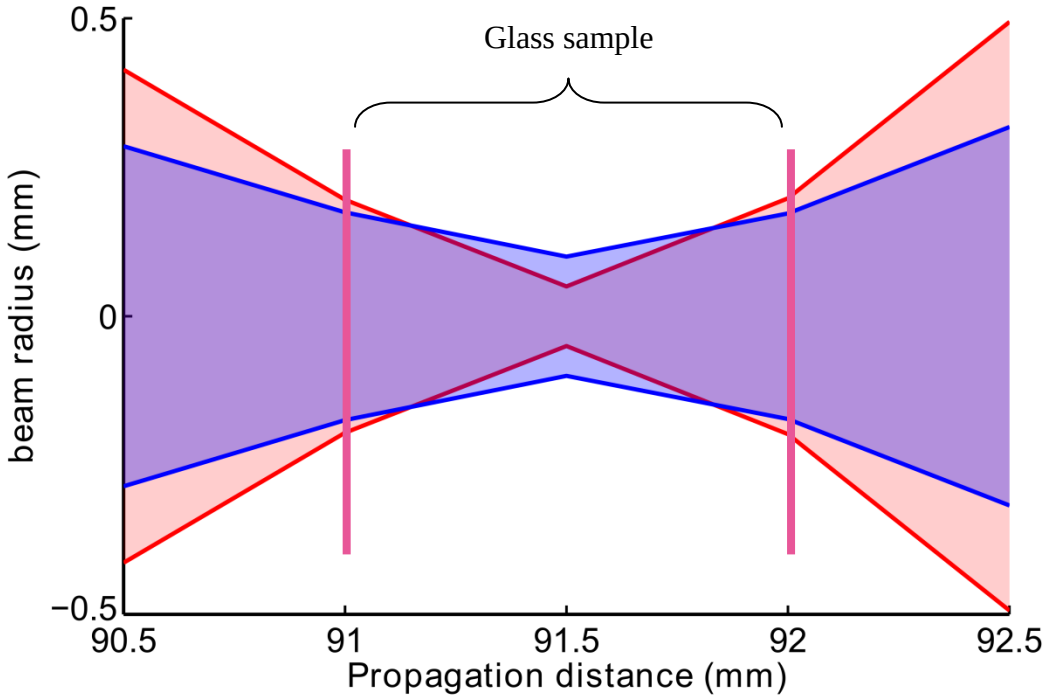

Figure 80: Plot illustrating the difference in pump beam diameters through the glass sample when collimating with a 20mm (blue) or 40mm (red) lens.

To generate a smaller focus spot size, the pump beam could be collimated and then re-focussed with a shorter focal length lens. An example is provided in Figure 80 where the focus of the pump beam through the glass sample is illustrated for 1:1 imaging using two 20mm focal length lenses and when collimating with a 40mm focal length lens and then focusing with a 20mm focal length. As was expected, the pump diameter at the focus is reduced as a larger diameter collimated beam was focussed through the glass sample. The average beam diameter was also reduced slightly when using this pump configuration. However, with the smaller diameter at the focus a much smaller cavity mode diameter would be required if it were to be contained within the pumped region.

The most desirable pump configuration was determined to be when the pump beam was imaged 1:1 into the middle of the glass slab using two equivalent focal length lenses. This pump configuration was used for the bulk glass experiments presented in this chapter.

With 11W available using the multimode pump source, a pump diameter of 275µm is used in the next section as the pump diameter within which the cavity mode could be aligned within the pumped volume.

5.2.1.3 Cavity length modelling

The cavity mode diameter was modelled as a function of cavity length to ensure where the glass slab is positioned, the diameter of the resonator mode was less than the diameter of the pumped volume. This would enable there to be a full overlap between the resonator mode and the pumped volume when they are aligned well.

A flat-curved resonator was initially used in the laser setup. In this type of resonator the waist of the cavity mode is located against the flat mirror. The cavity mode diameter was modelled as a function of the resonator length using Mathcad. The modelling used ABCD Gaussian propagation matrices for a round trip of the laser resonator and equated the initial and final beam size and divergence.

A 50mm radius of curvature 99% reflective output coupler was used for one of the cavity mirrors and the other was a flat dichroic. The dichroic was highly transparent at the pump wavelength of 974nm and highly reflective at 1.55µm. The use of the short radius of curvature mirror reduced the diameter of the cavity mode. A 50mm radius of curvature mirror and a flat mirror were therefore used in the modelling.

The output of the modelling for a cavity length of 25mm is presented in Figure 81(a). The diameter through the 1mm glass sample for this resonator length is given in Figure 81(b). The diameter was calculated to be 220µm and there was minimal variation in this diameter across the thickness of the glass sample.

The waist diameter as a function of cavity length is presented in Figure 82. From this plot it can be seen that any resonator length could be used to achieve a waist diameter that is less than the required 275µm. This meant that there were no restrictions on the cavity length in the bulk glass laser experiments.

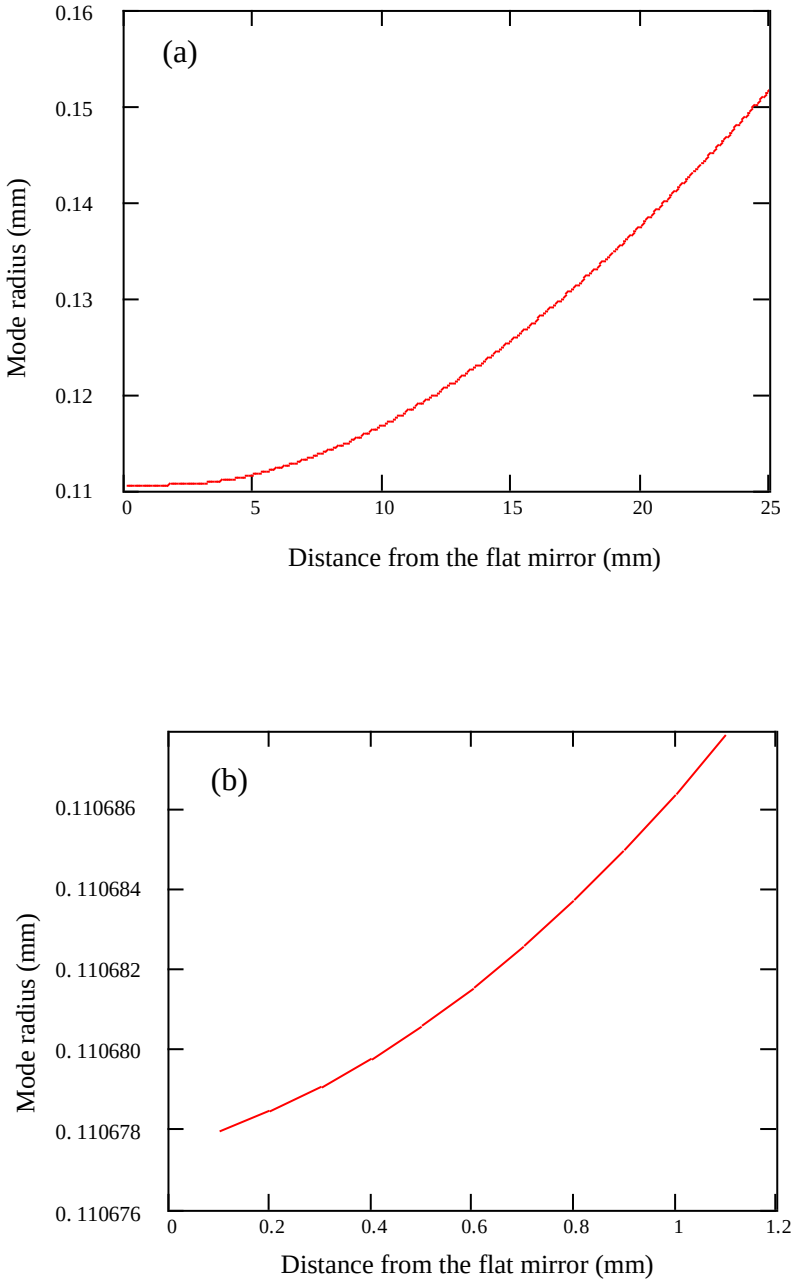

Figure 81: Plot of the cavity mode diameter for a flat-curved resonator length of 25mm (a) and the mode diameter through the glass sample positioned at the waist (b).

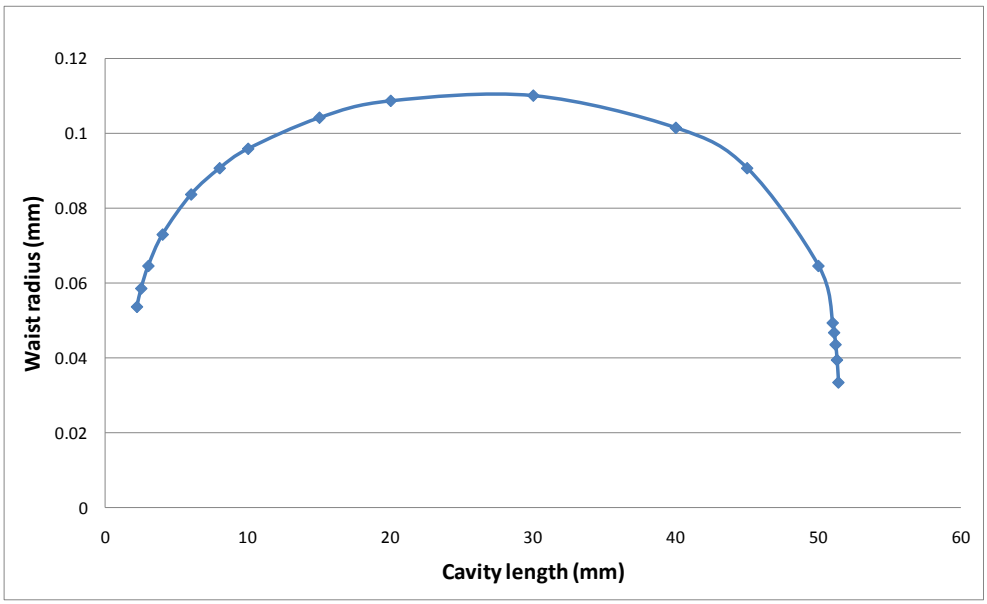

Figure 82: Plot of the cavity mode waist radius as a function of the cavity length.

Due to the simplicity of a flat-flat resonator, to maintain stability in the resonator, a slight positive thermal lens would be required in the glass slab.

5.2.1.4 Bulk glass laser setup

The pump source used for these experiments was a 15W LIMO fibre coupled laser diode. The bulk glass laser setup is illustrated in Figure 83. The pump setup used to pump the bulk glass samples consisted of two 20mm focal length lenses, the first to collimate the output of the pump fibre and the second to focus the pump light into the glass sample.

The aberrations associated with the use of spherical lenses motivated the use of large diameter aspheric lenses in the laser experiments. The measured beam diameter at the focus when using a spherical lens in this setup was double what was calculated using the ray tracing model presented in Section 5.2.1.2. The use of aspheric lenses reduced the measured beam diameter to 250µm, which was considerably closer to the diameter of the imaged 200µm patch fibre core.

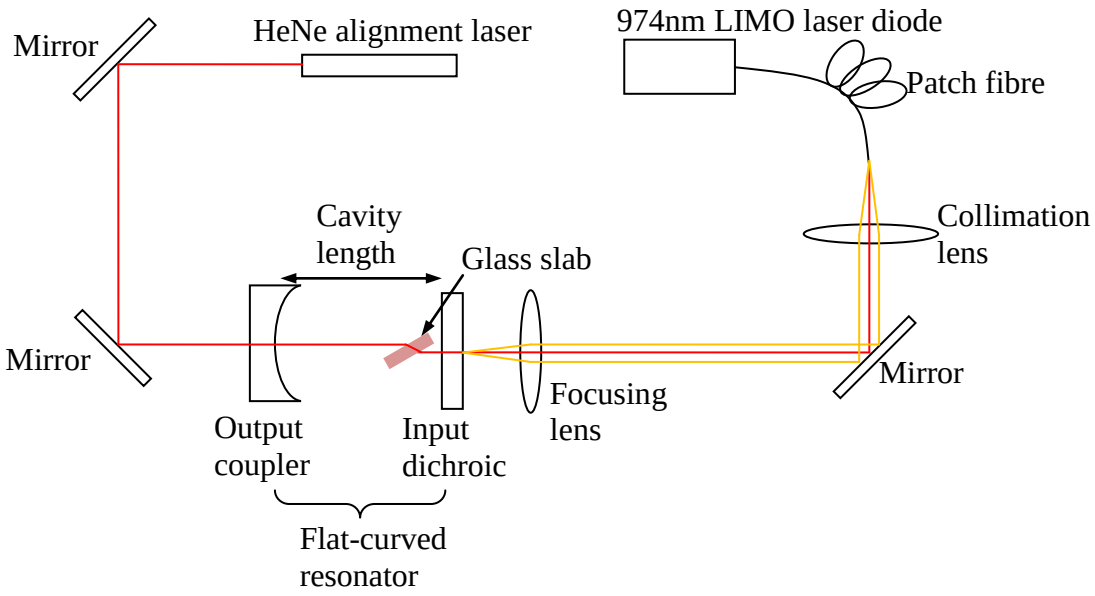

Figure 83: Setup used for the bulk glass laser experiments.

As discussed in the cavity modelling, the cavity initially consisted of a flat dichroic and a 99% reflective (at 1.5μm) 50mm radius of curvature output coupler. Prior to entering the glass sample the pump beam passed through the input dichroic of the laser resonator.

5.2.2 Free space laser testing using phosphate glass slab

To test the resonator setup for its use in a bulk tellurite system, a commercial erbium-ytterbium doped phosphate glass slab was purchased from Kigre Inc. South Carolina, USA. A phosphate glass slab was used for testing due to its well known characteristics and thermal behaviour.

The Kigre QX phosphate glass (www.kigre.com/glass.html) is said to be athermal, meaning that as the glass is heated, there is very little increase in its optical thickness. This is achieved by having a balance between the glass expansion and the glass' negative refractive index change when it is heated.

The strength of the emission cross-section for the erbium III doped phosphate glass is also comparable to that of the erbium III doped tellurite glass [190] making the

achievable gain comparable between the two glasses. The slab was 3.6mm thick and was doped with 1.69 x $10^{21}Yb^{3+}$ ions/cm^3 and 1.28 x $10^{19}Er^{3+}$ ions/cm^3. The addition of ytterbium to the glass increased the pump absorption which allowed for the doping with a lower erbium III concentration. The erbium III concentration in this sample is comparable to the fabricated fibre laser described in the next section (Section 5.3.4). The flat-curved laser cavity was constructed using the modelling from the previous section. In initial experiments, the glass slabs were positioned parallel to the input dichroic. The setup was aligned with a HeNe laser and the elements of the cavity were inserted from the pump end first ensuring the back reflection from each element propagated back through the pin holes to the HeNe laser.

With all the resonator elements roughly aligned using the HeNe laser, the slab was pumped and fine adjustments were made to the cavity alignment through the tilt of the curved output mirror. To reduce the thermal stress on the glass, the pump was run QCW with an on time of 10ms and a duty cycle of between 5 and 10Hz. The low duty cycle of the pump, meant that very slow adjustment of the cavity alignment was required.

With guidance by Dr Jim Richards, lasing was achieved with this setup using the phosphate glass slab. The threshold was measured to be 6W, which corresponded to just less than half the available pump power.

The difference in the Fresnel reflection between the phosphate glass slab (4%) and the tellurite (11%) would cause a significant increase in the cavity loss when changing to the tellurite glass slab. Although Fresnel reflection would act to reflect some of the unabsorbed pump light back into the slab, Fresnel reflection of the 1550nm laser radiation would not be coupled into the cavity mode and would be lost. To reduce this Fresnel reflection loss, the phosphate glass test slab was rotated to Brewster's angle and the laser resonator was re-aligned. When using this configuration, the output power did not increase linearly with the incident pump power. Since the slab was not cooled, this was believed to be due to thermal stress in the slab.

The cavity setup was then altered to a flat-flat cavity to test this simpler geometry. With the removal of the curved mirror, alignment of this configuration was simplified considerably. This configuration used a 98% reflective output coupler and the same input dichroic. The two mirrors were placed very close to either side of the glass slab

and the setup relied on the thermal lens that formed in the glass to reduce the diameter of the cavity mode and stabilize the laser cavity. The output power as a function of input power is provided in Figure 84.

A significantly higher output was achieved, when using this configuration, compared to the flat-curved cavity. This output could have been increased further through increasing the pump duration which was optimised for the erbium III doped tellurite glass. The lifetime of the $^4I_{13/2}$ energy level in the phosphate glass is double the measured lifetime for the tellurite glass. Despite not optimising the pump duration, slab thickness, erbium III and ytterbium III concentrations and the output coupling the slope efficiency of this laser of 9.5% was comparable to slope efficiencies, of 10.69%, reported in the literature for flat-flat CW bulk glass phosphate glass lasers [191]. The threshold of the constructed bulk phosphate glass laser was above that reported by Liu et al. [191] (2W compared to 188mW) but with only 60mW of output power generated by Liu et al. [191], the output power achieved within this research was significantly higher with over 1W of output power generated.

From these experiments it was demonstrated that of the different resonator configurations, the flat-flat configuration was the most efficient for lasing in the phosphate glass samples.

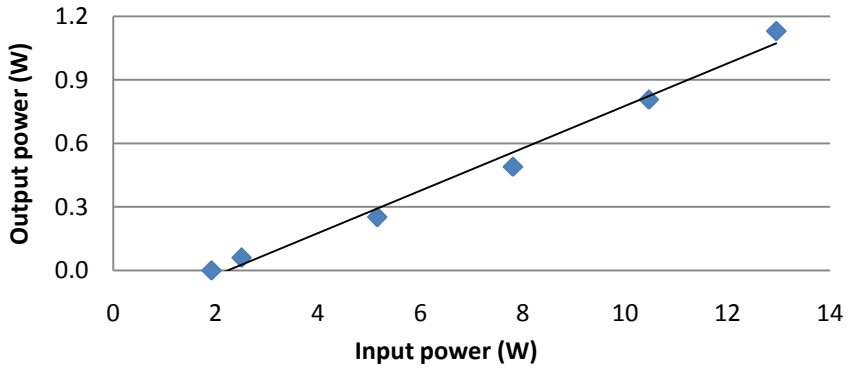

Figure 84: Output power vs input power for the free space bulk Kigre QX phosphate glass laser.

5.2.3 Bulk tellurite laser experiments

The simple alignment and the higher efficiency of the flat-flat laser cavity, dictated that this cavity configuration was used for the bulk tellurite laser experiments.

Initial tellurite glass laser experiments used 10 x 10^{20} ions/cm^3 erbium III doped TZNL glass samples, described in Chapter 2 of this thesis, which were polished to a thickness of 1mm. Despite many attempts to get the glass to lase, threshold was not reached. For better comparison to the successful phosphate glass experiments, a new tellurite glass sample was fabricated with the same erbium III and ytterbium III concentrations as the phosphate glass and was cut and polished to the same 3.6mm thickness. A high energy transfer efficiency between the ytterbium III in tellurite glass has been shown previously [56, 192-194]. From literature [190] and stated previously, the emission cross-section for erbium III in the phosphate glass was approximately the same as that measured for the tellurite glass. This meant that, with the same number of excited ions, the available gain for the new slab would be comparable to that in the phosphate laser tests.

Lasing was not, however, achieved in any of the tellurite glass slabs. Due to a number of similar properties between the phosphate glass and tellurite glass, the reasons for the difference in lasing capability could be narrowed to a few of the tellurite glass properties which differed. The differences between the phosphate glass slab and the tellurite glass include the following;

- the increased amount of green, $^4S_{3/2}$ to $^4I_{15/2}$ (see Figure 2), fluorescence observed when using the tellurite glass slab (Section 5.2.4),
- the increase in the losses due to Fresnel reflection (from 4% to 11%) of the laser radiation within the cavity, associated with the higher refractive index of the tellurite glass (~2 compared to ~1.5 for the phosphate glass),
- the tellurite glass' different thermal properties including its thermal expansion coefficient and refractive index dependence on temperature, which result in a difference in the temperature dependence of the glass' optical thickness ($16\times10^{-6}K^{-1}$ for tellurite glass compared to $2.1\times10^{-6}K^{-1}$ for the Kigre QX glass),

- an increase in scattering from the surfaces of the tellurite slab due to limitations to the polish quality because of the softness of the tellurite glass (surface scratches were observable on the polished tellurite samples),
- the lower phonon energy of the tellurite glass causing more radiative decay from the energy levels above the laser level. The higher phonon energies of the phosphate glass resulted in the rapid thermal decay of any upconverted ions across the smaller energy gaps until they reached the larger energy gap of the laser transition.
- a different energy transfer efficiency between the ytterbium III and the erbium III [190, 193]
- and the shorter lifetime of the $^4I_{13/2}$ energy level in the tellurite glass.

See Section 5.2.4 for more detail.

5.2.4 Bulk glass experimental outcomes

By looking into the differences between the phosphate glass and the tellurite glass presented in the previous section, the relevance of each to a fibre laser system was considered. In a fibre system, the losses caused by Fresnel reflection, surface roughness are not relevant. Since the laser mode is determined by the fibre geometry, thermal distortion of the laser mode would also be less of a loss mechanism in a fibre laser system. Due to the longer absorption length available when using a fibre, ytterbium III is not required to achieve sufficient pump absorption so the energy transfer between the erbium III and ytterbium III in the glass does not apply in the fibre case. As such, only the increased upconversion in the tellurite glass (described in Section 5.2.4.1) and the different temperature coefficient (defined and described in Section 5.2.4.2) of the tellurite glass were studied in more detail.

5.2.4.1 Upconversion experiments

The amount of upconversion in the tellurite glass was investigated experimentally. The amount of green fluorescence (emitted from the $^4S_{3/2}$ energy level) was measured as a function of the incident pump power and the concentration of erbium III in the TZNL

glass sample. The amount of fluorescence emitted from the $^4I_{13/2}$ energy level was also measured to see if there was quenching of this level due to upconversion.

Initial experiments were performed using CW excitation. When pumping at higher intensities, the heating up of the diode caused a shift in its emission wavelength of up to 5nm. This wavelength shift caused a reduction in the pump absorption for the higher pump powers and a roll off in the fluorescence intensity from all of the erbium III emission bands. The measurements were repeated QCW and it was found that there was reduced roll off in the fluorescence intensity when increasing the pump power. The two energy levels considered were the $^4S_{3/2}$, green (545nm), and $^4I_{13/2}$, 1550nm (IR), energy levels.

The pump power dependence of the fluorescence intensity from the $^4I_{13/2}$ energy level is illustrated in Figure 85 for a TZNL sample doped with 2 x 10^{20} ions/cm^3. This concentration was chosen over the lower concentration samples as there is more upconversion. Further for the higher concentration samples, the glass melted when exposed to comparatively low CW pump powers (>4W) or cracked during the pulsed measurements for powers >9W when using a frequency of 2Hz and a duty cycle of 2%.

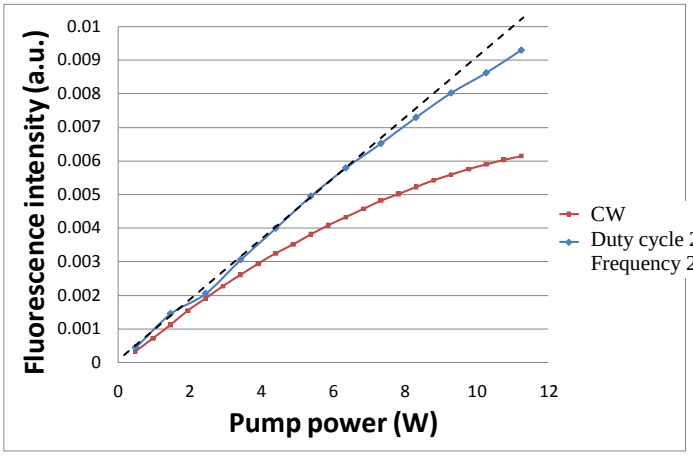

Figure 85: Increase in the amount of 1550nm fluorescence with incident pump power for a TZNL glass sample doped with 2×10^{20} ions/cm^3. The blue dashed line is linear and plotted for comparison.

When pulsing the laser diode, the average power was reduced considerably to 2% of the CW power. As such the air cooling of the laser diode did not have to dissipate as

much heat and the diode was able to be maintained at a constant temperature throughout the experiment. With better cooling of the laser diode a linear pump power dependence of the fluorescence intensity would be expected. These measurements demonstrated that there was not significant bleaching of the $^4I_{13/2}$ energy level for these erbium III concentrations and pump intensities. The significantly brighter green fluorescence observed when using the tellurite glass was believed to be caused by excited state absorption (ESA) which decayed radiatively due to the low phonon energy of the tellurite glass. In the phosphate glass, the higher phonon energy resulted in the non-radiative decay from the $^4S_{3/2}$ energy level and there was less green fluorescence emitted.

5.2.4.2 Thermal behaviour

Bleaching of the $^4I_{13/2}$ energy level was not observed in the upconversion experiments in the previous section. The thermal behaviour of the tellurite glass, which includes any changes to the laser level emission properties (emission spectra and lifetime) and the thermal lensing that would occur in the glass when it is pumped, was therefore believed to be the reason why threshold was not reached and no laser activity was observed in the bulk tellurite laser.

The temperature dependence of the emission spectra was presented in Section 4.3 and Figure 74 is reproduced as Figure 86. From this plot the fluorescence spectra was unchanged with increasing pump power and hence glass temperature.

The temperature dependence of the $^4I_{13/2}$ energy level lifetime was studied by measuring the lifetime using a short and a long duty cycle pump source. This measurement used the same 12W LIMO multimode pump that was used in the bulk glass laser experiments and its pulse duration and duty cycle was controlled electronically. The lifetime of the (1×10^{20} ions/cm^3) doped glass was measured at a low duty cycle (5%) where there would have been little heating of the glass and at a high duty cycle (95%). The temperature of the glass was expected to be significantly higher when pumped at this higher duty cycle. This was evident through the melting of the glass, which occurs at temperatures above 600ºC, during the higher duty cycle measurements on the higher concentration samples. The fluorescence intensity decay

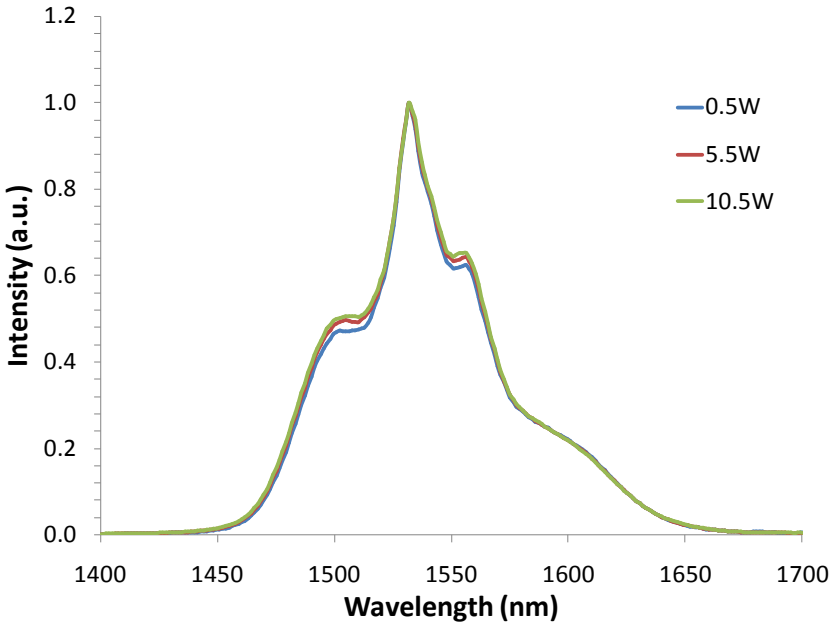

Figure 86: Fluorescence emission spectra for varying pump powers of a 0.5 x 10^{20} ions/cm^3 doped sample, reproduced from Figure 74 with fewer pump intensities plotted.

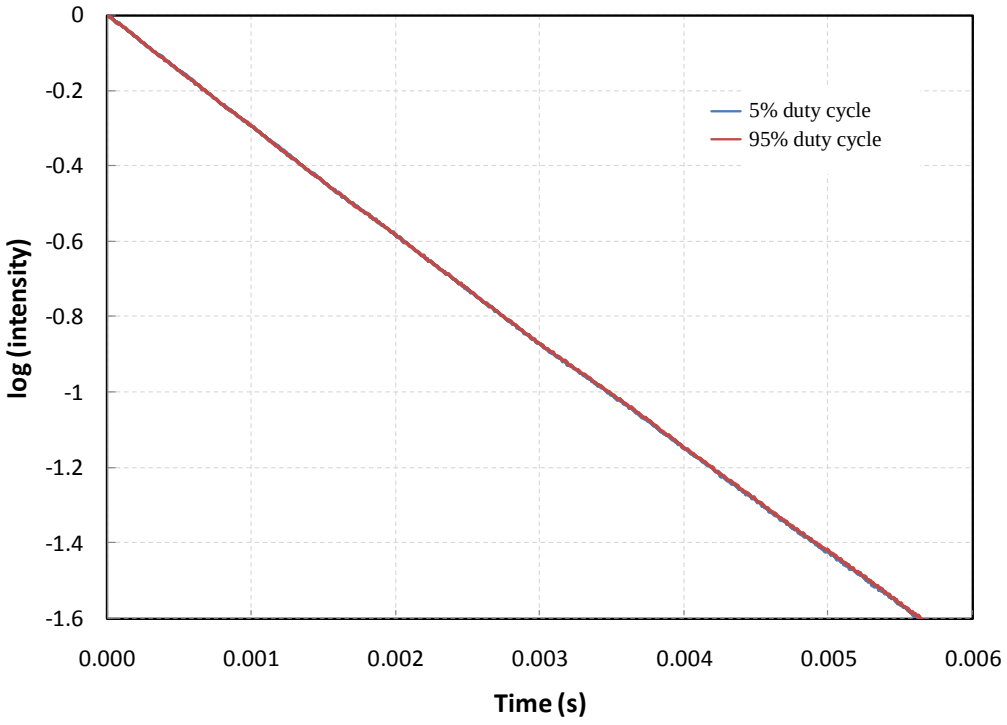

Figure 87: Log of the intensity decay when pumped at a 5% (blue) and 95% (red) duty cycle. In both cases the erbium III was exposed to the pump for 10ms.

measured for the samples at the two different duty cycles are presented in Figure 87 were it can be seen that the lifetimes were within experimental error of each other. This implied that there was no thermal quenching of the laser level lifetime due to the heating of the glass.

The thermal lensing that occurred in the glass when it was pumped was investigated. If a significant thermal lens was formed in the tellurite glass slab, the laser cavity would become unstable and not be able to support a laser mode. When using the phosphate glass in the flat-flat cavity configuration, a small positive thermal lens was required to stabilize the laser cavity and reduce the cavity mode diameter. The thermal expansion and thermally induced change in refractive index can be found in literature for both the Kigre QX phosphate glass [195] and the tellurite glass [196-198].

A prediction of the temperature coefficient of the optical path length change (ds/dT) for tellurite glass, silica [199], the ZBLAN fluoride based glass [200] and the QX Kigre phosphate glass [195] are presented in Table 9. From these values the very high sensitivity of the tellurite glass' optical thickness to the temperature is evident. From this table the relatively athermal nature of the phosphate glass is clear from the very low temperature sensitivity. The value for tellurite glass given in this table is an average of the values corresponding to different tellurite glass compositions found from literature [196-198]. It was assumed that the optical path length change for the TZN and TZNL glasses would lie around this value.

Table 9: Temperature coefficients for the optical path length change when the glasses are heated.

Glass type	Temperature coefficient of the optical path length change: $(ds/dT) \times 10^{-6}K^{-1} \pm 10\%$
Silica [199]	9.6
QX Kigre phosphate glass [195]	2.1
ZBLAN [200]	-5.9
Tellurite [196-198]	16

From the optical path length change, the focal length of the thermal lens that forms in the glass when it is pumped can be explained via Equation (37) [201].

$$f_{th} = \frac{1}{l}\frac{K}{Q}\left(\frac{ds}{dT}\right)^{-1} \quad \textbf{(37)}$$

In Equation (37) f_{th} (cm) is the focal length of the thermal lens, l (cm) is the slab thickness, K (W cm^{-1} K^{-1}) is the thermal conductivity, Q (W cm^{-3}) is the heat deposited per unit volume into the slab and ds/dT is the temperature coefficient of the optical path length change as defined in Equation (38) [195-198].

$$\frac{ds}{dT} = \frac{dn}{dT} + \alpha(n-1)(1+\nu) + \frac{\alpha}{4}n^3E(B_{\perp} + B_{//}) \quad \textbf{(38)}$$

In this equation, dn/dT is the change in the glass' refractive index with temperature, α is the thermal expansion coefficient, n is the glass refractive index, ν is the Poisson ratio, E is the Young modulus and $B_{\perp}$ and $B_{//}$ are the stress optic coefficients perpendicular and parallel to the polarisation axis of a crystal.

Using l = 0.36mm, which corresponds to the slab thickness used in the bulk glass laser experiments, K = 8×10^{-3} for tellurite glass [198] and 10.1×10^{-3} for the phosphate glass [195] and the values of ds/dT provided in Table 9, the focal lengths as a function of the heat deposited into the two glass slabs are calculated through Equations (39) and (40).

$$f_{th} = \frac{1.4\times10^3}{Q} \quad \textbf{(39)}$$

$$f_{th} = \frac{1.3\times10^4}{Q} \quad \textbf{(40)}$$

The 15W of pump power that was available in the bulk glass laser experiments was focussed down to a 250μm diameter. Considering the quantum efficiency of 63% for the 1.5μm laser transition, when pumped at 980nm, and the pump volume, the Q for the bulk glass experiments is calculated to be 2.4×10^4 Wcm^{-3}. Using Equations (39) and (40),

gives the focal lengths of 0.5mm and 5mm for the tellurite and phosphate glass slabs, respectively.

When determining what impact the thermal lens would have on the resonator stability, the flat-flat resonator that surrounds the glass slab containing the thermal lens can be represented by a flat-curved resonator with a radius of curvature of the curved mirror equal to twice the thermal lens focal length [201]. The requirement for a stable resonator is given by Equation (41).

$$0 \leq \left(1 - \frac{l}{R1}\right)\left(1 - \frac{l}{R2}\right) \geq 1 \quad \textbf{(41)}$$

From Equation (41) where l is the resonator length and $R1$ and $R2$ are the radii of curvature of the two resonator mirrors ($R1 = \infty$ and $R2 = 2f_{th}$) it can be determined that a stable resonator requires the thermal lens focal length to be longer than the cavity length. The flat mirrors used in the bulk glass laser were placed against the edges of the glass slabs giving a resonator length of 3.6mm.

The inability to lase in the tellurite glass could therefore be explained by the thermal lens that formed in the glass when it was pumped since the thermal lens had a focal length of 0.5mm which is significantly shorter than the 3.6mm resonator length. The resonator would therefore have been unstable. The thermal lens that formed in the phosphate glass was less significant at 5mm which is longer than the cavity length. This explains why lasing was achieved in this glass slab.

5.3 Fibre laser setup, modelling and results

The microstructured tellurite fibre laser developed within this research used the wagon wheel fibre that was fabricated within the fibre development described in Chapter 3 using the TZNL host glass composition presented in Section 2.1. For reasons indicated earlier, including the increased loss due to OH absorption at 2.7μm and the short lifetime of the $^4I_{11/2}$ energy level when compared to the $^4I_{13/2}$ energy level lifetime, the tellurite fibre laser development focussed on the $^4I_{13/2}$ to $^4I_{15/2}$ erbium III transition lasing at 1.5μm.

Prior to the fabrication of the wagon wheel fibre, two level QCW modelling, described in the previous section (Section 5.2.1.1), was used to ascertain the optimum fibre length given an erbium III concentration. This was used to determine the erbium III concentration to be added to the fabricated wagon wheel fibre. This is discussed in Section 5.3.1.

With only three struts suspending the core of the fibre, heat dissipation from the gain region is potentially restricted. Both an analytical and a finite element modelling (FEM) were used to model the temperature profile of the fibre as it dissipates heat from its core (Section 5.3.2).

In Section 5.3.3, the fibre laser setup is described and in Section 5.3.4 the fibre laser results are presented. These results are compared to a range of three energy level models, one of which included the bottlenecking of excited ions in the energy levels above the laser transition which limited the output power achieved from the laser system and the other included the distributive loss of the along the fibre in its prediction of the laser performance.

This subsection concludes with a future outlook where ways to improve on the laser output and efficiency are presented.

5.3.1 Determining the optimal dopant concentration

The QCW two level model, discussed in Section 5.2.1.1, was used to determine an appropriate erbium III concentration for the fibre laser development. As with Figure 78, Figure 88 is a plot of the excited state population and the available gain ((a) and (b), respectively) using the QCW modelling, however this time, the geometry and concentration of the fabricated wagon wheel fibre (described in Section 3.4.3) were used as input parameters into the model. This corresponds to a concentration of 0.1×10^{20} ions/cm^3 and a core diameter of 2.5μm. The achievable gain was calculated for a range of fibre lengths assuming a coupled pump power of 30mW (which corresponds to 10% coupling efficiency from a 300mW single mode source). From this plot, it can be seen that the gain, when using the fibre of length 75cm, was significantly higher than the rest of the lengths plotted. The optimal length was calculated more precisely to be

approximately 70cm. This length of fibre would correspond to just under triple the absorption length and a pump absorption of approximately 95%.

The optimum gain medium length decreased proportionally with concentration increase as the optimum length remained at triple the absorption length. Since, within the

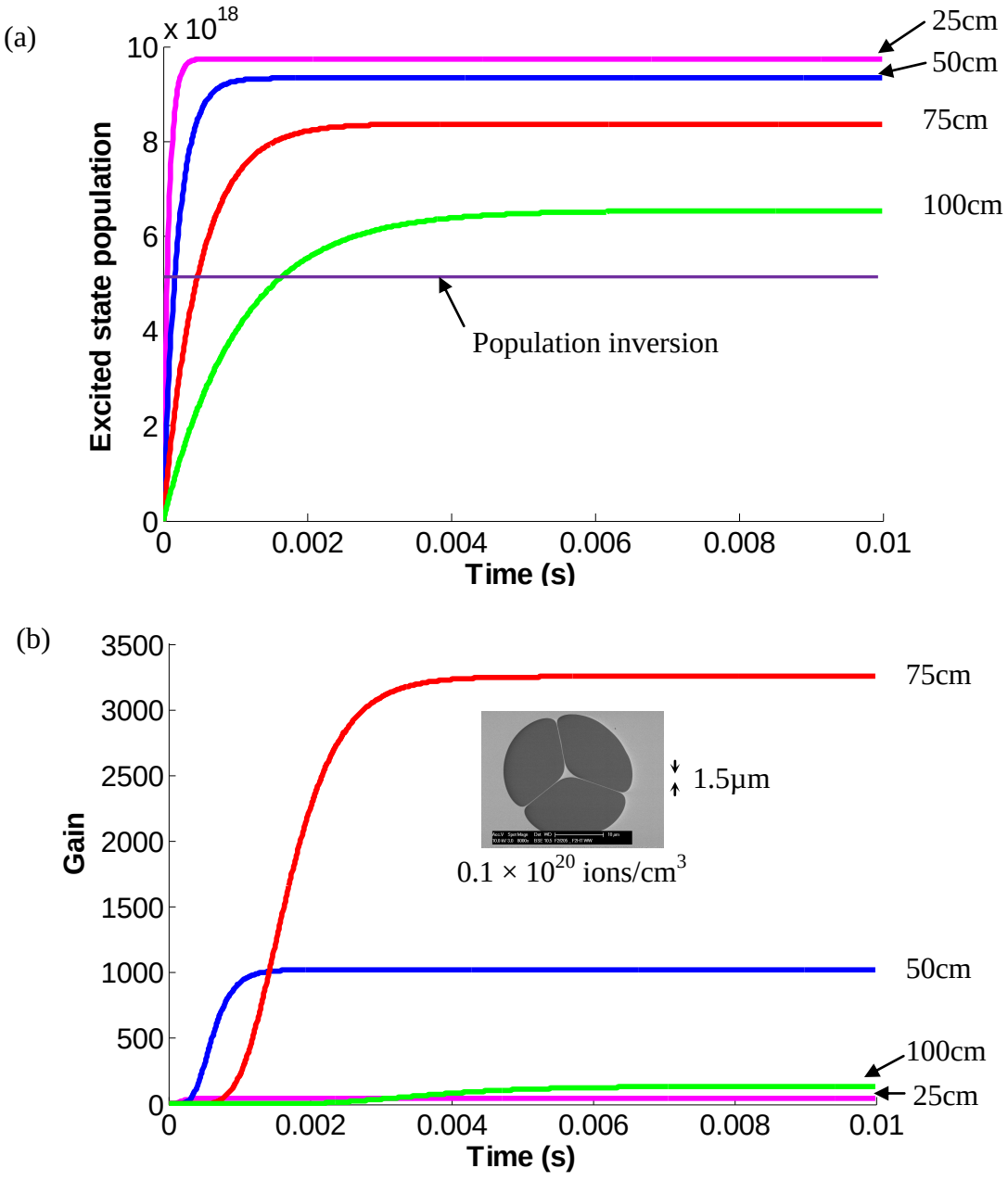

Figure 88: Modelled excited state population (a) and gain (b) for the fabricated wagon wheel fibre (cross-section provided as the inset) as a function of pump duration for various fibre lengths. The TZNL glass used was doped with 0.1 × 10^{20} ions/cm^3 erbium III.

concentration range studied, all the spectroscopic properties of the erbium III doped tellurite were found to be independent of the erbium III concentration, the concentration used in this fibre was chosen based upon what was believed to be a convenient fibre length to handle. A fibre length of 70cm, which corresponded to the optimum length calculated for the 0.1×10^{20} ions/cm^3 erbium III doped fibre, was determined to be suitable. A fibre of this length is manageable and the fibre loss was not believed to be significant.

Using this model, the threshold for the fibre laser system was calculated to be 2.0 and 3.5mW for a 1 and 2.2m fibre lengths, respectively.

Figure 88 also illustrates the significantly higher available gain when using the fibre when compared to the bulk glass plots presented in Figure 78. Despite the lower inversion population when using the fibre, the increased gain is due to the considerably longer gain medium length.

5.3.2 Thermal modelling of the wagon wheel fibre

The ability of the wagon wheel fibre to dissipate heat from its core was studied analytically using the approach presented by Limpert et al. [100]. The structure was approximated by a cylindrical core (diameter 2.5μm) surrounded by a cylindrical air region containing three glass bridges (thickness of 100nm and length 10μm) and then surrounded by a glass jacket, with outer diameter of 250μm (this is a reasonable approximation for the fibre cross-section pictured in Figure 58). The different regions of the wagon wheel fibre that are referred to in the thermal modelling are illustrated in Figure 89.

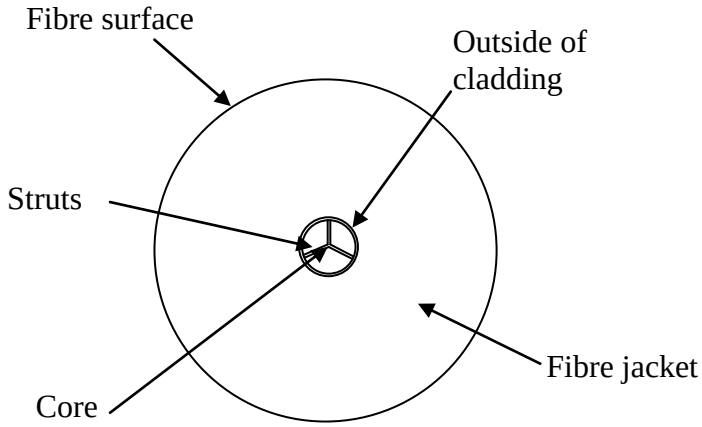

Figure 89: Illustration of the wagon wheel fibre defining the regions and surfaces refered to in the thermal modeling.

The thermal analysis starts from the outside of the fibre where the heat is transferred to the surrounding air either convectively or radiatively. The convective heat transfer is given by:

$$d\Phi = \alpha_k \Delta T dA \tag{42}$$

where Φ is the heat transfer. The heat transition coefficient α_k is defined as

$$\alpha_k = C_1 \left(\frac{\Delta T}{d}\right)^{1/4}, \tag{43}$$

ΔT is the temperature difference, dA is the unit area element, d is the fibre diameter and C_1 is a temperature dependant coefficient equal to 1.38 $W/m^{1.75}K^{1.25}$ when the fibre is surrounded by room temperature air. The C_1 parameter decreases with increasing temperature.

The radiative heat transfer is given by:

$$d\Phi = \sigma \varepsilon dA(T_1^4 - T_2^4) \tag{44}$$

where σ is the Stefan-Boltzmann constant, T_1 - T_2 is the temperature difference and ε is the glass emissivity assumed to be 0.9, which is a commonly used value for silica glass [202]. This value, however, could differ for tellurite glass.

In the region of glass between the cladding and the outside of the fibre, the dominant heat transfer mechanism is through conduction where the heat transfer through a hollow cylinder is given by:

$$d\Phi = k\pi \frac{(R_2 + R_1)}{R_2 - R_1} dl\Delta T \quad \textbf{(45)}$$

where k is the thermal conductivity and R_1 and R_2 are the inner and outer radii, respectively.

Finally there is the heat dissipation across the air cladding and three glass bridges. The heat transfer through the air regions via convection and radiation are described by Equations (42) to (44) and the heat transfer through the cladding struts is calculated by:

$$d\Phi = k \frac{number\ of\ struts\ \times width\ of\ struts}{length\ of\ struts} dl\Delta T \quad \textbf{(46)}$$

The glass transition temperature for the TZNL tellurite glass was measured to be 315˚C (Section 2.4). This was used as a rough limit to the temperature the glass can reach before it begins to soften.

It was found when 8W/m of heat is dissipated from the core, the core temperature would reach 300ºC which is just below the 315ºC softening temperature. When dissipating this amount of heat from the fibre core, the temperature in the core, just outside the air cladding and at the surface of the fibre are provided in Table 10. The greatest temperature drop in the fibre is across the cladding where there is approximately 100ºC temperature difference between the core and the inside of the jacket.

The heat dissipation via each of the three processes across each of the regions is also provided in Table 10. Despite the very few, thin struts, when not including the conduction of the heat through the air in the cladding holes, conduction through these struts provided 98% of the heat transfer out of the core.

Table 10: Temperature at the core-cladding, cladding-jacket and fibre-air interfaces dissipating its limit of 8W/m (top) and 0.4W/m (bottom) of heat.

Temperature in core	Heat transfer process across cladding			Temperature outside cladding	Heat transfer across jacket			Temperature at fibre surface	Heat transfer from fibre surface		
8W/m											
299°C	Rad.	Conv.	Cond.	198°C	Rad.	Conv.	Cond.	194.4°C	Rad.	Conv.	Cond.
	0.4%	1.2%	98.4%		0%	0%	100%		26%	74%	0%
0.4W/m											
23.8°C	Rad.	Conv.	Cond.	18.7°C	Rad.	Conv.	Cond.	18.5°C	Rad.	Conv.	Cond.
	0%	0.5%	99.5%		0%	0%	100%		22%	78%	0%

These analytical calculations were compared to thermal FEM modelling in Comsol. A SEM image of a previously fabricated lead silicate fibre with a similar geometry was imported into COMSOL. If all 300mW of the available pump power was coupled into the fibre and absorbed by an 80cm fibre length a maximum heat load of 0.4W/m would need to be dissipated from the fibre core. Therefore, a heat source of 0.4W/m was added to the core of the fibre. This heat was applied to a circular region that fit within the fibre core. As illustrated in Figure 90, when this heat load is applied to the core, the thermal modelling returned the temperature profile of the core and cladding regions of the fibre. Figure 90 includes both the temperature profile when assuming there was no heat transfer through the holes in the cladding (a) and when considering the conduction through the air in the cladding (b). This comparison was undertaken to test the assumption made in the analytical modelling that the heat transfer out of the core was only radiative or via conduction through the cladding struts. As illustrated in Figure 90 (a), the temperature difference between the core and outside the cladding (when excluding the air in the structure) was calculated to be 5°C. This agrees with the analytically calculated temperature difference, between the core and outside the cladding (provided in Table 10) of 5.1°C. When including the conduction by the air in the cladding structure, the temperature difference was calculated to be approximately 3°C.

(a)

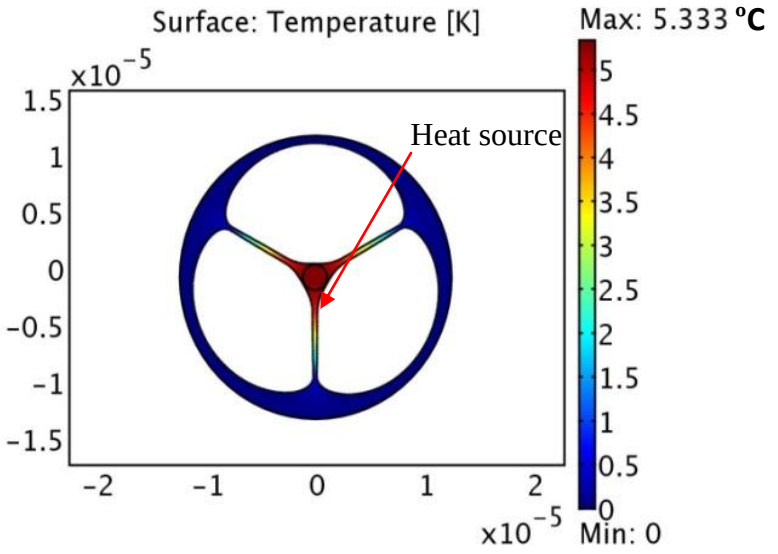

(b)

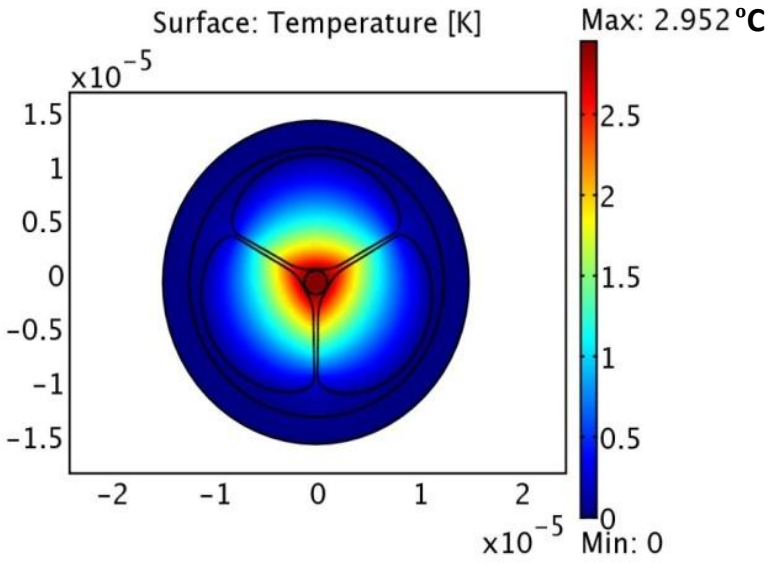

Figure 90: Temperature profile of the TZNL glass three strut fibre dissipating 0.4W/m from its core when omitting any heat transfer across the air in the cladding (a) and including the heat conduction through the cladding holes (b).

This reduction in the temperature difference indicated that due to the very few, thin struts that were used to support the core, heat transfer through the air in the cladding contributed to the heat transfer out of the fibre core.

From both the analytical and numerical FEM analyses, it was shown that when using this fibre, there will be minimal heating of the core of the fibre when it is pumped with the currently available pump diodes.

5.3.3 Fibre laser setup

The setup used for the laser system is illustrated in Figure 91. The fibre in the diagram was the wagon wheel fibre which was fabricated with a dopant concentration of 0.1×10^{20} ions/cm^3 and is pictured in Figure 58. This concentration corresponds to an absorption coefficient of 0.04cm^{-1}. The laser setup consisted of the 300mW single mode 974nm fibre coupled pump source. The pigtail fibre had a core diameter of 6μm. It was collimated using a 20mm focal length aspheric. The collimated beam was reflected off two mirrors to control the direction and alignment into a second 20mm aspheric lens. This lens focussed the pump beam through the input dichroic and onto the fibre end. The dichroic was highly transparent at the pump wavelength of 974nm and highly reflective at 1550nm. This dichroic was positioned against the input end of the fibre with its position controlled by a micron adjustment stage and monitored using a long focal length microscope. The input of the fibre was controlled using a nano-positioning stage to maximising the coupling efficiency using this pump configuration. The output of the fibre was also mounted on a stage and a microscope objective was used to image the output of the fibre onto a power meter or optical spectrum analyser.

Initial experiments incorporated a 95% reflective output coupler however the output power reached was just measureable and due to the small core of the fibre the threshold was already sufficiently low. The 95% reflective output coupler was removed and the resonator feedback was provided by the 11% Fresnel reflection from the cleaved fibre end. The output power achieved, using this higher output coupling, was greatly improved.

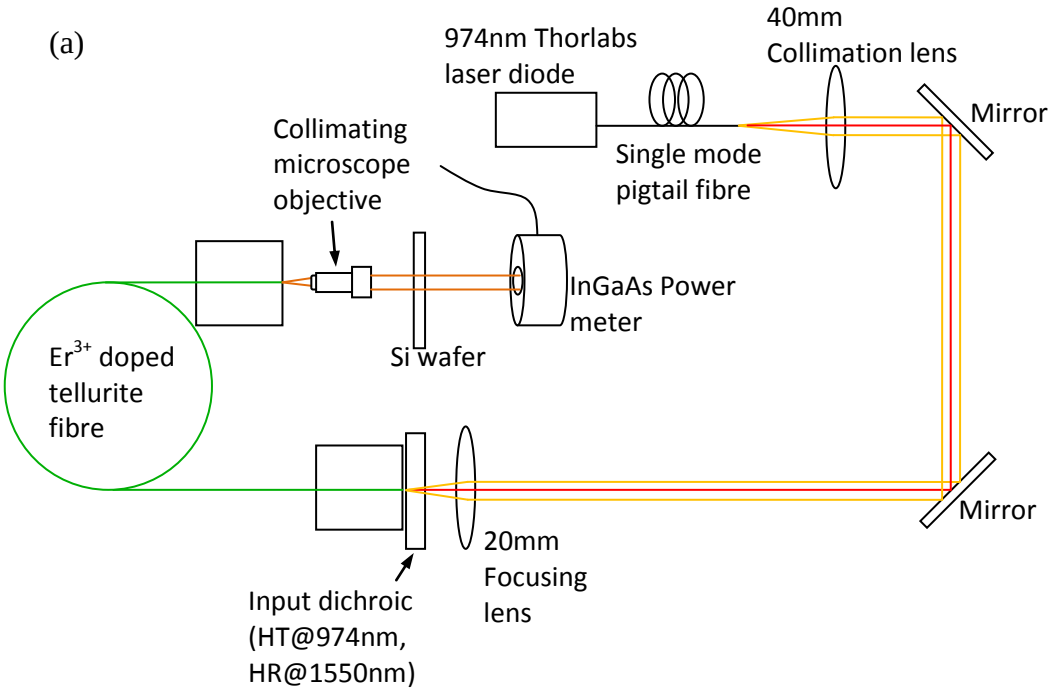

(b)

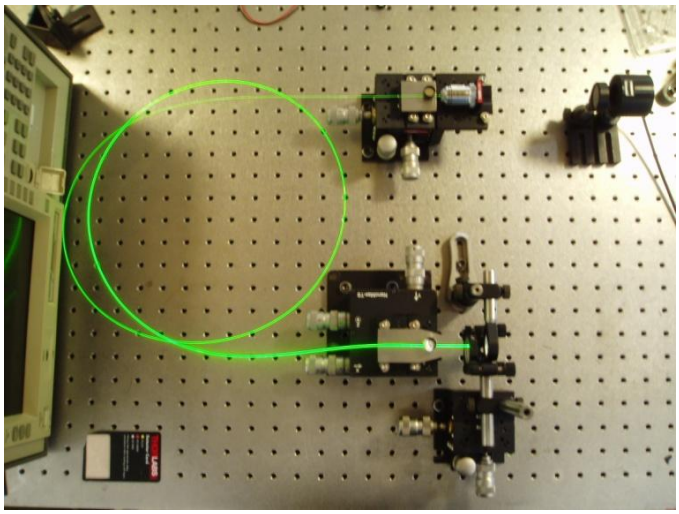

Figure 91: (a) Illustration of the fibre laser setup. (b) Photograph of the erbium III doped TZNL glass fibre laser.

5.3.4 Fibre laser results

The 1.5µm fibre laser was constructed to test the erbium III doped TZNL tellurite glass (described in Section 2.1) as a host material and wagon wheel fibre fabricated for its

lasing performance. The wagon wheel fibre used in the fibre laser was uniformly doped with 0.1×10^{20} ions/cm^3 erbium III and the details of the fibre's fabrication and cross-sectional profile are described in Section 3.4.3. This concentration corresponds to an absorption length of 25cm. For this absorption length, an optimal fibre length of 70cm, which corresponds to 95% absorption of the pump, was predicted from the modelling presented at the start of this section (Section 5.3.1). For this reason an initial fibre length of 1m was used for the first laser experiment, and the intention was to cut the fibre back to optimise its length. A maximum output power of 0.25mW was achieved using this fibre length and the output as a function of coupled pump power is provided in Figure 92.

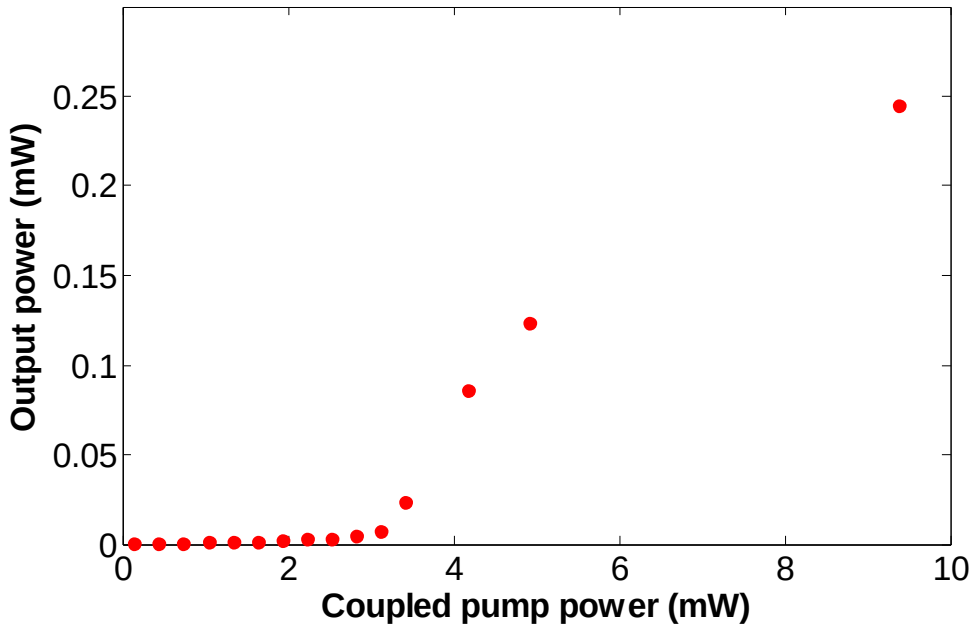

Figure 92: Measured output power from the erbium III doped TZNL glass 1m fibre laser.

The coupling efficiency was measured by measuring the transmission through a 3cm length of fibre. The pump absorption for this length of fibre was considered to be negligible due to the short fibre length and the bleaching of the erbium III that is described later in this section. This maximum coupled pump power was found to be 10mW which, corresponds to a coupling efficiency of 3.3%. The majority of this low coupling efficiency was caused by the very small core (≈1.5µm) and the significantly larger pump beam diameter (≈5µm) at the fibre tip.

The roll off in the output power for the higher coupled pump powers was believed to be caused by ground state depletion and a bottlenecking of the excited erbium III ions in the energy levels above the $^4I_{13/2}$ upper laser level.

The emission wavelength with 5mW of coupled pump power from this laser system is provided in Figure 93. The laser emission occurred at 1532nm, which corresponds to the peak of the fluorescence emission and ground state absorption spectra. Due to re-absorption of the laser emission, it was expected that the emission preferentially occurs at longer wavelengths. The lasing at 1532nm can be explained by a lack of ions in the ground state to re-absorb the emitted radiation, which agrees with the theory that the excited erbium III ions were bottlenecking in and above the pumped energy level. This bottlenecking and ground state depletion would have caused the roll-off observed in the output power at higher pump powers.

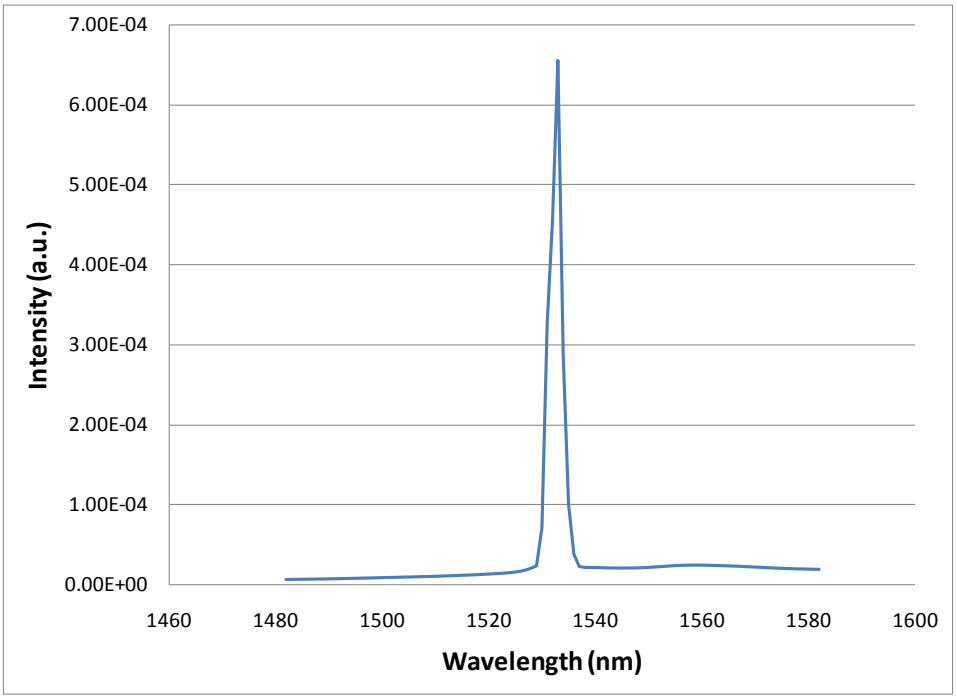

Figure 93: Spectral output from the erbium III doped TZNL glass 1m fibre laser

An analytical model was used to represent the laser behaviour. This model was based on a paper by Barnard et al. [203] and took into consideration pump bleaching caused by the previously proposed bottlenecking of the erbium III ions in and above the

pumped energy level due to their non-zero lifetimes. The lifetime of the pumped ($^4I_{11/2}$) energy level was measured to be 0.2ms (Figure 69 in Section 4.2.3).

The analytical model takes into consideration the losses at either end of the fibre, however it makes the approximation that the distributive losses along the length of the fibre are negligible. In the case of the tellurite glass fibre laser, these distributive losses would include the tellurite glass' material loss and the fibre's confinement loss.

The modelling is described in Appendix 2 and the output power was calculated for a given input power using Matlab. If the lifetime of the pumped energy level was set to zero this analysis reduces to the two level rate equation analysis. In each of the following plots the output from the two energy level analysis is plotted for comparison (red).

Figure 94 is a plot of the theoretical output for a laser constructed from a 1m length of the wagon wheel fibre. The model therefore used a concentration of 0.1×10^{20} ions/cm^3, a core diameter corresponding to the fabricated wagon wheel fibre of 2.5µm and a length of 1m. The measured output powers are also included in the plot for comparison.

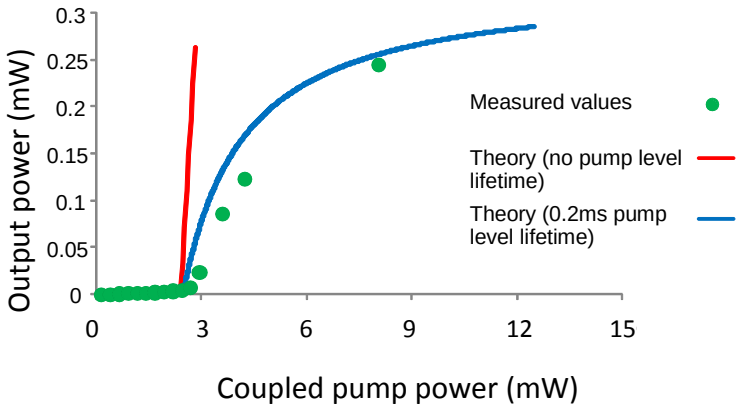

Figure 94: Plot of the output power as a function of input power with (blue) and without (red) the inclusion of pump bleaching in the calculation. The measured output powers are included (green) erbium III doped TZNL glass three strut fibre laser for comparison to the model

The saturation that was observed in the laser measurements for this fibre length is well represented by this model.

The ground state depletion associated with the observed bleaching resulted in an increase in the transmitted pump power. With the aim of increasing the pump absorption and hence increase the output power, the model was used to study the effect of increasing the fibre length. The output power as a function of input power for 1, 2, 3 and 4m fibre lengths is provided in Figure 95. Recalling that only 10mW of pump power was coupled into the fibre, 10mW is illustrated on the plot as the dotted line. It can therefore be seen that a fibre length of 3m would have the greatest output power.

For fibre lengths longer than this, threshold would not be reached with only 10mW of pump power coupled into the fibre.

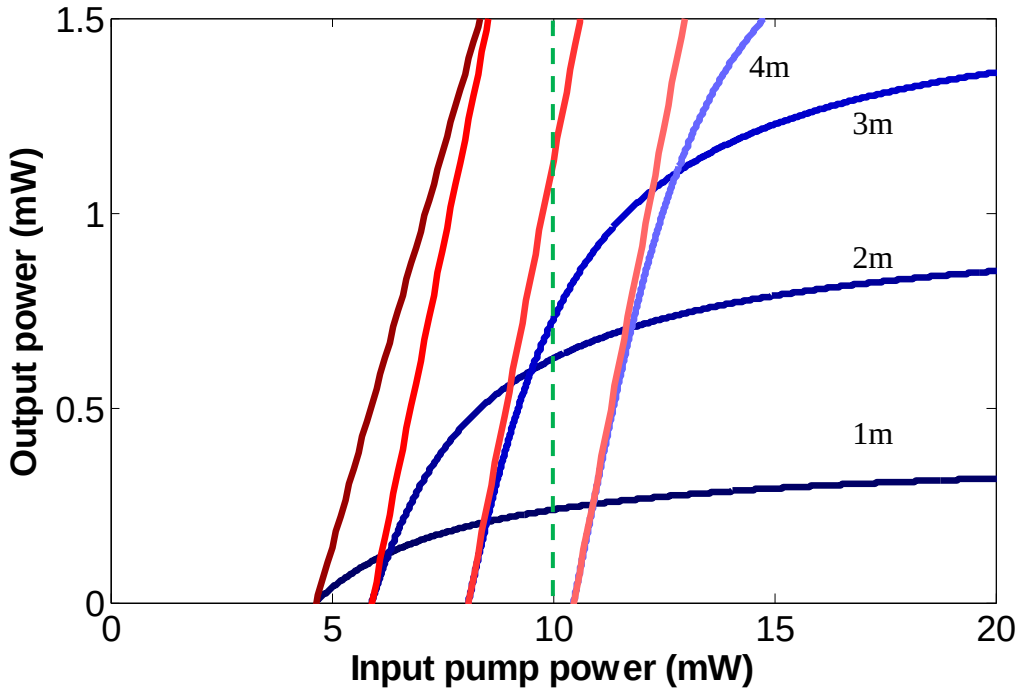

Figure 95: Plot of the output power as a function of the coupled pump power for increasing fibre length, assuming a TZNL glass host and the 0.1 × 10^{20} ions/cm^3 Er_2O_3 concentration. The predicted laser efficiency calculated using the two level rate equation analysis is plotted in brown/red and the three level analysis generated the output plotted in blue. 10mW of coupled pump power is indicated by the green dashed line.

Based on the expected improvement gained through increasing the fibre length, the fibre laser length was increased to 4m with the intention of cutting back the fibre length.

Although it was expected that threshold would not quite be reached with this fibre length, threshold was reached using the 4m fibre length but it was at the limit of the available pump power and only 0.5μW of output power was measured.

The fibre length was then shortened to 3m with the aim to reduce the threshold. The output power achieved from this length of fibre, at 0.06mW, was less than that achieved using the 1m length of fibre (0.22mW) despite being modelled as the optimum fibre length. The fibre was shortened to 2.2m. This fibre length generated a significantly higher output power with almost 1mW of output power measured. The maximum output power achieved for the four fibre lengths studied are provided in Table 11.

Table 11: Table of the output powers achieved with different lengths of fibre.

Fibre length (m)	Maximum output power achieved (mW)
1	0.22
2.2	0.95
3	0.06
4	0.0005

The output power as a function of coupled pump powers for the 2.2m fibre laser is plotted in Figure 96. For the lower laser powers, the slope efficiency of the 2.2m fibre laser was measured at 13%. This efficiency decreased at higher powers due to the bottlenecking of the excited ions above the laser level. This laser efficiency is considerably lower than the Stokes efficiency of 62%, irrespective of this, the efficiency was an improvement over the 1m fibre laser and a significant improvement on the 0.65% slope efficiency achieved by Mori et al. [34]. The improvement in laser efficiency could have been due to an improvement in the fibre loss or through some optimisation of the fibre length. In the Mori paper [34], a fibre loss of 3dB/m at 1.3μm was stated and a fibre length of 85cm was used. This loss is considerably higher than the loss of the "wagon wheel" fibre fabricated as part of this research at 1.3dB/m at 1.3μm.

Despite its improved efficiency, it was believed that the long fibre length and the loss of the fibre were responsible for the significant reduction in the laser efficiency

from the Stokes efficiency. The assumption made in the previously used theoretical model, that the fibre losses were negligible, was found to be not valid for this fibre length. A new model was used, which was based the theoretical modelling presented in Refs. [204-206]. This model used Equations (47) to (49) to calculate the inversion population from the forward and backward propagating pump and laser fields.

$$\pm\frac{dP_p^{\pm}(z)}{dz} = -\Gamma_p P_p^{\pm}(z)\left(\sigma_{ap}N + \left[\sigma_{ESA} - \left(\sigma_{ap} + \sigma_{ep}\right)\right]N_2(z)\right) - \alpha_p P_p^{\pm}(z) \quad \textbf{(47)}$$

$$\pm\frac{dP_s^{\pm}(z)}{dz} = -\Gamma_s P_s^{\pm}(z)[(\sigma_{as} + \sigma_{es})N_2(z) - \sigma_{as}N] + \Gamma_s\sigma_{es}N_2(z)P_{s0} + \alpha_s P_s^{\pm}(z) \quad \textbf{(48)}$$

$$\frac{N_2(z)}{N} = \frac{\frac{\left[P_p^{+} + P_p^{-}\right]\sigma_{ap}\Gamma_p}{h\nu_p A} + \frac{[P_s^{+} + P_s^{-}]\sigma_{as}\Gamma_s}{h\nu_s A}}{\frac{\left[P_p^{+} + P_p^{-}\right](\sigma_{ap} + \sigma_{ep})\Gamma_p}{h\nu_p A} + \frac{1}{\tau} + \frac{[P_s^{+} + P_s^{-}](\sigma_{as} + \sigma_{es})\Gamma_s}{h\nu_s A}} \quad \textbf{(49)}$$

Where z is the distance along the fibre and $P_{s0} = 2\pi c^2\Delta\lambda/\lambda^3$ is the initial spontaneous emission contribution, where c is the seed of light and $\Delta\lambda$ and λ are the linewidth and wavelength of the laser oscillation. $P_p^{\pm}$ corresponds to the pump power in the forward (+) and backward (-) directions and similarly $P_s^{\pm}$ corresponds to the signal power in the forward and backward directions. Γ_s is the overlap factor between the laser mode and the doped region, Γ_p is the fraction of the pump which interacts with the doped ions, σ_{ap} and σ_{as} are the absorption cross-sections of the pump and signal, respectively, σ_{ep} and σ_{es} are the emission cross-sections for the pump and signal wavelengths, respectively, N is the concentration and N_2 is the excited population, σ_{ESA} is the excited state absorption cross-section, h is Planck's constant, A is the cross-sectional area of the core region, ν_p and ν_s are the pump and signal frequencies and α_p and α_s are the distributive losses of the fibre at the pump and signal wavelengths.

When solving the differential equations, the boundary conditions are given by Equations (50) to (53) . These boundary conditions equate the forward and backward fields at either end of the fibre taking into consideration the output coupling fraction and the incident pump light.

$$P_s^+(0) = R_{s0}P_s^-(0) \quad \textbf{(50)}$$

$$P_s^-(L) = R_{sL}P_s^+(L) \quad \textbf{(51)}$$

$$P_p^+(0) = R_{p0}P_p^-(0) + P(0) \quad \textbf{(52)}$$

$$P_p^-(L) = R_{pL}P_p^+(L) + P(L) \quad \textbf{(53)}$$

Where R_{s0}, R_{sL}, R_{p0} and R_{pL} are the reflectivities of the mirrors for the signal and pump at z=0 and L, respectively.

The Matlab code used to solve these equations was initially developed by Nemanja Jovanovic and presented in his PhD thesis [207]. This model includes distributive scattering losses, however, assumes the immediate filling of the upper laser level. It therefore does not consider the trapping of the erbium III ions above the laser transition which was seen to occur for the higher pump powers. The output from the model is included in Figure 96.

The input parameters used in this model are provided in Table 12. The uncertainty in the modelled result corresponds to a combination of the 10% uncertainty in the core diameter and the 10% uncertainty in the fibre loss. From Figure 96 it can be seen that, prior to the roll-off in output power at the higher pump powers, there was reasonable agreement between the measured output powers and the modelled result. This agreement validates the theory that the high fibre loss was the cause of the reduced laser efficiency.

Table 12: Input parameters used in the modelling of the 2.2m fibre laser.

parameter	value	parameter	value
N	1×10^{25} m^{-1}	λ_s	1.558×10^{-6} m
τ	3.1×10^{-3} s	ϕ (core diameter)	$1.2\text{-}1.5\times10^{-6}$ m
σ_{ESA}	0	Γ_p	1
σ_{ap}	4×10^{-25} m^2	Γ_s	1
σ_{ep}	4×10^{-25} m^2	α_p	0.32 m^{-1}
σ_{as}	2×10^{-25} m^2	α_s	0.48-0.58 m^{-1}
σ_{es}	5×10^{-25} m^2	R_{s0}	99.9 %
λ_p	9.74×10^{-7} m	$R_{p0} = R_{pL} = R_{sL}$	10 %

Future work would include the development of a model that includes both the populations of the energy levels above the laser transition, to model the bleaching of the output power, and the reduction in the laser efficiency due to distributive losses along the fibre laser.

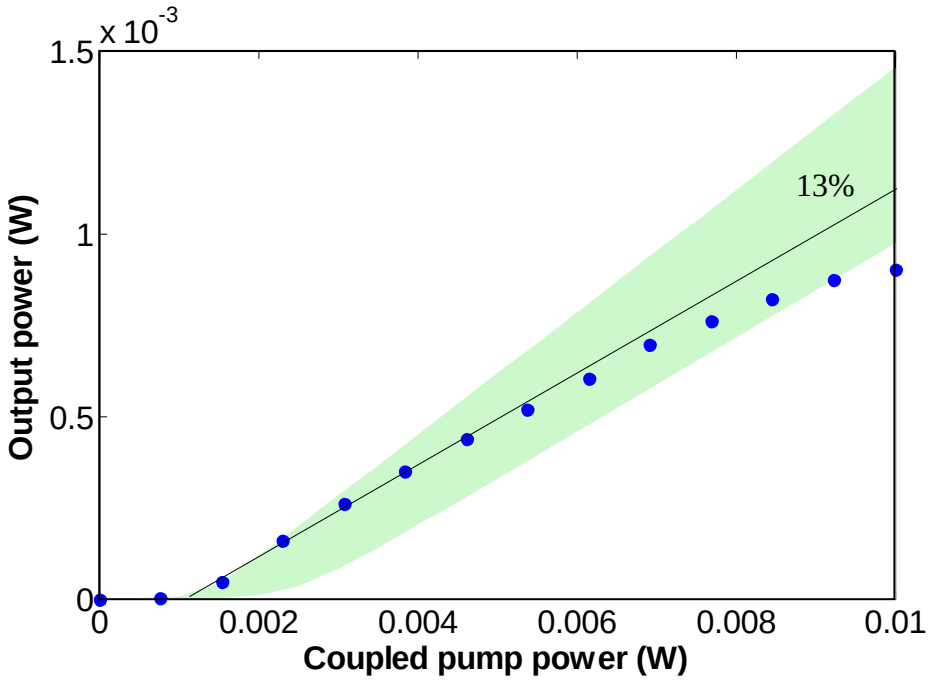

Figure 96: Erbium III doped TZNL glass microstructured fibre laser output plotted against the coupled pump power for a fiber length of 2.2 m (blue) the modelled output including the fibre loss is included in green.

The emission spectra averaged over several optical spectrum analyser scans for the 2.2m fibre laser is provided in Figure 97. From this plot laser emission can be seen to occur at a range of wavelengths. Although laser emission was observed at 1532nm, the preference to lase at longer wavelengths indicated that, unlike for the 1m fibre laser, re-absorption losses were more apparent for this longer fibre length.

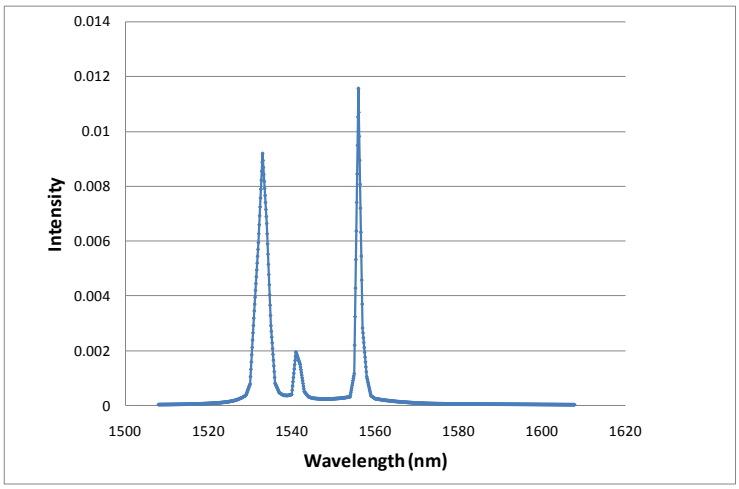

Figure 97: Spectral output from a 2.2m length of the erbium III doped TZNL glass three strut fibre, averaged over a series of scans

5.3.5 Future Outlook

In agreement with the calculated outputs from the three level model, the first wagon wheel fibre fabricated, which was doped with 0.1×10^{20} ions/cm^3, only had small output powers at 1.5µm of less than 1mW (see Section 5.3.4 for more details). Due to the accuracy of the model for the shorter fibre lengths, the model was used to look at different techniques to reduce the amount of bleaching and improve the laser performance whilst maintaining a short fibre length.

Some of the techniques that were considered included reducing the lifetime of the pumped energy level in the fabricated wagon wheel fibre through heating the fibre or designing a new fibre and co-doping the glass with cerium, increasing the erbium III concentration or increasing the core diameter.

The effect of heating the fibre was tested experimentally. The aim of this experiment was to increase the non-radiative decay from the $^4I_{11/2}$ energy level reducing its lifetime to fill the $^4I_{13/2}$ laser level. The application of a heat gun to the fibre whilst the fibre was lasing caused a reduction in the laser output power of up to 50%. This reduction in the output power was attributed to a reduction in the absorption by the fibre. This was believed to be due to either a shift in the peak of the absorption or a change in the coupling when the fibre was heated. As such there was no advantage gained through the heating of the fibre.

The addition of cerium to the glass composition has been shown to improve the inversion efficiency of the 1.5µm laser transition in tellurite glass [208-212]. As illustrated in Figure 98, this improved inversion efficiency is due to the energy transfer between the erbium III and the cerium.

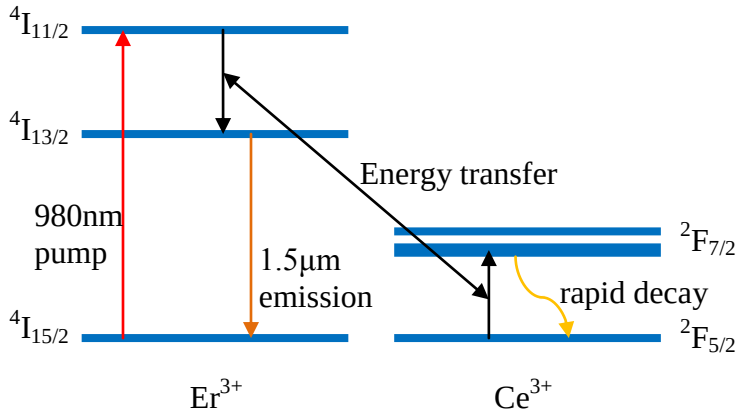

Figure 98: Energy level diagram for erbium III and cerium illustration the energy transfer process used to depopulation the pumped $^4I_{11/2}$ energy level.

This energy transfer process occurs when some of the energy from an excited erbium III ion in the $^4I_{11/2}$ energy level is transferred to a cerium ion in its ground state. The erbium III ion drops to the $^4I_{13/2}$ laser level and the cerium ion is excited to the $^2F_{7/2}$ energy level. The excited cerium ion then rapidly decays back to its ground state. This process acts to depopulate the $^4I_{11/2}$ energy level and fills the $^4I_{13/2}$ laser level. From erbium-cerium co-doped spectroscopy measurements presented in literature, the lifetime of the $^4I_{11/2}$ energy level was found to reduce by a factor of two through the addition of the cerium co-dopant. The reduced lifetime for the $^4I_{11/2}$ energy level was used in the model and the increase in the laser performance of a 1m fibre is illustrated in Figure 99 where it is compared to the performance of the solely erbium III doped wagon wheel fibre laser. The improvement observed from the modelling was, however, not significant

as, despite halving the pump energy level lifetime, once above threshold (when stimulated emission occurs) the ions would still bottleneck in this energy level.

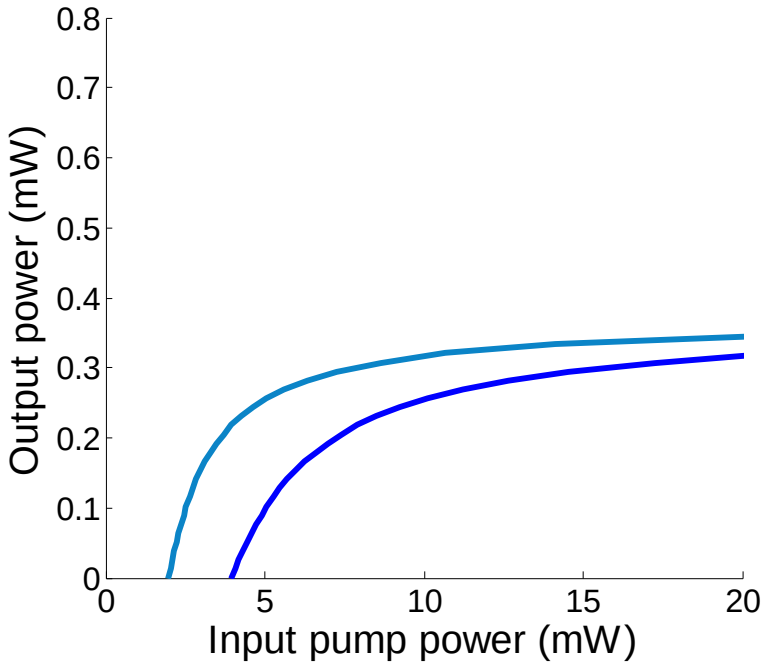

Figure 99: Plot of the predicted improvement in output power with (light blue) and without (dark blue) the co-doping with cerium.

Figure 100 gives the modelled output when increasing the erbium III concentration or the core diameter. The concentration was increased, by a factor of four (i.e. to 4×10^{-20} ions/cm^3) and when the core diameter was doubled (i.e. to 5µm). In the modelling, fibre lengths of 1m were used. In this figure, the predicted output power curves are compared to the modelled output of the fabricated wagon wheel fibre. By increasing the erbium III concentration by this amount, the optimum fibre length was reduced from the original 3m length to approximately 1m in length. From this plot it can be seen that a significant increase in the output power could be achieved through these fibre modifications.

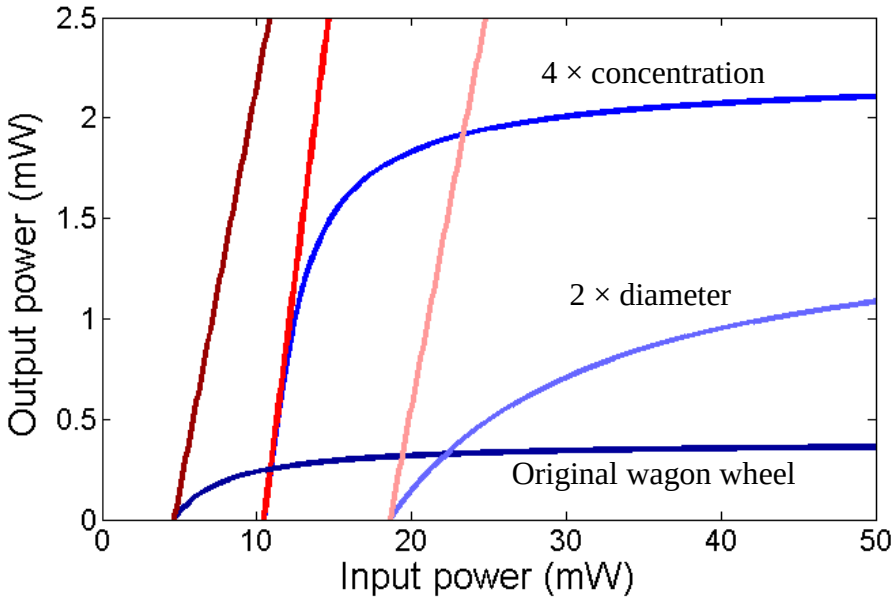

Figure 100: Plot illustrating the potential increase in output power when increasing the erbium III concentration and core diameter. The three level model (red) is compared to the two level model (blue) to see the impact of the pump bleaching.

From this modelling, since little gain is predicted through the addition of cerium to the glass, it was decided to increase both the core diameter and the erbium III concentration. By combining these two changes, the optimum fibre length could be reduced to 1m and the increased core size will increase the coupling efficiency by a factor of 4 and hence increase the potential output power by a factor of 4. The modelled output for this fibre is provided in Figure 101. The increased core size would also reduce the loss of the fibre [213] and allow for the use of longer lengths of fibre. The predicted threshold for this fibre is, however, considerably above that of the fabricated wagon wheel fibre laser due to the larger core diameter. A predicted output of 4mW was calculated for this fibre given a coupled pump power of 60mW.

Attempts are being made to fabricate this fibre as described in Section 3.4.4, but this work is yet to be completed.

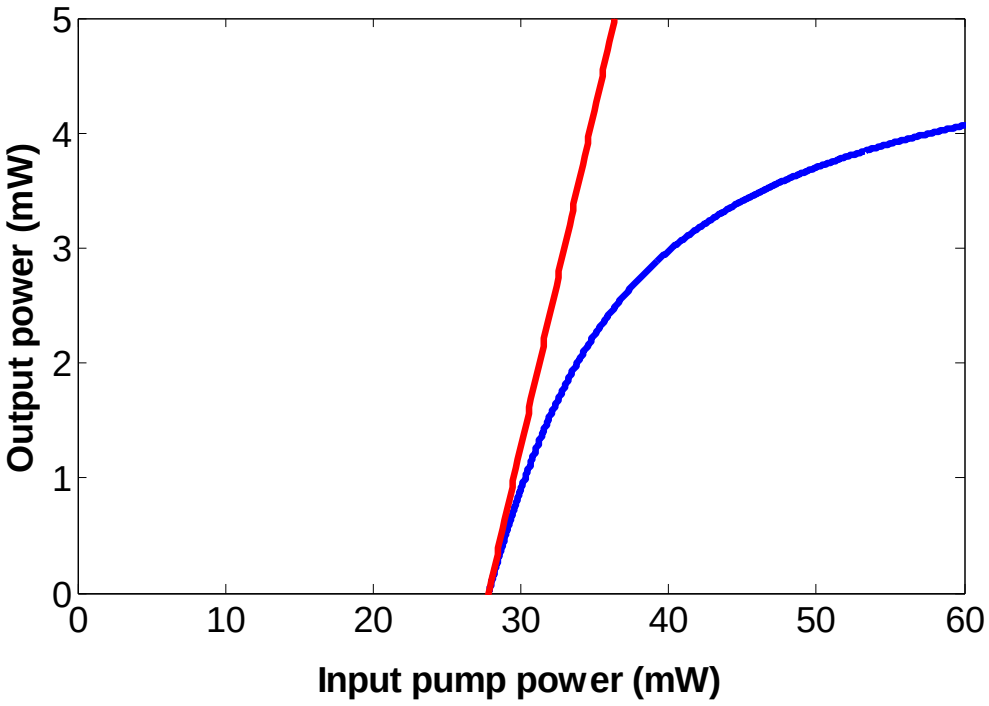

Figure 101: Predicted output power from the geometry targeted in the final preforms fabricated (Section 3.4.4) with (blue) and without (red) the inclusion of pump bleaching in the calculation. The preforms were doped with 0.5 × 10^{20} ions/cm^3 erbium III and a target fibre core diameter of 3µm.

The fibre laser development component of this research demonstrated the potential use of microstructured tellurite glass fibres in laser systems through the construction of an erbium III doped laser emitting at 1.5µm.

This fibre laser also demonstrated the potential use of the extrusion technique to fabricate soft glass fibre lasers. Prior to this research, microstructured fibre laser systems have been limited to silica and phosphate glasses and have been fabricated through the stacking and drilling of the preforms. The extrusion technique therefore opens up the area of microstructured fibre laser development to beyond tellurite glass, to a very diverse range of extrudeable soft glasses and polymers.

6. Conclusions

This thesis has demonstrated the potential of soft oxide based glasses for use in the development of mid-infrared fibre lasers. The TZNL tellurite glass was chosen as a host material for this research.

Measurements of the physical properties of the TZNL glass has demonstrated good crystallisation stability and a low fibre loss. The measurement of the viscosity allowed for the determination of appropriate extrusion and fibre drawing temperatures. The fabrication of the structured preforms, through extrusion, and the drawing of structured fibres from this glass, has demonstrated the robustness of the glass and the potential of the extrusion technique for use in the development of the microstructured fibre lasers. The extrusion technique has allowed for the fabrication of a diverse range of fibre geometries, from large mode area, increasing the damage threshold of the fibre, to small core fibres, greatly reducing the population inversion threshold for a laser system built around this fibre. The high NA structures able to be generated using the extrusion technique will lead to the development of high NA double clad fibres in the future.

The non-hygroscopic nature of the tellurite glasses have allowed for the melting of the glass in open air furnaces and the use of uncoated fibres. This would not be possible with the fluoride glasses which feature a similar transmission range but absorb atmospheric moisture and degrade rapidly with time. The mid-infrared transmission of tellurite glass could see the development of lasers at wavelengths beyond the transmission of silica.

This research was initially directed towards the development of a 3µm erbium III laser however due to the high OH absorption at this wavelength, the laser performance of an erbium III doped tellurite, structured, fibre was tested through lasing at 1.5µm, whilst efforts were made to reduce the OH concentration in the glass. Although only low output powers were achieved, the fabrication of the microstructured tellurite fibre lasers were still the first of their kind.

In Chapter 2 the tellurite glass properties are presented. Refractive index measurements indicated the significant reduction in the index of the glass when it was doped and motivated the change in the glass composition through the incorporation of

lanthanum oxide to the glass and the replacement of some of the lanthanum oxide with the erbium oxide when the glass was doped. This change to the glass composition was also seen as advantageous through DSC measurements where an improvement in the crystallisation stability was observed with the new glass composition. Through the extrusion of glass rods the glass viscosity as a function of temperature was calculated, illustrating the steep viscosity curve for the glass and its high sensitivity to small temperature variations. The temperature dependence of the viscosity was used to explain the preform bending during extrusion and the fluctuations in the fibre geometry during the fibre pulls. Glass rods were pulled down to bare fibres for loss measurements. These measurements provided insight into the glass quality and were used to refine the glass and fibre fabrication techniques in order to generate the best quality fibres. Losses below 0.2dB/m at 1.3µm were achieved in the glass. The loss in the mid-IR at around 3µm was however very high, ranging between 50 and 1200dB/m, due to OH absorption. As such the development of a 3µm erbium III laser would first require a significant reduction in the glass' OH concentration. Although this was improved significantly, the loss was however too high to pursue the laser development at this wavelength within this research.

Chapter 3 details the fibre fabrication component of this research. Preforms were fabricated using the extrusion technique. The versatility of this technique allowed for the generation of circular holes, also achievable through the stacking of glass tubes, and also irregular shapes, which were used in the fabrication of high air fractions in the cladding. The fibre development was motivated by the fabrication of an air jacketed double clad microstructured fibre. Following the bare fibre fabrication and the modelling required to determine the guidance behaviour of a microstructured fibre given its structure, large mode area fibres were fabricated designed to propagate only a single mode. These fibres featured a mode area of approximately 1000µm^2 ideal when requiring a high damage threshold for the fibre. These large mode area fibres were then modified to have the erbium III dopant only in the core of the fibre, a requirement if the fibre were to be cladding pumped. To test the laser performance of a fibre made from this glass the core size was reduced to reduce the laser threshold when it is core pumped. The final successful fibre fabricated featured a very high NA cladding and a small core, providing

good confinement to the core of the fibre and the desired lower threshold. The loss of the fibre was measured to be 1.3dB/m at 1.3μm. This type of geometry with such a high air would have been ideal for the outer cladding of a double clad fibre.

In Chapter 4 the spectroscopic properties of the erbium III doped glass are detailed. This includes the absorption and emission cross-sections and the lifetimes of the pumped and 1.5μm laser energy levels. These measurements enabled rate equation modelling and the determination of appropriate dopant concentrations and optimum fibre lengths. The lifetime of the pumped level was reduced significantly due to non-radiative decay where as the lifetime of the 1.5μm energy level decayed almost entirely radiatively. The significant difference in the lifetimes of these two energy levels caused by the non-radiative decay would have amplified the difficulties associated with overcoming the self termination of the 2.7μm laser transition if a laser at this wavelength was constructed.

Chapter 5 includes the laser modelling, results and performance of a laser built with a structured tellurite fibre. Initial modelling was used to predict optimum fibre lengths and dopant concentrations. High concentration bulk glass samples were used to study the behaviour of the glass using a free space flat curved resonator cavity. The inability to get the glass to lase motivated a closer look into upconversion in the glass, but despite the high concentrations of erbium III used, the increased loss, when comparing the tellurite glass to a phosphate glass test slab, was due to the thermal behaviour of the tellurite glass. This was confirmed through gain measurements in the glass. With this in mind the thermal behaviour of the fabricated structured fibres was looked into in more detail prior to its incorporation into the laser setup. When dissipating 0.4W/m of heat from the fibre core of the microstructured wagon wheel fibre laser, the increase in temperature of the core was calculated to be only three degrees. Successful lasing was achieved in a fabricated microstructured wagon wheel fibre which is believed by this Author to be the first microstructured tellurite fibre laser as well as the first extruded microstructured fibre laser. The output powers from this laser were quite low (≈ 1mW) due to a low coupling efficiency into the small core of the fibre. The laser featured greatly improved slope efficiency when compared to the erbium III doped tellurite slope efficiencies presented in literature. This was obtained through increasing the fibre laser length. Modelling was used to explain the laser performance and provide suggestions for

reducing the pump bleaching, which reduced the achieved output power, and improving the laser system in the future.

The results presented in this thesis demonstrated the feasibility of using tellurite glass as a host for a microstructured laser emitting in the mid-IR. There is however a significant amount more work required to demonstrate a double clad erbium III 3µm laser. This work would involve the further development of the glass, the overcoming of the self termination of the 2.7µm transition and the development of a low loss fibre. In the glass development, significant improvement has been achieved in the reduction of the OH concentration in the glass reducing the peak loss at 3.3µm from 1200dB/m down to 50dB/m. This in turn would have significantly reduced the loss of the glass at 2.7µm. By reducing this loss the gain required to overcome the cavity losses would also be reduced. The combination of using a higher erbium III concentration and hence a shorter length of fibre along with the lower loss glass would further reduce the cavity loss. To overcome the self termination of the 2.7µm transition initial work would probably be aimed at a cascade lasing scheme removing the reliance on upconversion processes to deplete the population of the $^4I_{13/2}$ energy level. In the fibre fabrication the target would be a double clad fibre. The doping of only the core of the fibre has been demonstrated along with the fabrication of high NA structures ideal for the outer cladding. Through the combination of these two geometries the fabrication of a double clad fibre is believed to be feasible. The use of a double clad fibre would allow for the use of high power pump sources with good coupling efficiency facilitating the generation of high laser output powers.

Appendix 1

A breakdown of the contributions by other members of the Centrre of Expertise in Photonics as the University of Adelaide during the glass development is broken into the different measurements performed on the glass and summarised in this appendix. The sections that contained a significant contribution by others included the glass fabrication as well as density and DSC measurements. Assistance was also provided in the experiments aimed at reducing the OH absorption and a small number of the refractive index measurements.

1.1 Glass Fabrication

As part of this research, a significant amount of glass needed to be fabricated.

- The early TZN glasses were fabricated by Herbert Foo.
    - These included the first set of erbium III doped 30g small samples and the larger 100g billets for the fabrication of the bare fibres and the 220g billets used in the fabrication of the LMA four ring fibres.
- The TZNL glasses were fabricated by Kevin Kuan and to a lesser extent Katarina Markulic.
    - The glasses fabricated included doped TZNL small samples for spectroscopic analysis and larger 220, 300 and 400g doped and undoped billets for bare fibre and structured fibre fabrication.
- The glovebox fabricated small doped glass samples as well as the undoped small samples used to study the OH concentration in the glass were melted by Kevin Kuan.
- The choice of glass billet size, composition and in the case of the doped glass the desired erbium III concentration were specified the Author based on my application for the glass.

1.1.1 Glass melting procedure:

The combination of raw materials into batches of a range of different sizes were used: 30 – 50g batches for small spectroscopic samples, 100g batches for preliminary

rod extrusions, and 220, 300 and 400g batches were used for structured preform extrusions.

- The raw materials were batched in a glovebox.
- The batches were inserted into a furnace at 700°C and heated up to 900°C in a gold crucible.
- The glass melt was kept at this temperature for around 45 minutes, during which the melt was removed twice and mixed to homogenise the glass components.
- The melt was removed from the furnace and swirled until it began to solidify and changed colour from the orange colour of the melt to a light yellow. Before the glass became too viscous to pour, it was cast into a brass mould preheated to 265°C.
- The brass mould was reheated to 310°C in a separate furnace, where the cast melt was annealed for 2 hours and cooled to room temperature at a rate of 0.1°C/min. For the 300 and 400g billets the annealing at 310°C was repeated to reduce further any stress trapped in the glass.

The same melting procedure was used for the open air and controlled atmosphere melted glasses. Exception was however made when trying to reduce the OH content in the glass through increasing the melt time and the number of times the melt was removed from the furnace and agitated.

The raw materials used were commercially available with unless otherwise stated a purity of 99.99%. The glovebox used to batch the raw material was purged with 99.99% N_2 which was dried using a molecular sieve. When the glass was melted in the glovebox, this nitrogen flowed through the furnace at a rate of 4l/min.

One of the early problems that arose in the glass fabrication was the presence of shiny gold particles distributed throughout some of the larger billets. It is believed that this was caused by crystallisation of some of the gold from the crucible that had leached into the glass melt. This crystallisation was reduced through increasing of the furnace temperature, used for melting, from 850˚C up to the 900˚C and casting the glass melt earlier. The improvement achieved through modifying the melting procedure is illustrated in Figure 18 where a billet melted at 850˚C, which contains quite obvious gold shiny particles, is compared to a 300g billet melted at the higher 900˚C.

1.1.2 Choice of crucible material:

When melting in a pure gold crucible, a gold lid was used to cover the crucible and minimize evaporation of the melt. As the tellurite glass was melted at around 900°C the gold crucible was quite malleable and the lid had a tendency to stick making at hard to reproducibly cast the melt at the same temperature. Due to the higher melting temperature of platinum, a pure platinum lid was subsequently used in place of the gold lid, allowing for easier removal of the lid. A gold crucible was used instead of a platinum crucible as the glass produced when using a platinum crucible had a significantly higher (>1dB/m) material loss for wavelengths less than 1μm (Figure 20). This increase in the loss was caused by leaching of platinum from the crucible into the glass melt.

1.1.3 Choice of mould material:

Alternative materials were tested for use as the casting mould including vitreous carbon and graphite. These carbon based moulds caused the formation of bubbles in the glass billets fabricated. In the case of the vitreous carbon mould, these bubbles were on the surface of the glass and were removed by polishing. When using the graphite mould, however, they were scattered uniformly throughout the glass. Due to the better surface quality of the glasses produced, the well polished brass moulds generated the best glass.

1.2 Density Measurements

Initial density measurements were generally performed by either Herbert Foo or Kevin Kuan following the fabrication of the billet. The later density measurements, particularly those fabricated for the fabrication of the small core fibres, were performed by the Author.

To calculate a glass billet or glass sample's density, the glass was weighed and then submerged in water of a known temperature and re-weighed. The density of the water was found from its temperature. By dividing the change in the mass of the glass sample when it was submerged by the density of the water, the volume of the billet was

calculated. Since the mass of the glass was measured before it was submerged, dividing the mass by the calculated volume gave the density of the sample. This is given by Archimedes Principle (Equation (54)).

$$Density\left(\frac{g}{cm^3}\right) = \frac{Mass\ (g)}{Mass(g) - Submerged\ mass\ (g)} \times Water\ density\ (\frac{g}{cm^3}) \quad \textbf{(54)}$$

Where *Mass* is the glass mass, the *Submerged Mass* is the mass of the billet once it has been submerged in water above the scales. The difference between the two is caused by the buoyancy of the water and the water density is found based on its temperature. The setup used is illustrated in Figure 102.

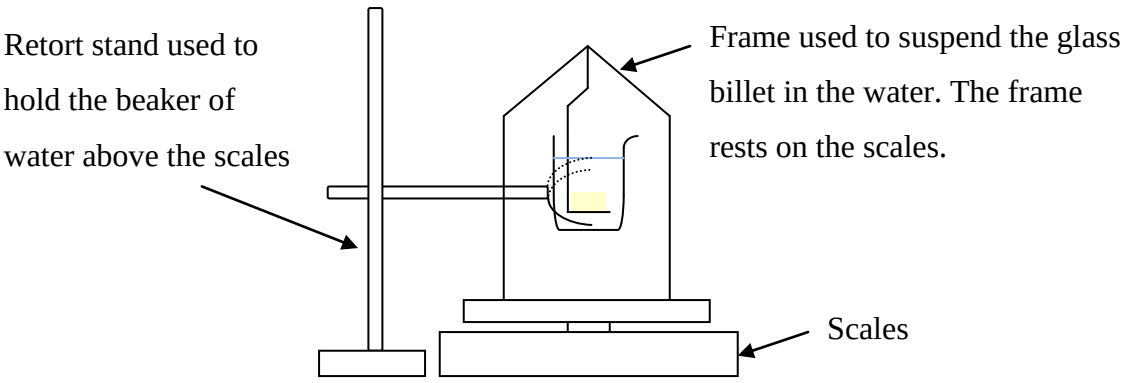

Figure 102: Setup used for the density measurements. The weight of the billet and the reduction in this weight when it is submerged in the suspended beaker of water are measured.

The error in the measurement (± 0.005) was determined statistically through the repeated measurements on each sample.

1.3 Refractive Index Measurements

Almost all the refractive index measurements were performed by the Author on a prism coupler at the Australian National University. These included the refractive index measurement of the undoped TZN glass, the erbium III doped TZN glasses doped with 0.2, 0.5, 1.0, 5.0, 10 x 10^{20} ions/cm^3, the undoped TZNL glass and the 1 x 10^{20} ions/cm^3 erbium III doped TZNL glass at 633, 1310 and 1550nm.

Later the refractive index of the undoped TZNL glass was measured by Sean Manning, using the same technique, at the additional wavelengths of 532 and 1064nm.

Additional details on the refractive index measurements is provided in Section 2.5.

1.4 Glass Stability Measurements

DSC measurements for a range of glass samples were arranged by Sean Manning to be done at Flinders University.

The instrument used was a TA Instruments DSC 2920. Gold sample pans were used in an open air environment as these conditions closely matched the melting conditions of the glasses used within this research. A baseline was obtained by heating two empty sample pans from 100ºC to 550ºC and a heating rate of 10ºC/min. The DSC's cell constant was calibrated using a zinc sample which has a well defined melting peak at 419.53ºC. The absolute temperature scale was calibrated by performing a DSC measurement of the melting temperature of tin, which melts at 231.93ºC. DSC measurements were then performed on all the tellurite glass samples over the temperature range from 250ºC to 500ºC with the same heating rate of 10ºC/min. The best results were obtained when using a single glass sample with a mass of approximately 20mg.

1.5 Reducing the OH concentration in the glass

The motivation for reducing the OH concentration in the glass was to improve the glass loss at the targeted laser wavelength of 2.7µm. All the glass samples were fabricated by Kevin Kuan at the Centre of Expertise in Photonics, along with the choices of melting times and amount of agitation provided to the melts. The effect of varying of the melting times and the use of the glovebox on the OH concentration was studied through FTIR measurements which were performed by Kevin Kuan and the Author.

Further details on the reduction of the OH concentration in the tellurite glasses are provided in Section 2.2.2.

Appendix 2: Analytical modelling of the three level laser modelling

The three level laser modelling was based in the paper by Barnard et al. [203].

The model begins with the calculation of cross-saturation and intrinsic saturation powers for the pumped and laser energy levels. The output power as a function of the input power was then able to be calculated incorporating the pump bleaching. The output power was calculated for a given input power using Matlab. If the lifetime of the pumped energy level was set to zero this analysis reduces to the two level rate equation analysis.

The output from the three level analysis (P_R^{out}) as a function of input pump power (P_p^{in}) was calculated using Equation (55).

$$P_s^{CS}[\alpha_s L - \ln(\epsilon R) + \frac{T_{eff}\, P_R^{out}}{P_s^{IS}}] = P_p^{in}\left(1 - (G_{max}\,\epsilon R)^{-\delta}\exp\left[P_R^{out}\,T_{eff}\left(\frac{\delta}{P_s^{IS}} - \frac{1}{P_p^{CS}}\right)\right]\right) \quad (55)$$

where α_s and α_p are the absorption coefficients at the laser and pump wavelengths calculated from their cross-sections using Equation (16), L is the gain medium length, ϵ and R are the product of the input and output coupling losses (ϵ_1 and ϵ_2) and reflectivities (R_1 and R_2), respectively, T_{eff} is the effective output transmission defined by Equation (56), G_{max} is the maximum achievable gain defined by Equation (57) and δ is the saturation power ration defined by Equation (58).

$$T_{eff} = (1 - \varepsilon_2^2 R_2) + \frac{(1 - \varepsilon_1^2 R_1)\varepsilon_2^2 R_2}{\varepsilon R} \quad (56)$$

$$G_{max} = \exp\left[\left(\frac{\alpha_p}{\delta} - \alpha_s\right)L\right] \quad (57)$$

$$\delta = \frac{\sigma_{13}}{\sigma_{12} + \sigma_{21}} \quad (58)$$

The σ_{ij} values correspond to either the absorption or emission cross-sections for the transition from the i^{th} energy level to the j^{th} energy level. P_s^{CS}, P_s^{IS} and P_p^{CS} are defined as

the coefficients of the cross-saturation of the laser emission, the intrinsic saturation of the laser emission and the cross-saturation of the pumped energy level, respectively. For a three level laser system, these coefficients are defined in Equations (59) to (61), respectively.

$$P_s^{CS} = \frac{A_{eff}}{\Gamma_s}\frac{\beta_{2e}}{\eta_p \tau_2}\frac{1}{\sigma_s^a + \beta_{2e}\sigma_s^e} \quad \textbf{(59)}$$

$$P_s^{IS} = \frac{A_{eff}}{\Gamma_s}\frac{1}{\tau_2}\frac{1}{\sigma_s^a + \sigma_s^e} \quad \textbf{(60)}$$

$$P_p^{CS} = \frac{A_{eff}}{\Gamma_s}\frac{1}{\tau_2}\frac{1}{\sigma_p^a} \quad \textbf{(61)}$$

A_{eff} is the effective dopant area and Γ_s is the overlap integral between the laser mode and the doped region. β_{ie} is the ratio of the number of ions in the i^{th} energy level to the total number of excited ions and the values for β_{2e} and β_{3e} are calculated from Equations (62) and (63), η_p is the pump efficiency defined by $\eta_p = \tau_3/\tau_{32}$, τ_i and τ_{ij} denote the lifetimes, including both the radiative and non-radiative decay, from the i^{th} energy level or for the i to j transition, respectively. The σ_s^a and σ_p^a terms are the absorption cross-sections for the laser energy level and pump energy level, respectively and σ_s^e is the emission cross-section of the laser transition.

$$\beta_{2e} = (1 + \frac{\tau_{32}}{\tau_2})^{-1} \quad \textbf{(62)}$$

$$\beta_{3e} = (\frac{\tau_{32}}{\tau_2})\beta_{2e} \quad \textbf{(63)}$$

The derivation and description of these equations is provided in more detail in Ref. [203].

Appendix 3: Publications during candidature

Journal publications:

M.R. Oermann, H. Ebendorff-Heidepriem, Y. Li, T.-C. Foo, T.M. Monro, "Index matching between passive and active tellurite glasses for use in microstructured fiber lasers: Erbium doped lanthanum-tellurite glass", Optics Express 17 (18), 15578-15584, August 2009

M. Oermann, H. Ebendorff-Heidepriem, D. Ottaway, D. Lancaster, P. Veitch, T.M. Monro, "Extruded microstructured fiber lasers", Submitted to Photonics Technology Letters

First author refereed conference papers (accepted for invited talk):

M. Oermann, D. Ottaway, H. Ebendorff-Heidepriem, P. Veitch, T.M. Monro "Tellurite Glass for use in 2.3μm Thulium Fibre Lasers" IQEC/CLEO Pacific Rim 2011, Sydney, August 2011

First author refereed conference papers (accepted for oral presentation):

M. Oermann, D. Ottaway, H. Ebendorff-Heidepriem, P. Veitch, T.M. Monro "Microstructured Erbium Doped Tellurite Fibre Laser" 19th Australian Institute of Physics Congress/35th Australian Conference on Optical Fibre Technology (ACOFT/AIP), Melbourne, December 2010

M.R. Oermann, D. Ottaway, P. Veitch, H. Ebendorff-Heidepriem, T.M. Monro, "Erbium-doped bulk tellurite glass laser at 1.5 μm", Australian Conference on Optics, Lasers and Spectroscopy (ACOLS), Adelaide, December 2009.

M.R. Oermann, H. Ebendorff-Heidepriem, Y. Li, T.M. Monro, "Spectroscopy of erbium in La^{3+}-doped tellurite glass & fibres", Australian Conference on Optical Fibre Technology (ACOFT), Sydney, July 2008

Co-author refereed conference papers (accepted for oral presentation):

Y. Li, M. Oermann, H. Ebendorff-Heidepriem, T.M. Monro, "Simultaneous infrared and visible emission in Er^{3+}-doped ZBLAN fibre", International Commission for Optics (ICO), Sydney, July 2008

H. Ebendorff-Heidepriem, T.C. Foo, Y. Li, M. Oermann, T.M. Monro, "New tellurite glasses for erbium fibre lasers", Australian Conference on Optical Fibre Technology (ACOFT), Sydney July 2008

Conference abstracts (accepted for oral presentation):

M.R. Oermann, Y. Li, H. Ebendorff-Heidepriem, T.M. Monro, "Core doped tellurite microstructured optical fibre for erbium fibre laser at 2.7μm", AIP Congress 2008 AOS, Adelaide, December 2008

Michael R. Oermann, Heike Ebendorff-Heidepriem, David Ottaway, Peter Veitch, Tanya M. Monro, “Tellurite glass microstructured fibre laser development”, PACRIM 2011, Cairns, July 2011

Index matching between passive and active tellurite glasses for use in microstructured fiber lasers: Erbium doped lanthanum-tellurite glass

Michael R. Oermann,* Heike Ebendorff-Heidepriem, Yahua Li, Tze-Cheung Foo, Tanya M. Monro

Centre of Expertise in Photonics, School of Chemistry & Physics, University of Adelaide, Adelaide, SA 5005, Australia

**Corresponding author: michael.oermann@adelaide.edu.au*

Abstract: Active and passive variants of La-containing tellurite glasses have been developed with matched refractive indices. The consequences of adding lanthanum to the glass was studied through measurements of the crystallization stability, glass viscosity and the loss of unstructured fibers. Doping the glass with erbium allowed for any spectroscopic changes to be observed through measurements of the absorption and energy level lifetimes. The fluorescence emission spectra were measured at 1.5 μm and, to the best of our knowledge, for the first time in tellurite glass at 2.7 μm.

OCIS codes: (160.2290) Fiber Materials; (160.5690) Rare-earth-doped materials; (160.3380) Laser materials

References and links

1. A. Mori, Y. Ohishi, S. Sudo, "Erbium-doped tellurite glass fibre laser and amplifier," Elec. Lett. **33**, 863-864 (1997)
2. B. Richards, Y. Tsang, D. Binks, J. Lousteau. A. Jha, "Efficient ~2μm Tm^{3+}-doped tellurite fiber laser," Opt. Lett. **33**, 402-404 (2008)
3. Y. Tsang, B. Richards, D. Binks, J. Lousteau. A. Jha, "Tm^{3+}/Ho^{3+} codoped tellurite fiber laser," Opt. Lett. **33**, 1282-1284 (2008)
4. J. S. Wang, E. M. Vogel, E. Snitzer, "Tellurite glass: new candidate for fiber devices," Opt. Mater. **3**, 187-203 (1994).
5. T. M. Monro, H. Ebendorff-Heidepriem, "Progress in microstructured optical fibers," Ann. Rev. Mater. Res. **36**, 467-495 (2006).
6. K. Patek, *Glass Lasers*, (CRC Press, 1970)
7. Raouf A. H. El-Mallawany, *Tellurite Glasses Handbook: physical properties and data*, (CRC Press, 2002)
8. G. Nunzi Conti, V. K. Tikhomirov, M. Bettinelli, S. Berneschi, M. Brenci, B. Chen, S. Pelli, A. Speghini, "Characterization of ion-exchanged waveguides in tungsten tellurite and zinc tellurite Er^{3+}-doped glasses," Opt. En. **42,** 2805-2811 (2003).
9. L. Li, A. Schulzgen, V. L. Temyanko, H. Li, S. Sabet, M. M. Morrell, A. Mafi, J. V. Moloney, N. Peyghambarian, "Investigation of modal properties of microstructured optical fibers with large depressed-index cores," Opt. Lett. **30**, 3275-3277 (2005).
10. S. Dai, C. Yu, G. Zhou, J. Zhang, G. Wang, L. Hu, "Concentration quenching in erbium-doped tellurite glasses," J. Lumin. **117**, 39-45 (2006).
11. T. A. Birks, J. C. Knight, P. St. J. Russel, "Endlessly single-mode photonic crystal fiber," Opt. Lett. **22**, 961-963 (1997).
12. H. Ebendorff-Heidepriem, T. M. Monro, "Extrusion of complex preforms for microstructured optical fibers" Opt. Exp., **15** Issue 23, 15086-15092 (2007)
13. E. Roeder, "Extrusion of glass" J. Non-Cryst. Solids **5**, 377-388 (1971)
14. M. Braglia, S. Mosso, G. Dai, E. Billi, L. Bonelli, M. Baricco, L. Battezzati, "Rheology of tellurite glasses", Mater. Res. Bull. **35**, 2343-2351 (2000)
15. G. Ghosh, "Sellmeier coefficients and chromatic dispersions for some tellurite glasses," J. Am. Ceram. Soc. **78**, 2828-2830 (1995).
16. S. Shen, A. Jha, E. Zhang, S. J. Wilson, "Compositional effects and spectroscopy of rare earths (Er^{3+}, Tm^{3+}, and Nd^{3+}) in tellurite glasses," C. R. Chimie **5**, 921-938 (2002)

17. H. Ebendorff-Heidepriem, D. Ehrt, M. Bettinelli, A. Speghini, "Effect of glass composition on Judd-Ofelt parameters and radiative decay rates of Er^{3+} in fluoride phosphate and phosphate glasses" J. Non-Cryst. Solids **240**, 66-78 (1998)
18. R. S. Grew, H. Ebendorff-Heidepriem, P. J. Veitch, T. M. Monro, "Concentration effects in erbium doped tellurite glass," Proc. COMMAD, 196-199 (2006).
19. R. Reisfeld, Y. Eckstein, "Radiative and non-radiative transition probabilities and Quantum yields for excited states of Er^{3+} in germanate and tellurite glasses," J. Non-Cryst. Solids **15**, 125-140 (1974)
20. H. Kuhn, S. T. Fredrich-Thornton, C. Krankel, R. Peters, K. Petermann, "Model for the calculation of radiation trapping and description of the pinhole method," Opt. Lett. **32**, 1908-1910 (2007)
21. H. Ebendorff-Heidepriem, T. C. Foo, Y. Li, M. R. Oermann, T. M. Monro, "New tellurite glasses for erbium fibre lasers," proc. OECC/ACOFT, paper TuD-2 (2008)
22. R. Rolli, M. Montagna, S. Chaussedent, A. Monteil, K. Tikhomirov, M. Ferrari, "Erbium-doped tellurite glasses with high quantum efficiency and broadband stimulated emission cross section at 1.5μm," Opt. Mater. **21**, 743-748 (2003)
23. H. Ebendorff-Heidepriem, D. Ehrt, J. Philipps, T. Topfer, A. Speghini, M. Bettinelli, R. W. S. Fat, "Properties of Er^{3+} Doped Glasses for Waveguide and Fiber Lasers," Proc. SPIE, Vol. 3942, 29-39 (2000)

1. Introduction

Tellurite glasses are promising hosts for fiber lasers operating in the mid-IR[1-3]. They have low phonon energies, high refractive indices, high rare earth solubility, infrared transmission up to 5 μm and high gain per unit length [4]. Compared to fluoride glasses, which also feature low phonon energies, they exhibit a higher thermal stability and improved corrosion resistance [4]. In this paper, erbium was used as the rare-earth dopant as it can be pumped with commercially available diode lasers at 790 nm and 980 nm and emits in the mid-IR.

Microstructured optical fiber (MOF) technology [5] is a promising route to high power double-clad tellurite fiber lasers. Holey claddings offer novel properties such as the combination of large mode area, high power transmission without damage and single mode guidance at all wavelengths [5]. Cladding pumping requires the active dopant(s) to be confined to the core region. The refractive index of the active region must therefore closely match to that of the passive glass. It is well known that doping silicate glasses with rare earth ions increases the refractive index (n) [6]. In contrast to silicate glasses ($n \approx 1.5$), tellurite glasses have higher refractive indices ($n \approx 2.0$) and considerably higher polarizability [7]. When doping tellurite glass, the tellurium ions are replaced by rare earth ions which have a lower polarizability. As a result the Er-doped tellurite glass has a lower refractive index than the undoped glass [8]. This is of particular importance when doping only the core of a MOF as the refractive index of the core may be reduced to below the effective index of the holey cladding, thus preventing index guiding. The guidance can be restored by increasing the air fraction of the microstructure in the cladding [9], or by modifying the composition of the core and cladding glasses to minimize the difference in their refractive indices. The addition of La_2O_3 to a tellurite glass promises index matching between undoped and rare earth doped glasses. The La^{3+} ions have similar properties to the active rare earth ions, such as Er^{3+}, but do not absorb in the same wavelength range. The potential of La_2O_3 for index matching in tellurite glass is illustrated by the bulk glass measurements reported in Ref [10].

The $5Na_2O$-$20ZnO$-$75TeO_2$ tellurite glass composition was demonstrated to be a promising host for rare-earth doped lasers [4]. In this paper, we explore the potential of this glass composition (hereafter referred to as base glass) for the development of a core doped tellurite MOF, using erbium as the active ion. We demonstrate that modification of the cladding structure alone is insufficient to compensate for the Er_2O_3 induced refractive index decrease, whereas addition of La_2O_3 to the base glass enables index matching between the Er-doped core and passive cladding glass. The thermal and optical properties of the undoped and Er-doped La-Na-Zn-tellurite glass (hereafter referred to as La-glass) are compared with the undoped and Er-doped base glass. The suitability of the La-glass for low-loss fiber fabrication is demonstrated via bare fibers made using the extrusion technique for preform fabrication.

2. Modeling of tellurite MOFs

The effective refractive index of the cladding region can be approximated by the effective index of the fundamental space filling mode (FSM) that would propagate through an infinite variant of the cladding lattice [11]. The impact of increasing the air fraction of the cladding microstructure on its effective index was modeled by increasing d/Λ (d = hole diameter and Λ = hole to hole spacing) of a variety of hexagonally periodic cladding geometries. The modeled structures had Λ = 20μm and varied hole diameters resulting in d/Λ's ranging from 0.3 up to 0.7. For fibers made solely from the host glass, increasing d/Λ across this range would cause the difference in refractive index (Δn) between the core and the numerically calculated FSM index for the cladding region to increase from 1.5×10^{-4} for d/Λ = 0.3 up to 9.8×10^{-4} for d/Λ = 0.7. Evidence given in previous tellurite glass papers as well as measured refractive indices (Table 1) indicate that the refractive index change due to rare earth doping ($\Delta n=1\times10^{-3}$ for a concentration of 1×10^{20}ions/cm^3 and $\Delta n=7\times10^{-3}$ for a concentration of 5×10^{20}ions/cm^3) exceeds this microstructure induced Δn between the core and cladding (1×10^{-3}). Hence, for a tellurite glass MOF with an Er-doped core of moderate concentration (1.0×10^{20}ions/cm^3) and undoped holey cladding, guidance cannot be achieved even with a predominantly air cladding without modification to either the core or cladding glass compositions.

3. Glass and fiber fabrication

Modeling demonstrated that index matching via modification of the glass composition is essential to create a core doped tellurite MOF. We selected La_2O_3 addition as a promising approach for index matching. To explore the impact of La_2O_3 addition on the thermal and optical properties of glass, we prepared Er-doped and undoped base glass and Er-doped and undoped La-glass (Table 1). These glasses were melted at 900 ^oC in gold crucibles, cast into brass moulds and then slowly cooled to room temperature. In the Er-doped base glasses and in the undoped La-glass, Er_2O_3 and La_2O_3 were added to the base glass prior to melting. In the Er-doped La-tellurite glass some of the La_2O_3 was replaced by Er_2O_3 keeping the lanthanide ion concentration constant (Table 1). Glass blocks made from 30 g batches were used for preparation of polished glass plates of 2 mm thickness. These plates were used for refractive index, absorption and fluorescence lifetime measurements. Cylindrical glass billets of 30 mm diameter were produced from 100 g batches. These billets were used to fabricate 10 mm diameter rods using the billet extrusion technique [12] and reduced in scale on a fiber drawing tower into bare (unstructured) fibers. These bare fibers enabled the measurement of the glass loss and illustrated the suitability of this glass as a fiber material.

Table 1. Density, refractive indices, experimentally measured and theoretically calculated Er^{3+} lifetimes for undoped and Er-doped base glasses, and for undoped and Er-doped La-tellurite glasses

	Glass	Ln^{3+} (10^{20} cm^{-3})		density	Refractive index			Lifetime (ms) for $^4I_{13/2}$		Lifetime (ms) for $^4I_{11/2}$	
		Er^{3+}	La^{3+}		633nm	1310nm	1550nm	calc	meas	calc	meas
base glass	undoped	-	-	5.34	2.0515	-	-	-	-	-	-
	B-Er1	1	-	5.37	2.0505	-	-	3.4	3.0	0.23	0.20
	B-Er5	5	-	5.40	2.0435	-	-	3.4	3.1	0.23	0.18
La-glass	undoped	-	10	5.37	2.0360	1.987	1.983	-	-	-	-
	La-Er1	1	9	5.37	2.0355	1.987	1.983	3.4	3.1	0.23	0.21
	error			*± 0.1*		*± 5×10^{-4}*		*± 0.3*	*± 0.3*	*± 0.02*	*± 0.02*

4. Thermal and optical properties of the glasses

4.1 Glass transition and crystallization stability

To determine the thermal and crystallization stability of the base and La-glass, we measured the glass transition temperature (Tg) and crystallization onset temperature (Tx) of the glasses. The thermal stability is indicated solely by the Tg and the crystallization stability of a glass is indicated by the temperature difference ΔT=Tx-Tg. These values were measured via differential scanning calorimetry using a heating rate of 10 ^{o}C/min. The base glass had a Tg of 302 ^{o}C and ΔT of 133 ^{o}C. The La-tellurite glass had both a higher Tg (315 ^{o}C) and higher ΔT (165 ^{o}C) compared with the base glass, which is of benefit for fiber fabrication.

4.2 Glass viscosity

Billet extrusion has been demonstrated to be a viable technique for the fabrication of microstructured fiber preforms [12]. This approach forces a glass billet at elevated temperature through a die into free space. To avoid glass crystallization, preform deformation and die breakage, the extrusion temperature needs to be selected with care, which requires knowledge of the temperature dependence of the glass viscosity. Simple and complex preforms are extruded in the viscosity range of 10^{7}-10^{10} dPa.s. In this relatively narrow range, measured temperature-viscosity-data can be well fitted with an Arrhenius equation. We used extrusion of rods from glass billets to determine the temperature-viscosity-curve for our glasses. The flow through dies with a circular channel obeys the Poiseuille law [13], which allows calculation of the glass viscosity at a fixed extrusion temperature from the extrusion speed and pressure as well as the die channel length and diameter. The temperature-viscosity-curve η(T) of the base glass has been reported previously by Braglia et al [14]. The base glass viscosity data measured here agree well with the Arrhenius equation based viscosity curve presented in Braglia's paper, proving how a rod extrusion is a suitable method for calculating a glass's viscosity. For the La-glass, the η(T) curve was calculated by fitting our measured viscosity data to an Arrhenius equation. Figure 1(a) shows that the La-tellurite glass has a higher viscosity than the base glass, which is consistent with the higher Tg of this glass. The similar viscosities of the Er-doped glasses compared with the corresponding undoped glasses indicate that, unsurprisingly, small rare earth amounts do not change the glass viscosity.

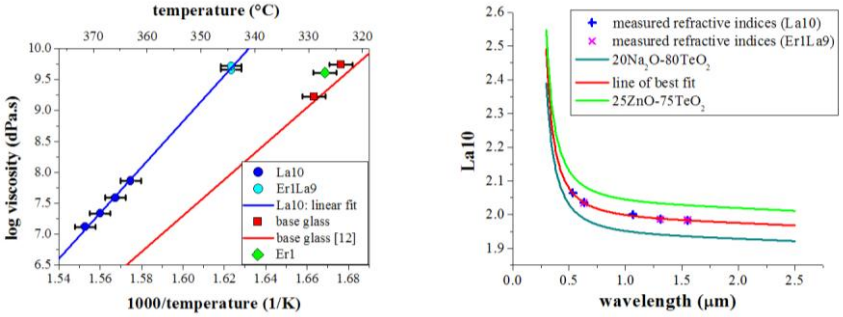

Fig. 1: (a) Glass viscosity as a function of temperature. (b) Refractive index dispersion for La-glasses, along with Sellmeier curves for two other tellurite glasses [15].

4.3 Refractive index

The refractive indices of the glasses were measured using a prism coupler. The glass plates were positioned against the prism such that there was good contact. A rutile ($Ti0_2$) prism was used for these refractive index measurements as the index of the tellurite was known to lie between 2 and 2.6. The index was measured for all the samples at 632.8 nm to investigate the Er^{3+} concentration dependence on the refractive index and the La-samples were measured at a range of wavelengths (632.8nm, 1310nm and 1550nm for the Er1La9 glass and for the La10 glass also at 532nm and 1064nm) to evaluate the index matching in undoped and doped La-samples at different wavelengths. The index measurements (Table 1) verify that Er-doping of

the La-free base glass reduces the refractive index, whereas the refractive index of the Er-doped La-glass closely matches that of the undoped La-glass within the measurement error. The indices of the undoped and Er-doped La-glasses are plotted against the Sellmeier curves for binary sodium tellurite and zinc tellurite glasses [15] in Fig. 1(b). It is evident that the measured refractive indices follow a similar dispersion curve.

4.4 Bare (unstructured) fibers

Bare (unstructured) fibers were made from undoped base glass as well as undoped and Er-doped La-glass. The bare fiber loss is a useful indicator of the glass loss, and also demonstrates the impact of La- and Er-doping on the loss. The bare fiber loss spectra (Fig. 2(a)) were measured using the standard cutback measurement technique on 200μm outer diameter bare fibers. This fiber diameter was chosen for its handleability (the ability to handle the fiber without breakage) and reproducibility in cleave quality. The fiber loss is independent of the fiber diameter as it is dominated by the material losses. A broadband white light source was collimated and then focused into the test fibers. The output signal was launched into an OSA directly using a bare fiber adaptor. Both the undoped base and La-glass bare fibers have low minimum losses of ≈0.2 ± 0.1 dB/m at 1.3 μm. The Er-doped La-glass fiber has a higher minimum loss of ≈0.4 ± 0.1 dB/m at 1.2 μm. These losses are comparable to the fiber loss measured by Shen et al [16] also for a Na-Zn-tellurite glass and demonstrate the suitability of the La-tellurite glass as a fiber material.

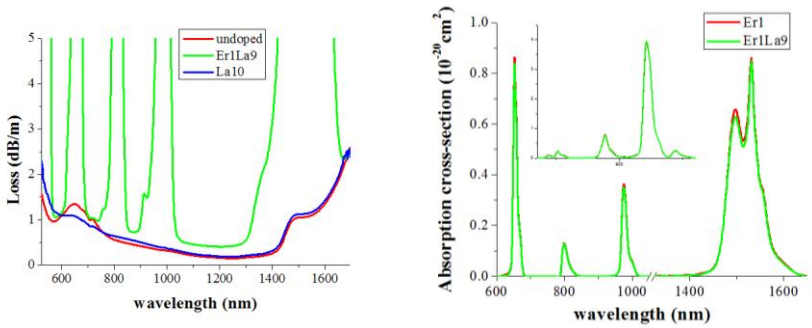

Fig. 2. (a) Loss spectra of the bare (unstructured) fiber made from undoped, La10 and Er1La9 glasses, (b) Er^{3+} absorption cross-section for Er-doped base and La-tellurite glass.

5. Spectroscopic properties of Er^{3+} in the tellurite glasses

5.1 Absorption

The absorption spectra in the visible to near-infrared region were measured using a CARY spectrophotometer. The absorption cross section, α, (Fig. 2(b)) was calculated from the measured absorbance spectrum using the sample thickness and Er^{3+} ion concentration. Note the area under the absorption cross-section for each energy level, $\int \alpha \, d\lambda$, is proportional to $(n^2+2)^2/9n$, where n is the refractive index of the glass. A full derivation of this relationship is presented by Ebendorff-Hiedepriem et al [17]. When comparing the doped base glass (Er1) and the doped lanthanum glass (La-Er1), which exhibit slightly different refractive indices, one would expect variation in their absorption cross-sections. According to the measured refractive indices, the lower index of the La-Er1 glass would theoretically result in a 1% reduction in the integral of its absorption cross-section, which is samller that the 5% error in the glass sample thickness measurement. Thus, the expected 1% difference between the B-Er1 and La-Er1 absorption cross-sections is not evident, and the absorption cross-section is unchanged with the addition of lanthanum to the glass composition within the measurement error.

5.2 Energy level lifetimes and fluorescence measurements

The total radiative decay rate (A) and lifetime of the Er^{3+} $^4I_{13/2}$ and $^4I_{11/2}$ energy levels were calculated from the absorption cross-section spectra using the Judd-Ofelt analysis [17,18]. The

non-radiative multiphonon decay rate was calculated through the extrapolation of the results presented by Reisfeld et al [19] for their sodium-tellurite glass. The fluorescence lifetimes of the Er^{3+} $^4I_{11/2}$ and $^4I_{13/2}$ energy levels were measured by directly pumping the $I_{11/2}$ level with a pulsed 974 nm laser and analyzing the fluorescence decay curve. The pinhole technique described by Kuhn et al [20] and a 300μm pinhole was used to minimize reabsorption effects (radiation trapping). Filters were used to observe the fluorescence decay to the ground state ($^4I_{15/2}$) for each energy level individually.

Due to the wide gap between the $^4I_{13/2}$ level and the next lower level $^4I_{15/2}$, the multiphonon decay rate for this transition ($W < 1\ s^{-1}$) is negligible compared with the radiative decay rate ($A = 290\ s^{-1}$), and thus the theoretically predicted lifetime is effectively the radiative lifetime of ≈3.4 ms. This is seen in our measurements of this level's lifetime which agree with the radiative decay time within the measurement error. For all three Er-doped glass samples, the measured lifetime of the $^4I_{13/2}$ level (Table 1) is similar to the predicted lifetime. This demonstrates that for both the base and the La-tellurite glass, concentration quenching is not significant for Er^{3+} concentrations up to 5×10^{20} ions/cm^3. This is in contrast to other tellurite glasses, where quenching of the $^4I_{13/2}$ level via energy transfer to OH groups in the glass (OH quenching) occurs from very low Er^{3+} concentrations (0.2×10^{20} ions/cm^3) [10,16] although our tellurite glasses exhibit similar OH contents (i.e. similar OH absorption coefficients at ~3.3 μm [21]) compared to other tellurite glasses that were also melted in ambient atmosphere [10,16]. Tellurite glasses melted in a glove box under a nitrogen atmosphere also do not suffer from OH quenching for concentrations up to 5×10^{20} ions/cm^3 [8,22]. In phosphate glasses, the OH quenching at low Er^{3+} concentrations is attributed to clustering between Er^{3+} ions and OH groups [23]. The absence of OH quenching in our glass indicates that the Er^{3+} ions are evenly distributed and do not form clusters with OH groups.

For the $^4I_{11/2}$ to $^4I_{13/2}$ transition, the multiphonon decay rate ($W \approx 4000\ s^{-1}$) is considerably larger than the calculated radiative decay rate ($A = 370\ s^{-1}$) and thus the multiphonon decay rate is included in the theoretically predicted lifetime of 0.23 ms. For all three Er-doped glass samples, the measured lifetime of the $^4I_{11/2}$ level (Table 1) is similar to the theoretically predicted lifetime, which confirms that the lifetime of this level is shortened considerably by non-radiative decay. The 2.7μm fluorescence spectra (Fig. 3) illustrate that the decay over the 2.7μm transition is not completely quenched by this non-radiative decay, although due to the shortened lifetime, achieving population inversion across this transition will not be trivial.

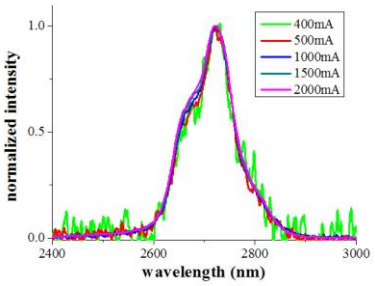

Fig. 3. Normalized fluorescence spectra at 2.7μm for a range of pump powers.

For the two Er^{3+} energy levels considered, the base glass and La-tellurite glass samples have the same measured lifetimes within the measurement errors, which demonstrates that the addition of La_2O_3 does not have a detrimental impact on the Er^{3+} fluorescence lifetimes.

6. Conclusion

We demonstrate that the addition of La_2O_3 to tellurite glass is a powerful approach to achieve index matching between active and passive glasses. Replacement of ~10% of the passive La^{3+} ions by active Er^{3+} ions resulted in the same index in the near infrared region for both glasses. This will facilitate the development of practical core-doped tellurite MOFs. More generally,

this advance will enable the placement of the doped glass anywhere in a MOF with no impact on the fiber's guidance, something that is not possible in more conventional active fibre designs, a feature that could potentially lead to new and more flexible control of fibre laser properties. We have demonstrated that the Er^{3+} absorption intensities and fluorescence lifetimes are not detrimentally affected by the La_2O_3 addition, whereas the thermal and crystallization stability are observed to improve in the La-tellurite glass. The loss of the bare fibers demonstrates that the addition of La_2O_3 does not impact the material loss. The Er-doped La-glass exhibits strong fluorescence at both 1.5 μm and, to the best of our knowledge, for the first time in tellurite glass at 2.7 μm.

Acknowledgements

We acknowledge the ARC for their funding (DP20101384); DSTO (Australia) for support and funding to the Centre of Expertise in Photonics and this work; P. Veitch and D. Ottaway at the University of Adelaide, K. Mudge, B. Claire, K. Grant, A. Hemming and D. Lancaster at DSTO for useful discussions; S. Manning, R. Moore at Adelaide University for DSC measurements and fiber drawing, and S. Madden for use of the ANU prism coupler for refractive index measurements. T. Monro acknowledges the support of an ARC Federation Fellowship.

Oermann,M., Ebendorff-Heidepriem, H., Ottaway, D., Lancaster, D., Veitch, P. & Monro, T.M. (2012)
Extruded microstructured fiber lasers.
IEEE Photonics Technology Letters, v. 24 (7), pp. 578-580

Tellurite Glass for use in 2.3µm Thulium Fibre Lasers

Michael R. Oermann, Heike Ebendorff-Heidepriem, David J. Ottaway, Peter J. Veitch, Tanya M. Monro
Institute for Photonics & Advanced Sensing and School of Chemistry & Physics, University of Adelaide, Adelaide, Australia
michael.oermann@adelaide.edu.au

Abstract: The fabrication of extruded-microstructure tellurite glass fibers for erbium-doped fiber lasers has demonstrated the versatility of this fibre fabrication technique. We also show that tellurite glass should allow the development of Tm-doped fibre laser systems.

1. Introduction

Tellurite glass has its advantages as a laser host because of its high rare earth solubility, its high absorption and emission cross-sections. The glass has good transmission in the wavelength range from 0.35 to 5µm, and also has good crystallization stability and improved corrosion resistance when compared to the fluorozirconate-based glasses, which have a similar transmission range.

To date, tellurite-based fibre lasers systems have produced output powers up to about 300mW and emission wavelengths as long as 2.1µm. These systems emit within the transmission window of silica and do not exploit the improved transmission and lower phonon energy of the tellurite glass.

In this abstract we report on the planned development of a thulium-doped extruded-microstructure tellurite glass fibre laser emitting at 2.35µm. As a precursor, an erbium-doped microstructured fibre laser, emitting at 1.5µm, has been constructed to demonstrate the suitability of the extrusion technique for producing microstructured tellurite fibre lasers.

Absorption measurements using small thulium-doped samples and a Judd-Ofelt analysis have been used to calculate the lifetimes of the thulium energy levels and to demonstrate the feasibility of lasing at 2.35µm. Results from fibre laser experiments will be presented.

2. Tellurite glass

The tellurite glass used was based on the $75TeO_2$-$20ZnO$-$5Na_2O$ composition first proposed by Wang et al. [1]. We added lanthanum to the glass composition to improve the glass stability. Additionally, replacement of the lanthanum by the lasing dopant reduced their impact on the glass properties [2]. In the erbium-doped fibre laser presented in this abstract, the glass composition used was $73.3\ TeO_2 - 19.6\ ZnO - 4.9\ Na_2O - (2.2 - x)\ La_2O_3 - x\ Er_2O_3$ where $x = 0.025$ mol %, corresponding to an erbium concentration of 0.1×10^{20} ions/cm^3. The thulium-doped samples used in the absorption measurements had concentrations of 1.2×10^{20} ions/cm^3 and 2.8×10^{20} ions/cm^3.

3. Erbium-doped extruded-microstructure tellurite fibre laser

The die, preforms and SEM images of the fiber are shown in Fig. 1 [3]. The fiber consists of a small diameter core of approximately 1.5µm, where the core diameter is defined as the largest circle that can be fit entirely within the triangular core. The core is surrounded by three large air-filled holes that are defined by thin struts that, due to their 100 nm thickness, have a negligible effect on the fiber's guidance characteristics. The minimal overlap between the guided mode and the glass cladding allowed uniform doping of the entire fibre cross-section, as there is negligible absorption of the laser emission within the cladding.

The laser resonator consisted of a dichroic mirror (transparent at 970 nm and highly reflective at 1550 nm) abutted to one end of the fiber and the 10 % Fresnel reflection at the cleaved output end of the fiber. It was pumped with a 300 mW, single mode, fibre coupled, 974 nm laser diode, however, due to the small diameter of the fibre core and a significantly larger pump diameter at the fibre tip, only about 10 mW of the pump power was coupled into the fibre.

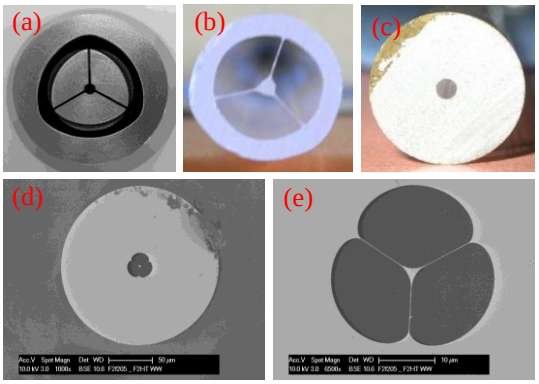

Figure 1: Photographs of the stainless steel die exit used for the extrusion of the structured preform (a) and the extruded structured and jacket preforms (b) and (c) respectively. SEM images of the fabricated fiber cross-section (d) and the enlarged SEM image of the fiber's core and cladding (e).

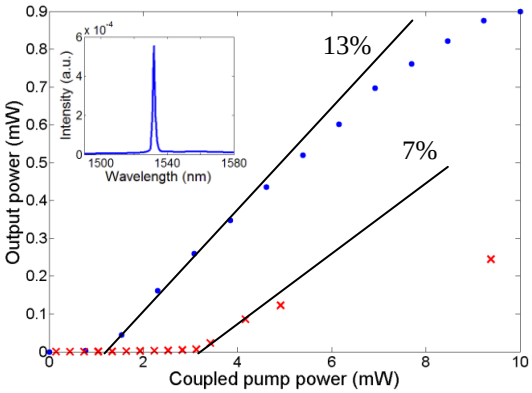

Figure 2: Fiber laser output power plotted against the coupled pump power for a fiber length of 1 m (crosses) and 2.2 m (circles). The figure inset is a plot of the laser output spectrum for 5 mW of pump power coupled into the 1 m length of fiber.

Fig. 2 shows the measured laser output power when using fibre lengths of 1 m and 2.2 m. Due to the long lifetime of the energy levels above the upper state of the laser transition, there was population trapping in these energy levels and, therefore, longer than expected fibre lengths were required to absorb sufficient pump light. The lasing for the 1 m fibre length at 1532 nm, close to the peak of the absorption spectrum for an un-pumped fibre also confirmed this ground state depletion.

The slope efficiency of the 2.2 m fiber laser (13 %) is much less than the Stokes efficiency of 63 %, probably due to the high loss of the fiber, which was measured to be 2.3 dB/m. This loss was estimated using the bulk glass loss and a cutback loss measurement at 1.3 μm.

This microstructured fibre laser demonstrated lasing using an extruded-microstructure fiber. It is expected that the output power of our extruded laser could be increased considerably through modifications to the fiber geometry, as a larger core diameter would increase the number of dopant ions in the core and alleviate the limitations associated with the ground state depletion.

4. Thulium tellurite spectroscopy

An energy level diagram for Tm is shown in Fig. 3. Absorption measurements were performed on small samples of thulium-doped tellurite glass to determine the lifetimes of the upper ($^3H_4$) and lower ($^3H_5$) energy levels of the 2.3μm transition and of the $^3F_4$ energy level that must decay to the ground state. Radiative lifetimes were calculated using the Judd-Ofelt analysis and non-radiative decay rates were calculated from previous analyses of the erbium tellurite glass spectroscopy [4].

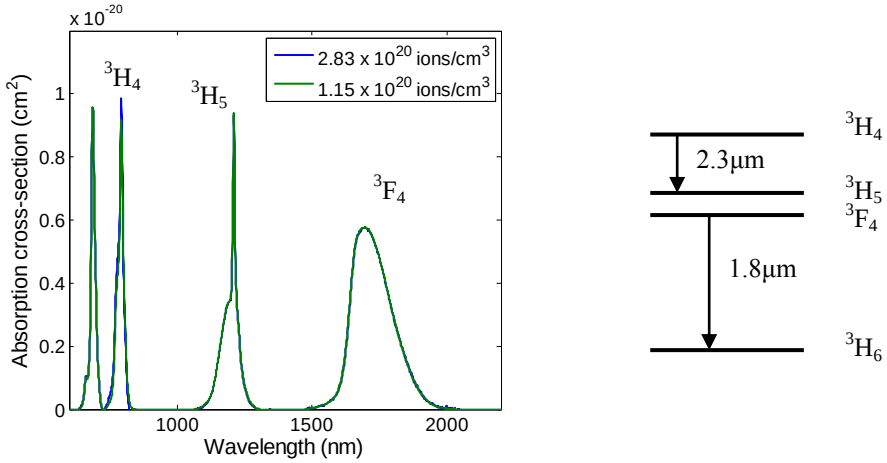

Figure 3: Absorption cross-sections of the thulium energy levels, calculated using two different thulium concentrations, and the Tm energy level diagram.

Absorption spectra were measured using a spectrophotometer. The absorption cross-sections of the thulium energy levels in the tellurite glass were then calculated and are plotted in Fig. 3.

The radiative lifetimes calculated using a Judd-Ofelt analysis were approximately 1.8 ms for both the $^3F_4$ and $^3H_5$ energy levels and approximately 0.3 ms for the $^3H_4$ level. The rate of non-radiative decay from the $^3H_5$ level to the $^3F_4$ level was calculated to be 4×10^4 s^{-1}, which would reduce the lifetime of the $^3H_5$ energy level to 25 μs. The non-radiative decay from the $^3H_5$ level to the $^3F_4$ level quickly depopulates the lower laser level. Non-radiative decay from the $^3H_4$ level to the $^3H_5$ level is negligible due to the much larger energy gap, and therefore would not affect the lifetime of the $^3H_4$ level.

Other glass hosts are less suitable for lasing at 2.35 μm. The higher maximum phonon energy of silica glass (1100 cm^{-1}) quenches the lifetime of the $^3H_4$ energy level. In fluorozirconate-based glasses , the low maximum phonon energy (550 cm^{-1}) results in significantly less non-radiative decay rate (1×10^3 s^{-1}) [5] across the $^3H_5$ to $^3F_4$ transition, which results in a lifetime of 0.85 ms for the $^3H_5$ energy level in this glass, only slightly smaller than that for the $^3H_4$ energy level (1.36 ms) [6]. The maximum phonon energy of the tellurite glass (800 cm^{-1}) is well matched for efficient removal of the Tm^{3+} ions from the $^3H_5$ energy level while not quenching the lifetime of the upper laser level, and thus should improve the efficiency of this system.

5. Conclusions

Demonstration of lasing in a, extruded-microstructure tellurite glass fibre has opened up the possibility for the construction of a microstructured thulium doped tellurite fibre laser operating at 2.35 μm. Preliminary lifetime calculations suggest that tellurite glass would be a very suitable host for this laser system.

6. Acknowledgements

T.M. Monro acknowledges the support of an ARC Federation Fellowship. The authors acknowledge the support of the South Australian Government and DSTO for this work.

7. References

1. J. Wang, E. Vogel, and E. Snitzer, "Tellurite glass: a new candidate for fiber devices," Optical Materials **3**, 187-203 (1994).
2. M. R. Oermann, H. Ebendorff-Heidepriem, Y. H. Li, T. C. Foo, and T. M. Monro, "Index matching between passive and active tellurite glasses for use in microstructured fiber lasers: Erbium doped lanthanum-tellurite glass," Optics Express **17**, 15578-15584 (2009).
3. M. R. Oermann, H. Ebendorff-Heidepriem, D. J. Ottaway, D. G. Lancaster, P. J. Veitch, and T. M. Monro, "Extruded microstructured fiber lasers," Optics Letters **Submitted** (2011).
4. L. Gomes, A. P. H. Librantz, S. D. Jackson, M. R. Oermann, H. Ebendorff-Heidepriem, D. J. Ottaway, and T. M. Monro, "Energy level decay and excited state absorption processes in erbium-doped tellurite glass," Journal of Applied Physics **Submitted** (2011).
5. J. L. Adam, "Lanthanides in non-oxide glasses," Chemical reviews **102**, 2461-2476 (2002).
6. M. Kozak, D. Goebel, R. Caspary, and W. Kowalsky, "Spectroscopic properties of thulium-doped zirconium fluoride and indium fluoride glasses," Journal of Non-Crystalline Solids **351**, 2009-2021 (2005).

Oermann, M., Ottaway, D., Ebendorff-Heidepriem, H., Veitch, P. & Monro, T.M. (2010) `Microstructured Erbium Doped Tellurite Fibre Laser`, paper presented at the 19th Australian Institute of Physics Congress/35th Australian Conference on Optical Fibre Technology (ACOFT/AIP), Melbourne, December 2010

Oermann, M., Ottaway, D., Veitch, P., Ebendorff-Heidepriem, H. & Monro, T.M. (2009) `Erbium-doped bulk tellurite glass laser at 1.5 μm', paper presented at the Australian Conference on Optics, Lasers and Spectroscopy (ACOLS), Adelaide, December 2009

Oermann, M., Ebendorff-Heidepriem, H., Li, Y. & Monro, T.M. (2008) `Spectroscopy of erbium in La^{3+}-doped tellurite glass & fibres', paper presented at the Australian Conference on Optical Fibre Technology (ACOFT), Sydney, July 2008

Li, Y., Oermann, M., Ebendorff-Heidepriem, H. & Monro, T.M. (n.d.) `Comparison of upconversion emission in Er^{3+}-doped ZBLAN and tellurite fibre laser'.

Ebendorff-Heidepriem, H., Foo, T.C., Li, Y., Oermann, M. & Monro, T.M. (2008) `New tellurite glasses for erbium fibre lasers', paper presented at the Australian Conference on Optical Fibre Technology (ACOFT), Sydney July 2008

Oermann, M., Li, Y., Ebendorff-Heidepriem, H. & Monro, T.M. (2008) `Core doped tellurite microstructured optical fibre for erbium fibre laser at 2.7μm', paper presented at the AIP Congress 2008 AOS, Adelaide, December 2008

Oermann, M., Ebendorff-Heidepriem, H., Ottaway, D., Veitch, P. & Monro, T.M. (2011) `Tellurite glass microstructured fibre laser development', paper presented at the PACRIM 2011, Cairns, July 2011

References

1. Pollnau, M., Ghisler, C., Bunea, G., Bunea. M., Willy, A., Luethy, W., *Erbium 3-um fiber laser in the power range for surgery*. Proc. SPIE 2629, 264, 1996.
2. Stoneman, R. and L. Esterowitz, *Efficient resonantly pumped 2.8-μm Er^{3+}: GSGG laser*. Optics Letters, 1992. **17**: p. 816-818.
3. Jensen, T., Diening, A., Huber, G., Chai, B., *Investigation of diode-pumped 2.8-μm Er: $LiYF_4$ lasers with various doping levels.* Optics Letters, 1996. **21**(8): p. 585-587.
4. Chen, D.W., Chen, D., Fincher, C., Rose, T., Vernon, F., Fields, P., *Diode-pumped 1-W continuous-wave Er: YAG 3-μm laser.* Optics Letters, 1999. **24**(6): p. 385-387.
5. Bedo, S., Pollnau, M., Lüthy, W., Weber, H., *Saturation of the 2.71μm laser output in erbium-doped ZBLAN fibers.* Optics Communications, 1995. **116**(1-3): p. 81-86.
6. Srinivasan, B., Poope, E., Tafoya, J., Jain, R., *High-power (400 mW) diode-pumped 2.7μm Er: ZBLAN fibre lasers using enhanced Er-Er cross-relaxation processes.* Electronics Letters, 1999. **35**(16): p. 1338-1340.
7. Zhu, X. and R. Jain, *Compact 2 W wavelength-tunable Er: ZBLAN mid-infrared fiber laser*. Optics Letters, 2007. **32**(16): p. 2381-2383.
8. Zhu, X. and R. Jain, *10-W-level diode-pumped compact 2.78 μm ZBLAN fiber laser*. Optics Letters, 2007. **32**(1): p. 26-28.
9. Zhu, X. and R. Jain, *Watt-level Er-doped and Er-Pr-codoped ZBLAN fiber amplifiers at the 2.7-2.8 μm wavelength range.* Optics Letters, 2008. **33**(14): p. 1578-1580.
10. Allain, J., M. Monarie, and H. Poignant, *Erbium-doped fluorozirconate single-mode fibre lasing at 2.71 μm.* Electronics Letters, 1989. **25**(1): p. 28-29.
11. Frerichs, C., *Efficient Er^{3+}-doped CW fluorozirconate fiber laser operating at 2.7μm pumped at 980 nm.* International Journal of Infrared and Millimeter Waves, 1994. **15**(4): p. 635-649.
12. Schneider, J., Hauschild, D., Frerichs, Ch., Wetenkamp, L., *Highly efficient Er^{3+}: Pr^{3+}-codoped CW fluorozirconate fiber laser operating at 2.7 μm.* International Journal of Infrared and Millimeter Waves, 1994. **15**(11): p. 1907-1922.
13. Linden, K.J., *Fiber laser with 1.2-W CW-output power at 2712 nm.* Photonics Technology Letters, IEEE, 2004. **16**(2): p. 401-403.
14. Jackson, S.D., T.A. King, and M. Pollnau, *Diode-pumped 1.7-W erbium 3-μm fiber laser*. Optics Letters, 1999. **24**(16): p. 1133-1135.
15. Pollnau, M., Ghisler, Ch., Bunea, G., Bunea, M., Lüthy, W., Weber, H., *150 mW unsaturated output power at 3 μm from a single mode fiber erbium cascade laser*. Applied Physics Letters, 1995. **66**: p. 3564.
16. Pollnau, M., Ghisler, Ch., M., Lüthy, Weber, H., Schneider, J., Unrau, U., *Three-transition cascade erbium laser at 1.7, 2.7, and 1.6 μm.* Optics Letters, 1997. **22**(9): p. 612-614.
17. Pollnau, M. and S. Jackson, *Mid-infrared fiber lasers.* Solid-State Mid-Infrared Laser Sources, 2003: p. 225-261.

18. Pollnau, M. and S.D. Jackson, *Erbium 3-μm fiber lasers.* IEEE Journal of Selected Topics in Quantum Electronics, 2001. **7**(1): p. 30-40.
19. Pollnau, M. and S.D. Jackson, *Energy recycling versus lifetime quenching in erbium-doped 3-μm fiber lasers.* Quantum Electronics, IEEE Journal of, 2002. **38**(2): p. 162-169.
20. Pollnau, M., Spring, R., Ghisler, C., Wittwer, S., Lüthy, W., Weber, H., *Efficiency of erbium 3-μm crystal and fiber lasers.* Quantum Electronics, IEEE Journal of, 1996. **32**(4): p. 657-663.
21. Sandrock, T., A. Diening, and G. Huber, *Laser emission of erbium-doped fluoride bulk glasses in the spectral range from 2.7 to 2.8 μm.* Optics Letters, 1999. **24**(6): p. 382-384.
22. Sandrock, T., Fischer, D., Glas, P., Leitner, M., Wrage, M., Diening, A., *Diode-pumped 1-W Er-doped fluoride glass M-profile fiber laser emitting at 2.8 μm.* Optics Letters, 1999. **24**(18): p. 1284-1286.
23. Poppe, E., B. Srinivasan, and R. Jain, *980 nm diode-pumped continuous wave mid-IR (2.7 μm) fibre laser.* Electronics Letters, 1998. **34**(24): p. 2331-2333.
24. Schneider, J., *Mid-infrared fluoride fiber lasers in multiple cascade operation.* Photonics Technology Letters, IEEE, 1995. **7**(4): p. 354-356.
25. Srinivasan, B., J. Tafoya, and R. Jain. *Diode-pumped high power CW 2.7 μm Er fiber lasers*: IEEE. CLEO 1999, Paper CPD23 (post deadline)
26. Srinivasan, B., J. Tafoya, and R. Jain, *High-power" Watt-level" CW operation of diode-pumped 2.7 μm fiber lasers using efficient cross-relaxation and energy transfer mechanisms.* Optics Express, 1999. **4**(12): p. 490.
27. Yanagita, H., Masuda, I., Yamashita, T., Toratani, H., *Diode laser pumped Er^{3+} fibre laser operation between 2.7-2.8 μm.* Electronics Letters, 1990. **26**(22): p. 1836-1838.
28. Busse, L.E., G. McCabe, and I.D. Aggarwal, *Wavelength dependence of the scattering loss in fluoride optical fibers.* Optics Letters, 1990. **15**(8): p. 423-424.
29. France, P., *Fluoride glass optical fibers*. 1990: Blackie (Glasgow and Boca Raton, Fla.)
30. Wang, J., E. Vogel, and E. Snitzer, *Tellurite glass: a new candidate for fiber devices.* Optical Materials, 1994. **3**(3): p. 187-203.
31. Cankaya, H. and A. Sennaroglu, *Bulk Nd^{3+}-doped tellurite glass laser at 1.37 μm.* Applied Physics B: Lasers and Optics, 2010. **99**(1): p. 121-125.
32. Iparraguirre, I., Azcargorta, J., Fernández-Navarro, J., Al-Saleh, M., Fernández, J., Balda, R., *Laser action and upconversion of Nd^{3+} in tellurite bulk glass.* Journal of Non-Crystalline Solids, 2007. **353**(8-10): p. 990-992.
33. Lei, N., B. Xu, and Z. Jiang, *Ti: sapphire laser pumped Nd: tellurite glass laser.* Optics Communications, 1996. **127**(4-6): p. 263-265.
34. Mori, A., Y. Ohishi, and S. Sudo, *Erbium-doped tellurite glass fibre laser and amplifier.* Electronics Letters, 1997. **33**(10): p. 863-864.
35. Richards, B., Jha, A., Tsang, Y., Binks, D., Lousteau, J., Fusari, F., Lagatsky, A., Brown, C., Siblet, W., *Tellurite glass lasers operating close to 2 μm.* Laser Physics Letters, 2010. **7**(3): p. 177-193.
36. Richards, B., Tsang, Y., Binks, D., Lousteau, J., Jha, A., *Efficient~ 2 μm Tm^{3+}-doped tellurite fiber laser.* Optics Letters, 2008. **33**: p. 402.

37. Richards, B., Tsang, Y., Binks, D., Lousteau, J., Jha, A., *2 μm Tm^{3+}/Yb^{3+}-doped tellurite fibre laser.* Journal of Materials Science: Materials in Electronics, 2009. **20**: p. 317-320.
38. Tsang, Y., Richards, B., Binks, D., Lousteau, J., Jha, A., *Tm^{3+}/Ho^{3+} codoped tellurite fiber laser.* Optics Letters, 2008. **33**(11): p. 1282.
39. Tsang, Y., Richards, B., Binks, D., Lousteau, J., Jha, A., *A $Yb^{3+}/Tm^{3+}/Ho^{3+}$ triply-doped tellurite fibre laser.* Optics Express, 2008. **16**(14): p. 10690.
40. Wang, J., Machewirth, D., Wu, F., Snitzer, E., Vogel, E., *Neodymium-doped tellurite single-mode fiber laser.* Optics Letters, 1994. **19**(18): p. 1448-1449.
41. Fusari, F., Lagatsky, A., Richards, B., Jha, A., Sibbett, W., Brown, C., *Spectroscopic and lasing performance of Tm^{3+}-doped bulk TZN and TZNG tellurite glasses operating around 1.9 μm.* Optics Express, 2008. **16**(23): p. 19146-19151.
42. Stanworth, J., *Tellurite glasses.* Nature, 1952. **169**: p. 581-582.
43. Yakhkind, A., *Tellurite glasses.* Journal of the American Ceramic Society, 1966. **49**(12): p. 670-675.
44. Narazaki, A., Tanaka, K., Hirao, K., Soga, N., *Effect of poling temperature on optical second harmonic intensity of sodium zinc tellurite glasses.* Journal of Applied Physics, 1998. **83**(8): p. 3986-3990.
45. Feng, X., Monro, T., Finazzi, V., Moore, R., Frampton, K., Petropoulos, P., Richardson, D., *Extruded singlemode, high-nonlinearity, tellurite glass holey fibre.* Electronics Letters, 2005. **41**(15): p. 835-837.
46. Domachuk, P., Wolchover, N., Cronin-Golomb, M., Wang, A., George, A., Cordeiro, C., Knight, J., Omenetto, F., *Over 4000 nm bandwidth of mid-IR supercontinuum generation in sub-centimeter segments of highly nonlinear tellurite PCFs.* Optics Express, 2008. **16**(10): p. 7161-7168.
47. Liao, M., Chaudhari, C., Qin, G., Yan, X., Suzuki, T., Ohishi, Y., *Tellurite microstructure fibers with small hexagonal core for supercontinuum generation.* Optics Express, 2009. **17**(14): p. 12174-12182.
48. Liao, M., Yan, X., Qin, G., Chaudhari, C., Suzuki, T., Ohishi, Y., *A highly non-linear tellurite microstructure fiber with multi-ring holes for supercontinuum generation.* Optics Express, 2009. **17**(18): p. 15481-15490.
49. Feng, X., Loh, W., Flanagan, J., Comerlingo, A., Dasgupta, S., Petropoulos, P., Horak, P., Framton, K., White, N., Price, J., Rutt, H., Richardson, D., *Single-mode tellurite glass holey fiber with extremely large mode area for infrared applications*. 2008: Optical Society of America.
50. Feng, X., Loh, W., Flanagan, J., Comerlingo, A., Dasgupta, S., Petropoulos, P., Horak, P., Framton, K., White, N., Price, J., Rutt, H., Richardson, *Single-mode tellurite glass holey fiber with extremely large mode area for infrared nonlinear applications.* Optics Express, 2008. **16**(18): p. 13651-13656.
51. Mori, A., Shikano, K., Enbutsu, W., Oikawa, K., Naganuma, K., Kato, M., Aozasa, S., *1.5 μm band zero-dispersion shifted tellurite photonic crystal fibre with a nonlinear coefficient of 675 W^{-1} km^{-1}*. European Conference in Optical Communications (ECOC) 2004.
52. Kumar, V., George, A., Knight, J., Russell, P., *Tellurite photonic crystal fiber.* Optics Express, 2003. **11**(20): p. 2641-2645.

53. Amorim, H., Vermelho, M., Gouveia-Neto, A., Cassanjes, F., Ribeiro, S., Messaddeq, Y., *Red-green-blue upconversion emission and energy-transfer between Tm^{3+} and Er^{3+} ions in tellurite glasses excited at 1.064 μm.* Journal of Solid State Chemistry, 2003. **171**(1-2): p. 278-281.
54. Babu, P., Seo, H., Jang, K, Kumar, K., Jayasankar, C., *1.55 μm emission and upconversion properties of Er^{3+}-doped oxyflurotellurite glasses.* Chemical Physics Letters, 2007. **445**(4-6): p. 162-166.
55. Boyer, J., Vetrone, F., Copabianco, Speghini, A., Bettinelli, M., *Optical transitions and upconversion properties of Ho doped ZnO- TeO glass.* Journal of Applied Physics, 2003. **93**: p. 9460.
56. Jin, Z., Nie, Q., Xu, T., Dai, S., Shen, X., Zhang, X., *Optical transitions and upconversion luminescence of Er^{3+}/Yb^{3+} codoped lead-zinc-tellurite oxide glass.* Materials Chemistry and Physics, 2007. **104**(1): p. 62-67.
57. Kanoun, A., Jaba, N., Mejri, H., Maaref, H., Selmi, A., *Effects of Activator Ion Concentration on the Upconversion Processes in Er^{3+}-Doped TeO_2-ZnO Glass.* Physica Status Solidi (a), 2001. **188**(3): p. 1145-1151.
58. Kumar, K., S. Rai, and D. Rai, *Upconversion studies in Er^{3+} doped TeO_2-M_2O (M= Li, Na and K) binary glasses.* Solid State Communications, 2006. **139**(7): p. 363-369.
59. Kumar, K., S. Rai, and D. Rai, *Upconversion and concentration quenching in Er^{3+}-doped TeO_2-Na_2O binary glasses.* Journal of Non-Crystalline Solids, 2007. **353**(13-15): p. 1383-1387.
60. Rai, V.K., K. Kumar, and S. Rai, *Upconversion in Pr^{3+} doped tellurite glass.* Optical Materials, 2007. **29**(7): p. 873-878.
61. Shen, X., Nie, Q., Xu, T., Dai, S., Wang, X., *Optical transitions and upconversion luminescence of Er^{3+}-doped tellurite glass.* Physica B: Condensed Matter, 2006. **381**(1-2): p. 219-223.
62. Shen, X., Nie, Q., Xu, T.,Peng, T., Gao, Y., *Green and red upconversion emission and energy-transfer between Er^{3+} and Tm^{3+} ions in tellurite glasses.* Physics Letters A, 2004. **332**(1-2): p. 101-106.
63. Vetrone, F., Boyer, J., Capobianco, J., Speghini, A., Bettinelli, M., *980 nm excited upconversion in an Er-doped ZnO-TeO_2 glass.* Applied Physics Letters, 2002. **80**(10): p. 1752-1754.
64. Yang, J., Dai, N., Dai, S., Wen, L., Hu, L., Jiang, Z., *Enhancement of upconversion luminescence in Er^{3+} doped tellurite glasses due to the introduction of $PbCl_2$.* Chemical Physics Letters, 2003. **376**(5-6): p. 671-675.
65. Yu, C., Zhang, J., Wen, L., Jiang, Z., *New transparent Er^{3+}-doped oxyfluoride tellurite glass ceramic with improved near infrared and up-conversion fluorescence properties.* Materials Letters, 2007. **61**(17): p. 3644-3646.
66. Zhang, J., Dai, S., Wang, G., Zhang, L., Sun, H., Hu, L., *Investigation on upconversion luminescence in Er^{3+}/Yb^{3+} codoped tellurite glasses and fibers.* Physics Letters A, 2005. **345**(4-6): p. 409-414.
67. Conti, G.N., Tikhomirov, V., Seddon, A., Bettinelli, M., Spaghini, A., Berneschi, S., Brenci, M., Pelli, S., Righini, G., Chan, B., *Characterization of ion-exchanged waveguides in tungsten tellurite and zinc tellurite Er-doped glasses.* Optical Engineering, 2003. **42**: p. 2805.

68. Le Neindre, L., Jiang, S., Hwang, B., Luo, T., Watson, J., Peyhambarian, N., *Effect of relative alkali content on absorption linewidth in erbium-doped tellurite glasses.* Journal of Non-Crystalline Solids, 1999. **255**(1): p. 97-102.
69. Dai, S., Yu, C., Zhou, G., Zhang, J., Wang, G., Hu, L., *Concentration quenching in erbium-doped tellurite glasses.* Journal of Luminescence, 2006. **117**(1): p. 39-45.
70. Hocdé, S., Jiang, S., Peng, X., Peyhambarian, N., Luo, T., Morrell, M., *Er^{3+} doped boro-tellurite glasses for 1.5 μm broadband amplification.* Optical Materials, 2004. **25**(2): p. 149-156.
71. Dai, S., Wu, J., Zhang, J., Wang, G., Jiang, Z., *The spectroscopic properties of Er^{3+}-doped TeO_2-Nb_2O_5 glasses with high mechanical strength performance.* Spectrochimica Acta Part A: Molecular and Biomolecular Spectroscopy, 2005. **62**(1-3): p. 431-437.
72. Rolli, R., Montagna, M., Chaussedent, S., Monteil, A., Tikhomirov, V., Ferrari, M., *Erbium-doped tellurite glasses with high quantum efficiency and broadband stimulated emission cross section at 1.5 μm.* Optical Materials, 2003. **21**(4): p. 743-748.
73. Brovelli, S., Galli, A., Lorenzi, R., Meinardi, F., Spindo, G., Tavassi, S., Sigaev, V., Sukhov, S., Pernice, P., Aronne, A., Fanelli, E., Paleari, A., *Efficient 1.53 [mu] m erbium light emission in heavily Er-doped titania-modified aluminium tellurite glasses.* Journal of Non-Crystalline Solids, 2007. **353**(22-23): p. 2150-2156.
74. Ghosh, G., *Sellmeier coefficients and chromatic dispersions for some tellurite glasses.* Journal of the American Ceramic Society, 1995. **78**(10): p. 2828-2830.
75. Mori, A., Kobayashi, K., Yamada, M., Kanamori, T., Oikawa, K., Nishida, Y., Ohishi, Y., *Low noise broadband tellurite-based Er3+-doped fibre amplifiers.* Electronics Letters, 1998. **34**(9): p. 887-888.
76. Mori, A., Ono, H., Shikano, K., Shimizu, M., *980 nm band pumped Er3+-doped tellurite-based fibre amplifier with low-noise figure of less than 4.5 dB.* Electronics Letters, 2002. **38**(23): p. 1419-1420.
77. Mori, A., Sakamoto, T., Kobayashi, K., Shikano, K., Oikawa, K., Hoshino, K., Kanamori, T., Ohishi, Y., Shimizu, M., *1.58-um Broad-Band Erbium-Doped Tellurite Fiber Amplifier.* Journal of Lightwave Technology, 2002. **20**(5): p. 794.
78. Ohishi, Y., Mori, A., Yamada, M., Ono, H., Nishida, Y., Oikawa, K., *Gain characteristics of tellurite-based erbium-doped fiber amplifiers for 1.5-μm broadband amplification.* Optics letters, 1998. **23**(4): p. 274-276.
79. Shen, S., Jha, A., Liu, X., Naftaly, M., Bindra, K., Bookey, H., Kar, A., *Tellurite glasses for broadband amplifiers and integrated optics.* Journal of the American Ceramic Society, 2002. **85**(6): p. 1391-1395.
80. Yamada, M., Mori, A., Kobayashi, K., Ono, H., Kanamori, T., Oikawa, K., Nishida, Y., Ohishi, Y., *Gain-flattened tellurite-based EDFA with a flat amplification bandwidth of 76 nm.* Photonics Technology Letters, IEEE, 1998. **10**(9): p. 1244-1246.
81. Mori, A., *Tellurite-based fibers and their applications to optical communication networks.* Journal of the Ceramic Society of Japan, 2008. **116**(1358): p. 1040-1051.

82. Oermann, M.R., Ebendorff-Heidepriem, H., Li, Y., Foo, T., Monro, M., *Index matching between passive and active tellurite glasses for use in microstructured fiber lasers: Erbium doped lanthanum-tellurite glass.* Optics Express, 2009. **17**(18): p. 15578-15584.
83. Reisfeld, R., Boehm, L., Eckstein, Y., Lieblich, N., *Multiphonon relaxation of rare earth ions in borate, phosphate, germanate and tellurite glasses.* Journal of Luminescence, 1975. **10**(3): p. 193-204.
84. Reisfeld, R. and Y. Eckstein, *Radiative and non-radiative transition probabilities and quantum yields for excited states of Er^{3+} in germanate and tellurite glasses.* Journal of Non-Crystalline Solids, 1974. **15**(1): p. 125-140.
85. Chen, H., Liu, Y., Zhou, Y., Jiang, Z., *Spectroscopic properties of Er^{3+}-doped tellurite glass for 1.55 μm optical amplifier.* Journal of alloys and compounds, 2005. **397**(1-2): p. 286-290.
86. Chen, H., Liu, Y., Zhou, Y., Zhang, Q., Jiang, Z., *Spectroscopic properties of Er^{3+} doped TeO_2-BaO (Li_2O, Na_2O)-La_2O_3 glasses for 1.5-μm optical amplifiers.* Journal of Non-Crystalline Solids, 2005. **351**(37-39): p. 3060-3064.
87. Miniscalco, W., *Erbium-doped glasses for fiber amplifiers at 1500 nm.* Lightwave Technology, Journal of, 2002. **9**(2): p. 234-250.
88. Kumar, G., E. De la Rosa, and H. Desirena, *Radiative and non radiative spectroscopic properties of Er^{3+} ion in tellurite glass.* Optics Communications, 2006. **260**(2): p. 601-606.
89. Judd, B.R., *Optical absorption intensities of rare-earth ions.* Physical Review, 1962. **127**(3): p. 750.
90. Ofelt, G., *Intensities of Crystal Spectra of Rare Earth Ions.* The Journal of Chemical Physics, 1962. **37**: p. 511.
91. Lin, H., Liu, K., Pun, E., Ma, T., Peng, X., An, Q., Yu, J., Jiang, S., *Infrared and visible fluorescence in Er^{3+}-doped gallium tellurite glasses.* Chemical Physics Letters, 2004. **398**(1-3): p. 146-150.
92. Rolli, R., Montagna, M., Chiasera, A., Righini, G., Pelli, S., Jha, A., Tikhomirov, V., Tikhomirov, S., Monteil, A., Chaussedent, S., Ferrari, M., *A comparative study of the spectroscopic properties at 1.5 μm of erbium-activated fluoride and tellurite glasses.* Philosophical Magazine Part B, 2002. **82**(5): p. 573-585.
93. Rolli, R., Gatterer, K., Wachtler, M., Bettinelli, M., Speghini, A., Ajò, D., *Optical spectroscopy of lanthanide ions in ZnO-TeO_2 glasses.* Spectrochimica Acta Part A: Molecular and Biomolecular Spectroscopy, 2001. **57**(10): p. 2009-2017.
94. Jaba, N., H. Mansour, and B. Champagnon, *The origin of spectral broadening of 1.53 μm emission in Er^{3+}-doped zinc tellurite glass.* Optical Materials, 2009. **31**(8): p. 1242-1247.
95. Luo, Y., Zhang, J., Sun, J., Lu, S., Wang, X., *Spectroscopic properties of tungsten-tellurite glasses doped with Er^{3+} ions at different concentrations.* Optical Materials, 2006. **28**(3): p. 255-258.
96. Glas, P. and D. Fisher, *Cladding pumped large-mode-area Nd-doped holey fiber laser.* Optics Express, 2002. **10**(6): p. 286-290.
97. Knight, J., Birks, T., Cragan, R., Russell, P., de Sandro, P., *Large mode area photonic crystal fibre.* Electronics Letters, 1998. **34**(13): p. 1347-1348.

98. Kozlov, V., Hernandez-Cordero, J., Shu bochkin, R., Carter, A., Morse, T., *Silica-air double-clad optical fiber.* Photonics Technology Letters, IEEE, 2000. **12**(8): p. 1007-1009.
99. Limpert, J., Roser, F., Klingebiel, S., Schreiber, T., Wirth, C., Peschel, T., Eberhardt, R., Tünnermann, A., *The rising power of fiber lasers and amplifiers.* Selected Topics in Quantum Electronics, IEEE Journal of, 2007. **13**(3): p. 537-545.
100. Limpert, J., Schreiber, T., Liem, A., Nolte, S., Zellmer, H., Peschel, T., Guyenot, V., Tünnermann, A., *Thermo-optical properties of air-clad photonic crystal fiber lasers in high power operation.* Optics Express, 2003. **11**(22): p. 2982-2990.
101. Limpert, J., Schreiber, T., Nolte, S., Zellmer, H., Tünnermann, A., Iliew, R., Lederer, F., Broeng, J., Vienne, G., Petersson, A., Jakobsen, C., *High-power air-clad large-mode-area photonic crystal fiber laser.* Optics Express, 2003. **11**(7): p. 818-823.
102. Mortensen, N., Nielsen, M., Folkenberg, J., Petersson, A., Simonsen, H., *Improved large-mode-area endlessly single-mode photonic crystal fibers.* Optics Letters, 2003. **28**(6): p. 393-395.
103. Ramachandran, S., Nicolson, J., Ghalmi, S., Yan, M., Wisk, P., Monberg, E., Dimarcello, F., *Light propagation with ultralarge modal areas in optical fibers.* Optics Letters, 2006. **31**(12): p. 1797-1799.
104. Sahu, J., Jeong, Y., Richardson, D., Nilsson, J., *A 103 W erbium-ytterbium co-doped large-core fiber laser.* Optics Communications, 2003. **227**(1-3): p. 159-163.
105. Wong, W.S., Peng, X., McLaughlin, J., Dong, L., *Breaking the limit of maximum effective area for robust single-mode propagation in optical fibers.* Optics Letters, 2005. **30**(21): p. 2855-2857.
106. Wadsworth, W., Percival, R., Bouwmans, G., Knight, J., Russell, P., *High power air-clad photonic crystal fibre laser.* Optics Express, 2003. **11**(1): p. 48-53.
107. Furusawa, K., Kogure, T., Sahu, J., Lee, J., Monro, T., Richardson, D., *Efficient low-threshold lasers based on an erbium-doped holey fiber.* Photonics Technology Letters, IEEE, 2005. **17**(1): p. 25-27.
108. Monro, T.M., Richardson, D., Broderick, N., Bennett, P., *Modeling large air fraction holey optical fibers.* Journal of lightwave technology, 2000. **18**(1): p. 50.
109. Birks, T., J. Knight, and P.S.J. Russell, *Endlessly single-mode photonic crystal fiber.* Optics Letters, 1997. **22**(13): p. 961-963.
110. Knight, J., Birks, T., Russell, P., Atkin, D., *All-silica single-mode optical fiber with photonic crystal cladding.* Optics Letters, 1996. **21**(19): p. 1547-1549.
111. Brechet, F., Marcou, J., Pagnoux, D., Roy, P., *Complete analysis of the characteristics of propagation into photonic crystal fibers, by the finite element method.* Optical Fiber Technology, 2000. **6**(2): p. 181-191.
112. Li, Y., Wang, C., Chen, Y., Hu, M., Liu, B., Chai, L., *Solution of the fundamental space-filling mode of photonic crystal fibers: numerical method versus analytical approaches.* Applied Physics B: Lasers and Optics, 2006. **85**(4): p. 597-601.

113. Li, Y., Wang, C., Wang, Z., Hu, M., Chai, L., *Analytical solution of the fundamental space filling mode of photonic crystal fibers.* Optics & Laser Technology, 2007. **39**(2): p. 322-326.
114. Midrio, M., M.P. Singh, and C.G. Someda, *The space filling mode of holey fibers: an analytical vectorial solution.* Journal of lightwave technology, 2000. **18**(7): p. 1031.
115. Mortensen, N.A., *Effective area of photonic crystal fibers.* Arxiv preprint physics/0204008, 2002.
116. Sorensen, T., Broeng, J., Bjarker, A., Knudsen, E., Libori, S., *Macro-bending loss properties of photonic crystal fibre.* Electronics Letters, 2001. **37**(5): p. 287-289.
117. Tsuchida, Y., K. Saitoh, and M. Koshiba, *Design of single-moded holey fibers with large-mode-area and low bending losses: The significance of the ring-core region.* Optics Express, 2007. **15**(4): p. 1794-1803.
118. Vasantha Jayakantha Raja, R. and K. Porsezian, *A fully vectorial effective index method to analyse the propagation properties of microstructured fiber.* Photonics and Nanostructures-Fundamentals and Applications, 2007. **5**(4): p. 171-177.
119. Park, K.N. and K.S. Lee, *Improved effective-index method for analysis of photonic crystal fibers.* Optics Letters, 2005. **30**(9): p. 958-960.
120. Wadsworth, W., Knight, J., Reeves, W., Russell, P., Arriaga, J., *Yb^{3+}-doped photonic crystal fibre laser.* Electronics Letters, 2000. **36**(17): p. 1452-1454.
121. Dong, L., J. Li, and X. Peng, *Bend-resistant fundamental mode operation in ytterbium-doped leakage channel fibers with effective areas up to 3160 μm.* Optics Express, 2006. **14**(24): p. 11512-11519.
122. Dong, L., X. Peng, and J. Li, *Leakage channel optical fibers with large effective area.* JOSA B, 2007. **24**(8): p. 1689-1697.
123. Dong, L., Wu, T., McKay, H., Fu, L., Li, J., Winful, H., *All-Glass Large-Core Leakage Channel Fibers.* IEEE Journal of Selected Topics in Quantum Electronics, 2009. **15**(1): p. 47-53.
124. Fini, J., *Design of solid and microstructure fibers for suppression of higher-order modes.* Optics Express, 2005. **13**(9): p. 3477-3490.
125. Fini, J.M., *Bend-resistant design of conventional and microstructure fibers with very large mode area.* Optics Express, 2006. **14**(1): p. 69-81.
126. Kumar, A., V. Rastogi, and K. Chiang, *Leaky optical waveguide for high power applications.* Applied Physics B: Lasers and Optics, 2006. **85**(1): p. 11-16.
127. Fini, J.M. and S. Ramachandran. *Bend resistance of large-mode-area higher-order-mode fibers*. 2006: IEEE. LEOS Summer Topical Meetings, 2006
128. Wu, T.W., L. Dong, and H. Winful, *Bend performance of leakage channel fibers.* Optics Express, 2008. **16**(6): p. 4278-4285.
129. Fini, J.M., *Design of large-mode-area amplifier fibers resistant to bend-induced distortion.* JOSA B, 2007. **24**(8): p. 1669-1676.
130. Fini, J.M., *Bend-compensated design of large-mode-area fibers.* Optics Letters, 2006. **31**(13): p. 1963-1965.
131. Rastogi, V. and K. Chiang, *Leaky optical fibre for large mode area singlemode operation.* Electronics Letters, 2003. **39**(15): p. 1110-1112.

132. Rastogi, V. and K.S. Chiang, *Propagation characteristics of a segmented cladding fiber.* Optics Letters, 2001. **26**(8): p. 491-493.
133. Rastogi, V. and K.S. Chiang, *Holey optical fiber with circularly distributed holes analyzed by the radial effective-index method.* Optics Letters, 2003. **28**(24): p. 2449-2451.
134. Rastogi, V. and K.S. Chiang, *Analysis of segmented-cladding fiber by the radial-effective-index method.* JOSA B, 2004. **21**(2): p. 258-265.
135. D'Orazio, A., de Sario, M., Mescia, L., Petruzzelli, V., Prudenzano, F., *Design of double-clad ytterbium-doped microstructured fibre laser.* Applied surface science, 2005. **248**(1-4): p. 499-502.
136. Furusawa, K., Malinowski, A., Price, J., Monro, T., Sahu, J., Nilsson, J., Richardson, D., *Cladding pumped Ytterbium-doped fiber laser with holey inner and outer cladding.* Opt. Express, 2001. **9**(13): p. 714-720.
137. Knight, J., *Photonic crystal fibers and fiber lasers (Invited).* JOSA B, 2007. **24**(8): p. 1661-1668.
138. Monro, T.M. and H. Ebendorff-Heidepriem, *Progress in microstructured optical fibers.* Annu. Rev. Mater. Res., 2006. **36**: p. 467-495.
139. Snyder, A.W. and J.D. Love, *Optical waveguide theory*. 1983: Springer.
140. Richards, B., Shen, S., Jha, A., Tsang, Y., Binks, D., *Infrared emission and energy transfer in Tm^{3+}, Tm^{3+}-Ho^{3+} and Tm^{3+}-Yb^{3+}-doped tellurite fibre.* Optics Express, 2007. **15**(11): p. 6546.
141. Allen, R., L. Esterowitz, and R. Ginther, *Diode pumped single mode fluorozirconate fiber laser from the $^4I_{11/2}$ $^4I_{13/2}$ transition in erbium.* Applied Physics Letters, 1990. **56**(17): p. 1635-1637.
142. Bedo, S., W. Luthy, and H. Weber, *Limits of the output power in Er^{3+}: ZBLAN singlemode fibre lasers.* Electronics Letters, 1995. **31**(3): p. 199-200.
143. Brierley, M.C. and P.W. France, *Continuous wave lasing at 2.7 μm in an erbium-doped fluorozirconate fiber.* Electronics Letters, 1988. **24**(15): p. 935-937.
144. Dickinson, B., Golding, P., Pollnau, M., King, T., Jackson, S., *Investigation of a 791-nm pulsed-pumped 2.7-μm Er-doped ZBLAN fibre laser.* Optics Communications, 2001. **191**(3-6): p. 315-321.
145. Pollnau, M., Graf, T., Balmer, J., Lüthy, W., Weber, H., *Explanation of the cw operation of the Er^{3+} 3-μm crystal laser.* Physical Review A, 1994. **49**(5): p. 3990.
146. Zhu, X. and R. Jain, *Watt-level 100-nm tunable 3-μm fiber laser.* Photonics Technology Letters, IEEE, 2008. **20**(2): p. 156-158.
147. Pollnau, M., Ghisler, C., Lüthy, W., Weber, H., *Cross sections of excited-state absorption at 800 nm in erbium-doped ZBLAN fiber.* Applied Physics B: Lasers and Optics, 1998. **67**(1): p. 23-28.
148. Bogdanov, V.K., Booth, D., Gibbs, W., Javorniczky, J., Newman, P., MacFarlane, D., *Population dynamics in Er^{3+}-doped fluoride glasses.* Physical Review B, 2001. **63**(20): p. 205107.
149. Lupei, V. and S. Georgescu, *Erbium 3-μm laser as an upconversion system.* Optical Engineering, 1996. **35**: p. 1265-1272.

150. Golding, P., Jackson, S., King, T., Pollnau, M., *Energy transfer processes in Er^{3+}-doped and Er^{3+}, Pr^{3+}-codoped ZBLAN glasses.* Physical Review B, 2000. **62**(2): p. 856.
151. Jackson, S., T. King, and M. Pollnau, *Modelling of high-power diode-pumped erbium 3 µm fibre lasers.* Journal of Modern Optics, 2000. **47**(11): p. 1987-1994.
152. Knowles, D.S. and H.P. Jenssen, *Upconversion versus Pr-deactivation for efficient 3 µm laser operation in Er.* Quantum Electronics, IEEE Journal of, 1992. **28**(4): p. 1197-1208.
153. Zhu, X. and R. Jain, *Numerical analysis and experimental results of high-power Er/Pr: ZBLAN 2.7 µm fiber lasers with different pumping designs.* Applied Optics, 2006. **45**(27): p. 7118-7125.
154. Allain, J., M. Monerie, and H. Poignant, *Energy transfer in Er^{3+}/Pr^{3+}-doped fluoride glass fibres and application to lasing at 2.7 µm.* Electronics Letters, 1991. **27**(5): p. 445-447.
155. Coleman, D., Golding, P., King, T., Jackson, S., *'Spectroscopic and energy transfer parameters for Er^{3+}-doped and Er^{3+}, Pr^{3+}-codoped GeGaS glasses.* J. Opt. Soc. Am. B, 2002. **17**: p. 1982–1989.
156. Choi, Y.G., K.H. Kim, and J. Heo, *Spectroscopic Properties of and Energy Transfer in PbO–Bi_2O_3–Ga_2O_3 Glass Doped with Er2O3.* Journal of the American Ceramic Society, 1999. **82**(10): p. 2762-2768.
157. Coleman, D.J., Jackson, S., Golding, P., King, T., *'Measurements of the spectroscopic and energy transfer parameters for Er^{3+}-doped and Er^{3+}, Pr^{3+}-codoped PbO–Bi_2O_3–Ga_3O_3 glasses.* J. Opt. Soc. Am. B, 2002. **19**: p. 2927–2937.
158. dos Santos, E.A., Courrol, L., Kassab, L., Gomes, L., Wetter, N., Vieira, N., Ribeiro, S., *Evaluation of laser level populations of erbium-doped glasses.* Journal of Luminescence, 2007. **124**(2): p. 200-206.
159. Ebendorff-Heidepriem, H. and T.M. Monro, *Extrusion of complex preforms for microstructured optical fibers.* Optics Express, 2007. **15**(23): p. 15086-15092.
160. Shen, S., Jha, A., Zhang, E., Wilson, S., *Compositional effects and spectroscopy of rare earths (Er^{3+}, Tm^{3+}, and Nd^{3+}) in tellurite glasses.* Comptes Rendus Chimie, 2002. **5**(12): p. 921-938.
161. Conti, G.N., Berneschi, S., Bettinelli, M., Brenci, M., Chan, B., Pelli, S., Speghini, A., Righini, G., *Rare-earth doped tungsten tellurite glasses and waveguides: fabrication and characterization.* Journal of Non-Crystalline Solids, 2004. **345**: p. 343-348.
162. Sakida, S., T. Nanba, and Y. Miura, *Refractive-index profiles and propagation losses of Er^{3+}-doped tungsten tellurite glass waveguide by Ag^{+}-Na^{+} ion-exchange.* Materials Letters, 2006. **60**(28): p. 3413-3415.
163. Xu, T.F., Shen, X., Nie, Q., Gao, Y., *Spectral properties and thermal stability of Er^{3+}/Yb^{3+} codoped tungsten-tellurite glasses.* Optical Materials, 2006. **28**(3): p. 241-245.
164. Ebendorff-Heidepriem, H. and D. Ehrt, *Determination of the OH content of glasses.* Glass science and technology, 1995. **68**(5): p. 139-146.

165. O'Donnell, M., Miller, C., Furniss, D., Tikhomirov, V., Seddon, A., *Fluorotellurite glasses with improved mid-infrared transmission.* Journal of Non-Crystalline Solids, 2003. **331**(1-3): p. 48-57.
166. Furniss, D. and A.B. Seddon, *Principles and Applications of Thermal Analysis*, in *Thermal Analysis*, P. Gabbot, Editor. 2007, Blackwells.
167. Vogel, W., *Glass chemistry*. 1994: Springer-Verlag Berlin.
168. Barakos, G. and E. Mitsoulis, *Non-isothermal viscoelastic simulations of extrusion through dies and prediction of the bending phenomenon.* Journal of non-newtonian fluid mechanics, 1996. **62**(1): p. 55-79.
169. Roeder, E., *Extrusion of glass.* Journal of Non-Crystalline Solids, 1971. **5**(5): p. 377-388.
170. Ebendorff-Heidepriem, H., C. Voyce, and T.M. Monro, *Flow through extrusion dies.* submitted for publication, 2011.
171. Braglia, M., Mosso, S., Dai, G., Billi, E., Bonelli, L., Baricco, M., Battezzati, L., *Rheology of tellurite glasses.* Materials research bulletin, 2000. **35**(14-15): p. 2343-2351.
172. Saitoh, K. and M. Koshiba, *Numerical modeling of photonic crystal fibers.* Lightwave Technology, Journal of, 2005. **23**(11): p. 3580-3590.
173. Voyce, C.J., Fitt, A., Hayes, J., Monro, T., *Mathematical modeling of the self-pressurizing mechanism for microstructured fiber drawing.* Journal of lightwave technology, 2009. **27**(7): p. 871-878.
174. Kuhn, H., Fredrich-Thornton, S., Kränkel, C., Peters, R., Petermann, K., *Model for the calculation of radiation trapping and description of the pinhole method.* Optics Letters, 2007. **32**(13): p. 1908-1910.
175. Reisfeld, R., *Radiative and non-radiative transitions of rare-earth ions in glasses.* Rare Earths, 1975: p. 123-175.
176. Van Dijk, J. and M. Schuurmans, *On the nonradiative and radiative decay rates and a modified exponential energy gap law for 4f–4f transitions in rare earth ions.* The Journal of Chemical Physics, 1983. **78**: p. 5317.
177. Ebendorff-Heidepriem, H. and D. Ehrt, *Spectroscopic properties of Eu^{3+} and Tb^{3+} ions for local structure investigations of fluoride phosphate and phosphate glasses.* Journal of Non-Crystalline Solids, 1996. **208**(3): p. 205-216.
178. Weber, M., *Probabilities for Radiative and Nonradiative Decay of Er^{3+} in LaF_3.* Physical Review, 1967. **157**(2): p. 262.
179. Carnall, W., P. Fields, and K. Rajnak, *Spectral intensities of the trivalent lanthanides and actinides in solution. II. Pm^{3+}, Sm^{3+}, Eu^{3+}, Gd^{3+}, Tb^{3+}, Dy^{3+}, and Ho^{3+}*. Journal of Chemical Physics, 1968. **49**: p. 4412-4423.
180. Carnall, W., P. Fields, and K. Rajnak, *Electronic energy levels in the trivalent lanthanide aquo ions. I. Pr^{3+}, Nd^{3+}, Pm^{3+}, Sm^{3+}, Dy^{3+}, Ho^{3+}, Er^{3+}, and Tm^{3+}*. Journal of Chemical Physics, 1968. **49**: p. 4424-4442.
181. Carnall, W.T., P. Fields, and B. Wybourne, *Spectral intensities of the trivalent lanthanides and actinides in solution. I. Pr^{3+}, Nd^{3+}, Er^{3+}, Tm^{3+}, and Yb^{3+}*. Journal of Chemical Physics, 1965. **42**: p. 3797-3806.
182. Layne, C., W. Lowdermilk, and M. Weber, *Multiphonon relaxation of rare-earth ions in oxide glasses.* Physical Review B, 1977. **16**(1): p. 10.

183. Reisfeld, R. and Y. Eckstein, *Dependence of spontaneous emission and nonradiative relaxations of Tm and Er on glass host and temperature.* The Journal of Chemical Physics, 1975. **63**: p. 4001.
184. Ebendorff-Heidepriem, H. and D. Ehrt, *Optical spectroscopy of rare earth ions in glasses.* Glass science and technology, 1998. **71**(10): p. 289-299.
185. McCumber, D., *Einstein relations connecting broadband emission and absorption spectra.* Phys. Rev, 1964. **136**(4A): p. A954-A957.
186. Miniscalco, W.J. and R.S. Quimby, *General procedure for the analysis of Er^{3+} cross sections.* Optics Letters, 1991. **16**(4): p. 258.
187. Philipps, J., Töpfer, T., Ebendorff-Heidepriem, H., Ehrt, D., Sauerbrey, R., *Spectroscopic and lasing properties of Er^{3+}: Yb^{3+}-doped fluoride phosphate glasses.* Applied Physics B: Lasers and Optics, 2001. **72**(4): p. 399-405.
188. Zou, X. and H. Toratani, *Evaluation of spectroscopic properties of Yb^{3+}-doped glasses.* Physical Review B, 1995. **52**(22): p. 15889.
189. Zemon, S., Lambert, G., Andrews, L., Miniscalco, W., Hall, B., Wei, T., Folweiler, R., *Characterization of Er^{3+} doped glasses by fluorescence line narrowing.* Journal of Applied Physics, 1991. **69**(10): p. 6799-6811.
190. Liu, K. and E. Pun, *Comparative studies of spectroscopic properties in Er^{3+}-Yb^{3+} codoped phosphate glasses.* Journal of alloys and compounds, 2009. **470**(1-2): p. 340-346.
191. Liu, S., Song, F., Cai, H., Li, T., Zhang, X., Wu, Z., Tian, J., *Investigation of the roundtrip cavity loss in laser diode pumped erbium: ytterbium-phosphate glass microchip lasers.* Journal of Applied Physics, 2007. **102**(10): p. 103101-103101-4.
192. Dai, S., Xu, T., Nie, Q., Shen, X., Wang, X., *Fabrication and gain performance of Er^{3+}/Yb^{3+}-codoped tellurite glass fiber.* Journal of Rare Earths, 2008. **26**(6): p. 915-918.
193. Desirena, H., de la Rosa, E., Shulzgen, A., Shabet, S., Peyghambarian, N., *Er^{3+} and Yb^{3+} concentration effect in the spectroscopic properties and energy transfer in Yb3+/Er3+ codoped tellurite glasses.* Journal of Physics D: Applied Physics, 2008. **41**: p. 095102.
194. Gao, Y., Nie, Q., Xu, T., Shen, X., *Study of luminescence properties of novel Er^{3+} single-doped and Er^{3+}/Yb^{3+} co-doped tellurite glasses.* Spectrochimica Acta Part A: Molecular and Biomolecular Spectroscopy, 2005. **61**(6): p. 1259-1262.
195. Jacinto, C., Messais, D., Andrade, A., Lima, S., Baesso, M., Catunda, T., *Thermal lens and Z-scan measurements: Thermal and optical properties of laser glasses-A review.* Journal of Non-Crystalline Solids, 2006. **352**(32-35): p. 3582-3597.
196. Kassab, L., Kobayashi, R., Bell, M., Carmo, A., Catunda, T., *Thermo-optical parameters of tellurite glasses doped with Yb^{3+}*. Journal of Physics D: Applied Physics, 2007. **40**: p. 4073.
197. Lima, S., Falco, W., Bannwart, E., Andrade, L., de Oliveira, R., Moraes, J., Yukimitu, K., Araújo, E., Falcäo, E., Steimacher, A., Astrathm N., Bento, A., Medina, A., Baesso, M., *Thermo-optical characterization of tellurite glasses by thermal lens, thermal relaxation calorimetry and interferometric methods.* Journal of Non-Crystalline Solids, 2006. **352**(32-35): p. 3603-3607.

198. Pilla, V., Chillcce, E., Neves, A., Munin, E., Catunda, T., Cesar, C., Barbosa, L., *Thermal-lens study of thermo-optical properties of tellurite glasses.* Journal of materials science, 2007. **42**(7): p. 2304-2308.
199. Jacinto, C. and T. Catunda. *High-sensitivity absorption coefficients measurements using thermal lens spectrometry*. 2005.
200. Lima, S., Sampaio, J., Catunda, T., Bento, A., Miranda, L., Baesso, M., *Mode-mismatched thermal lens spectrometry for thermo-optical properties measurement in optical glasses: a review.* Journal of Non-Crystalline Solids, 2000. **273**(1-3): p. 215-227.
201. Koechner, *Solid-State Laser Engineering*. Optical Sciences, ed. W.T. Rhodes. 2006: Springer.
202. *http://www.infrared-thermography.com/material-1.htm*.
203. Barnard, C., Mylinski, P., Chrostowski, J., Kavehrad, M., *Analytical model for rare-earth-doped fiber amplifiers and lasers.* Quantum Electronics, IEEE Journal of, 1994. **30**(8): p. 1817-1830.
204. Hardy, A. and R. Oron, *Signal amplification in strongly pumped fiber amplifiers.* Quantum Electronics, IEEE Journal of, 1997. **33**(3): p. 307-313.
205. Kelson, I. and A.A. Hardy, *Strongly pumped fiber lasers.* Quantum Electronics, IEEE Journal of, 1998. **34**(9): p. 1570-1577.
206. Xue, D., Q. Lou, and J. Zhou, *Comparison of Yb-doped fiber laser with one-end and double-end pumping configuration.* Optics & Laser Technology, 2007. **39**(4): p. 871-874.
207. Jovanovic, N., *Novel Fibre Laser Sources based on Ultrafast Laser Inscribed Bragg Gratings*, in *MQ Photonics Research Centre*. 2010, Macquarie University: North Ryde, NSW.
208. Choi, Y., Lim, D., Kim, K., Cho, D., Lee, H., *Enhanced $^4I_{11/2}$ - $^4I_{13/2}$ transition rate in Er^{3+}/Ce^{3+}-codoped tellurite glasses.* Electronics Letters, 1999. **35**(20): p. 1765-1767.
209. Choi, Y.G., Kim, K., Park, S. ,Heo, J., *Comparative study of energy transfers from Er to Ce in tellurite and sulfide glasses under 980 nm excitation.* Journal of Applied Physics, 2000. **88**: p. 3832.
210. Shen, S., Huang, L., Joshi, P., Jha, A., *Gain characteristics of Er/ Ce codoped tellurite short fbre amplifier pumped at 980 nm.* Electronics Letters, 2003. **39**: p. 1797.
211. Shen, S., B. Richards, and A. Jha, *Enhancement in pump inversion efficiency at 980 nm in Er^{3+}, Er^{3+}/Eu^{3+} and Er^{3+}/Ce^{3+} doped tellurite glass fibers.* Optics Express, 2006. **14**: p. 5050-5054.
212. Yang, J., Zhang, L., Wen, L., Dai, S., Hu, L., Jiang, Z., *Comparative investigation on energy transfer mechanisms between Er^{3+} and Ce^{3+} (Eu^{3+}, Tb^{3+}) in tellurite glasses.* Chemical Physics Letters, 2004. **384**(4-6): p. 295-298.
213. Ebendorff-Heidepriem, H., S.C. Warren-Smith, and T.M. Monro, *Suspended nanowires: Fabrication, design and characterization of fibers with nanoscale cores.* Optics Express, 2009. **17**(4): p. 2646-2657.